Aero-acoustic Shape Optimization of a Supersonic Business Jet

Andrea Minelli

ONERA

THE FRENCH AEROSPACE LAB

UNIVERSITE DE NICE-SOPHIA ANTIPOLIS - UFR Sciences
Ecole Doctorale de Sciences Fondamentales Appliquées (EDSFA)

THESE

pour obtenir le titre de
Docteur en Sciences
de l'Université de Nice-Sophia Antipolis
Discipline : **Mathématiques Appliquées**

présentée et soutenue par
Andrea Minelli

Aero-acoustic Shape Optimization of a Supersonic Business Jet

Thèse dirigée par **Jean-Antoine DESIDERI**
et encadrée par **Itham SALAH EL DIN** et **Gérald CARRIER**
soutenue le 25/11/2013

Jury :

M. Christophe CORRE	INP Grenoble	Rapporteur
M. François COULOUVRAT	UPMC	Rapporteur
M. Bijan MOHAMMADI	CERFACS	Rapporteur
M. Juan Jose ALONSO	Stanford University	Examinateur
M. Gérald CARRIER	ONERA	Examinateur
M. Franck DAGRAU	Dassault Aviation	Examinateur
M. Itham SALAH EL DIN	ONERA	Examinateur
M. Atsushi UENO	JAXA	Examinateur
M. Jean-Antoine DESIDERI	INRIA - OPALE	Directeur

After the finishing touch had been placed on the work, the craftsman balanced his body in twin wings and suspended his body in the open air; "I warn you to travel in the middle course, Icarus, if too low the waves may weigh down your wings, if you fly too high the fires will scorch your wings. Stay between both. I order you not to look at Boötes, or Helice, or the drawn sword of Orion. Seize the road with me as your leader!"

Ovidius , Metamorphoses, Vol. VIII. 183-235, AD 8

Acknowledgments

During these three passionate years, many people and many events have contributed to the development of this thesis.

First of all, I would like to thank Jean-Antoine Désidéri that first believed in me, giving me the opportunity to join his staff and then to conduct this research at ONERA. His competence has guided me towards optimization and its secrets, his passion for research has also motivated myself to carry on this experience. His guide was the focal point of inspiration througout my PhD work.

Heartfelt thanks to my ONERA supervisors Itham Salah el Din and Gérald Carrier. I owe a lot to them, beyond their technical competence and their professionalism which I benefited, it is on the human scale that a friendship has been established.

I would like to thank Prof. Juan J. Alonso (Stanford University) for the valuable discussions on the design of low-boom configurations, Adrien Loseille (INRIA) and Gilles Chaineray (ONERA-DSNA) for their expertise and guidance in unstructured grids and mesh adaptation.

The Department of Applied Aerodynamics and in particular the Civil Aircraft Unit have provided an excellent environment for this research. I would like to thanks all the engineers, the PhD students and the internship students with whom I have discussed about everything or simply I have crossed in the corridors or in the cafeteria. A special thank to my office collegues who are now also my friends Ludovic and Mehdi. Together we passed very good times.

I will not forget neither the support from my friends Paolo, Andrea, Nicola, Imane, Eleonora, Dounia, Sophie and many others..

Last but not least I would thank my family. Their love always supported me during good and bad times.

Contents

Nomenclature

Chapter 1

AIDA	Acoustic Inverse Design Approach
CFD	Computational Fluid Dynamics
SCT	Supersonic Civil Transportation
SSBJ	Supersonic Business Jet

Chapter 2

A	Ray tube area, $[m^2]$
a	Local speed of sound, $[m/s]$
A_e	Equivalent area distribution, $[m^2]$
A_l	Lift term of the equivalent area, $[m^2]$
A_n	Amplitude of g_n functions
$A-SEL$	A-weighted sound exposure level
A_v	Volume term of the equivalent area, $[m^2]$
β	Prandtl-Glauert factor $\beta = \sqrt{M_\infty^2 - 1}$
$B-SEL$	B-weighted sound exposure level
$\mathcal{C}$	Mesh complexity parameter
CFD	Computational Fluid Dynamics
c_n	Wavefront propagation velocity, $[m/s]$
$C-SEL$	C-weighted sound exposure level
e	Mesh edge
F	Whitham F-function, $m^{0.5}$
γ	Specific heat ratio
$\mathcal{H}$	Computational grid
H	Transfer function
H_R	Approximation of the second derivative
L	Aircraft body length, $[m]$
l	Lift per unit length, $[N/m]$
$l_\mathcal{M}$	Length of an edge element
M_∞	Mach number
$\mathcal{M}$	Solution metric
μ	Mach angle, $\mu = asin(1/M)$ [deg]
$\mathbf{n}$	Normal to the wavefront
p	Local pressure, $[Pa]$
$PLdB$	Perceived loudness decibel
$\mathcal{Q}_\mathcal{M}$	Mesh quality function
R	Radius of the cylinder for pressure extraction, $[m]$

r	Vertical distance from the acoustic source, $[m]$
ρ_∞	Free stream density, $[kg/m^3]$
$\mathcal{S}$	Computational solution
SEL	Sound exposure level
SSBJ	Supersonic Business Jet
t	Time instant, $[s]$
$\tau_{0.1-0.9}$	Rise time, $[ms]$
θ	Azimuthal angle, [deg]
U_∞	Free stream density, $[m/s]$
u	Wind velocity, $[m/s]$
x, τ, ξ	Horizontal coordinate, $[m]$

Chapter 3

α	Angle of attack, $[deg]$
α_0	Zero lift angle of attack, $[deg]$
AAA	Automatic Anisotropic Adaptation
A_e	Equivalent area distribution, $[m^2]$
A_l	Lift term of the equivalent area, $[m^2]$
BC	Boundary condition
$\mathcal{C}$	Mesh complexity parameter
CAD	Computer aided design
$c_{D_{MIN}}$	Minimum drag coefficient
$c_{D_{wv}}$	Volume wave drag coefficient
CFD	Computational Fluid Dynamics
c_{L_0}	Lift coefficient at $\alpha = 0$ deg
Δ	Wing sweep angle
F	Whitham F-function, $[m^{0.5}]$
Φ	Perturbation velocity potential
L	Body length, $[m]$
$l_{\mathcal{M}}$	Length of an edge element
M	Local Mach number
M_∞	Free-stream Mach number
μ	Mach angle, $[deg]$
n	Multipole decomposition order
p	Local pressure, $[Pa]$
p_0	Free-stream pressure, $[Pa]$
$PLdB$	Perceived loudness decibel
$\mathcal{Q}_{\mathcal{M}}$	Mesh quality function
R	Radius of the cylinder for pressure extraction, $[m]$
S	Aircraft area distribution, $[m^2]$
σ	Source strength
SSBJ	Supersonic Business Jet
t/c	Wing thickness over chord ratio

Chapter 4

A	F-function coefficient, $[m^{0.5}]$
a	Local speed of sound, $[m/s]$
A_e	Equivalent area distribution, $[m^2]$
A_{eng}	Engine stream tube area, $[m^2]$

A_h	Area of ray tube at altitude h, $[m^2]$
a_h	Local speed of sound at altitude h, $[m/s]$
AIDA	Acoustic Inverse Design Approach
A_l	Lift term of the equivalent area, $[m^2]$
A_v	Volume term of the equivalent area, $[m^2]$
B_*	F-function coefficient, $[m^{0.5}]$
β_*	F-function coefficient, $[m^{-0.5}]$
C_*	F-function coefficient, $[m^{0.5}]$
CFD	Computational Fluid Dynamics
c_p	pressure coefficient, $c_p = \frac{p-p_\infty}{\frac{1}{2}\rho_\infty U_\infty^2}$
D_*	F-function coefficient, $[m^{0.5}]$
F	Whitham F-function, $[m^{0.5}]$
H	F-function coefficient, $[m^{0.5}]$
h	Cruise altitude, $[m]$
J_{A_e}	Objective function based on equivalent area
J_F	Objective function based on F-function
J_f	Objective function for fuselage tailoring
J_P	Objective function based on Ground signature
J_{comb}	Combined objective cost function
l	Lift per unit length, $[N/m]$
L	Aircraft body length, $[m]$
λ_*	F-function coefficient, $[m]$
M_∞	Mach number
M_h	Mach number at altitude h
μ	Mach angle, $[deg]$
η_*	F-function coefficient
p	Local pressure, $[Pa]$
W	Aircraft weigth, $[kg]$
p_h	Local pressure at altitude h, $[Pa]$
p_∞	Free stream pressure, $[Pa]$
U_∞	Free stream velocity, $[m/s]$
ρ_∞	Free stream density, $[kg/m^3]$
P_f	Bow shock amplitude, $[Pa]$
$PLdB$	Perceived loudness decibel
P_r	Rear shock amplitude, $[Pa]$
r	Radial co-ordinate
s	Slope of the area balance line, $[m^{-0.5}]$
t	F-function coefficient, $[m]$
y_f	F-function coefficient, $[m]$
y_r	Total signal length, $[m]$

Chapter 5

A	Total surface, $[m^2]$
A_e	Equivalent area distribution, $[m^2]$
A_{sh}	Sears-Haack area distribution, $[m^2]$
β	Sideslip angle, $[deg]$
C	Covariance matrix
C_*	F-function coefficient, $[m^{0.5}]$
C_D	Drag coefficient
c_{D_f}	Friction drag coefficient
c_{D_l}	Lift-induced drag coefficient

$c_{D_{wl}}$	Lifting wave drag coefficient
$c_{D_{wv}}$	Volume wave drag coefficient
C_f	Friction coefficient
CFD	Computational Fluid Dynamics
C_L	Lift coefficient
C_L^{target}	Lift target coefficient
D_*	F-function coefficient, $[m^{0.5}]$
δ	Variable perturbation
DV	Design variable
F	Whitham F-function, $[m^{0.5}]$
g	Constraint function
Γ	Dihedral angle, $[deg]$
H	F-function coefficient, $[m^{0.5}]$
$\mathcal{H}$	Computational grid
h	Cruise altitude, $[m]$
J_{acou}	Acoustic cost function
J_{aero}	Aerodynamic cost function
K_I	Shape parameter for induced drag, Osswald factor
K_L	Shape parameter for lift dependent wave drag
K_V	Shape parameter for volume wave drag
L	Total aircraft length, $[m]$
l	Lifting length, $[m]$
LB	Low boom
LD	Low drag
m	Mean of a points distribution
p	Local pressure, $[Pa]$
p_∞	Free-stream pressure, $[Pa]$
$\mathcal{S}$	Computational solution
S	Reference surface, $[m^2]$
sf	Equivalent area distribution scaling factor
SI	Sensitivity index
σ	CMA-ES step size
V	Total aircraft volume, $[m^3]$
x_i	Optimization variable
x_C	Beginning of the fuselage cabin, $[m]$

Chapter 6

A_e	Equivalent area distribution, $[m^2]$
C_D	Drag coefficient
C_L	Lift coefficient
C_{L_0}	Target lift coefficient
DV	Design variable
ϵ	Continuation parameter
g	Constraint function
I_S	Split index
J	Objective cost function
J_U	Composite objective cost function
K	Number of constraint functions
N	Number of design variables
n	Number of objective functions
ω	Descent direction

Ω_H	Split matrix
P	Projection matrix
θ	Relaxation factor
U	Utopia point
$\bar{U}$	Convex hull
W	Aircraft weigth, $[kg]$
WSA	Weighted sum approach
x	Design variable

Appendix A

a	Atmospheric local speed of sound, $[m/s]$
C_D	Total drag coefficient
C_{D_P}	Pressure drag coefficient
C_{D_f}	Friction drag coefficient
CFD	Computational Fluid Dynamics
d_{mic}	Microphone distance, $[m]$
g	Model acceleration, $[m/s^2]$
γ	Angle between the aircraft velocity and its projection in the horizontal plane, $[deg]$
H	Estimated model altitude, $[m]$
$JSGD$	Jones-Seebass-George-Darden shaped sonic boom theory
LBM	Low-boom model
M	Mach number
μ	Mach angle, $[deg]$
NWM	N-wave model
p_{atm}	Atmospheric pressure, $[Pa]$
ψ	Complementary angle of the velocity in the horizontal plane, $[deg]$
t	Time, $[s]$
T_{atm}	Atmospheric temperature, $[K]$
θ	Azimuth angle, $[deg]$
θ_x, θ_y	Pitching angles, $[deg]$
u_x, u_y	Components of the cross wind, $[m/s]$
v_{south}, v_{west}	South and west wind velocity, $[m/s]$
v_x, v_y, v_z	Model velocity components, $[m/s]$
x, y, z	Model trajectory, $[m]$
ξ	Angle between the wave front normal **n** and its projection in the horizontal plane **n'**, $[deg]$
z_{launch}	Model launching altitude, $[m]$
z_{mic}	Microphone altitude, $[m]$
z_{model}	Model altitude at each time step, $[m]$

Appendix B

A_e	Equivalent area distribution, $[m^2]$
A_{eng}	Engine stream tube area, $[m^2]$
A_l	Lift term of the equivalent area, $[m^2]$
A_v	Volume term of the equivalent area, $[m^2]$
B_*	F-function coefficient, $[m^{0.5}]$
β_*	F-function coefficient, $[m^{-0.5}]$
C_*	F-function coefficient, $[m^{0.5}]$
C_D	Drag coefficient
CFD	Computational Fluid Dynamics

C_L	Lift coefficient
F	Whitham F-function, $[m^{0.5}]$
γ	Specific heat ratio
H	F-function coefficient, $[m^{0.5}]$
L	Aircraft body length, $[m]$
l	Lift per unit length, $[N/m]$
λ_*	F-function coefficient, $[m]$
M_∞	Mach number
η_*	F-function coefficient
p	Local pressure, $[Pa]$
p_∞	Free stream pressure, $[Pa]$
$PLdB$	Perceived loudness decibel
R	Radius of the cylinder for pressure extraction, $[m]$
ρ_∞	Free stream density, $[kg/m^3]$
t	F-function coefficient, $[m]$
θ	Azimuth angle, $[deg]$
U_∞	Free stream velocity, $[m/s]$
W	Aircraft weigth, $[kg]$
y_f	F-function coefficient, $[m]$
y_r	Total signal length, $[m]$

Appendix C

cd	Crowding distance
f	Objective function
$\mathcal{F}$	Pareto front
I_ϵ	Ynary epsilon indicator
I_H	Hypervolume indicator
$\hat{I}_H$	Unary hypervolume indicator
J	Objective function
N	Nadir point
n_p	Domination count, number of solutions which dominate the solution p
P	Population of individuals
p	Solution of the population P
Q	Population of individuals
q	Solution of the population Q
S_p	Set of solutions dominated by the solution p
x	Design variable

Chapter 1

Introduction

When once you have tasted flight, you will forever walk the earth with your eyes turned skyward, for there you have been, and there you will always long to return.
Leonardo da Vinci

1.1 Towards the definition of a viable civil supersonic aircraft

After the breaking of the sound barrier in 1949 by the NASA Bell-X1 prototype, the idea of a supersonic civil transportation (SCT) program that is efficient, environmentally friendly and economically and technologically viable has joined the dreams of several engineers in the last six decades. No other project in aeronautics has involved the same number of studies, people and money as the development of a SCT [1] program. Concorde is the last and unique[1] commercial example of civil supersonic aircraft that has been proven to be a technological success, although an economic failure. Several technological and non technological barriers limit today the development of a new generation of SCT. Non technological barriers such as economical, political or emotional are far beyond the capabilities of the researchers, but are also tightly related to the success of SCT. Concerning technical issues, numerous, dependant disciplines are involved among which: aerodynamics, propulsion, structures and materials, stability and control, performances, noise and environmental impact all play a key role. The strong coupling of the different disciplines can be seen in the design of a supersonic configuration. High swept wings that are very efficient in the supersonic regime to reduce wave drag, have reduced efficiency at low speed. This determines high angle of attack during landing, low-visibility thus producing concept as the nose dropping system designed for Concorde. The same problem occurs at takeoff, where an increased thrust is required to produce more lift, which consequently generates high noise levels. Due to the increased thrust, engine materials have to resist to temperatures 2.5 times above the limit of aluminum alloys. Off-design conditions, in particular in the subsonic regime, are key problems for performance and propulsion. Engine cycles designed to be efficient in supersonic conditions lead to low bypass ratio as a contrast to typical subsonic engine cycles, thus producing high noise levels at low-speed. Weight reduction is an important aspect in any aircraft design, but it acquires increased importance for the design of a supersonic configuration where the payload is five times lower than

[1] The Russian TU-144 was a failure and was used in a limited period compared to Concorde.

a subsonic aircraft, due essentially to fuel consumption.[2] Several concerns involve environment, in particular supersonic fleet emissions and ozone depletion, but also radiation exposure at high altitude. Each of these problems determines a technological challenge, but one of the main limiting factor, unexpected during the firsts supersonic flight tests, is the sonic boom phenomenon. An aircraft flying at a supersonic regime produces pressure perturbations that reach the ground and may be perceived by human beings as detonations possibly source of unacceptable annoyance. The minimized sonic boom levels are required to satisfy environmental noise requirements, thus relaxing the actual prohibition for civil aircraft to fly supersonically overland that implies flight in an off-design regime where the performance are very poor. Indeed, the current regulation is very drastic concerning supersonic flight. The US FAR regulation 91.817 enacted in 1973 assumes all sonic booms unacceptable and prohibits civil aircraft flight exceeding Mach 1. This constitutes a blank prohibition, alleviating any standard that supersonic aircraft could satisfy in order for the FAA to allow supersonic flight. At international level the ICAO resolution 33-7 aims at ensuring that no unacceptable situation for the public is created by sonic boom from aircraft in commercial service. The regulation is so strict because, despite airport noise which is limited to a specific region, sonic boom of a single medium range flight impacts a surface in the order of hundred thousands of square kilometers, reaching typically around one million person in medium dense populated areas. Supersonic corridors, where supersonic civil flight is allowed, exist between Canada, Siberia and Australia and in some regions of the United States for military purposes. The definition of supersonic corridors over regions sparsely populated can limit the number of people affected, but compromise time savings due to an increased travel distance. New solutions and concepts have to be identified. Actually supersonic business jets are considered good candidates for a new generation of civil supersonic aircraft that could overcome the regulation limitations. This is due to the fact that to reduce sonic boom perception it is necessary to reduce the mass of the aircraft, however it is not sufficient to achieve an acceptable annoyance at ground.

Two main questions arise when the minimization of the sonic boom impact of a SSBJ configuration is considered: first is how to accurately predict the sonic boom phenomenon? Second is how to reduce the sonic boom impact at ground? Sonic boom prediction is a combination of aerodynamics, aero-acoustics and atmospheric science. A CFD computation over the complete analysis domain of interest, taking into account atmosphere stratification, turbulence, maneuvers, wind could ideally answer the first question. In practice, due to the different scales required to accurately predict acoustics $\mathcal{O}$(cm) over the computational domain of the analysis $\mathcal{O}$(km), researchers have pointed out that performing CFD computations today on the complete physical domain is out of reach due to the high computational cost [2]. For this reason multi-zonal approaches [2], where aerodynamic and acoustic models are coupled, represent the standard for sonic boom prediction. Aerodynamics can be based on first order correction of the supersonic linearized theory [3], or it can be evaluated using non-linear CFD to solve Euler or Navier-Stokes equations over a near-field domain that describes the region close to the aircraft [4]. Acoustic models describe the propagation of the pressure disturbances created by the aircraft along the ray tubes until they reach the ground as the sonic-boom ground signature. If one can create the paths that the ray tubes will follow, the solution of the sonic-boom-propagation problem reduces to the nonlinear problem of wave propagation of a complex signature along a ray tube of not constant cross-sectional area. Several acoustic codes exist [5],[6],[7] using aerodynamic initial conditions to propagate the acoustic signature along ray paths to the ground taking into account maneuvers, atmosphere stratification and wind gradients. Recently more accurate models have been introduced. Among these, Rallabhandi [8] recently used an augmented Burger's equation within the context of ray-tracing/geometrical acoustics to propagate the source disturbances to the ground while accounting for viscous effects that lead to nonzero thickness shock discontinuities. The coupling between the aerodynamic and acoustic models can be performed using a direct extrapolation of the F-function that describes the acoustic source properties, or using an intermediate matching based on multipole decomposition of the F-function [2]. This technique aims to make compliant the two models when complex geometrical configurations are considered [9].

[2] Concorde has a payload of 6% of the TOGW, while a subsonic aircraft shows values around 25%.

Once the sonic boom is predicted, a design technique for the definition of a low-boom configuration is required. Several studies conducted in the past [1],[10],[11] and recently [12],[4] have demonstrated that it is possible to reduce the sonic boom impact and/or re-shape the ground signature by modifying the aircraft shape. The methods developed in these studies are generally based on design procedures applied to complex and realistic configurations. The first low-boom designs were based on experience or on simplified theories, such as the first order correction of the supersonic linearized theory [3]. The classical design approach is based on the shaped sonic boom theory that has been developed in the late 1960s and early 1970s with the work of Jones [13], Petty [14], Seebass and George [15] and Darden [16]. This method, that aims at reducing the sonic boom at ground via the configuration shaping, has been recently validated with in-flight test in the context of the DARPA shaped sonic boom demonstrator [17] and the JAXA D-SEND 1 project [18]. Note that only the acoustic discipline is taken into account by this method.

It is known from the studies of Darden [16] that a trade-off between aerodynamics and acoustics is required because a low-boom configuration has the tendency to increase the volume wave drag. The evaluation of aerodynamics with CFD has become a standard and nowadays it can be used in the design phases combined with optimization techniques for the definition of supersonic optimal shape configurations as in Reuther and Jameson [19], Reuther et al. [20], Sasaki et al. [21], Mohammadi et al. [22]. More recently, multi-objective shape optimization problems for the simultaneous reduction of drag and sonic boom have been considered [4]. Multi-objective algorithms result in a set of optimal configurations, thus providing a trade-off between aerodynamics and acoustics. Optimal solutions form a finite set in which an improvement in one objective would lead to a degradation in other objectives. Usually these algorithms are based on evolutionary strategies or genetic algorithms, thus requiring a considerable amount of function evaluations. To avoid a dramatic increase of the computational time, simplified method for the bang prediction or surrogate models for function evaluations during the optimization have been adopted in past studies as in Choi et al. [23] and Seto et al. [24].

To sum up the first answer to the reduction of the sonic boom phenomenon is the development of the shaped sonic boom theory. Valuable tool for the preliminary design phases due to its reduced computational time, this design approach permits to analyze several configurations and their performance evaluations, but as main drawback, this theory uses a correction of the linearized theory and not a complete non-linear model. Furthermore, it only takes into account some sonic boom metrics for the definition of a shaped ground signature.
It is important to clarify at this stage what is defined as low or high fidelity prediction models. Low-fidelity models consists in surrogate models of the actual performance or in the adoption of simplified theory, while high-fidelity sonic boom prediction models are based on CFD computations. The tendency of past shape optimization studies was to use low-fidelity models based upon surrogate models, thus avoiding an increase of the computational time.
Such studies have as main objective the definition of a Pareto-set of solutions aiming at demonstrating the trade-off feasibility between low-boom and low-drag configurations. To our best knowledge, no coupling of an high-fidelity prediction methodology to optimize the shape of a supersonic business jet in order to reduce at the same time the sonic boom and the drag with innovative optimization algorithms based on the concept of cooperation and competition has been found in literature. The general trend is to analyze independently a complex multi-objective problem and an innovative algorithm that in general is applied to academic test cases.

This study aims at defining a trade-off between low-boom and low-drag configurations of a supersonic business jet using high-fidelity prediction tools based on CFD and multi-zonal sonic-boom prediction approaches. Different development have been made and analyzed to improve the prediction accuracy. Multipole matching method and anisotropic unstructured mesh adaptation based on interpolation error have to be investigated. Prediction is only a part of the optimization process that also involves the optimizer. Two innovative strategies based on cooperation and Nash game are analyzed and adopted to evaluate the Pareto front and the Nash equilibrium of the aero-acoustic problem. The aim here is not only the definition of a Pareto front but also the definition of a low-boom configuration close to

aerodynamic optimality.

The manuscript is structured as follows: after an introduction to the sonic boom phenomenon, three sonic boom prediction methods are analyzed, emphasizing the advantages and limitations of each approach (Chapter 2). The first two which are investigated are based respectively on the first order correction of the supersonic linearized theory (two layer approach) and on CFD near field computations (three-layer approach). Each approach is introduced and the general properties analyzed. The third approach is completely based on CFD and adopts anisotropic mesh adaptation. When the prediction is based on CFD it is demonstrated that the application of anisotropic mesh refinement increases the accuracy of the near-field solution avoiding numerical shocks dissipation. The two and three layer methodologies are then adopted to analyze the sonic boom properties of a supersonic business jet configuration coupled with an aerodynamic analysis (Chapter 3).
The sonic boom minimization is considered first using an inverse design approach (Chapter 4). A module called AIDA, based on the shaped sonic boom theory, has been developed and implemented. This method has been generalized and improved in Minelli et al. [25] in order to take into account more general configurations and different acoustic metrics than classical shaped sonic boom theory. The inverse design provides a valuable tool for preliminary design phases, but due to the lack of information concerning the aerodynamic performance, direct shape optimization methods have been investigated first on single-discipline problems (Chapter 5). Sensitivity analysis of acoustics and aerodynamics with respect to geometrical parameters is provided with the objective to identify a relevant shape parameterization for the optimization problem. The reduction of sonic boom and drag is considered separately on the same reference configuration resulting in the identification of the shape modifications required in the two cases and the analysis of the relationship between geometry parameters and physical phenomena. Finally, aerodynamics and acoustics are considered together in order to define a trade-off between low-boom and low-drag configurations (Chapter 6). The state of the art in terms of multi-objective algorithms have been adopted to evaluate the Pareto front of the aero-acoustic problem and the result has been compared to those obtained with innovative multi-objective algorithms. These algorithms based on cooperation and competition are exploited to explore the trade-off between aerodynamics and acoustics using the concept of Pareto optimality and Nash equilibrium as in Minelli et al. [26]. Cooperation is performed using a multiple gradient descent algorithm, while the competitive phase consists in virtual Nash games between acoustics and aerodynamics acting as virtual players on their own subset of variables to reach the Nash equilibrium. The continuum of Nash equilibrium is investigated, where the optimal aerodynamic configuration that belongs to the Pareto front is modified using Nash game strategies. The objective is to introduce the antagonism between disciplines progressively to reach a low-drag configuration with a reduced sonic boom. Finally cooperation and competition are exploited together for the identification of the Pareto front with an original technique. All the main results and future perspectives are summed up in the final conclusions (Chapter 7).

This thesis work has provided the following technical communications:

- Salah el Din, I., Carrier, G., Grenon, R., Le Pape, M.-C., Minelli, A., *Overview of Sonic Boom CFD Prediction Methodology in Use at ONERA and its Application to Supersonic Business Jet Configuration Design*, in proceedings of 11th ONERA-DLR Aerospace Symposium, ODAS, Toulouse, February 2011.

- Salah el Din, I., Le Pape, M.-C., Minelli, A., Grenon, R., Carrier, G., *Impact of Multipole Matching Resolution on Supersonic Aircraft Sonic Boom Assessment*, in proceedings of 4th EUCASS, St. Petersburg, July 2011.

- Minelli, A., Salah el Din, I., Carrier, G., *Advanced Optimization Approach for Supersonic Low-Boom Design.*, in proceedings of AIAA-CEAS Aeroacoustic conference, Colorado Springs, June 2012.

- Minelli, A., Salah el Din, I., *Sonic Boom Prediction and Inverse Design of the JAXA Supersonic Wing-Body Configuration using Unstructured Mesh*, ONERA RT 1/18167 DAAP, October 2012.

- Salah el Din, I., Minelli, A., *ONERA-JAXA - Low-Boom / Low-Drag Small Size Supersonic Aircraft design - Task 1.1 - D-SEND1 Drop Test Database - ONERA Analysis - Part 1*, ONERA RT 2/19342 DAAP, February 2013.

- Minelli, A., Loseille, A., *Anisotropic Unstructured Mesh Adaptation for Sonic Boom Prediction*, ONERA RT 4/18167 DAAP, February 2013.

- Désidéri, J.-A., Minelli, A., and Zerbinati, A., *A Cooperative Algorithm for Multi-Objective Optimization: Multiple-Gradient Descent Algorithm (MGDA)*, in proceedings of 4th Inverse Problems, Design and Optimization Symposium (IPDO-2013) Albi, France, June 2013.

- Désidéri, J.-A., Minelli, A., and Roca Leon, E., *A Competitive Algorithm for Two-Objective Optimization: Nash Game with Territory Splitting*, in proceedings of 4th Inverse Problems, Design and Optimization Symposium (IPDO-2013) Albi, France, June 2013.

- Minelli, A., Salah el Din, I., Carrier, G., Zerbinati, A. and Desideri, J.-A., *Cooperation and Competition Strategies in Multi-objective Shape Optimization -Application to Low-boom/Low-drag Supersonic Business Jet*, in proceedings of AIAA Applied Aerodynamics conference, San Diego, June 2013.

- Salah el Din, I., Le Pape, M.-C., Minelli, A., Grenon, R., Carrier, G., *Impact of Multipole Matching Resolution on Supersonic Aircraft Sonic Boom Assessment*, Progress in Flight Physics 5, pages 601-620, 2013.

This thesis work has provided the following submissions:

- Minelli, A., Salah el Din, I., Carrier, G., *Inverse Design Approach for Low-Boom Supersonic Configurations*, submitted to AIAA Journal 2013.

- Zerbinati, A., Minelli, A., Ghazlane, I., Desideri, J.-A., *Meta-model Assisted MGDA applied to Multi-objective Aerodynamic Shape Optimization*, submitted to Computer & Fluids 2013.

- Désidéri, J.-A., Minelli, A., and Roca Leon, E.,*Algorithms for Multi-Objective Optimization : a Quest for the Pareto Front* EUROGEN, Las Palmas, October 2013.

- Salah el Din, I., Minelli, A., Loseille, A., *Sonic Boom Assessment of Supersonic Configurations using Advanced Coupled CFD and Mesh Adaptation techniques* 29th ICAS, St. Petersburg, 2014.

- Carrier, G., Salah el Din, I., Minelli, A., *Validation and Verification of Numerical Sonic Boom Methods using JAXA D-SEND#1 Experiments and Code-to-Code Comparisons* 29th ICAS, St. Petersburg, 2014.

Chapter 2

Fundamentals of sonic boom prediction

Later, I realized that the mission had to end in a let-down because the real barrier wasn't in the sky but in our knowledge and experience of supersonic flight.
Chuck Yeager

Contents

The objective of this chapter is to introduce the main aspects of the sonic boom problem from a physical and a numerical point of view. The physical phenomenon is described, identifying the different regions concerned during the acoustic wave propagation from the source to the ground. Aspects that influence the sonic boom at ground are investigated in order to define their relative importance and different prediction models are proposed with a critical analysis of their limits.
The first order correction of the supersonic linearized theory is introduced and adopted to define a prediction model based on a two-layer approach. To overcome the limitations of the linearized theory, a CFD based three-layer approach is then presented. The analysis of the prediction methods is completed with a mono-layer approach based on CFD and on highly anisotropic mesh refinement. An introduction to error based mesh adaptation is also provided. Once prediction is ensured, it is required to quantify the annoyance due to the sonic boom phenomenon. Several sonic boom metrics are introduced and analyzed to define an acoustic cost function that will later be adopted in the optimization problems.

2.1 Physical description

Each body moving in a fluid produces pressure waves. Since a slight pressure change is propagated at the sound velocity, an aircraft flying faster than the speed of sound moves faster than the perturbations created by itself in the free-stream. These pressure disturbances, at some distance from the body, tend to pile up producing shock waves. The pressure field around the body is characterized by a pattern of shock and expansion waves generated at each geometrical discontinuities of the body such as wing, engine nacelle and control surfaces.

Two reference systems can be associated to the analysis of this problem: an aerodynamic reference system in motion with the body or an acoustic one, fixed with an inertial observator at ground. When the aerodynamic reference system is considered, the boundary between the undisturbed flow and the region in which the disturbances generated by the aircraft propagate is the so-called Mach cone which summit originates at the nose of the aircraft. Ahead of the shock generated at the nose, the flow is undisturbed forming a silent zone. An observer at ground level is aware of the sonic boom only if he is inside the Mach cone. In this domain, defined in the aerodynamic reference system, it is possible to distinguish three regions: near-field, mid-field and far-field. The near-field is practically defined as

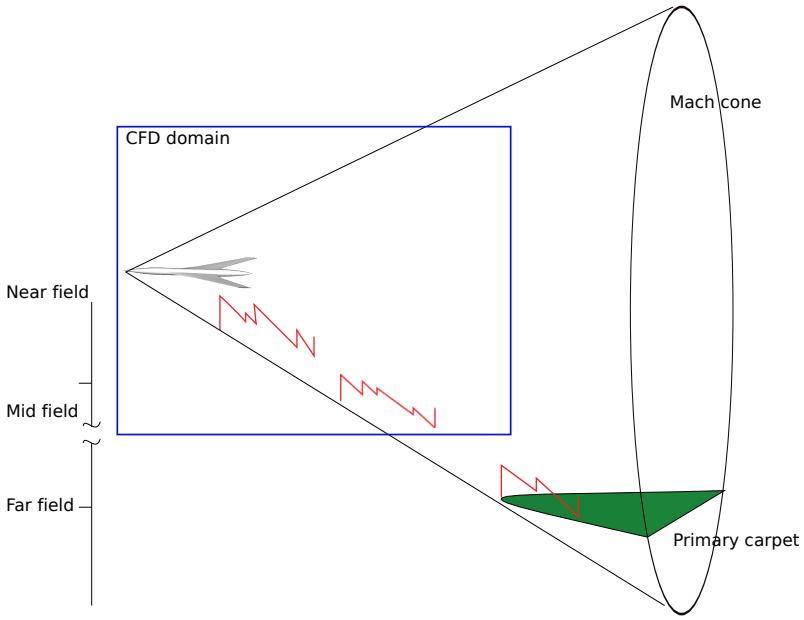

Figure 2.1: Physical domain of the sonic boom phenomenon. (Aerodynamic reference system).

the region that goes from the acoustic source to a distance equal to about ten body lengths and is dominated by non viscous equations as long as boundary layer interactions are neglected.
In the mid-field, defined as the region between about 10 and 100 body lengths, non linear effects mainly due to atmospheric non uniformity impact the propagation of the acoustic waves. Existing shocks tend to coalesce and new shocks can arise. The perturbations composing the signal propagate at their own local speed of sound through the atmosphere as a function of its local amplitude which possibly leading to multivalued signals. This is not physically acceptable, the actual solution is the appearance of a new shock pattern.
The remaining region that goes from about 100 body lengths to the ground is the far-field. The atmospheric propagation in this region introduces a source of large variability for sonic boom due to local weather, wind gradient, temperature, humidity and turbulence [27],[28],[29]. Atmospheric absorption affects the rise time of the shocks, typically leading to a rise time increase from 1 ms to 10 ms for SCT configurations [4].

The acoustic waves which travel downward through the atmosphere reach the ground in the so-called primary carpet area. It is the intersection between the refracted Mach cone and the ground and can have a lateral extension from 10 to 100 km as a function of the aircraft configuration and

flight conditions. It is also possible to distinguish the primary carpet, the region directly impacted by the signal produced by the aircraft, and the secondary carpet defined as the remaining ground region impacted by pressure disturbances. Between these two carpets, a shadow region exists where no boom is perceived. The acoustic rays intersecting the ground in the secondary carpet have been refracted either by the upper atmosphere, the ground, or both. The sonic boom has the tendency to decrease its amplitude from the primary to the secondary carpet. Generally the under-track ground signature is the loudest region for the sonic boom in case of horizontal steady flight conditions and is therefore usually adopted to characterize the magnitude of the entire phenomenon.

For an aircraft which has not been designed for low-boom, the classical under-track ground signature is characterized by an N-wave shape. People perceive the abrupt front and aft pressure increases while the linear expansion between them is not of any concern. Annoyance of people and structural damages (e.g. broken windows, cracked buildings) are the main undesired effects. The ground signature is defined as an impulsive, loud and low-frequency signal, and it is perceived as a double detonation noise [30]. It is impulsive because of the short duration (0.1-0.3 ms). Its loudness is related to the shocks overpressure amplitude ranging from 10 to 100 Pa, while human auditory system is adapted to respond to very small pressure fluctuations. It is also low-frequency because most of the spectral energy density is confined in the low-audible, infrasonic frequency range (1-30 Hz). For example, Concorde, during its supersonic regime at Mach 2, produces a ground N-wave signature with a maximum peak around 100 Pa and a total duration of 0.23 s.

Considering a supersonic steady flight the amplitude of the pressure perturbation mainly depends on the aircraft weight, flight altitude and Mach number. As the weight and the Mach decreases and the altitude increases the sonic boom impact is reduced. Business jet configurations are actually considered for their reduced weight with respect to larger civil transport aircraft. Furthermore in the limit of low supersonic Mach numbers, an appropriate choice of Mach number and altitude can lead to the Mach cut-off: the acoustic perturbations are completely dissipated during the propagation and do not reach the ground. Aerion [31] SSBJ project bases its capability to flight boomless overland on the exploitation of the Mach cut-off regime at a Mach number equal to 1.15.

Other factors that impact sonic boom are related to aircraft maneuvers that can produce drastic variations from the typical N-wave signature. Aircraft maneuvers can generate local shock amplifications due to focalization of the signal in the caustic region that results in an U-wave signature [32]. Caustics are both physical objects - regions of wave amplification - and geometrical ones - surfaces where the approximate ray theory gets singular [33]. When the aircraft is maneuvering or accelerating/decelerating the wavefront undergoes a modulation thus generally leading an amplification of the boom at ground up to two to three times the steady flight signature amplitude and a modification of the signature shape.

2.2 Whitham's correction of the supersonic linearized theory

Different strategies can be used for the numerical prediction of sonic boom at ground. According to the classic theory, sonic booms are computed within the framework of geometrical acoustics and the aerodynamic solution is evaluated using linearized methods. The prediction model based on the classical linearized supersonic theory suffers from the fact that this theory cannot provide a fully accurate description of nonlinear phenomena such as shocks. The limitation is due to the fact that linear theory does not take into account the characteristics curvature due to local Mach changes that determines different propagation speed of the acoustic disturbances. Whitham [3] was the first to introduce a correction of the supersonic linearized theory in order to describe the acoustic perturbations generated by an axy-symmetric supersonic projectile. Walkden [34] improved the work of Whitham taking into account lifting bodies.

At a sufficient distance from the acoustic source ($x \gg x - \beta r$) (see Figure 2.2) but still sufficiently close in the near-field (2-10 body lenghts beneath the aircraft) the pressure disturbance can be thought as being produced by a body of revolution with an equivalent area A_e defined as:

$$A_e = A_v + A_l \tag{2.1}$$

where A_v is the volume term defined as the aircraft section generated using a cutting plane inclined at the Mach angle with respect to the flying trajectory (see Figure 2.2). A_l is the so-called lift term that describes lift as an equivalent area distribution using the following relation:

$$A_l(\tau,\theta) = \frac{\beta\cos\theta}{\rho_\infty U_\infty^2}\int_0^\tau l(x)dx \tag{2.2}$$

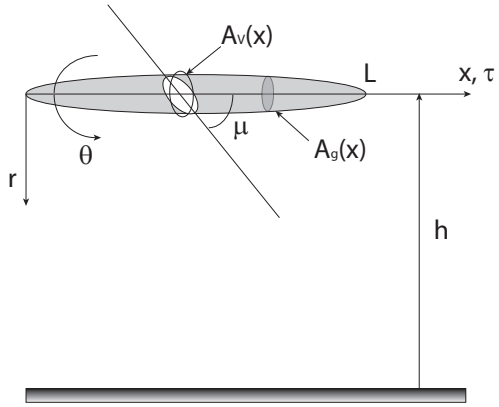

Figure 2.2: Nomenclature definitions.

The equivalent body of revolution produce the same disturbance (in the far field) as the real aircraft geometry so that pressure is related with the equivalent area distribution as:

$$\frac{\Delta p(x,r,\theta)}{\gamma p_\infty M_\infty^2} = \frac{1}{2\pi\sqrt{2\beta r}}\int_0^{x-\beta r}\frac{A_e''(\xi,\theta)}{\sqrt{(x-\beta r)-\xi}}d\xi \tag{2.3}$$

In classical sonic boom analysis, pressure is defined in terms of the Whitham F-function that represents a linear distribution of singularities:

$$F(\tau,\theta) = \frac{1}{2\pi}\int_0^\tau \frac{A_e''(x,\theta)}{\sqrt{\tau-x}}dx \tag{2.4}$$

so that equation (2.3) is re-written as:

$$\Delta P(\tau,\theta,r) = p_\infty\frac{\gamma M_\infty^2}{\sqrt{2\beta r}}F(\tau,\theta) \tag{2.5}$$

In shock regions the characteristics overlap to form a limit line where physical quantities are not unique. The remedy is the presence of shocks which cut-off the continuous solution before this occurs. Equation (2.5) clearly shows that a compression occurs when $F' > 0$, while an expansion appears when $F' < 0$. Respectively these regions represent zones where characteristics are converging and diverging.

It is important to point out that the Whitham theory provides a good approximation for sonic boom prediction if the Mach number is below M=3 ([35], [36]). Otherwise the theory quickly deviates from experimental data. The theory is applicable only in the case of weak shocks, as it assumes isentropic flow description. In addition, nonlinear regions typically located near the aircraft and caustics are not correctly described. Furthermore, it is assumed that the body is slender and pointed at the nose with the front shock attached. Nevertheless, even if these conditions are not strictly satisfied, the behavior of the pressure disturbances at large distance can be deduced. Despite these limitations the theory provides a valuable approach for both prediction and sonic boom minimization.

Equation (2.5) is fundamental in sonic boom prediction, because it shows that the F-function can be evaluated from a pressure field. The pressure field can be provided with any methods from simplified ones to full non linear CFD. This has driven a wide spectrum of techniques over the years for the prediction of the acoustic ground signature that we try to picture in Figure 2.3.

2.3 Boom prediction from the body to the ground

The ideal solution to predict sonic boom is to perform full CFD accurate calculations all the way to the ground. This essentially means to perform a simulation over a computational domain of the order of $\mathcal{O}(10^3$ km$^3)$ with a resolution able to avoid numerical dissipation of shocks thus capturing the acoustic phenomenon while taking into account external atmosphere factors.
The main obstacle to carry an accurate CFD solution from the flying altitude to the ground is the computational time required if no counter-measures are introduced. In particular the loss of shocks resolution due to spurious numerical dissipation dominates as the distance from the source increases. Multi-zonal methods are generally adopted to predict sonic boom from near-field to ground to by-pass this problem. These methods couple an aerodynamic model that describes the near-field with an acoustic model associated to the signal propagation to the ground. Figure 2.3 shows the different prediction methods available today to predict sonic boom. Each method has a different accuracy and

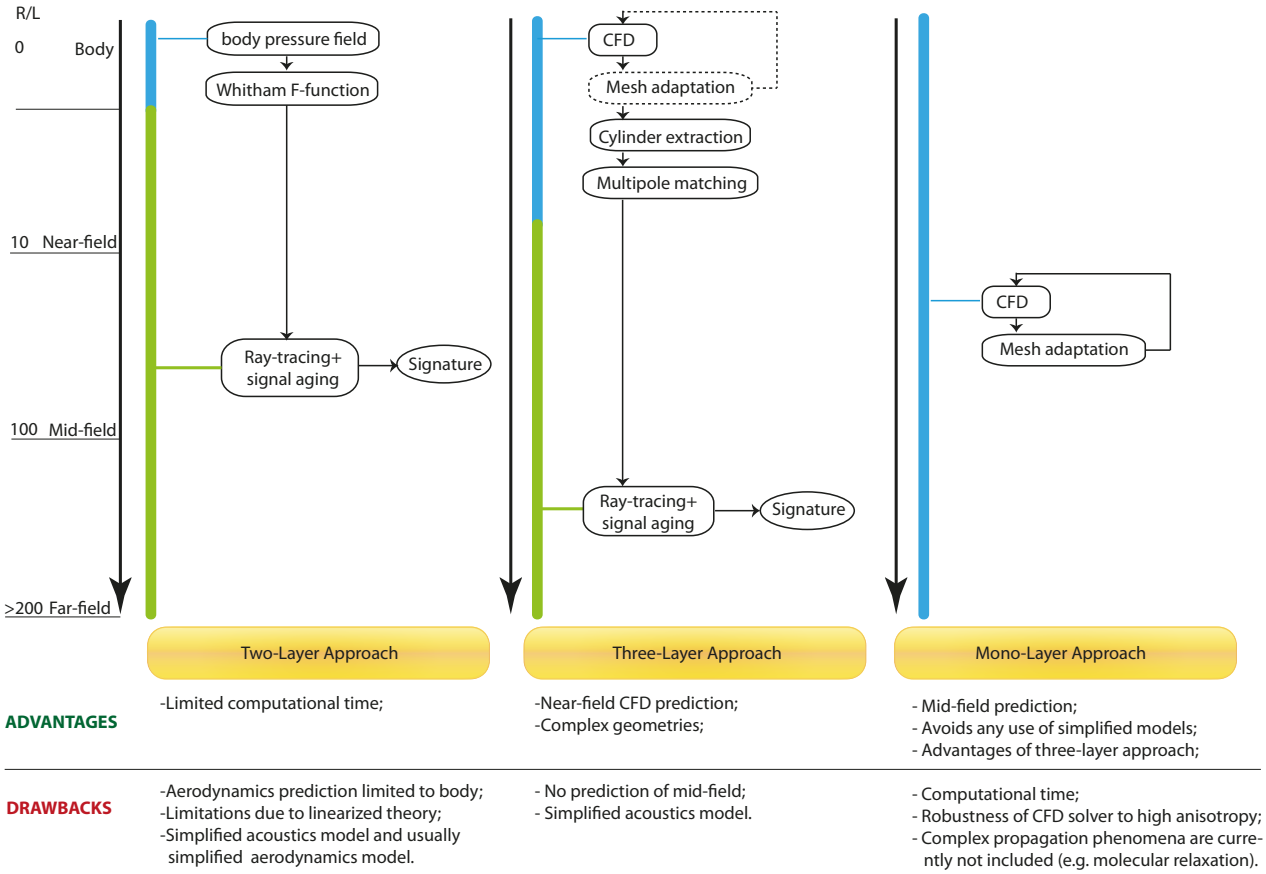

Figure 2.3: Sonic boom prediction methods. (The scheme shows where the aerodynamic model and the acoustic model are adopted during the propagation along the entire domain. Blue denotes aerodynamic CFD and green the acoustic propagation model).

maturity levels. None of these approaches should be preferred as each one shows advantages and drawbacks that will be introduced and described in the following sections.

Two-layer approach and ray-tracing propagation

The simplest approach is based on two zones: body and far-field. The body-field contribution is evaluated using the Whitham F-function and the equivalent area distribution. Both are evaluated using the Onera code *Surfcut*. The volume term of the equivalent area is evaluated directly on the three-dimensional geometry. *Surfcut* post-processes the body skin mesh and pressure distributions to reconstruct the section distribution along Mach planes. Any configuration defined with structured

and unstructured grids can be treated. The lift term A_l is evaluated using the pressure coefficient distribution on the body. The pressure coefficient can be obtained from high-fidelity CFD computations or simplified methods such as potential panel codes. The local lift contribution in equation 2.2 at the location x, is the vertical component of the pressure integrated over the contour of the section defined as a vertical plan normal to the velocity axis at x. It is important to note that the lift equivalent area distribution is generally non zero even in case of non-lifting axi-symmetric configurations at zero incidence. In fact only the integral of the distribution is equal to zero : $\int_0^l A_l(x)dx = 0$.
The corresponding F-function is then obtained from A_e solving equation (2.4) with finite difference and numerical integration. The propagation is performed using an acoustic model that requires as input the F-function. A classical approach in the sonic boom propagation community is the ray tracing based on geometrical refraction law. Ray tracing is the tracing of the waves as they propagate through the stratified atmosphere. When the aircraft moves with an almost-horizontal trajectory, the disturbances propagate downward and upward within an acceptable angular range: if the azimuthal angle $\theta = 0^o$ is set for the under track plane, then the usual range is $\pm 50^o$ for downward propagation. The continuous ray tracing generates a surface of ray paths, part of which intersects the ground, the remaining rays being completely refracted upward. Hayes et al. [6] have thoroughly reviewed the physics, the theoretical formulations as well as the practical equations to build the ray path of supersonic disturbances through a stratified atmosphere considering wind profiles. Wavefronts propagate at a velocity equal to:

$$c_n = a + \mathbf{n} \cdot \mathbf{u} \tag{2.6}$$

where a is the local sound velocity, $\mathbf{n}$ is the normal to the wavefront and $\mathbf{u}$ the wind velocity. Ray velocity is given as:

$$\frac{d\mathbf{r}}{dt} = a\mathbf{n} + \mathbf{u} \tag{2.7}$$

The propagation direction $\mathbf{n}$ is generally unknown thus equation (2.7) cannot be integrated. $\mathbf{n}$ can be related to the speed of sound and the wind velocity. If the wind is considered as horizontal a Snell's law can be defined as:

$$\frac{n'}{c_n} = \text{constant along each ray} \tag{2.8}$$

where n' is the horizontal component of $\mathbf{n}$. Combining (2.7) and (2.8) the ray equations can be obtained as:

$$\frac{dx}{d(-z)} = \frac{a(z)cos(\xi)sin(\nu) - u_x}{a(z)sin(\xi)} \tag{2.9}$$

$$\frac{dy}{d(-z)} = \frac{a(z)cos(\xi)cos(\nu) - u_y}{a(z)sin(\xi)} \tag{2.10}$$

$$\frac{dt}{d(-z)} = \frac{1}{a(z)sin(\xi)} \tag{2.11}$$

where:

z is the vertical axis directed upward
$a(z)$ is the local sound velocity
u_x is the x component of the cross wind
u_y is the y component of the cross wind
θ is the azimuth angle
ξ is the angle between the wave front normal $\mathbf{n}$ and its projection in the horizontal plane n'
γ is the angle between the aircraft velocity and its projection in the horizontal plane
ψ is the complementary angle of the velocity in the horizontal plane
$\nu = \psi - tan^{-1}\left\{\frac{cos(\mu)sin(\xi)}{sin(\mu)cos(\gamma)+cos(\mu)sin(\gamma)cos(\theta)}\right\}$

Four rays emitted at different instants and azimuths are required to identify a ray-tube area (see Figure 2.4). Ray-tube area can be defined as the Jacobian evaluated at a fixed altitude of the horizontal coordinates x and y with respect to two parameters: t and θ. t is the instant at which the ray is

emitted, while θ is the azimuth angle measured with respect to the aircraft path. Ray-tube area is written as:

$$A(t,\theta,z) = \frac{1}{c}\begin{vmatrix} \frac{\partial x}{\partial t} & \frac{\partial y}{\partial t} \\ \frac{\partial x}{\partial \theta} & \frac{\partial y}{\partial \theta} \end{vmatrix} \tag{2.12}$$

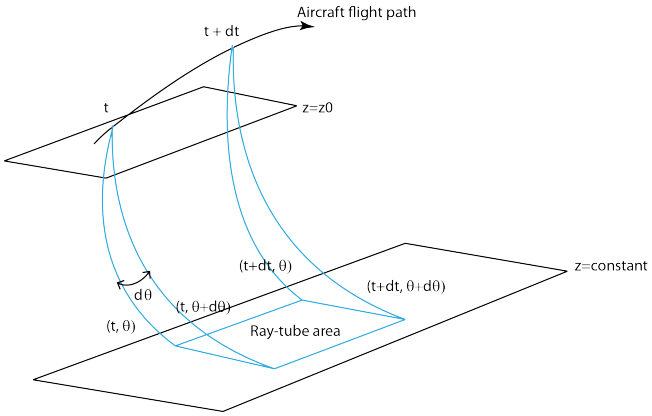

Figure 2.4: Ray-tube area definition.

It is possible to evaluate the signal at ground by solving the standard ray equations introduced by Hayes, and evaluating the variation of the ray-tubes area. The eikonal (signal phase) function is determined by the ray path, and the signal amplitude by the ray-tube area. The Ray-tracing software TRAPS [37] is adopted in this work to compute the acoustic signatures for different azimuthal angles. From an initial F-function, it evaluates the signature according to the ray paths using Aging and Hilbert transforms. The wave form of the pressure travels along a ray with the amplitude governed by the Blokhintzev invariant [38]. Concerning the shape of the wave, the age variable introduces non linear distortions of the signal. Age increases along a ray at a rate proportional to the amplitude of the signal and inversely proportional among other terms, to the ambient air density ρ. Non linearities are the consequence of variations of the propagation speed proportional with the signal amplitude. It happens that an overpressure at a given point so increases the air and sound speed at its location that it seems to overtake a lesser overpressure located ahead of it. When a section of the waveform

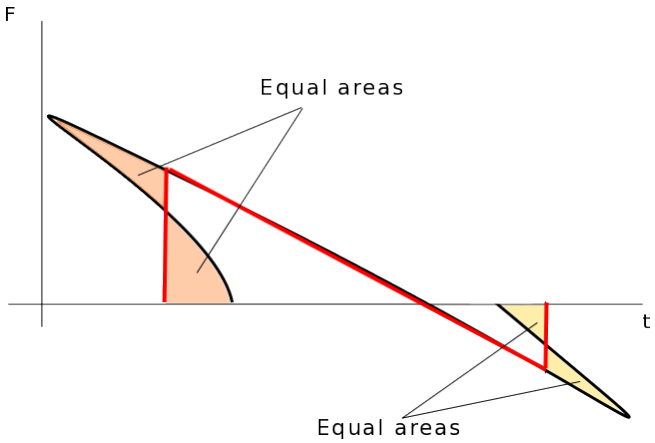

Figure 2.5: Signature aging process. Equal areas rule. In black the multi-valued signal, in red the post-processed signature.

overtakes one ahead of it, the lobes of the overtaking and overtaken portions are cutted and the shocks are located to balance the area within the cutoff lobes (see Figure 2.5) using the so-called "equal areas rule" [6].

This method represents the simplest approach and the quickest method to evaluate the sonic boom at ground, thus resulting in an efficient method to be adopted for the design. The two-layer approach

has the same limitations as the corrected linearized theory. In addition the aerodynamic pressure field is not predicted in the near-field.

Three-layer approach

Nowadays complex configurations are analyzed performing CFD computations. Limitations of the corrected linearized theory are avoided, thus providing an accurate solution in proximity of the body. The three-layer approach assumes that the acoustic and aerodynamic effects between the near and the far-field can be computed separately and added to each other. The problem that arises is : how to couple the near-field CFD solution with the acoustic propagation model?
CFD is too detailed for implicit assumptions assumed in classical sonic boom propagation models [2]. The most constraining one is related to the local axi-symmetry of the flow. This property is respected by adopting the three-layer approach developed by Plotkin and Page [2]. This method aims to incorporate CFD evaluations into sonic boom prediction being consistent with the undergoing evolution of the physics through the whole disturbances propagation process from the source to the ground.
In the vicinity of the supersonic aircraft, the steady aerodynamic flow is governed by the non linear Navier-Stokes equations and includes three dimensional features with scales proportional to the aircraft length. However, considering the current knowledge and computational means, using a non viscous CFD solver is very convenient to predict the near-field pressure disturbances far from the viscous boundary layer region, if one is not interested in the viscous drag term and neglects the boundary layer interaction with the non-viscous field. The pressure field is then extracted on a cylinder aligned with the flow direction that surrounds the aircraft . To avoid non axi-symmetrical flow field due to cross-flow, the extraction has to be performed sufficiently far from the source. The minimum distance from the body at which the methodology is applicable depends on the strength of cross-flow. As R/L (R being the radius of the extraction cylinder) increases, the axi-symmetry condition is respected, but as drawback spurious dissipation impacts the accuracy of the solution with an artificial reduction of the shocks amplitude. Meshing requirements and the limited available computational power have posed a practical limit. The cylinder pressure can be directly used for the ray-tracing propagation, but in this case the choice of the extraction radius (R/L) becomes crucial for an accurate prediction. Two solutions can be adopted to improve the three-layer approach: multipole matching method and/or mesh adaptation.

Multipole matching

The multipole matching is an improvement of the direct extrapolation matching of the three-layer approach. As demonstrated in Salah el Din et al. [9], this method relaxes the requirements in terms of R/L, thus allowing pressure extraction closer to the acoustical source and, as a consequence, alleviating the spurious numerical dissipation problem.
The modeling of the aircraft as a distribution of multipoles generating an equivalent near-field disturbance has been proposed by George [39] and the multipole matching method has been developed by Plotkin and Page [2]. The multipole matching makes the pressure field compliant with the acoustical assumption of local axi-symmetric flow field. The assumption made is that diffraction effects that appears between the near and the far-field can be cumulated and transposed over a finite cylinder.
The matching method is based on Fourier decomposition of the Whitham F-function into F_n components that depend upon the distance from the source and the length of the signal:

$$F(x,\theta,r) = \sum_{n=0}^{\infty} F_n(x,r)\cos(n\theta) \tag{2.13}$$

The pressure fluctuations with respect to the free-stream conditions are directly related to the Whitham function according to equation (2.5). Combining (2.5) and (2.13), the coefficient F_n can be expressed as:

$$F_n(x,r) = \sqrt{\frac{\beta r}{2}}\frac{2}{\pi}\int_0^{\pi} c_p(x,\theta,r)\cos(n\theta)d\theta \quad \forall n > 0 \tag{2.14}$$

with F_0 equal to:

$$F_0(x,r) = \sqrt{\frac{\beta r}{2}}\frac{1}{\pi}\int_0^{\pi} c_p(x,\theta,r)d\theta \tag{2.15}$$

Modeling the source signal as a multipole distribution provides an expression calling a multipole function family g_n with amplitude A_n. The G_n function is introduced as the ratio between the n^{th} order multipole function with the far-field multipole function g_∞ obtained by setting r to $+\infty$:

$$F_n(x,r) = \frac{1}{2\pi}\int_0^{\pi} \frac{A_n(\tau)}{\sqrt{x-\tau}} G_n(\tau-\xi,r)d\tau \tag{2.16}$$

with

$$G_n(\tau,r) = \frac{g_n(\tau,r)}{g_\infty(\tau,r)}; \qquad g_n(\tau,r) = -\frac{1}{2\pi}\frac{\cosh(n\arg\cosh(1+\tau/\beta r))}{\sqrt{\tau/2\beta r}\sqrt{(1+\tau/2\beta r)}}; \qquad g_\infty(\tau,r) = -\frac{1}{2\pi}\frac{1}{\sqrt{\tau/2\beta r}} \tag{2.17}$$

If the far-field matching functions are considered, then the dependency of F_n with respect to the distance to the source is suppressed. The resulting far-field matched Whitham function can be written as:

$$F_n(x,\infty) = \frac{1}{2\pi}\int_0^{\pi} \frac{A_n(\tau)}{\sqrt{x-\tau}} d\tau \tag{2.18}$$

$$F_\infty(x,\infty) = \sum_{n=0}^{\infty} F_n(x,\infty)\cos(n\theta) \tag{2.19}$$

The matched Whitham function can be used as an input for the non linear ray-tracing acoustic propagation to the far field using the code TRAPS. This method has been implemented in an ONERA in-house code following the work of Salah el Din [40]. In the following chapters, multipole matching is not applied during the optimization process because the configuration considered is simple enough for the non axi-symmetry of the flow-field to be limited with an adequate choice of the extraction radius. In addition as suggested in Plotkin [2] the method will amplify the loss of connection between ground boom and vehicle shape that is deleterious for a shape optimization problem.

Mesh adaptation

Instead of reducing the distance at which the pressure extraction is performed, another solution is to alleviate the numerical dissipation in the near-field using a relevant mesh adaptation technique. A classical strategy adopted in CFD is to define an *a priori* adapted mesh based on the knowledge of the phenomenon which is to be captured, instead of a baseline uniform mesh. When one wants to evaluate sonic boom generated by complex geometries using structured mesh, advanced meshing techniques are required due to the high sensitivities of the near-field signature to shape curvature. The CFD near-field computation of the F5-SSBD [41][42] shows a wide use of the Chimera meshing method enabling discretization of the flow equations in meshes composed of overset grids.
Generally unstructured meshes are well suited for the description of complex geometries due to their relative simplicity and automatic generation compared to structured meshes. In addition unstructured anisotropic grids are preferred to capture shocks: isotropic refinement that increases the number of grid elements in the proximity of shocks will improve accuracy in these regions but not necessarily improve the propagation in the flow-field [43]. This is mainly due to the fact that if no anisotropy is considered then the number of cells traversed by the shock waves in the propagation direction is increased but so is the resulting accumulated dissipation.

Current research focuses on increasing the extension of the CFD prediction domain to the mid-field region using anisotropic unstructured grid with an *a priori* [43] or an *a posteriori* [44][45] adaptation method that can be fully automated. *A posteriori* adaptation methods can be based on the estimation of an error metric. This can be performed directly using the numerical flow solution or solving an adjoint system. The adaptation technique controls the interpolation error aiming at taking into account the natural anisotropy of the physical phenomenon considered.

A metric-based mesh adaptation using the flow solution is adopted here using the *Fefloa* software developed by Loseille [46][47] to estimate the mesh requirements for the near-to-mid-field prediction. In this section, only the main phases that occur in the adaptation process as well as the parameters that drive the mesh adaptation are introduced. The theoretical development of the anisotropic mesh adaptation via interpolation error control is given in [48] and [49]. The metric-based mesh adaptation is based on an iterative process. Grids and the corresponding solutions tend to converge to a solution where the grid is adapted enabling the CFD solver to better capture the physical phenomena. This adaptation process requires four main steps (see Figure 2.6):

- Evaluation of the solution $\mathcal{S}_0^0$ on a first uniform mesh $\mathcal{H}_0$;
- Metric computation $\mathcal{M}_i$ via interpolation error estimation;
- Generation of the new adapted mesh $\mathcal{H}_{i+1}$;
- Projection of the solution from the old grid to the updated one, providing an interpolated solution $\mathcal{S}_{i+1}^0$.

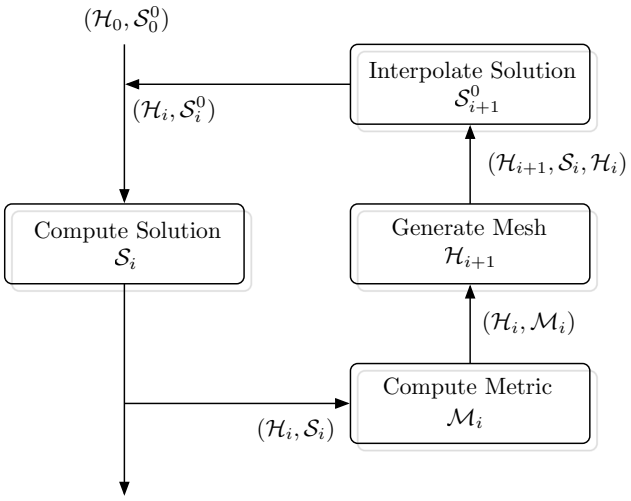

Figure 2.6: Adaptation iterative process.

Given the numerical variable u_h (density, pressure, Mach number, ..) extracted from the flow solution, a point-wise metric tensor is evaluated as:

$$\mathcal{M}_{L^P} = \det(|H_R(u_h)|)^{\frac{-1}{2p+3}} |H_R(u_h)| \tag{2.20}$$

where $H_R(.)$ is an approximation of the u_h second derivatives and p is the order of the norm. The choice of u_h is fundamental for the adaptation process that is strictly related to the metric. The desired accuracy is controlled in *Fefloa* using the complexity parameter $\mathcal{C}$ defined on the whole domain Ω as:

$$\mathcal{C}(\mathcal{M}_{L^P}(u_h)) = \int_\Omega \sqrt{\det(\mathcal{M}_{L^P}(u_h))} \tag{2.21}$$

To achieve the desired complexity $\mathcal{C}_N$ the initial metric field is scaled:

$$\mathcal{M}_{L^P}^N = \left(\frac{\mathcal{C}_N}{\mathcal{C}(\mathcal{M}_{L^P}(u_h))} \right)^{\frac{2}{3}} \mathcal{M}_{L^P}(u_h) \tag{2.22}$$

The complexity is linearly related to the number of nodes in the mesh and allows to manage the accuracy and achieve the convergence of the adaptive process.

The adaptive mesh generator builds a mesh only composed of unit lengths and unit volume elements with respect to $(\mathcal{M}_i)_{i=1,...,N}$. Each element K of the mesh $\mathcal{H}$ is defined by its list of edges $(\mathbf{e}_i)_{i=1,...6}$. Two geometrical operators evaluate the edge length and the volume of each element K in the Riemannian metric space $(\mathcal{M}(x))_{x\in\Omega}$. From a continuous formulation the length of an edge $\mathbf{e} = [\mathbf{x}_i, \mathbf{x}_j]$ and the Euclidean volume are defined as:

$$l_{\mathcal{M}}(\mathbf{e}) = \int_0^1 \sqrt{\mathbf{e}^T \mathcal{M}(\mathbf{x}_i + t\mathbf{e})\mathbf{e}}dt \qquad |K|_{\mathcal{M}} = \sqrt{\det(\mathcal{M}(x))}dx \tag{2.23}$$

In practice the mesh is discrete and the continuous metric field is computed by *Fefloa* by approximated interpolation :

$$l_{\mathcal{M}}(\mathbf{e}) \approx \sqrt{\mathbf{e}^T \mathcal{M}_i \mathbf{e}} \frac{r-1}{r \ln r} \qquad |K|_{\mathcal{M}} \approx \sqrt{\det\left(\frac{1}{4}\sum_{i=1}^{4} \mathcal{M}_i\right)}|K| \tag{2.24}$$

where r is defined as $\sqrt{\mathbf{e}'\mathcal{M}_i\mathbf{e}}/\sqrt{\mathbf{e}'\mathcal{M}_j\mathbf{e}}$. *Fefloa* at each adaptation iteration generates a new grid starting from the previous one by removing, inserting, moving or swapping mesh nodes. Using the two approximated geometrical operators as defined in [46] a mesh $\mathcal{H}$ is considered as a unit-mesh with respect to $(\mathcal{M}_i)_{i=1,...,N}$ when each tetrahedron $K \in \mathcal{H}$ verifies:

$$\forall i \in [1,6], \quad l_{\mathcal{M}}(\mathbf{e}_i) \in \left[\frac{1}{\sqrt{2}}, \sqrt{2}\right] \qquad \text{and} \qquad \mathcal{Q}_{\mathcal{M}}(K) \in [1, \alpha] \quad \text{with} \quad \alpha > 1 \tag{2.25}$$

where $\mathcal{Q}_{\mathcal{M}}$ is the quality function written as:

$$\mathcal{Q}_{\mathcal{M}}(K) = \frac{3^{\frac{1}{3}}}{36} \frac{\sum_{i=1}^{6} l^2_{\mathcal{M}}(\mathbf{e}_i)}{|K|^{\frac{2}{3}}_{\mathcal{M}}} \in [1, \infty] \tag{2.26}$$

The quality function $\mathcal{Q}_{\mathcal{M}}(K)$ provides the user an indicator to verify if the discrete mesh is a unit-mesh. The desired complexity $\mathcal{C}_N$ and the choice of the L^P norm are the two parameters that enable the user to control and evaluate the convergence of the adaptive process.
Using this method, extraction can be performed at distances superior to 2 body lengths ensuring the consistency with the acoustic model and at the same time reducing numerical spurious dissipation.

Mono-layer approach

Mesh adaptation can be used to evaluate the solution far from the source. Instead of the two and the three layer approach, the mono-layer approach (also called direct sonic boom prediction) does not require any acoustic model for the propagation. It essentially consists in the complete evaluation of the physical domain using CFD. A 3D physical domain has a size of $\mathcal{O}(1000\ km^3)$, if the shock resolution desired is the mm, mesh elements K will have a volume of $\mathcal{O}(1\ mm^3)$. A uniform mesh will contain more than 10^{10} elements to capture shocks propagation (around 10^{21} elements for a resolution of 1 mm over the entire domain). Despite the continuous increase of the computational power and the massive parallelization of the computations, this brute force approach is still unrealistic. Furthermore, it is also unlikely to have the same resolution of the shock regions overall the entire domain. At the same time an indiscriminate reduction of the number of elements will compromise the accuracy and increase the artificial numerical dissipation. The only viable solution for direct CFD sonic boom prediction is the use of efficient mesh adaptation techniques as those introduced in the previous section. Actually mesh adaptation appears mandatory for the development of a mono-layer approach. In Loseille and Lohner [46] the first direct sonic boom evaluation with a mono-layer approach is performed. The pressure signature is evaluated at various distances from the source up to 9 km that corresponds to R/L around 250 and a length of shock waves propagation of nearly 15 km. The unstructured adapted highly anisotropic mesh consists in only 19 millions tetrahedra. Atmosphere is considered as uniform, but a simple extension consists in considering variable inflow conditions that can take into account also atmosphere stratification and wind gradient.

This method actually has the lowest degree of maturity and requires further analysis on adaptation techniques, on the development of physical models (e.g. caustics can be predicted with unsteady computations) and requires cross-validations with the other approaches and experimental data. A direct boom prediction can provide information on the mid-field that the other approaches do not have. Concerning its utilization in the minimization process, the impact on the low-boom shape obtained has to be demonstrated yet. The first step suggested consists in the evaluation of the final configuration with this approach before a direct application within an optimization process that will inevitably result in an increased computational time required at each optimization iteration.

2.4 Metrics for the sonic boom quantification

When one analyzes sonic boom caused by a supersonic aircraft not only the prediction of the phenomenon is important, but also the quantification of the annoyance caused to people outdoor and indoor, the magnitude of structure vibrations and the measure of secondary effects such as rattle. In the present study the attention focuses on outdoor annoyance perceived by people, but some fundamental elements of indoor sonic boom estimation are also introduced.

Several community surveys [50][51], laboratory studies [52] and low-boom flight tests [53] have been conducted in the past years to identify the correlation between metrics and the sonic boom. A common metric to define a low-boom signature can provide not only a common objective for the sonic boom community, but also the redefinition of the current acceptable standards. Civil supersonic flights overland are prohibited by current US regulations mainly due to the sonic boom impact at ground. The US code federal regulation 14 Part 91.817 since 1973, assumes any sonic boom noise unacceptable and prohibits civil aircraft operating over US territory from exceeding Mach 1. At international level the ICAO resolution 33-7 (1998) affirms "*the importance to ensuring that no unacceptable situation for the public is created by sonic boom from supersonic aircraft in commercial service*".

Two specific problems distinguish sonic boom and its quantification: the area of effect and the subjectivity of the annoyance. Compared to airport noise where annoyance is limited to a small area, the sonic boom of a single supersonic flight impacts a vast region. The surface of the primary carpet of a 3000 km supersonic flight would be of the order of hundreds of thousands square kilometers. The number of people involved clearly depends on the population density of the region concerned by supersonic flights. In Europe one million of people will be impacted by each flight. For this reason supersonic corridors have been suggested, which on one hand reduces the annoyance impact of sonic boom in terms of number of people concerned, but on the other hand limit the benefits of supersonic flights with deviations from optimal trajectories.
The subjectivity is well identified by the psycho-acoustics analysis of the community surveys. In the Okhlahoma city survey [50] the results showed that the best correlation with the annoyance is achieved using the number of boom per day. The survey recommends a boom peak pressure level of $35.91[Pa]/\sqrt{N}$ where N is the number of boom per day.

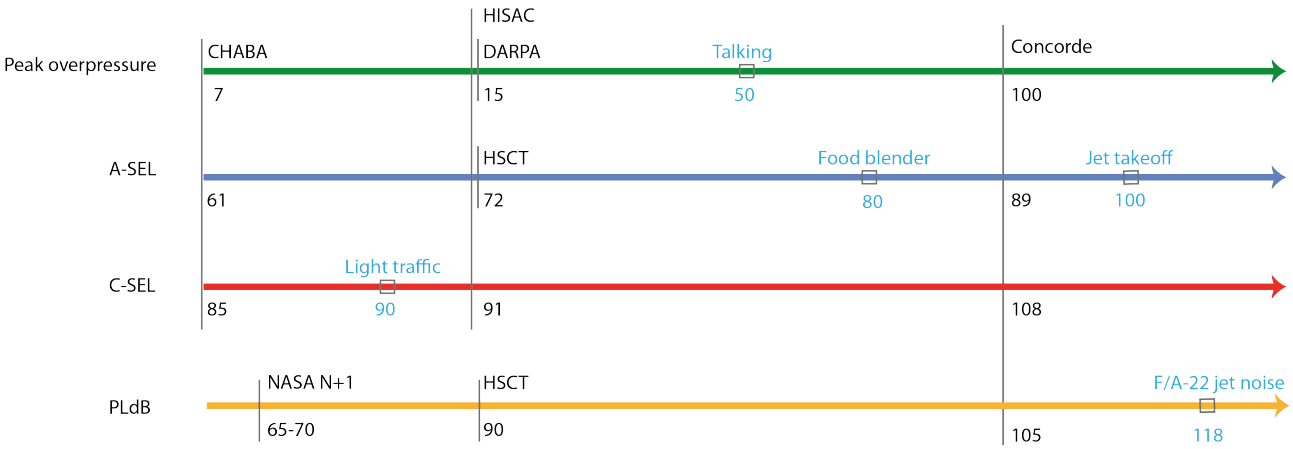

Figure 2.7: Sonic boom criteria proposed in the past compared to ordinary events.

Different metrics have been retained during the years as objective for sonic boom minimization (see Figure 2.7). They can be categorized in pressure based or loudness based. To the first category belongs the maximum peak overpressure, front shock overpressure, sum of the shock amplitudes, while Sound Exposure Level (SEL), A-weighted Sound Exposure Level (A-SEL), C-weighted Sound Exposure Level (C-SEL), Perceived Loudness deciBel (PLdB) belong to the second one. Pressure based metrics are the most current in optimization problems due to their simplicity of use, but they do not provide a cost function that synthesize at the same time the energy content and the full frequency of the signature. Loudness metrics are the result of several mathematical process that are cause of a decrease of dependencies between the geometry (the input of the problem) and the metrics (the output of the mathematical system). The choice of such an objective function is not a trivial process and results from a compromise between the accurate description of the physical phenomenon and the use of an objective function which is related with the design variables. For these reasons pressure based metrics will be retained for the optimization problems, while loudness based are adopted to analyze the reference configurations as well as the final one.

When it comes to evaluate loudness metrics, the pressure signal has to be transformed in the frequency domain using the Parseval's theorem:

$$\int_{-\infty}^{\infty} p(t)^2 dt = \frac{1}{\pi} \int_{0}^{\infty} |f(\omega)|^2 d\omega \tag{2.27}$$

where $f(\omega)$ is obtained from the Fast Fourier Transform (FFT) of the time domain signal. The power spectrum is discretized into 1/3 octave band energy levels and converted into band pressure levels. Weighting transfer function is then applied to pressure levels. The transfer function for dBA and dBC are respectively[1]:

$$H_{dBA}(s) = \frac{4\pi^2 \cdot 12200^2 \cdot s^4}{(s + 2\pi \cdot 20.6)^2 (s + 2\pi 12200)^2 (s + 2\pi \cdot 107.7)(s + 2\pi \cdot 737.9)} \tag{2.28}$$

$$H_{dBC}(s) = \frac{4\pi^2 \cdot 12200^2 \cdot s^2}{(s + 2\pi \cdot 20.6)^2 (s + 2\pi \cdot 12200)^2} \tag{2.29}$$

The procedure for the evaluation of the PLdB is more complex and is presented in Stevens [54]. In this case the frequency weightings are based on experimental data and vary with sound levels.
The best correlation between boom levels and metric is obtained using PLdB and dBA. This is due to the fact that the most annoying part of the boom are the shocks containing the high frequency regions of the boom spectrum. This explains why dBA performs better than dBC for the analysis of community surveys. dBC metric is recommend for high energy impulsive sounds in CHABA [55], it puts more weight on low-audible frequencies compared to A-weighting. For this reason dBC metrics are strongly correlated to the peak overpressure, while dBA metrics are more sensitive to rise-time. Perceived level is shown to take into account variability of the boom shape and its deviation from the N-waveform. Despite these considerations, poor correlation in general is observed between several metrics (such as peak pressure, PLdB, dBA or dBC) and annoyance, the best correlation is obtained with the number of boom perceived daily.
Each metric shows a different sensitivity to the ground signature characteristics. The latter are: the ground signature shape (e.g. N-wave, flat-top, ramp,..), the shock overpressures, the rise time, the maximum overpressure, the impulse and the time duration. Each of these elements has an influence on the measure of loudness and their relative importance depends also on the metric considered. One has to notice that the acoustic model adopted in this work provides only zero-thickness pressure jumps. Real signatures show a finite rise time that affect the high frequency content of the sonic boom energy and so it has a strong impact on the loudness metrics. Rise time is defined as the time delay separating the first value of the pressure equal to 10% of the peak overpressure from the first value of the pressure equal to 90% of the peak overpressure. Rise time is due mainly to relaxation effects and increases in a turbulent mean. Typical values range from 0.5 to 10 ms. Subjective loudness and annoyance intensity levels have the tendency to increase while the rise time drops. To introduce rise time, it is possible to

[1]The interested reader can refer to ANSI Standards S1.4-1983 and S1.42-2001.

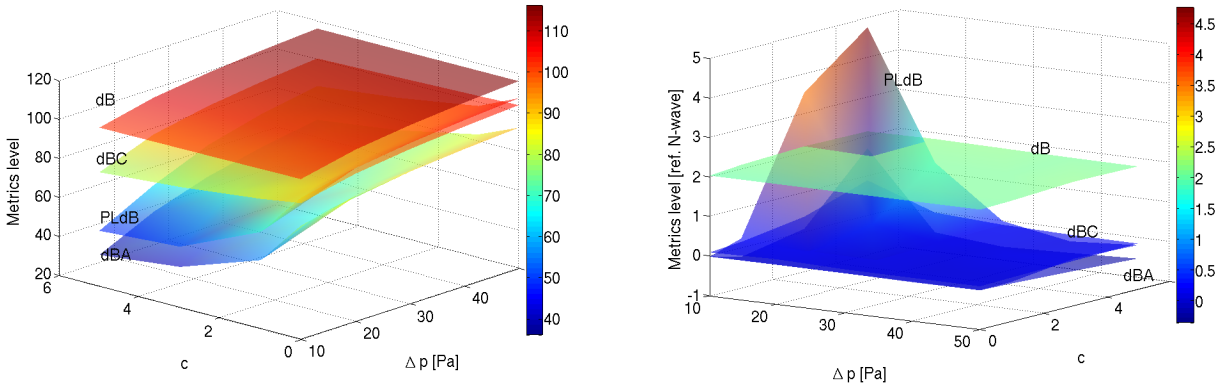

(a) Impact of Δp and τ for an N-wave signature of 200 ms.

(b) Impact of Δp and τ for a flat-top signature of 200 ms (Variation with respect to a reference N-wave).

Figure 2.8: Impact of ground signature on sonic boom metrics.

post-process the zero-thickness signal introducing rise time as function of the peak overpressure. The theoretical model developed by Kang and Pierce [56] is considered:

$$\tau_{0.1-0.9} = c/\Delta p \tag{2.30}$$

where c is a coefficient strongly affected by atmosphere humidity. In this study c is taken equal to 20.88e-3 Pa ms^{-1} [12]. Rise time is introduced by applying an hyperbolic tangent to the signature at the shock location as in [57]:

$$p(t)_{rt} = \frac{\Delta p(t)}{2}\left[1 + \tanh\left(c_r \frac{t}{\tau_{0.1-0.9}}\right)\right] \tag{2.31}$$

where c_r is a coefficient equal to 1.472 for the rise time definition (10%-90%).

As outlined in [58], considering N-waves the parameters that influence loudness the most are the rise time and the maximum overpressure. Modification on the duration gives less benefits. Considering ramp like signals the amplitude of the initial shock has more influence than maximum overpressure. An N-wave and a flat-top signature of the duration of 200 ms have been used to analyze the impact of the shock pressure rise and the rise time over the sonic boom loudness metrics (see Figure 2.8). All the loudness metrics are sensitive to the pressure amplitude, but only PLdB and dBA show variations as the rise time changes. Furthermore, in Figure 2.8b it is notable that only PLdB and dBA are impacted by differences in the waveform. As a general conclusion these two metrics are considered as the most representative candidates to characterize the outdoor sonic boom impact at ground.

The evaluation of sonic boom indoor perception is more delicate. Sonic boom indoor perception is characterized by three components:

1. the audible component, generally is the outdoor sonic boom filtered by the building;
2. tactile motion of the building;
3. rattling of the building and of the objects inside the building.

The indoor audible component has the similar trend that can be obtained for boom heard outdoors [59]. The other two components require the introduction of a building dynamics model. The simplest approximation is the lumped parameter single degree of freedom model (SDOF) [60]. The equation of motion of a spring-mass-dumper system is:

$$m\ddot{x} + c\dot{x} + kx = f(t) \tag{2.32}$$

where m is the mass, c is the damping factor, k is the spring constant and $f(t)$ is the load factor. The response to this system to a unit impulse load at $t = 0$ is:

$$h(t) = \frac{1}{m\omega_d} e^{-\delta\omega_n t} sin(\omega_d t) \tag{2.33}$$

where $\omega_n = \sqrt{\frac{k}{m}}$ is the undamped natural frequency, $c_c = 2\sqrt{km}$ is the critical damping coefficient, $\delta = \frac{c}{c_c}$ is the critical damping ratio and $\omega_d = \omega_n\sqrt{1-\delta^2}$ is the damped natural frequency. The response to the load factor $f(t)$, that corresponds to the pressure signal, is given by the Duhamel integral:

$$x(t) = \int_0^t h(t-\tau) f(\tau) d\tau \tag{2.34}$$

From equation (2.34) the acceleration can be evaluated as

$$a(t) = -\frac{\omega_d}{m} exp(-\delta\omega_n t) \left[1 - \left(\frac{\delta\omega_n}{\omega_d}\right)^2 \sin\omega_d t + 2\frac{\delta\omega_n}{\omega_d}\cos\omega_d t\right] \tag{2.35}$$

Acceleration is used directly as a measure of rattle and its spectrum provides an indicator for tactile motion.

Four signatures are considered for this analysis:

- 2 N-wave signatures with a total duration of 100 ms and pressure peak respectively equal to 50 Pa and 30 Pa;
- 2 flat-top signatures with a total duration of 100 ms, plateau duration of 20 ms, and pressure peak respectively equal to 50 Pa and 30 Pa.

A house wall is used to characterize the indoor perception of sonic boom. The wall has the following properties: surface density = 20 kg/m^2, resonance frequency = 20 Hz, damping ratio = 0.1.
The threshold L for tactile response is defined as in Sutherland [61]:

$L = 60dB, \quad f \leq 4Hz$

$L = 60 + 20log10(f/4)dB, \quad 4Hz < f \leq 40Hz$

$L = 80dB, \quad 40Hz < f \leq 200Hz$

$L = 80 + 66log10(f/200)dB, \quad f > 200Hz$

Figures 2.9 and 2.10 show the wall acceleration spectrum for the 4 signals:

- both signatures exceeds the threshold for low-frequencies;
- the amplitude of the peaks are dependent on the front shock overpressure;
- a shaped signature slightly reduces the acceleration maximum peak with respect to a N-wave signature.

Rattle is a phenomenon hard to model because it occurs for structural elements or objects not being well mounted. As in [59] a rattle threshold of 0.024 g is considered. Figures 2.11 and 2.12 show the wall acceleration due to the different sonic boom signals and the rattle threshold. As for the tactile vibration all the signatures exceed the threshold and the maximum peak is reduced when the front shock overpressure decreases. The flat-top signatures produce an higher acceleration with respect to N-waves at an equal amplitude of the front shock, as already shown in [59].

Consider a wall as a single degree of freedom is obviously a limitation. In general the wall dynamic behavior is coupled to the interior and a multimodal analysis is required [62].

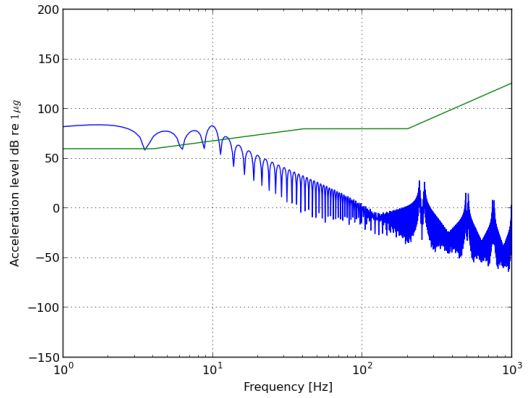

(a) N-wave with front shock overpressure equal to 50 Pa.

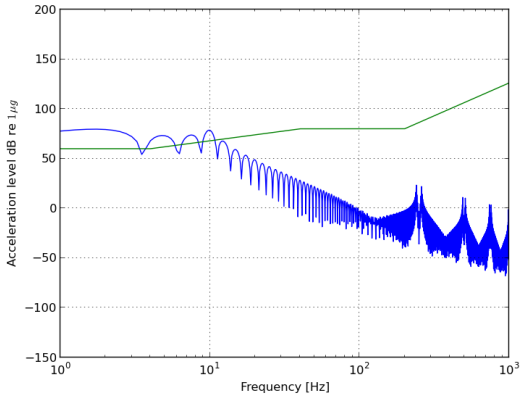

(b) N-wave with front shock overpressure equal to 30 Pa.

Figure 2.9: N-wave signatures. Sonic boom wall vibration (blue) compared to tactile vibration criteria (green).

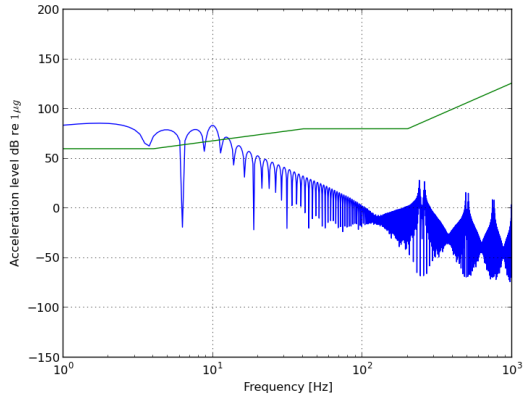

(a) Flat-top with front shock overpressure equal to 50 Pa.

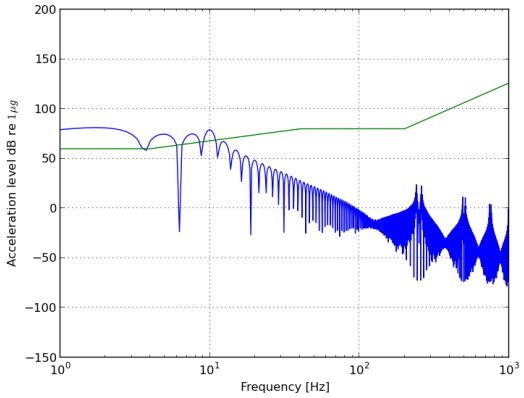

(b) Flat-top with front shock overpressure equal to 30 Pa.

Figure 2.10: Flat-top signatures. Sonic boom wall vibration compared to tactile vibration criteria.

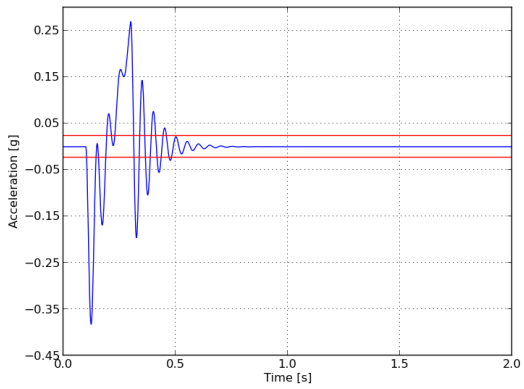

(a) N-wave with front shock overpressure equal to 50 Pa.

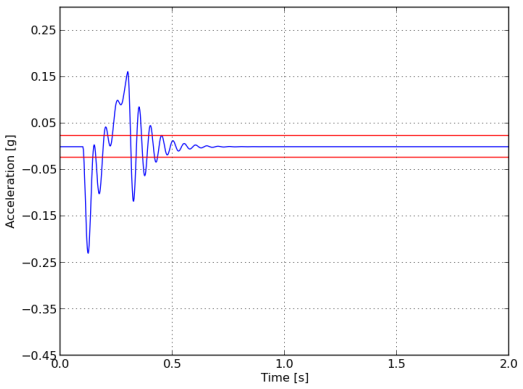

(b) N-wave with front shock overpressure equal to 30 Pa.

Figure 2.11: N-wave signatures. Wall rattling acceleration, in red rattle threshold.

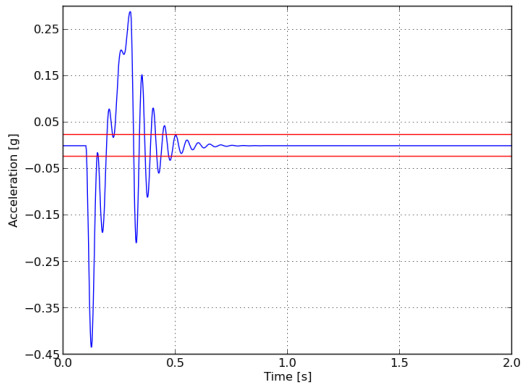

(a) Flat-top with front shock overpressure equal to 50 Pa.

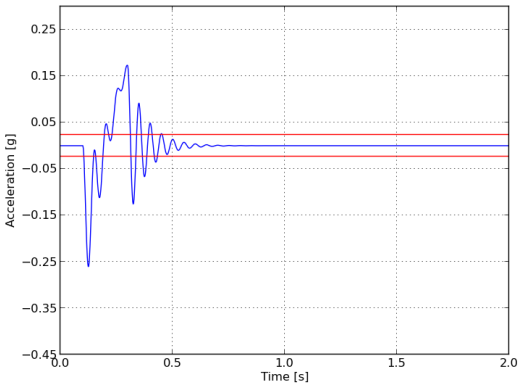

(b) Flat-top with front shock overpressure equal to 30 Pa.

Figure 2.12: Flat-top signatures. Wall rattling acceleration, in red rattle threshold.

Chapter 3

Prediction of the aeroacoustic performance of a SSBJ

When the weight of the paper equals the weight of the airplane, only then you can go flying.
Donald Douglas

Contents

In this chapter, the numerical methodologies adopted for the aerodynamic and acoustic performance assesment of a wing-body supersonic business jet configuration are described. A reference configuration is introduced and analyzed. The mesh requirements and the topology as well as the CFD computation parameters are detailed. Concerning the acoustic prediction, the sonic boom performance is evaluated using different approaches, and the results are analyzed and compared.

3.1 Reference configuration

The reference SSBJ wing-body configuration geometry is shown in Figure 3.1. This simplified shape is representative of actual supersonic business jet configurations [1]. It's main dimensions are an overall length of 30 m and a wingspan of 18 m. The fuselage is axi-symmetric with cylindrical cabin of length and diameter respectively equal to 11 m and 2.03 m. The wing is a double swept wing that presents a 3 degrees dihedral angle of the outer wing. The wing has a bi-convex symmetric profile with α_0 equal to zero. Along the wingspan no twist is applied, while t/c evolves linearly from 0.06 to 0.03.

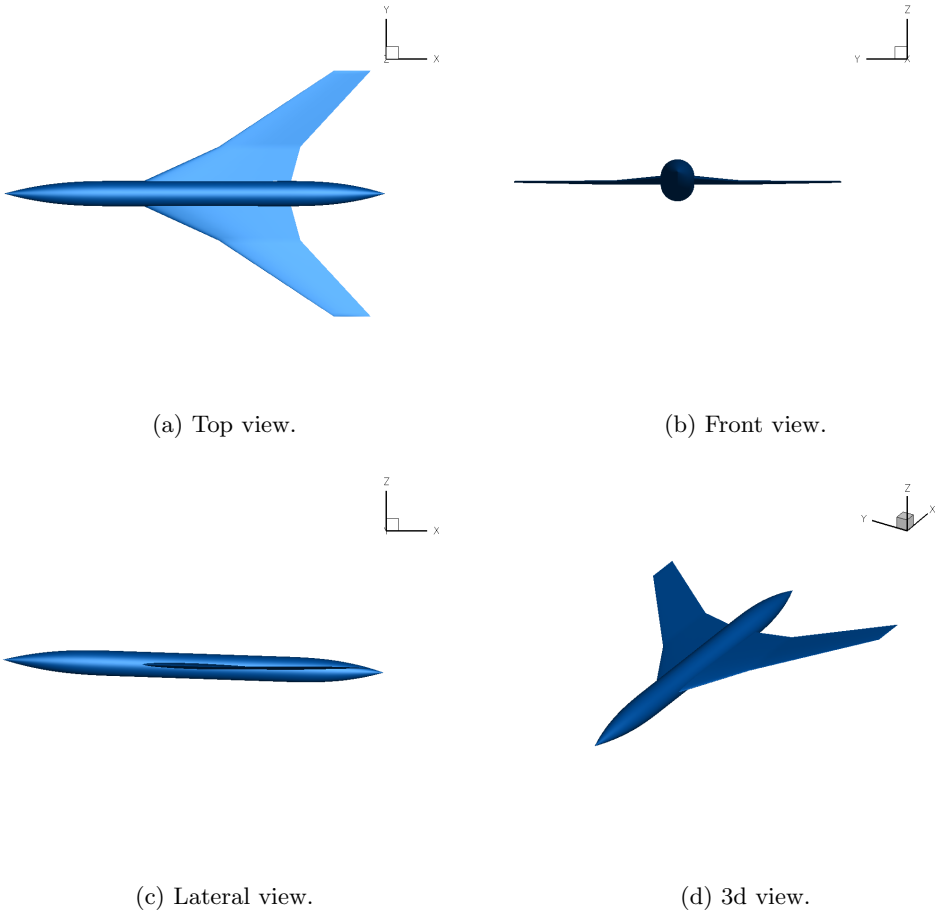

(a) Top view.

(b) Front view.

(c) Lateral view.

(d) 3d view.

Figure 3.1: Baseline geometry.

Steady flight conditions at an altitude of 18,000 m are considered. As typical flight altitude became higher, problems such as radiation exposure and ozone depletion due to high atmosphere emissions would arise. The drawback is that for configurations not designed for low-boom the ground signature amplitude can become significant. The Mach number and the angle of attack are respectively equal to $M_\infty = 1.6$ and $\alpha = 2$ degrees. The Mach range generally retained for such kind of configuration ranges between 1.6 and 1.8, result of a compromise between profitability and ground impact of the sonic boom phenomenon. These conditions follow the general trend of the $N + 1$ generation of supersonic civil aircrafts [63].
Flight conditions are chosen such that the boom at ground has reached an almost steady-state (Mach and flight altitude are large enough). For this reason the acoustic phenomenon can be treated using steady-state computations.

3.2 Aerodynamic performance

Various fidelity levels exist for the evaluation of the aerodynamic performance depending on the model adopted: linearized potential equations, full potential equations, Euler equations and Navier - Stokes equations. The aerodynamicist has to identify a model to adopt as a function of the accuracy and computational cost requirements of the problem to be analyzed.

To evaluate the aerodynamic performance of the configuration with a reduced computational cost the PANAIR code [64] is adopted. PANAIR is a program developed at Boeing that calculates flow properties about arbitrary three-dimensional configurations. The program uses a high-order panel method to solve the linearized potential flow boundary-value problem at subsonic and supersonic Mach numbers.

PANAIR solves the Prandtl-Glauert equation valid in the context of the supersonic linearized theory [65]:

$$(1 - M_\infty^2)\frac{\partial \Phi}{\partial x^2} + \frac{\partial \Phi}{\partial y^2} + \frac{\partial \Phi}{\partial z^2} \tag{3.1}$$

where Φ represents the perturbation velocity potential. The wing and the fuselage are described using sources and doublets. An indirect mass flux boundary condition is applied to the wing panels. The exterior surface is exposed to the onset upstream-steady flow in our case. The condition $\sigma = -V_\infty \cdot \mathbf{n}$ is imposed, where σ is the source strength. The interior region has a uniform onset flow with an interior surface boundary condition of $\Phi_L = 0$, where U defines the upper part of the panel (positive normal directed outside the geometry) and L defines the lower part of the panel. To simulate wakes originating at the trailing edge of a lifting surface a wake network has been modeled using additional panels aligned with the flow direction (see Figure 3.2). Concerning the fuselage, velocity impermeability on a thick surface is imposed. It is frequently used in supersonic analysis and simply consists in using an interior condition $\Phi_L = 0$, while the boundary condition on the exterior surface is defined as: $(\mathbf{v}_U - \mathbf{v}_L) \cdot \mathbf{n} = -V_\infty \cdot \mathbf{n}$.

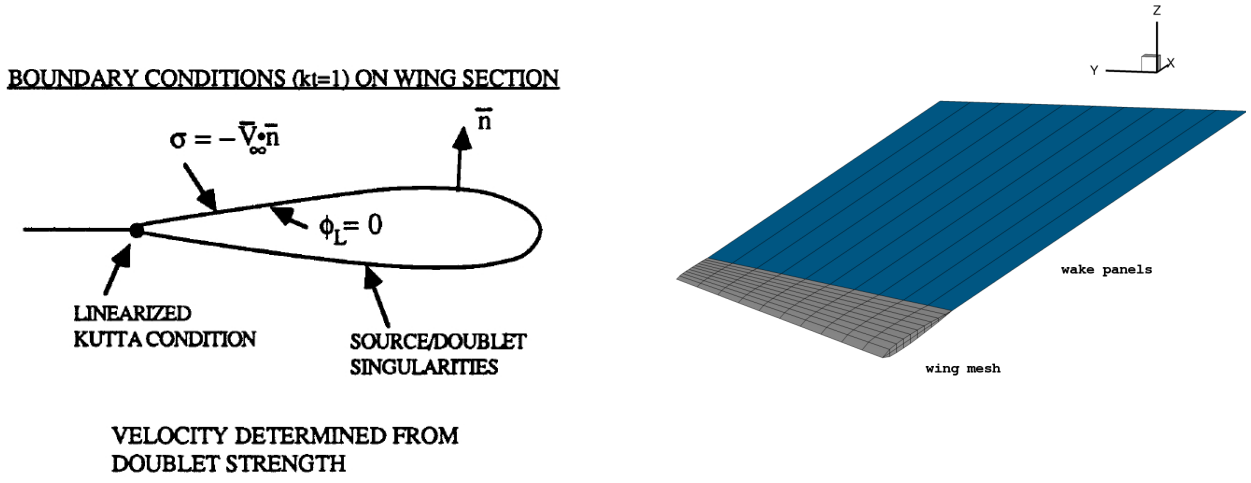

Figure 3.2: Boundary condition applied to the wing panels and paneling strategy adopted to define the wing geometry.

The wing is discretized by 484 panels, the lower and upper part of the inward and outward wing are both described by 121 panels. The fuselage is described using 930 panels (30 in the azimuth direction and 31 in the fuselage axis direction). PANAIR solves the problem in less than 30 seconds wall clock time on a 64 bits Intel Centrino Dual core 1.8 GHz.

The pressure coefficient surface distribution is shown in Figure 3.3. The induced drag produced by the configuration is equal to 52.3 drag counts, while the lift coefficient is equal to 0.10145. Wave drag is estimated outside PANAIR. For a slender body of revolution it is possible to apply the Karman formula to estimate volume wave drag as:

$$C_{D_{wv}} = -\frac{\rho V_\infty^2}{4\pi} \int_0^l \int_0^l S''(x_1) S''(x_2) \ln|x_1 - x_2| dx_1 dx_2 \tag{3.2}$$

where S'' is the second derivative of the area distribution. The wave drag evaluated using equation (3.2) is 45.84 drag counts, so that the total drag is equal to 98.14 drag counts. Figure 3.4 shows the complete configuration drag polar. The minimum drag coefficient or parasite drag $c_{D_{MIN}}$ is equal to 0.0064 obtained at $\alpha = 0$ deg where the lift coefficient c_{L_0} is equal to zero.

Actually the adoption of this kind of approach is limited to the predesign phases. Increase in the available computational power has encouraged the use of more accurate tool, such as CFD, to predict more accurately the performance of the aircraft. The aerodynamic performance evaluation is performed using the Onera elsA CFD code [66]. elsA is able to deal with internal and external

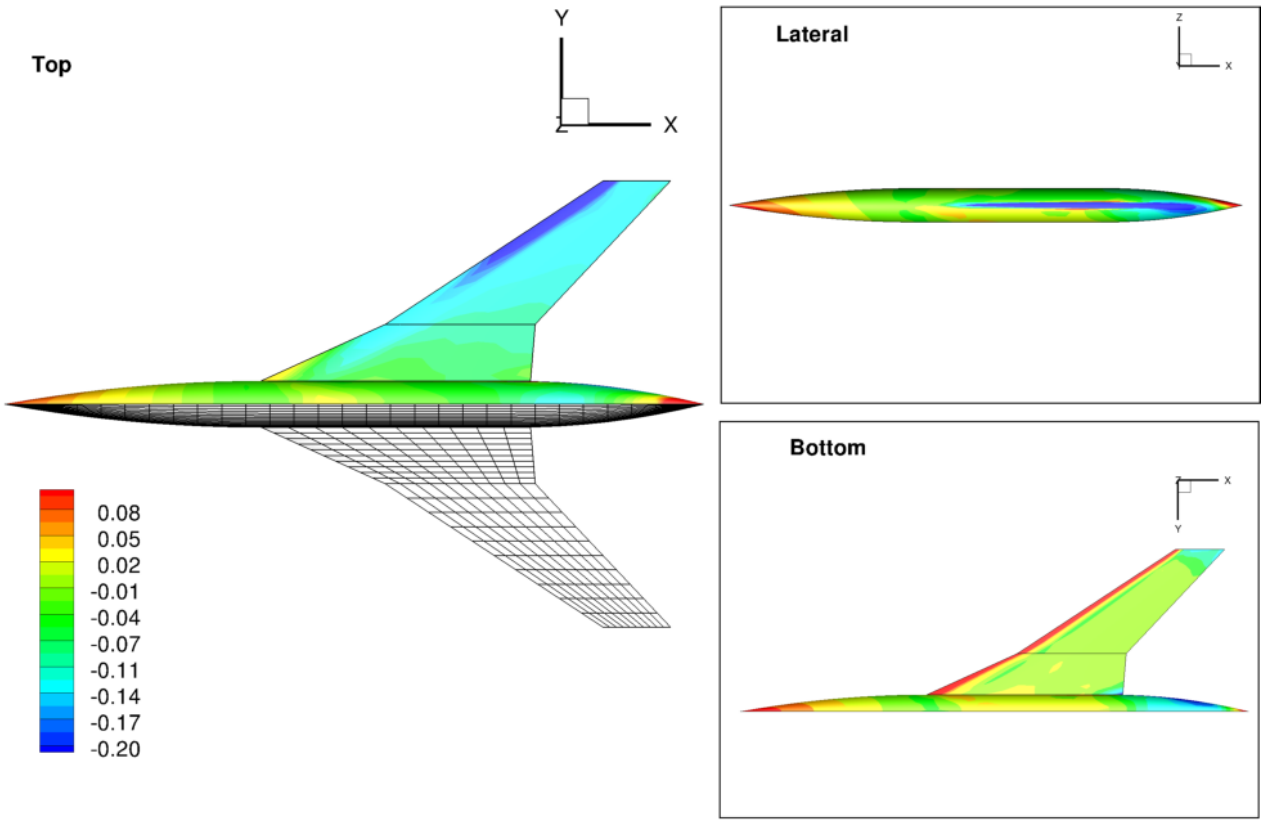

Figure 3.3: Pressure coefficient distribution over the configuration and paneling geometry definition.

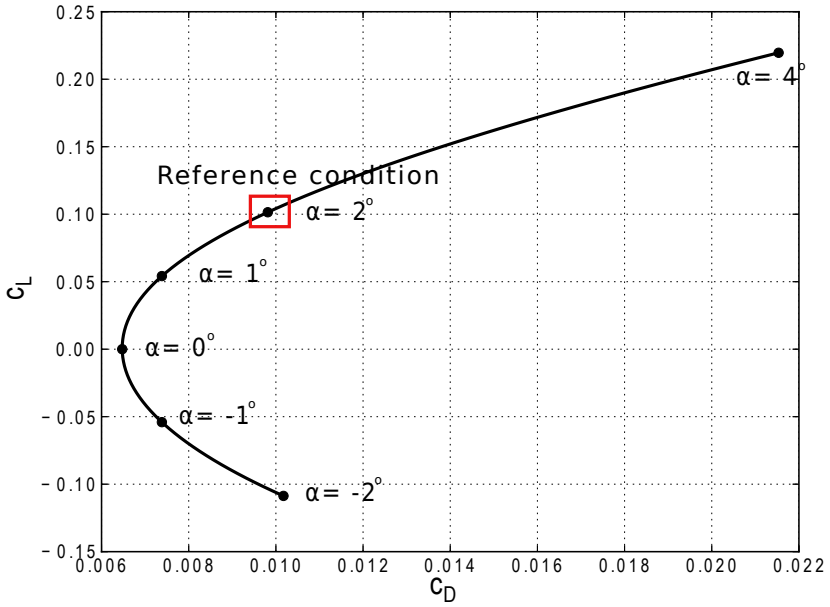

Figure 3.4: Drag polar obtained using PANAIR.

aerodynamics problems performing Euler, RANS, URANS, DES, or LES simulations for the mono-species perfect gas hypothesis on structured grids. The flow equations are solved by a cell centered finite-volume method, and the flow regimes range from the low subsonic to the high supersonic regime.

For the supersonic configuration considered, invisicid Euler equations are used to describe the flow

in the near-field. This choice is driven by the main following reasons:

- The pressure signature in the near-field is predicted with sufficient accuracy. Generally Euler solutions show sharper and more exaggerated peaks and dips in the pressure signature with respect to Navier-Stokes solutions [67];
- The CFD computation will be a part of an optimization process that requires several evaluations. Euler computations require less time to converge with respect to Navier-Stokes computations, thus resulting in a reduced computational cost.

The Roe flux scheme [68] with the Harten entropy correction [69] is used. Harten correction is required to filter the expansion shocks that will result as an invalid solution of the Euler equations. The Van Albada [70] flux limiter is used to preclude oscillations due to shocks and discontinuities by limiting the values of the spatial derivatives. Typically, a flux limiter is required for supersonic flows while it is not for subsonic flow computations.

Concerning the mesh, Figure 3.5 shows the grid topology adopted. Structured CFD grids on the half configuration are used in the calculations. Four blocks model the flow domain that extends from the configuration up to $R/L = 4$, where R is the domain radius and L is the body length. The domain is a half cylinder with a conical cap and base composed of 6,030,298 nodes. As outlined in [67] the pressure signature is very sensitive to the mesh. To reduce numerical dissipation the grid is aligned with the Mach cone angle. Non-reflection BCs are used at the inflow, at the outflow and on the lateral

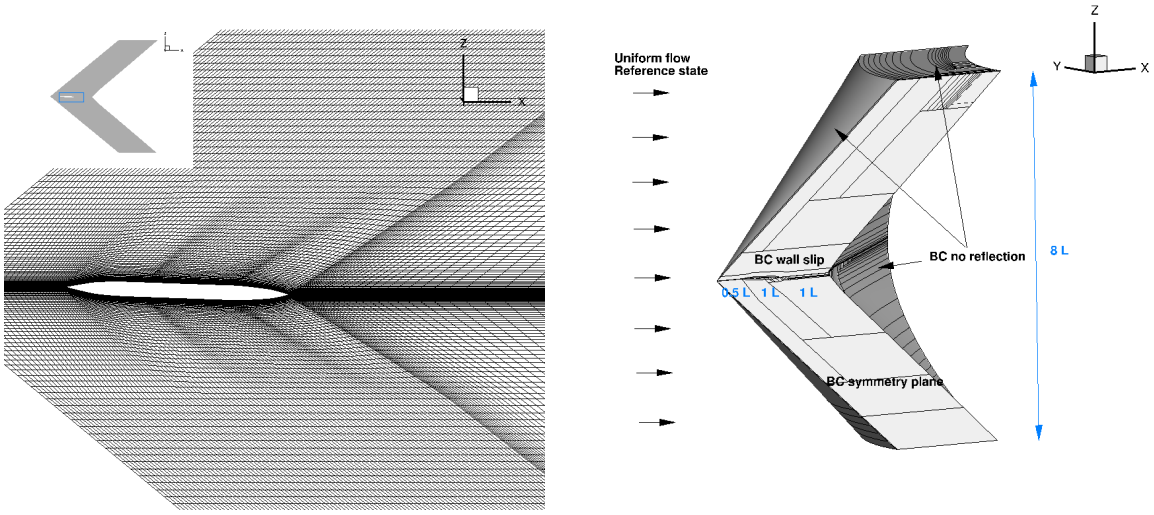

Figure 3.5: Symmetry plane mesh and domain boundary conditions adopted for the elsA computations.

far-field surface boundaries. Due to the symmetry of the configuration, a symmetry plane BC is used for $y = 0$ plane. This has permitted to limit the computations to only the half configuration. Inviscid wall BCs are used to model the fuselage and the wing. Uniform free-stream flow conditions are given as initial conditions throughout the computational domain. The following reference state conditions are specified in the CFD simulations: a Mach number of 1.6, total pressure of 11.598 kPa, and total temperature of 216.7 K. Less than five hundreds CFD iterations are sufficient for the aerodynamic coefficients to converge (see Figure 3.6). The number of iterations is set to 500 iterations for all the computations performed using the structured mesh as the best compromise between performance accuracy and computational time. The reference area considered for the half configuration is 65 m^2. The resulting inviscid drag and the lift coefficients are respectively equal to 0.0089 and 0.1 obtained at an incidence of two degrees.

The near-field solution is shown in Figures 3.7 and 3.8. Three main shocks are created by the nose, the wing leading edge and the fuselage tail. The strongest shock occurs at the nose, where the flow is decelerated from M=1.6 to M=1.3. The flow then re-accelerates in an expansion region which precedes the wing leading edge (see Mach iso-surfaces in Figure 3.8). The wing region shows a compression

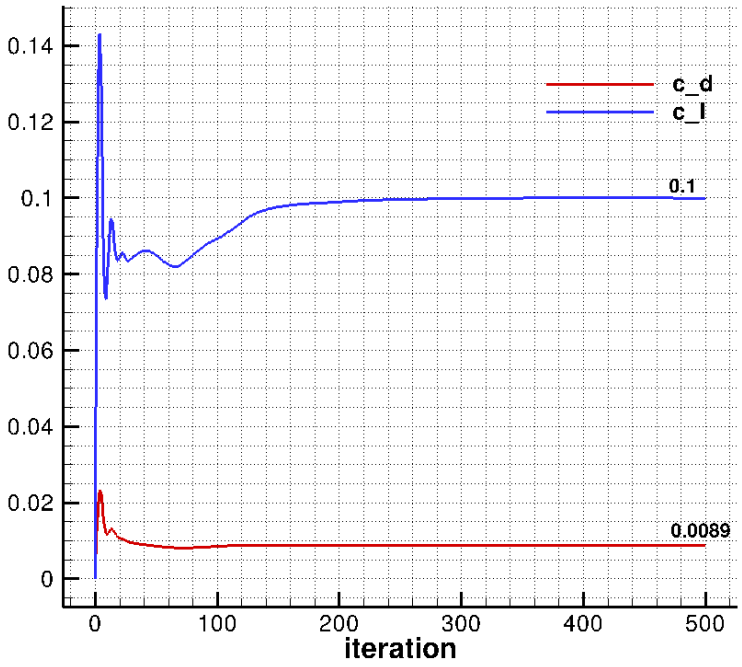

Figure 3.6: Drag and lift coefficients convergence history.

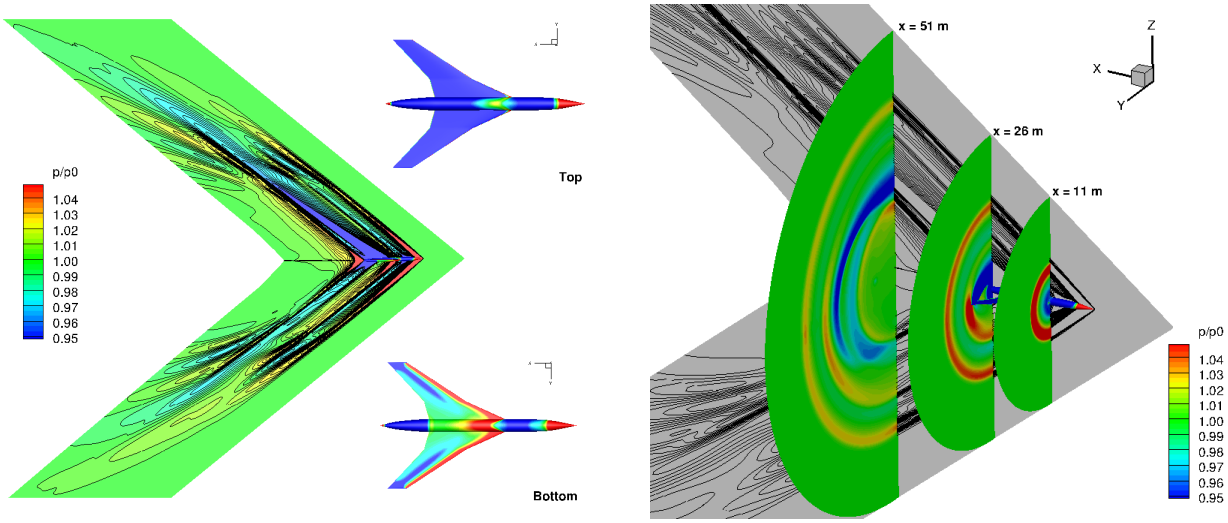

Figure 3.7: Near field pressure p/p_0.

shock beneath the aircraft while the flow is strongly accelerated over the extrados to M = 1.7. The wing leading edge is categorized as subsonic due to the fact that $\frac{\pi}{2} - \Delta < \mu$, where Δ is the sweep angle and μ the Mach angle. In this case the shock is attached at the apex of the wing.
The rear compression shock is necessary to recover the free-stream pressure after the flow acceleration that occurs in the wing region. This phenomenon is strictly three-dimensional and the complexity of the flow increases as direct consequence of the geometry complexity. Expansion waves and compression shocks interact in the conical region defined by the Mach cone.

One has to notice that as the distance increases, the shock waves amplitude dissipate and progressively deviate from the Mach cone normal. The spurious numerical dissipation is mainly due to the mesh which is adapted only in the proximity of the aircraft. Pressure extraction on this kind of grid

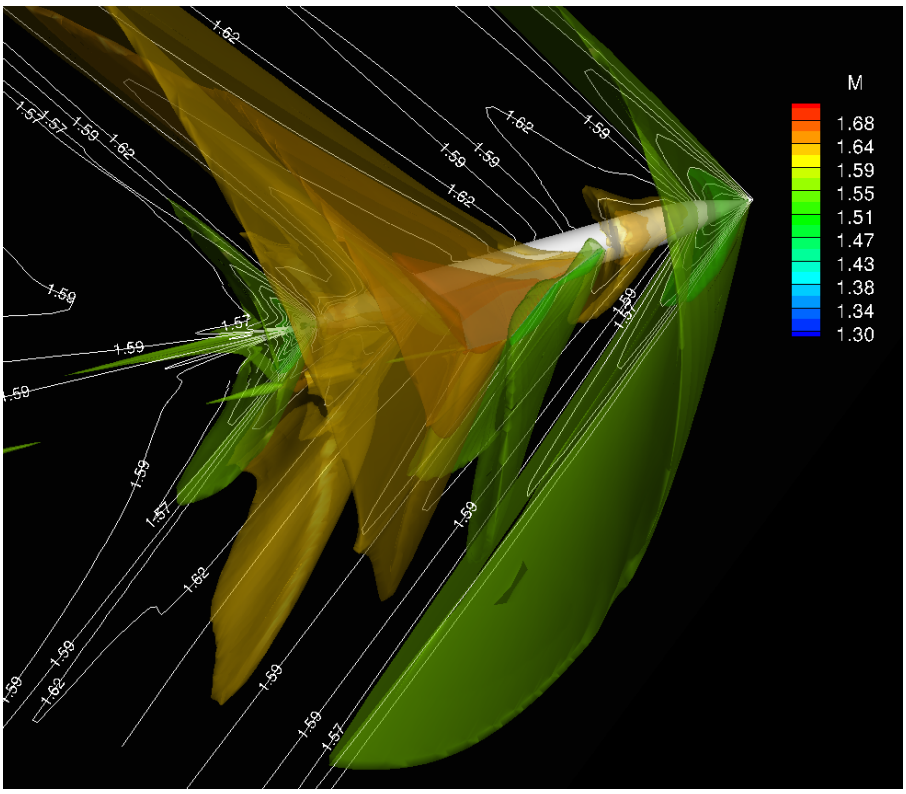

Figure 3.8: Mach iso-surfaces.

can be accurate only to distances up to 1.5-2 body lenghts. To extract farther from the source, mesh adaptation techniques are mandatory.

To sum up, if one considers that the results obtained with PANAIR in terms of aerodynamic coefficients show slight differences compared with the elsA solution and the reduced computational cost of PANAIR, one can argue that it is convenient to adopt the panel code in the aero-acoustic optimization. Several are the reasons why this strategy in practice is unappropriate:

- The geometry is discretized with a reduced number of elements (panels) if compared to a CFD mesh. The main drawback is that an accurate description of the configuration that is required for the design of low-boom configuration is impossible;
- The aerodynamic coefficients represent a global performance of the configuration. If one analyze the aerodynamic properties locally (pressure distribution over wing sections as shown in Figure 3.9), important differences arise that can prevent an accurate aerodynamic description of the configuration;
- The near-field solution provided by PANAIR consists only in the body skin pressure. This is a limitation not only for the aerodynamic analysis but also for the sonic boom prediction strategies available;
- The panel code has a computational cost unsignificant, but the computational cost of solving Euler equations on parallel architectures is reasonable also in the case of shape optimization where several configurations are evaluated.

For these reasons in the aerodynamic analysis that follow only CFD is considered.

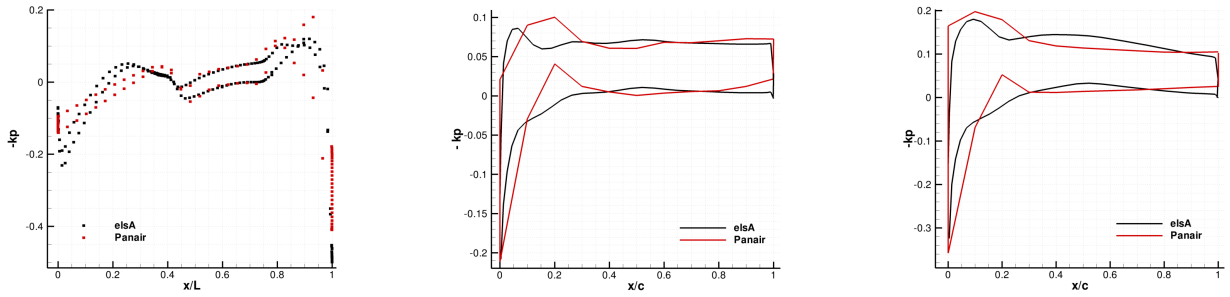

(a) y=0 m (b) y=1 m (c) y=4 m

Figure 3.9: Pressure coefficient distribution at the symmetry plane and at different wing sections. Comparison between Panair and elsA.

3.3 Acoustic properties

The aerodynamic CFD computation is a necessary input to evaluate the acoustic performance of the configuration. The sonic boom prediction methods presented in chapter 2 are here adopted.

Two-layer approach

Direct calculation of the lift and volume contribution to the equivalent area A_e is possible providing the skin geometry and the pressure distribution over it. The discretised information needed is obtained through a CFD Euler calculation (Figure 3.10b). The in-house code *Surfcut* is able then to build up the volume and the lift area distribution as well as the F-function, as shown in Figure 3.11a and Figure 3.11b.

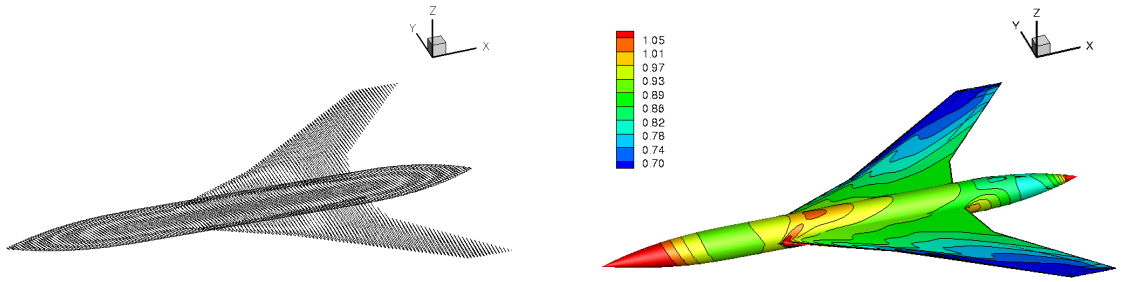

(a) Geometry cuts adopted for the evaluation of the volume area distribution.

(b) Pressure (p/p_0) over the configuration skin. ($M = 1.6$, $\alpha = 2$ degrees).

Figure 3.10: Information required for the evaluation of the equivalent area distribution.

The fuselage nose shows a minor contribution to the lift distribution that is mainly related to the presence of the wing, but from it originates the maximum positive peak of the F-function. The presence of the wing determines a modification of the curvature of the A_e distribution and, as a consequence, a second peak appears in the Whitham F-function responsible for a shock in the near-field. In the wing region (x between 11 m and 26 m in the chosen case), the cranked wing geometry combined with the complex pressure distribution generate several oscillations in the F-function.
The propagation is carried out using the F-function as the acoustic source signal. Results are obtained

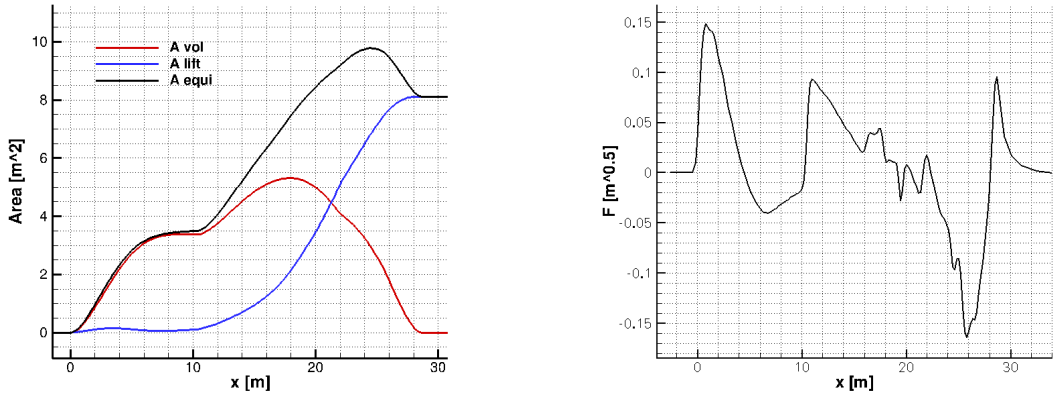

(a) Area distributions.

(b) Whitham F-function.

Figure 3.11: Equivalent area distribution and F-function evaluated with the two layer approach over the reference wing-body configuration. ($M = 1.6$, $\alpha = 2$ degrees, $h = 18,000$ m).

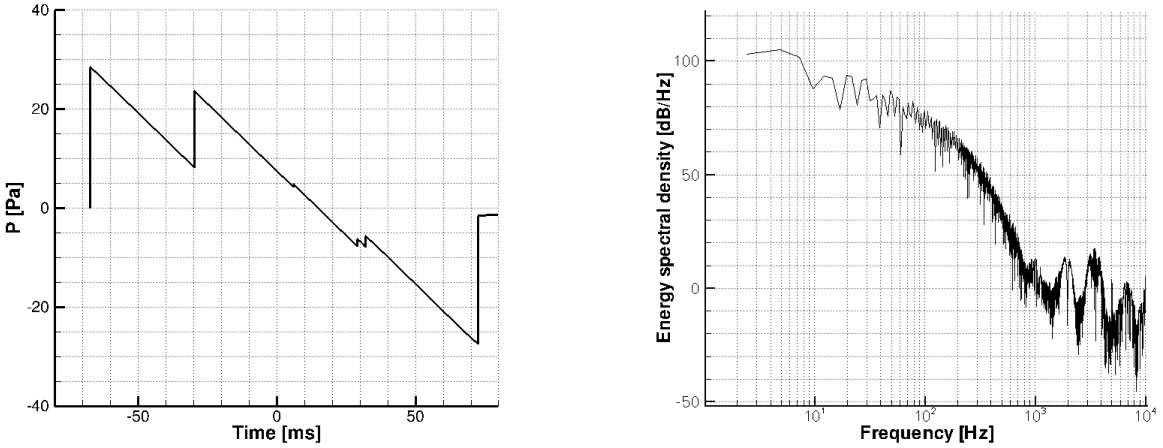

(a) Under-track ground signature.

(b) Energy density spectrum.

Figure 3.12: Reference configuration ground signature. ($M = 1.6$, $\alpha = 2$ degrees, $h = 18,000$ m).

using the TRAPS code. Figure 3.12 shows the under-track ground signature and the corresponding energy spectrum. The ground wave-form has three shocks as its corresponding signature in the near field and has a total duration of 140 ms. The front shock has the maximum overpressure equal to 28 Pa. The aft shock presents nearly the same amplitude, while the wing shock that follows the front one by 40 ms has half the amplitude of the others.
The spectrum shows that sonic boom energy is concentrated in the lowest frequencies of the audible range. Where human ear is most sensitive, between 2 and 5 kHz, the signal has lost half of its maximum energy. Indeed, to reduce sonic boom perception it is required to increase the energy decrease rate of the spectrum. This can be done acting on the shape of the waveform (Brown et al. [71]). Loudness

dB	dBA	dBC	PLdB
109.32	74.25	97.96	89.98

Table 3.1: Loudness Metrics. ($M = 1.6$, $\alpha = 2$ degrees, $h = 18,000$ m).

metrics are evaluated on the signal post-processed with rise time taken into account. The values in Table 3.1, if compared with the criteria proposed in past and recent studies for sonic boom acceptability show that, despite the reduced size of the configuration, shape modifications are still required to be able to respect anticipable criteria of acceptability for the next generation of supersonic civil aircrafts. The same operations can be performed on the paneled geometry using the surface pressure distribution

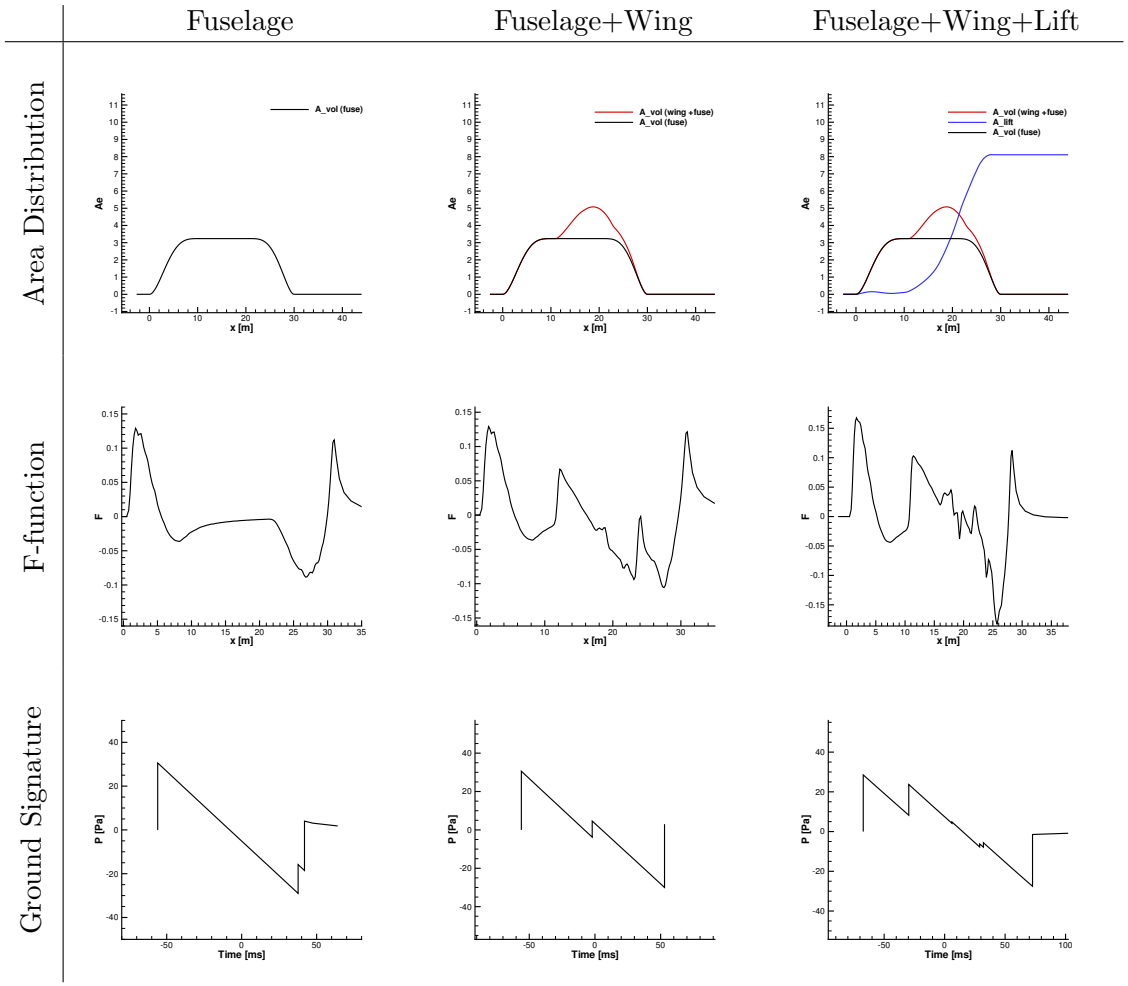

Table 3.2: Effects of configuration components.

evaluated on the body with PANAIR.

It appears interesting to analyze the break-down of the different terms that defines the A_e distribution of the reference configuration. Three different cases are considered:

- a zero incidence non-lifting fuselage;
- a zero incidence non-lifting wing-body configuration;
- a lifting wing-body configuration at 2 degrees.

The non-lifting fuselage configuration is defined by an equivalent area that consists only in the volume term. The corresponding F-function shows a first peak that corresponds to the front shock generated by the sharp nose and a following expansion region, which corresponds to the cabin. The rear part of the fuselage is characterized by an aft shock that shows almost the same amplitude as the front shock. Introducing a wing with symmetric profile and no camber to a zero incidence symmetric fuselage enables the extraction of the A_{vol}^{wing} term alone, if the lift area distribution is neglected. A modification of the curvature of A_e is introduced at the wing leading edge and causes a shock in the near field. Due to the fact that this shock is far enough from the first one, during the propagation, this shock does not coalesce with the front shock which maintains its amplitude. The wing introduces

a modification of the A_e curvature also in the rear part of the distribution, producing another strong shock in the near field. It can be seen from the F-function at a location near 25 m where a compression ($F' > 0$) is followed by an expansion ($F' < 0$). In this case the shock coalesces during the propagation with the rear shock. Introducing the lift distribution generates a modification of the F-function for $x \geq x_{wing\,init.}$, because the contribution of the fuselage to A_{lift} is almost negligible. An increase of the amplitude of the second peak of the F-function and the reduction of the distance from the first one induces a displacement of the middle shock at ground closer to the front shock. Further increase of the F-function second peak amplitude can determine a coalescence at ground of the two shocks. If it is not the case, results show that it is possible to modify the front and aft part of the ground signature separately. The second part of the F-function shows several small shocks that tend to coalesce with the aft shock during the propagation to the ground . A critical parameter which can radically change the ground signature is the wing position as it impacts directly the relative position of the multiple shocks pattern and it acts on the volume and the lift term of the equivalent area distribution. To reduce the impact of the wing introduction on the front shock, the position of the wing must be moved further downstream from the nose than its position on the original configuration.

Three-layer approach

The CFD near-field pressure is used as input for the three-layer approach. First pressure is directly extracted at three distances of interest, corresponding to cylinders at R/L equal to 0.5, 1 and 1.5 (Figure 3.13). These are discretized with structured uniform grids, and the pressure data is obtained

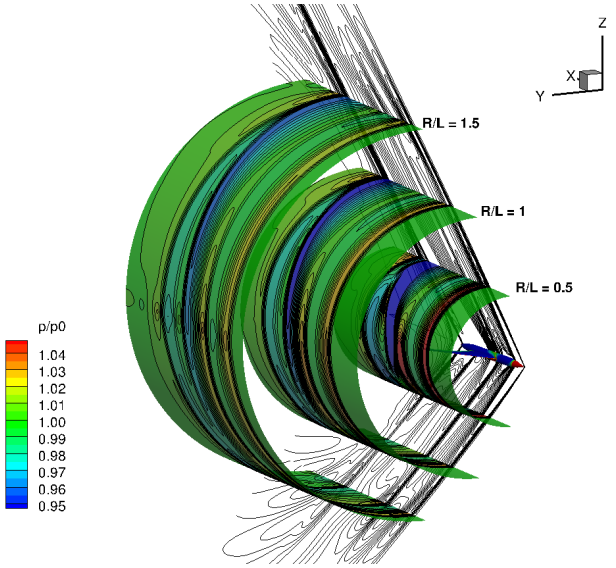

Figure 3.13: Direct pressure extraction over a structured uniform cylinder at different distances from the aircraft. ($c_L = 0.1$).

using linear interpolation in the volume of the CFD near-field solution.

As the distance increases, the cross-flow variation amplitudes diminish, which is expected physically but also results from numerical dissipation. These phenomena are clearly shown in Figure 3.14. The local axi-simmetry increases with distance especially in the region concerned by the flow that comes from the wing. Non axi-symmetries in the flow impact mainly the shape of the aft-part of the near field signature. The first peak of the near-field signature (Figure 3.15) reduces its magnitude by one-third as the distance increases from $R/L = 0.5$ essentially due to numerical diffusion. The impact of the different extraction distances is less straightforward, when looking at the far-field signatures (Figure 3.15). The ground signature for the different pressure extraction distances is less impacted compared to the near-field one excluding the bow shock. The signatures obtained after an extraction at $R/L = 0.5$ and $R/L = 1$ are similar with the exception of the tail shock that shows a difference of 4 Pa. The signature obtained starting from the cylinder at $R/L = 1.5$ is more similar to the one

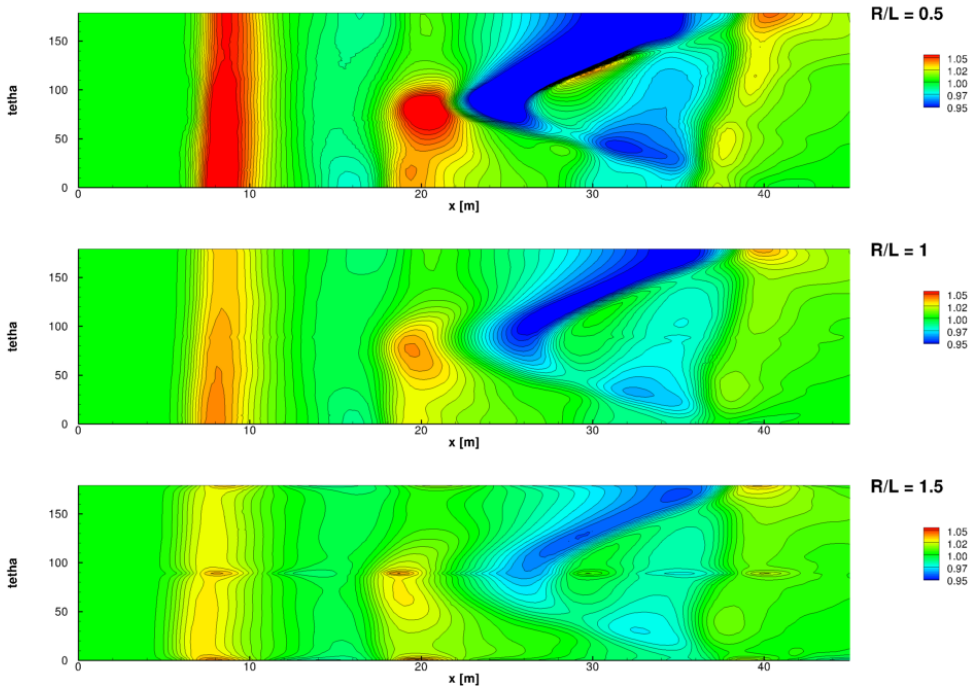

Figure 3.14: Comparison of the pressure field (p/p_0) extracted at different distances. ($c_L = 0.1$).

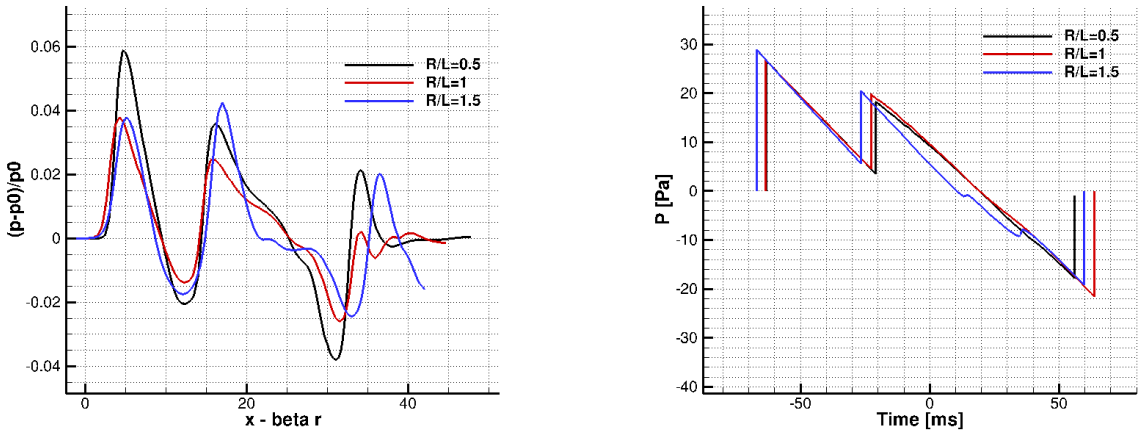

Figure 3.15: Near and far field signature at different distances from the source. Direct extrapolation method.

obtained with the two-layer approach. Cross flow in this case is reduced but with an increase of the spurious numerical dissipation.

3.4 Improvement of the three-layer approach

As already outlined in chapter 2, to overcome the problems that can occurs when considering direct extrapolation in the three-layer approach, multipole matching decomposition and mesh adaptation can be used for a better prediction of the near and far-field signatures.

Multipole-matching

An alternative to the pressure extraction at larger distances, to reduce the cross-flow effects and thus extract closer to the source, is provided by the multipole decomposition. Figure 3.16 shows the pressure field extracted over a cylinder at $R/L = 0.5$ decomposed with different multipole orders. The decomposition acts mainly modifying the flow generated by the wing and in particular the expansion region when the azimuth angle is below 50 degrees. The limits of the numerical method adopted are highlighted for high order decompositions. Oscillations appear downstream and propagate upstream beyond a critical $n = 22$. Figure 3.16 shows oscillations on the solution at $n = 25$, that reach the "useful" part of the signature. Such behavior is consistent with the multipole functions adopted for the composition that present higher values as the order is increased. The near-field and the ground signature obtained for different values of n are shown in Figure 3.17. The first shock converges quickly with multipole orders. The magnitude appears slightly increased with respect to the near-field signature directly extracted, while the front shock at ground is unmodified. Differences appear in the aft part of the signal. The tail expansion tends to be stronger as the multipole order is increased. In addition a small shock appears just before the rear shock in the ground signature.

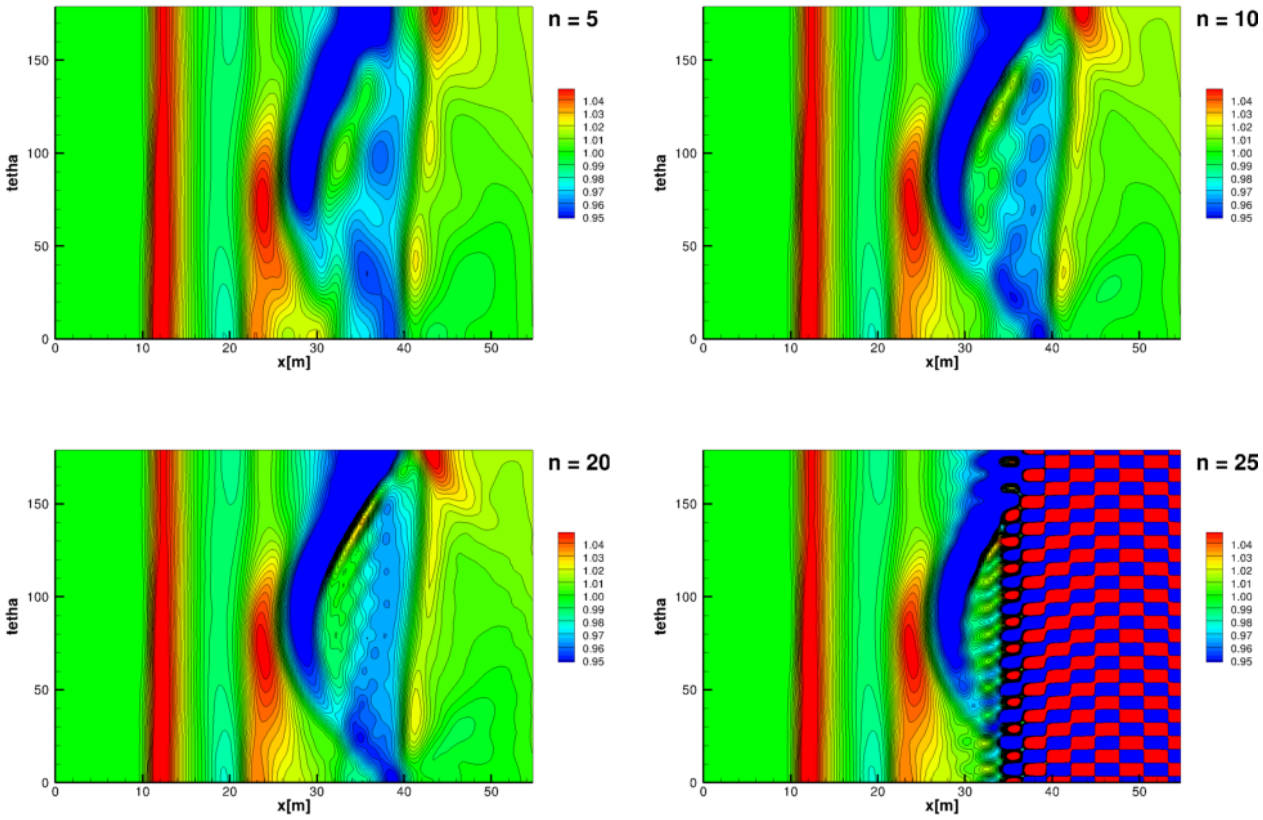

Figure 3.16: Pressure field (p/p_0) extracted over a cylinder at $R/L = 0.5$, with different multipole decompositions.

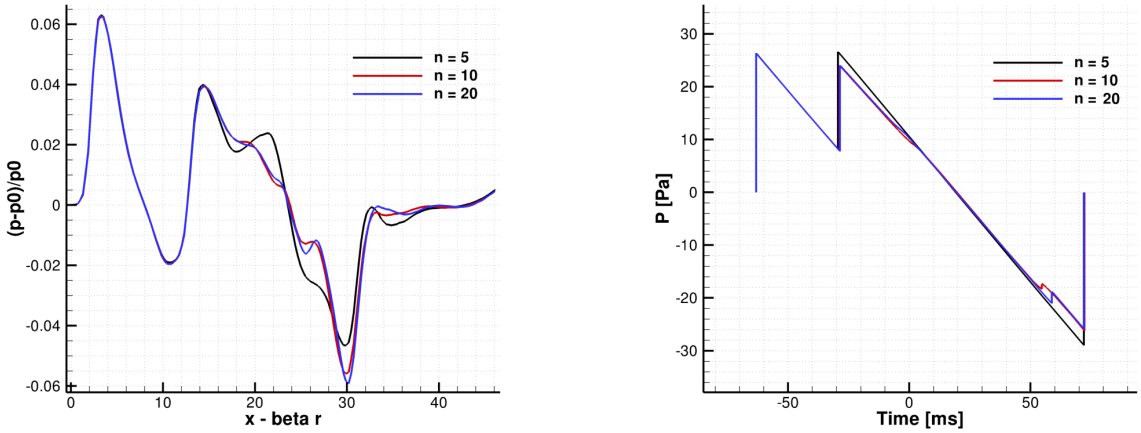

Figure 3.17: Undertrack near-field and ground signature for different order of multipole decomposition orders. $(R/L = 0.5)$.

Mesh adaptation

Mesh adaptation is a second axis of improvement that can provide an accurate numerical solution farther from the source. The mesh adaptation technique chosen is based on unstructured grids. The CFD computations with the elsA CFD software performed for the previous evaluations can therefore not be adopted here. New elements have to be introduced applying the grid adaptation technique.
The reference configuration introduced in section 3.1 has been modeled using the CAD software CATIA V5 by Dassault System. On this model an initial unstructured isotropic mesh is created using the Ansys ICEM software resulting in an 1,917,822 elements and 362,767 nodes mesh. The fuselage and the wing are respectively described using 32,691 and 89,075 triangular elements.

The flow solver is the Onera multi-physics polyhedral platform CEDRE [72] and its CFD solver CHARME. Invisicid Euler equations are used to describe the flow in the near-field. Concerning the numerical parameters adopted for the computations: the convective fluxes are computed using an AUSM+ method, while the space discretisation is resolved with the least square method. The mean gradients of each mesh element are evaluated using the information at the center of the cells in the neighborhood (short stencil). This choice combined with a limitation on the gradient values aims at improving the stability and the robustness of the computation. The Van Leer limiter is adopted to reduce the numerical dissipation. Supersonic inflow boundary condition (BC) is used at the inflow boundary specifying the following reference state conditions: a Mach number of 1.6, total pressure of 11.598 kPa, and total temperature of 216.7 K. At the outflow boundaries and at far-field supersonic outflow BCs are used. A symmetry plane BC is used to model the plane of symmetry to compute only a half configuration. Inviscid wall BCs are used to model the fuselage and the wing. Uniform free-stream flow conditions are defined as initial conditions throughout the computational domain. Figure 3.18 shows the initial mesh and its topology.

A Python framework $A^3 - SB$ (Automatic Anisotropic Adaptation for Sonic Boom prediction) has been developed to couple the mesh adaptation software and the CFD solver. The flowchart of the module is schemed in Figure 3.19.
The *Fefloa* adaptation software requires a mono-block domain and uses the INRIA Tetmesh format for both solution and mesh. CEDRE computations are run in parallel on a multi-block domain and the CEDRE proprietary format is used for meshes and solution manipulations. The interface is achieved using two tools: *Mangrove* and *Epinette*. The solution and the mesh are interpolated with *Mangrove* on a mono-block domain generated using the *Epinette* tool. *Mangrove* works in parallel: a sending process reads the old mesh and solution, while the other process interpolates the solution on the new mesh providing also the conversion to the Tetmesh format for both the mesh and solution. Once the solution is converted, *Fefloa* using a flow-variable reconstructs a metric field and generates a new

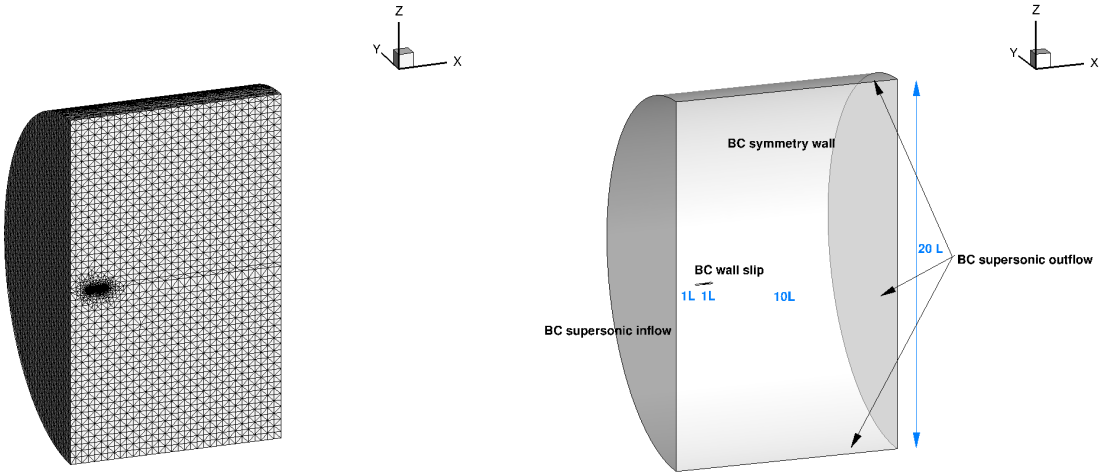

Figure 3.18: Initial isotropic mesh and domain boundary conditions adopted for the CEDRE computations.

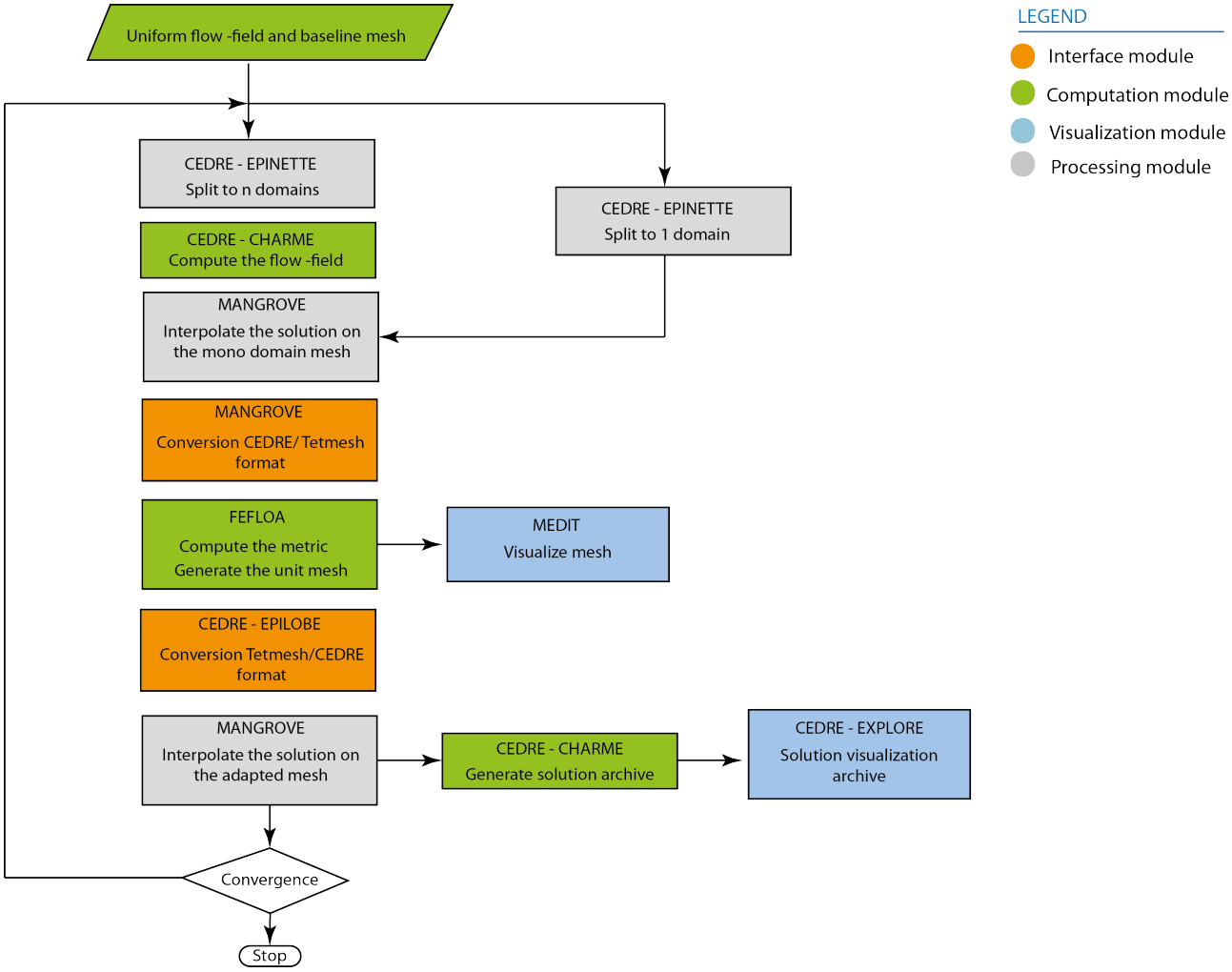

Figure 3.19: $A^3 - SB$ Flowchart scheme.

adapted mesh. The new mesh is then re-converted to the CEDRE format using the *Epilobe* tool and the old solution is interpolated on the new adapted mesh to provide an initial solution for the CFD solver. The domain is split in sub-domains with a uniform elements distribution among each processor using *Epinette* combined with the *Metis* mesh partitioner software. At this point a new

CFD computation can be performed thus beginning a new iteration of the adaptation cycle.

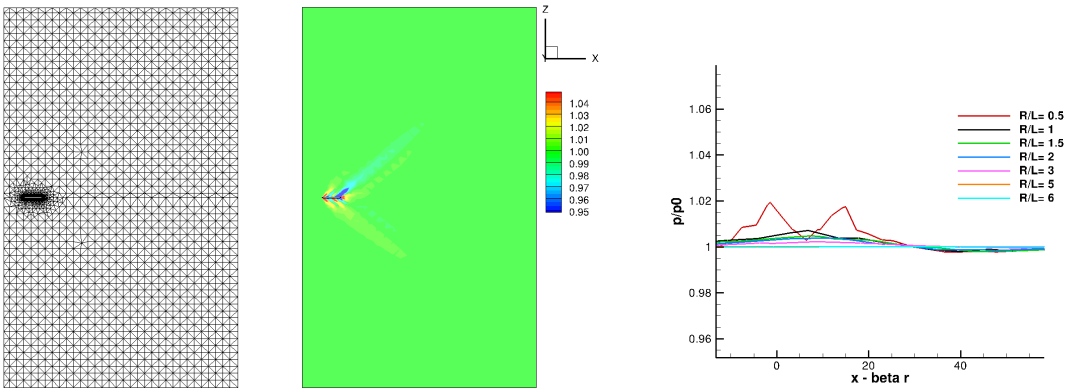

(a) Mesh and pressure field (p/p_0) in the symmetry plane. (b) p/p_0 signature at different R/L.

Figure 3.20: Initial isotropic not adapted mesh.

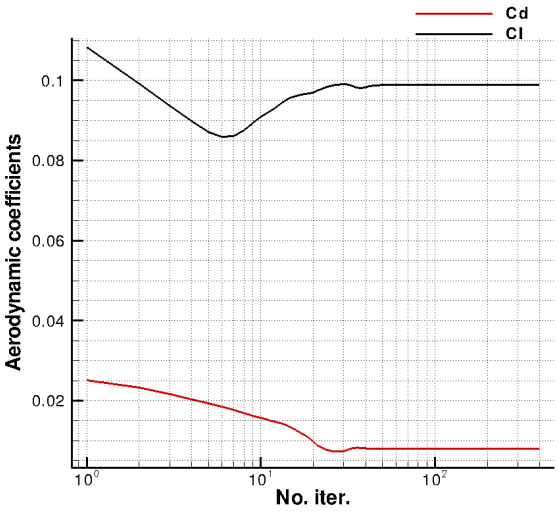

Figure 3.21: Aerodynamic coefficients convergence.

The solution obtained on the initial grid is shown in Figure 3.20. Despite the number of elements in the uniform grid, this kind of mesh is not able to predict shocks propagation in the near-field even at a short distance from the source ($R/L = 0.5$). Numerical dissipation strongly impacts the solution. None of the near-field pressure signatures is able to correctly describe shocks even at the smallest R/L in the proximity of the source. The convergence of the aerodynamic coefficients for the initial mesh is shown in Figure 3.21. Compared to those obtained with elsA it is possible to note that CEDRE for the same angle of attack, under-estimates the value of the drag and lift coefficients respectively equal to 0.0079 and 0.092. The discrepancies are mainly due to several aspects: slightly differences in the geometrical models, meshes and numerical options for the CFD computation. It is necessary to keep in mind also that the numerical scheme adopted for the unstructured computation is more dissipative compared to the one adopted for the structured grids computations.

The mesh and the pressure field in the symmetry plane and the pressure signatures p/p_0 in the near-field are shown for different grids in Figures from 3.22 to 3.25. Since the first adaptation, the shock and expansion waves propagate farther in the domain than in the initial mesh. The pressure signatures clearly show three shocks related to the nose, wing and fuselage tail.
When the complexity is increased to $\mathcal{C} = 40,000$, the shocks are less rounded compared to previous

Adaptation	No. elements	$\mathcal{C}$	ave($\mathcal{Q}_\mathcal{M}$)	ave($l_\mathcal{M}$)
1	622,308	20,000	1.46	1.020
5	705,664	20,000	1.46	1.020
10	712,860	20,000	1.46	1.019
11	990,861	40,000	1.42	1.019
15	1,059,821	40,000	1.42	1.019
20	1,086,200	40,000	1.42	1.019

Table 3.3: Adaptation iterations.

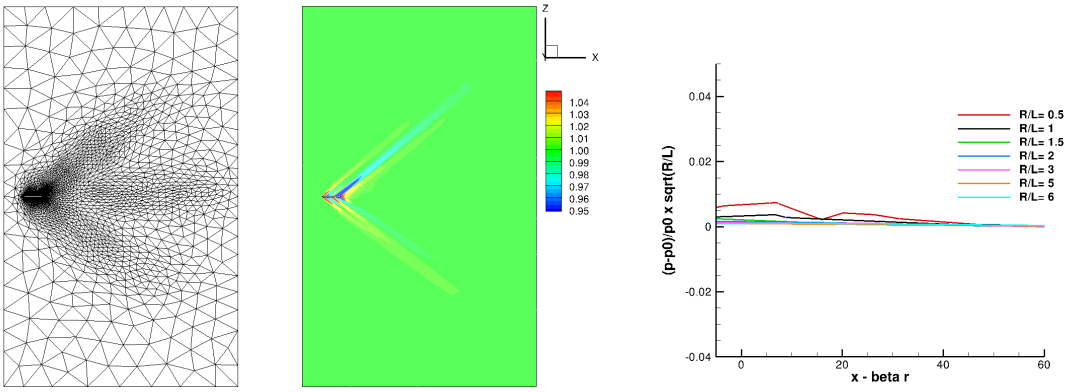

(a) Mesh and pressure field (p/p_0) in the symmetry plane. (b) p/p_0 signature at different R/L.

Figure 3.22: 1st adaptation at complexity $\mathcal{C} = 20,000$.

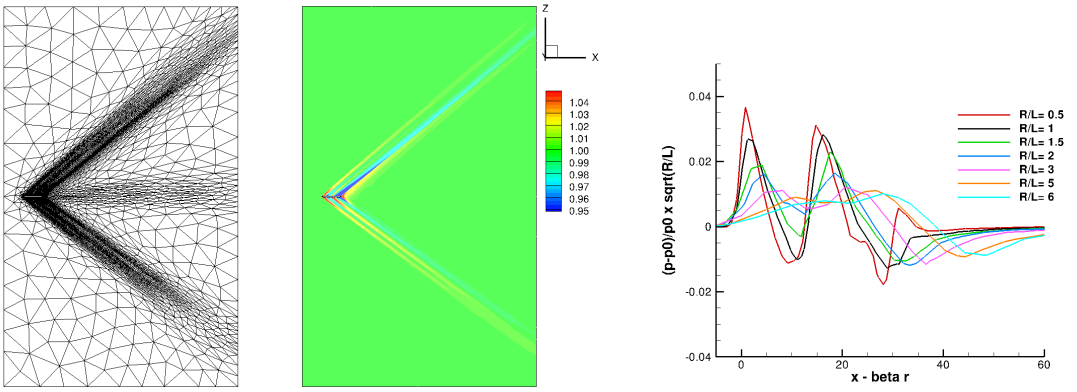

(a) Mesh and pressure field (p/p_0) in the symmetry plane. (b) p/p_0 signature at different R/L.

Figure 3.23: 5th adaptation at complexity $\mathcal{C} = 20,000$.

adaptations. At this complexity level, the number of mesh elements is increased to a ratio approximatively of 4/3 compared to the number of elements at $\mathcal{C} = 20,000$.
Adaptation iterations are shown in Table 3.3. The quality function and the Riemannian edge length highlight that during adaptation, meshes tend to the unit-mesh.

Figure 3.28 shows the convergence history of the pressure signature at $R/L = 6$ during the adaptation iterations. The initial mesh does not show perturbation of the free-stream conditions. Despite the high number of elements, this mesh shows a rapid dissipation of the solution in the near-field. The first ten iterations at $\mathcal{C} = 20,000$ are sufficient to capture the shocks pattern. At the 10th iteration the three shocks are clearly identified.
The last ten iterations at $\mathcal{C} = 40,000$ provide a better description of each shock reducing spurious dissipation. Peaks and dips appear sharper than on the previous grids. After 20 iterations the signal is almost converged, peaks are sharp and the second positive peak has the maximum pressure. The last

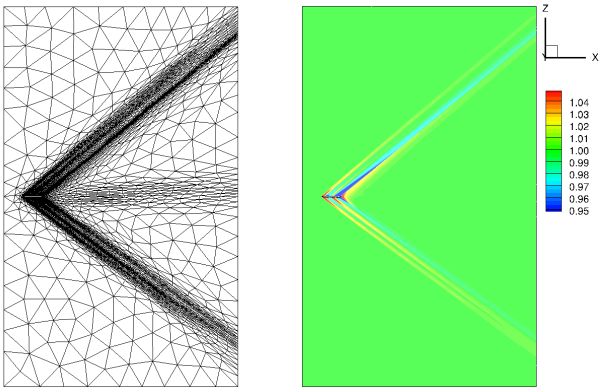

(a) Mesh and pressure field (p/p_0) in the symmetry plane.

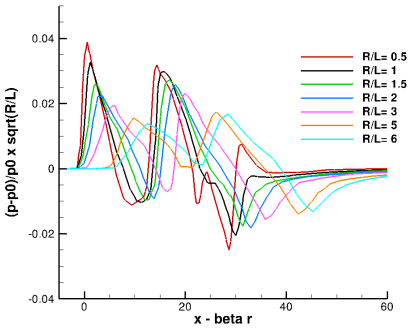

(b) p/p_0 signature at different R/L.

Figure 3.24: 10th adaptation at complexity $\mathcal{C} = 20,000$.

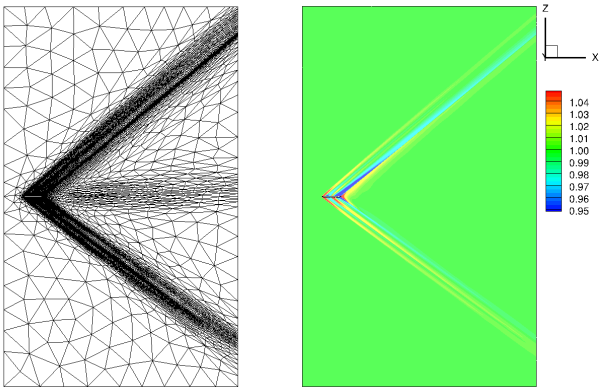

(a) Mesh and pressure field (p/p_0) in the symmetry plane.

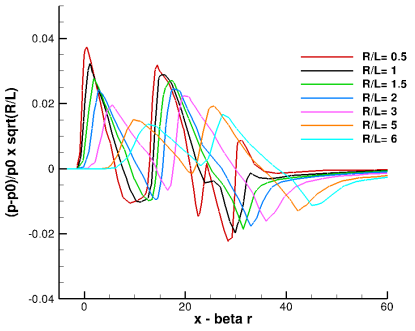

(b) p/p_0 signature at different R/L.

Figure 3.25: 11th adaptation at complexity $\mathcal{C} = 40,000$.

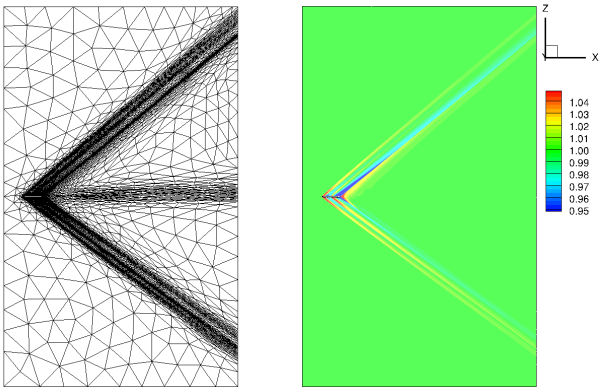

(a) Mesh and pressure field (p/p_0) in the symmetry plane.

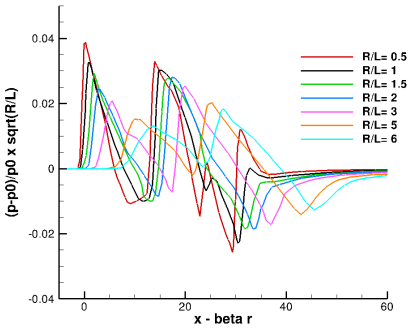

(b) p/p_0 signature at different R/L.

Figure 3.26: 15th adaptation at complexity $\mathcal{C} = 40,000$.

10 grids have high levels of anisotropy that can increase the required time for CFD convergence. The adaptation acts on the volume providing elements with a reduced volume and an increased anisotropy in the regions impacted by the pressure perturbation (see Figure 3.29). It has been shown in the three-layer approach that using different extraction distances have an impact on the ground signature. This is essentially due to the combination of two aspects:

- cross-flow;

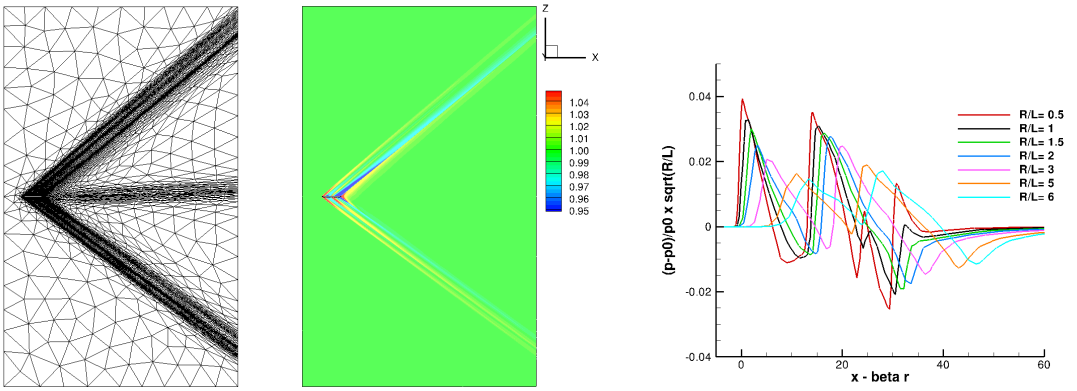

(a) Mesh and pressure field (p/p_0) in the symmetry plane. (b) p/p_0 signature at different R/L.

Figure 3.27: 20th adaptation at complexity $\mathcal{C} = 40,000$.

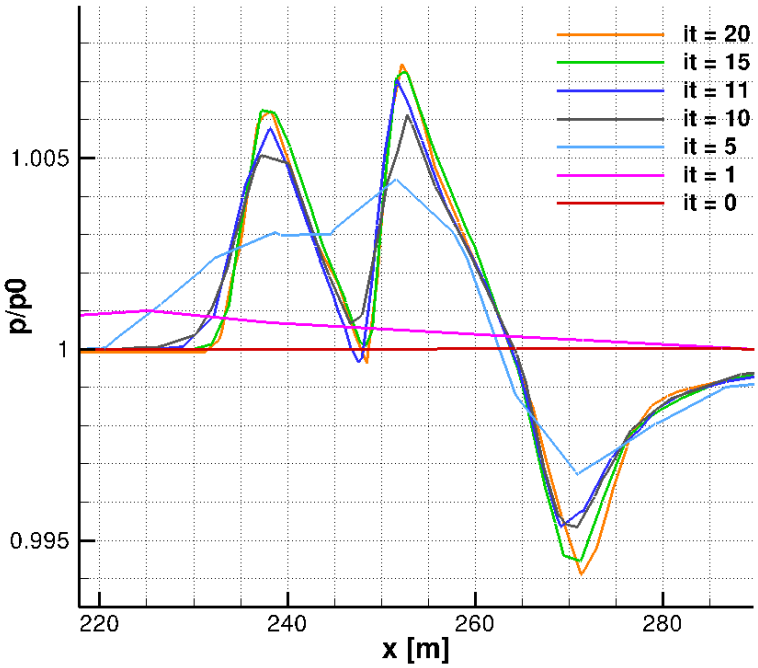

Figure 3.28: Pressure signature at $R/L = 6$ for different adaptation iterations.

- spurious dissipation.

Mesh adaptation reduces spurious dissipation so that cross-flow can be analyzed in detail in order to define an available range for direct pressure extraction. A measure of the local non axi-symmetry of the flow is provided by the azimuthal pressure gradient. If $\frac{\partial P}{\partial \theta}$ is equal to zero the flow-field is locally axi-symmetric so that it completely satisfies the hypothesis at the base of the acoustic propagation models. The region concerned by non axi-symmetries is clearly defined by the Mach cone generated at the nose. Looking behind the airplane we can observe the evolution of the flow-field non axi-symmetries. Figures 3.30 and 3.31 show that the non axi-symmetries are mainly produced by the wing and as we move away from the source the region impacted by non axi-symmetries extends, but the peaks of $\max|\frac{\partial P}{\partial \theta}|$ decrease in amplitude.

The identification of an available range of distances for pressure extraction can be provided by the analysis of a synoptic plan showing $\max_\theta|\frac{\partial P}{\partial \theta}(x/L, R/L)|$ and the corresponding θ at which the maximum is achieved (see Figure 3.32).

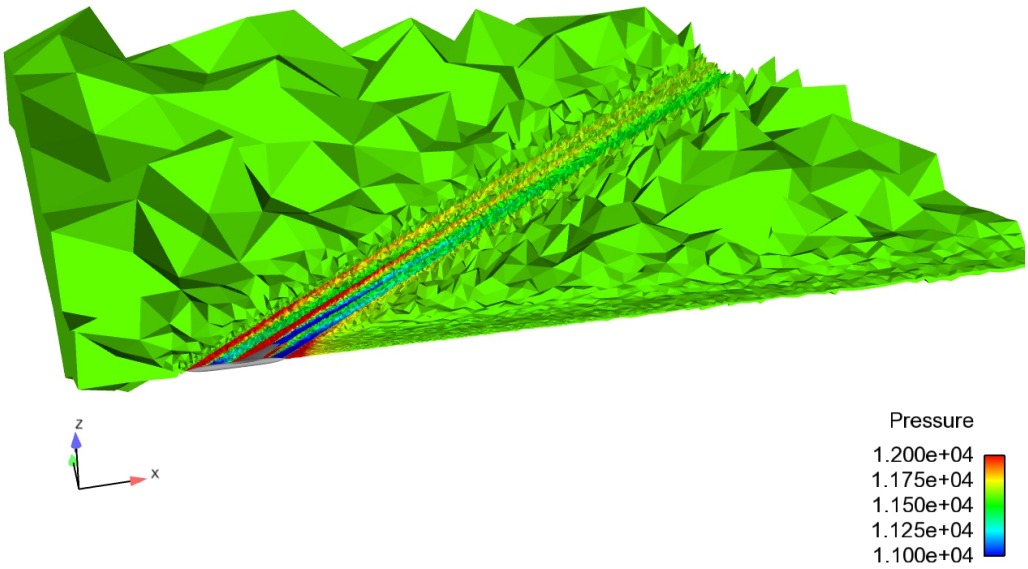

Figure 3.29: Crinkly plane showing pressure distribution in the plane $z = 0$. 20^{th} adaptation.

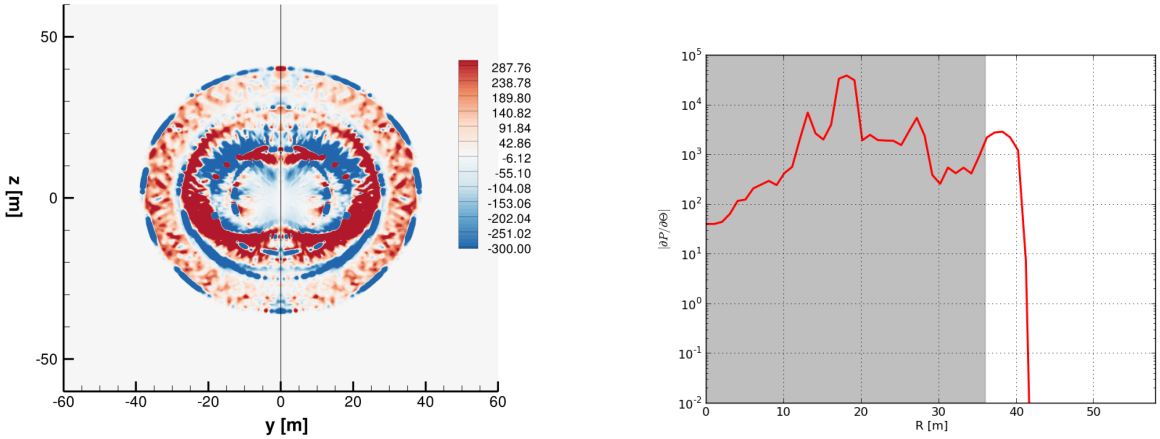

Figure 3.30: Azimuthal pressure gradient and $\max_\theta |\frac{\partial P}{\partial \theta}|$ in the near-field ($x = 2L$ after the nose top). In gray the estimated position of the front shock.

Different regions can be identified:

- $R/L \leq 1.5$: high values of the cross-flow occur in particular in the aft part of the configuration and affect the flow in the upper circular sector;
- $1.5 < R/L \leq 3$: the cross-flow generated by the wing becomes preponderant. The value of $\max_\theta |\frac{\partial P}{\partial \theta}(x/L, R/L)|$ is almost constant;
- $R/L > 3$: the value of the azimuthal gradient tends to slightly decrease mainly due to spurious dissipation.

Figure 3.33 shows the ground signature obtained after pressure extraction on cylinders at different distances from the source ranging from 1 to 6 body lengths over the solution obtained after 20 mesh adaptation iterations. Extraction performed at $R/L = 1$ highlights that high values of cross-flow are still present. Extractions performed below $R/L = 2$ are too close to the source, the signals at ground

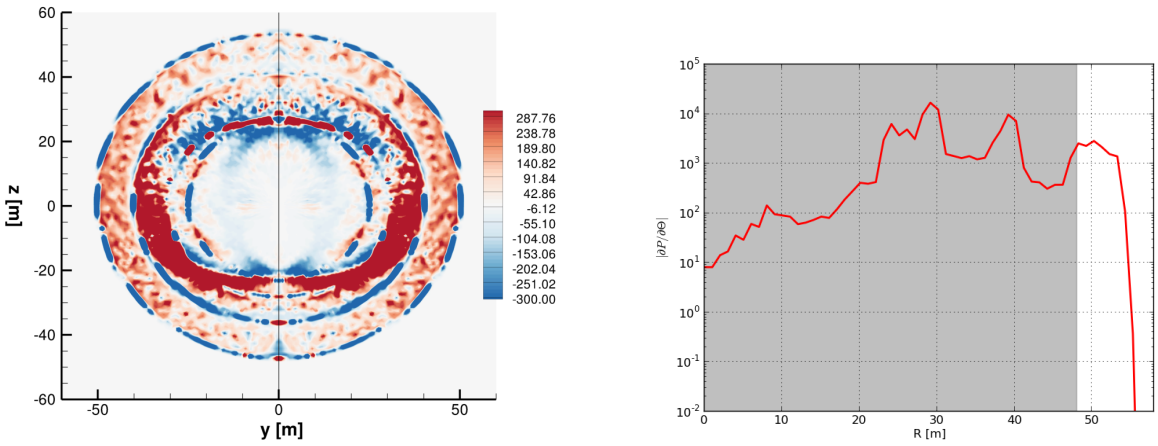

Figure 3.31: Azimuthal pressure gradient and $\max_\theta |\frac{\partial P}{\partial \theta}|$ in the near-field ($x = 3L$ after the nose top). In gray the estimated position of the front shock.

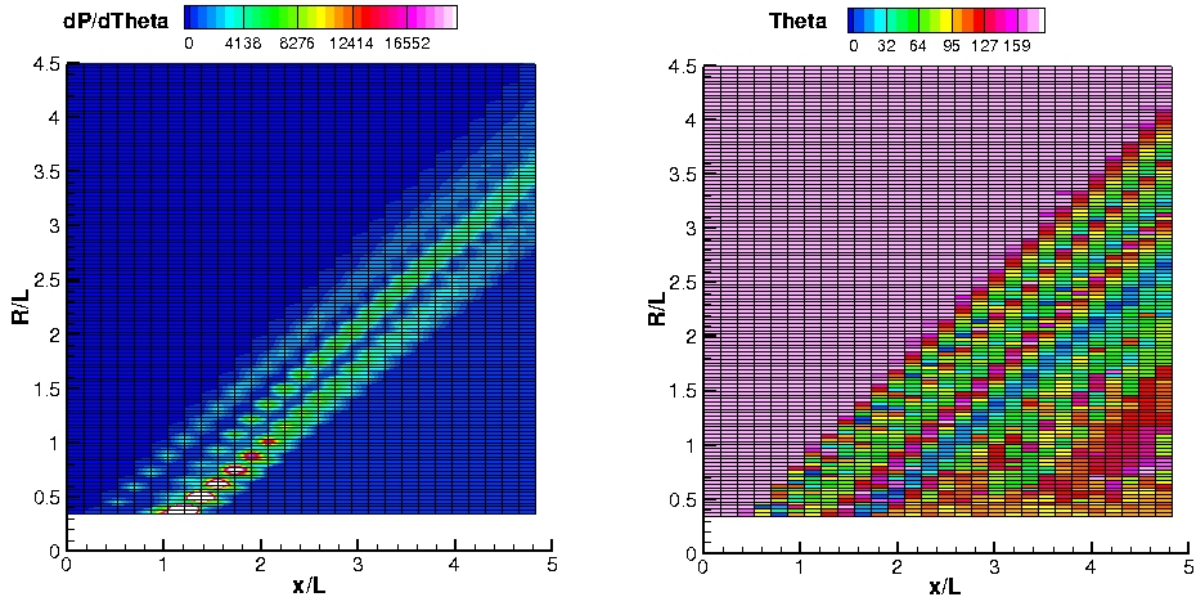

Figure 3.32: Synoptic plan for cross-flow evaluation, showings the maximum values of $|\partial P(x/L, R/L)/\partial\theta|$ and the azimuthal location.

show differences in the middle and in the aft shock. As the distance increases the signal at ground tends to converge to a double N-wave signature. The shock amplitudes remain almost constant also after extractions performed far from the acoustic source.

When the three-layer approach is coupled with mesh adaptation, the pressure extraction can be executed at a sufficient distance from the source (R/L between 2 and 3) to avoid at the same time cross-flow and numerical spurious dissipation. Further increases in the direct extraction distance, even if the mesh adaptation is incorporated into the prediction strategy, are not required for the simple wing-body configuration studied.

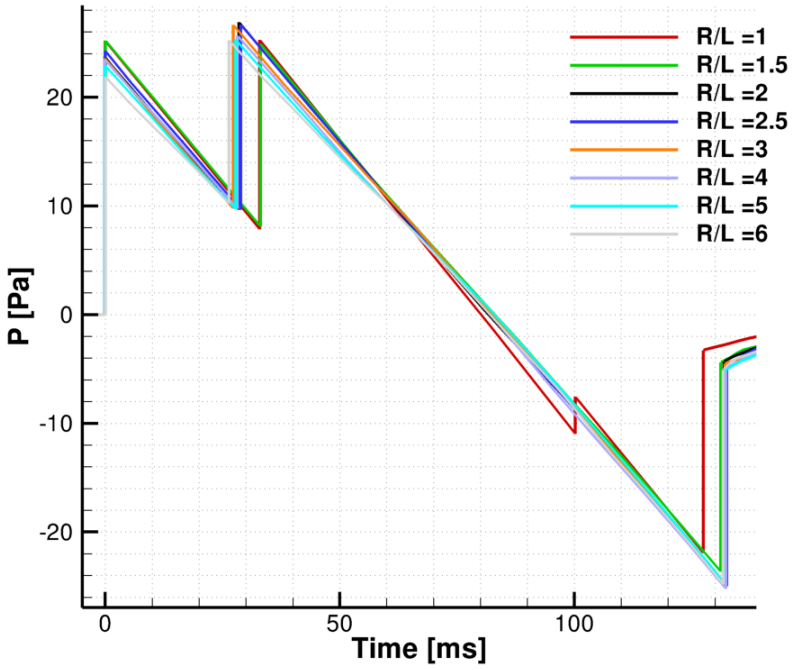

Figure 3.33: Ground signature obtained from the pressure field extracted at different distances from the source. The grid adopted is the one obtained after 20 adaptation iterations.

Surface adaptation

In the previous adaptation process the body skin grid was frozen. If one wants to accurately evaluate the aerodynamic performance of the configuration or the flow-field in the immediate proximity of the aircraft, the adaptation of the aircraft surface grid is needed.

Five cycles of adaptation of the body surface and volume mesh at different complexity $\mathcal{C} = [30,000, 60,000, 120,000, 240,000, 360,000]$ are performed using *Fefloa* and the A^3-SB framework. At each cycle, five adaptations are performed freezing the complexity. Inside each cycle the number of

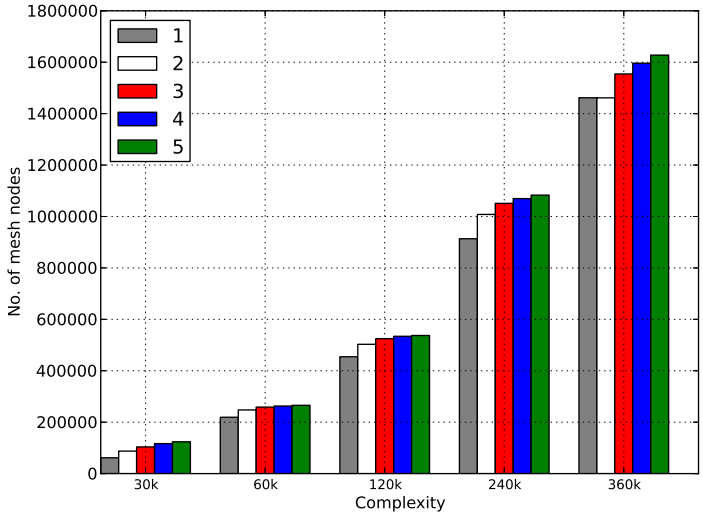

Figure 3.34: Evolution of the number of mesh nodes along the adaptation iterations.

mesh nodes tends to converge to a defined value, while as the complexity increases between different cycles the number of nodes in the whole domain increases proportionally (Figure 3.34). After 25 adaptation iterations the final mesh (Figure 3.35) has a total of 1,627,652 vertices and 9,589,872 tetrahedra, while the initial one consists of 61,515 vertices and 339,706 tetrahedra.

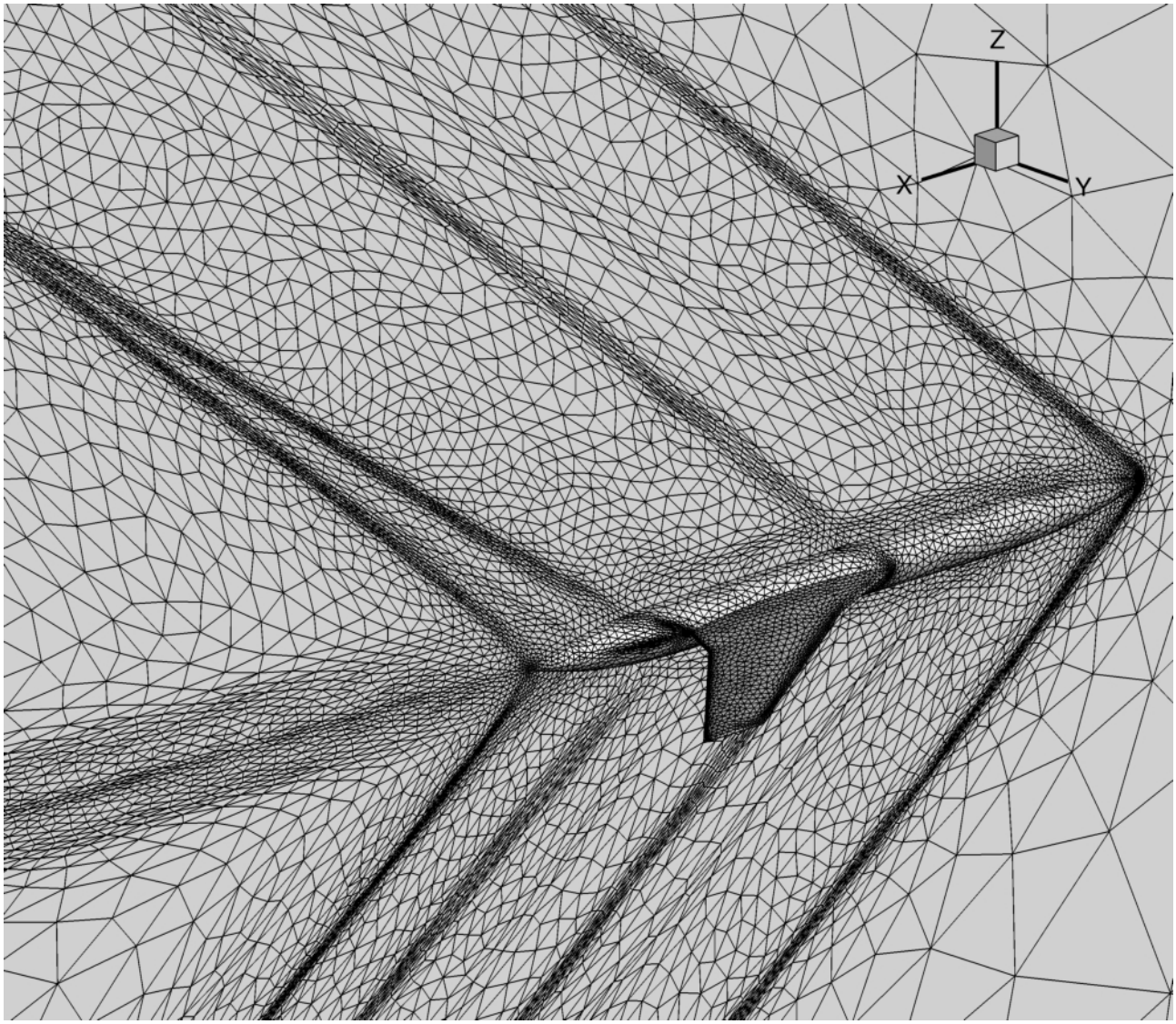

Figure 3.35: Final adapted mesh on the aircraft body and symmetry plane.

To evaluate the rate of convergence of the adaptation process, the final mesh is taken as reference and the solutions obtained at the final iteration of each fixed complexity cycle are interpolated on the reference mesh. The convergence rate is then evaluated with the norm L^p of the error:

$$errL^p = \|\sum_{k=1}^{N}(u_h^{\mathcal{C}} - u_h^{ref})\|_{L^p} \tag{3.3}$$

As demonstrated in [73] the continuous interpolation error model predicts an order of convergence of two on a sequence of embedded continuous meshes. Figure 3.36 shows the second order convergence obtained in the first three cycles. When the number of mesh nodes increases the rate of convergence is reduced. This is probably due to the fact that CFD computations require more iterations to achieve convergence.

When considering unstructured anisotropic grids we are also interested in quantifying the level of anisotropy. Two complimentary measures are adopted: anisotropic ratios (ratio) and anisotropic quotients (quo). The mesh $\mathcal{M}$ is characterized locally by the anisotropic ratio and the anisotropic

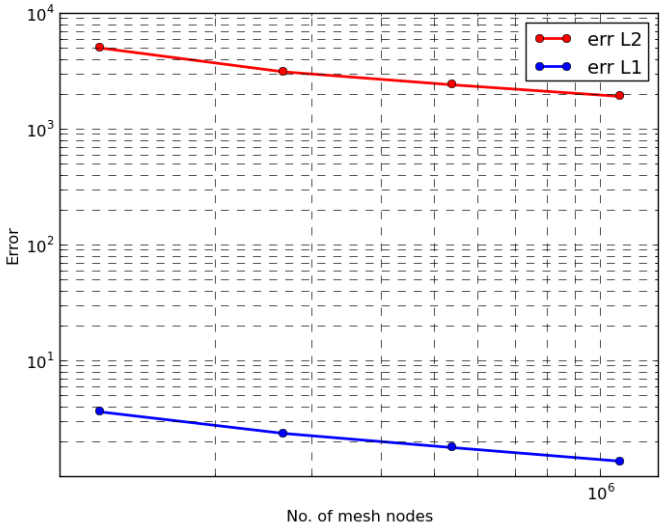

Figure 3.36: Solution convergence during the mesh adaptation process.

quotient. The anisotropic ratio stands for the maximum elongation of a tetrahedron by comparing two principal directions and is defined as:

$$ratio = \frac{\max_i h_i}{\min_i h_i} \tag{3.4}$$

where $(h_i)_{i=1,3}$ is the element size.

The anisotropic quotient represents the overall anisotropic ratio of a tetrahedron taking into account all the possible directions. It corresponds to the overall gain in three dimensions of an anisotropic adapted mesh as compared to an isotropic adapted mesh. The anisotropic quotient is the extension in n dimensions of the plan anisotropic ratio. To define a quotient consistent with a distance ratio in three dimensions the following definition is adopted:

$$quo = \frac{h_{max}^3}{h_1 h_2 h_3} \tag{3.5}$$

Adaptation cycle	Anisotropic ratio	Anisotropic quotient
5	7.06	42.28
10	8.45	62.47
15	8.73	69.05
20	8.89	73.67
25	8.93	75.30

Table 3.4: Evaluation of the average anisotropy ratio and quotient in the surface/volume adaptation process.

Table 3.4 shows the anisotropic ratio and the anisotropic quotient at the end of each adaptation cycle.

1	< ratio <	2	283473	2.96 %
2	< ratio <	3	1064060	11.10 %
3	< ratio <	4	983613	10.26 %
4	< ratio <	5	765613	7.98 %
5	< ratio <	10	2994298	31.22 %
10	< ratio <	**50**	3497568	**36.47** %
50	< ratio <	1e+02	1210	0.01 %
1e+02	< ratio <	1e+03	37	0.00 %

Table 3.5: Anisotropic ratios for the final adapted mesh.

1	< quo <	2	59933	0.62 %
2	< quo <	3	296264	3.09 %
3	< quo <	4	377745	3.94 %
4	< quo <	5	356332	3.72 %
5	< quo <	10	1210299	12.62 %
10	< quo <	**50**	3121395	**32.55** %
50	< quo <	1e+02	1871749	19.52 %
1e+02	< quo <	1e+03	2284629	23.82 %
1e+03	< quo <	1e+04	11518	0.12 %
1e+04	< quo <	1e+05	8	0.00 %

Table 3.6: Anisotropic quotients for the final adapted mesh.

Architecture and computational time

Two different architectures are adopted along the different $A^3 - SB$ processes: DaapUV (x86_64 - 32 cores 512Go) and Stelvio (SGI 3,000 cores Nehalem (4.5Go) / 1900 cores Westmere -(4Go) - 53.3 Tflops). The process distribution totalizes around 30 minutes on the different architectures. The different processes are shown in Table 3.7 and the mean time relative distribution for the different operations is shown in Figure 3.37. More than 60% of the time is spent for the CFD computations, while mesh adaptation impacts the 20% of the user time for each iteration. Further improvements

Architecture	Explore	Epilobe	Epinette	Mangrove	Fefloa	Cedre
DaapUV	-	1 proc.	1 proc.	-	1 proc.	-
Stelvio	1 proc.	-	-	32 proc.	-	16 proc.

Table 3.7: A^3 process distribution on the architecture available.

can be made performing the adaptation in parallel. Parallelization will avoid some of the processes required for solution interpolation and mesh generation for the mono-domain and it will reduce the total wall clock time required by the adaptation phase at each iteration.

3.5 Conclusions

In this chapter the reference wing-body configuration has been introduced. The CFD computations using the elsA solver has provided the near-field pressure and the aerodynamic performance of the configuration. This solution has been adopted to evaluate the acoustic properties in terms of loudness and sum of the shocks overpressure at ground. The sonic boom prediction based on the three-layer approach is actually the most accurate method available today to evaluate the sonic boom at ground. It essentially consists in coupling the CFD evaluation of the near-field with an acoustic ray-tracing approach. Near-field pressure evaluated with CFD is interpolated over a cylinder that surrounds the

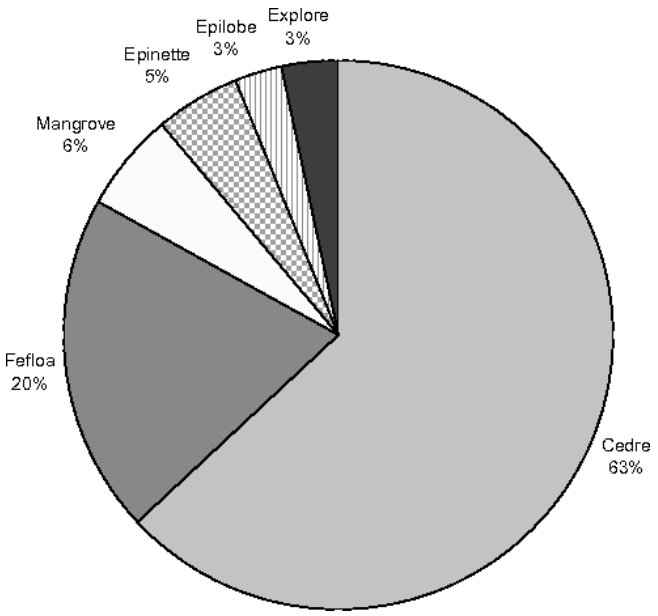

Figure 3.37: Mean time distribution for each adaptation iteration.

configuration and given as input to the acoustic code. The coupling requires particular care because the pressure associated to the CFD has to be extracted sufficiently far from the acoustic source in order to satisfy the condition of local axi-symmetry of the flow required by the acoustic propagation. Furthermore pressure extractions far from the aircraft suffer of spurious numerical dissipation. An intermediate phase is generally needed. Two techniques have been adopted to enhance the approach: multipole decomposition and anisotropic mesh adaptation.

The multipole matching relaxes the requirements in terms of R/L, thus allowing pressure extraction closer to the acoustical source and, as a consequence, alleviating the numerical dissipation. The matching makes the pressure field compliant with the acoustical assumption of local axi-symmetric flow field.

Anisotropic adapted meshes are actually preferred because of their limited computational time effort required when complex geometrical configurations are considered. In addition anisotropy is preferred to correctly predict shocks thus reducing numerical dissipation. The module $A^3 - SB$ is able to run a cycle of adaptation performing at each iteration mesh generation and the flow-field solution on the new grid. This methodology has been applied for the near-to-mid field sonic boom prediction of the supersonic business jet configuration. The results of the analysis show that isotropic meshes are unable to accurately predict the shock waves propagation, while adapted meshes since the first adaptation iterations are able to reduce artificial dissipation. The pressure signature is predicted with a sufficient accuracy to distances up to six body lenghts at the end of the process with a sufficient accuracy. Future work include the application of the $A^3 - SB$ module to other test cases and the development of a parallel version of *Fefloa* that will simplify the interface with CEDRE and at the same time will reduce the computational cost of mesh adaptation.

Chapter 4

Inverse design approach for low boom configurations

Design is to design a design to produce a design.
John Heskett

Contents

The objective of this chapter is to describe a complete inverse design approach developped that shapes the aircraft geometry starting from the desired ground signature. The correction of the supersonic linearized theory proposed by Whitham [3] is the basis of the shaped sonic boom theory. This chapter starts by an overview and the introduction of several improvements to the low-boom design approach based on the shaped sonic boom theory. This design methodology has been implemented in a module called AIDA and applied to test cases of increasing complexity. Limits of the inverse design approach are then investigated and solutions are proposed.

4.1 The shaped sonic boom theory

At the beginning of the sixties Mclean [74] and Hayes [75] have demonstrated that non asymptotic effects can act modifying the shape of the ground signature as a contrast with the common practice at the time which considered the ground signature shape independent from the aircraft shape. The vertical stratification of the atmosphere "freezes" the F-function shape in the mid-field, allowing it to reach the far-field in a shape different from the N-wave. This is due to the fact that in real atmosphere characteristics coalesce more slowly than in an uniform atmosphere. The mid-field F-function is explicitly related to the aircraft shape and to the lift distribution and, as a consequence, shaping the geometry of the acoustic source will result in a modification of the waveform that reaches the ground. This fundamental assumption has opened new possibilities in sonic boom minimization. Indeed the result suggests that, if a target shaped equivalent area distribution is achieved, it is possible to obtain a low boom signature at ground.
According to the shaped sonic boom theory, the acoustic source that generates the disturbance can be modelled with a body of revolution with an equivalent area that satisfies the following relationship:

$$A_e(L, \theta = 0^\circ) = \frac{\beta W}{\rho V^2} + A_{eng}(L, \theta = 0^\circ) \tag{4.1}$$

where A_{eng} corresponds to the stream-tube area changes resulting from engines, β is the Prandtl-Glauert factor, W is the aircraft weight, L is the aircraft length and V is the cruise speed.
Such approach is valid under the same assumptions as the Whitham's theory, but has the great advantage of being very efficient for preliminary design phases. The formulation is available for complex configurations for which an equivalent area can always be defined. In fact a limited number of CFD evaluations are required, thus limiting the computational cost of more expensive design strategies. Furthermore, the method effectiveness has been demonstrated recently with the JAXA's D-SEND#1 drop tests (see Appendix A) on a simple axi-symmetric configuration and in 2003 in the context of the shaped sonic boom demonstrator with the redesign of the F-5 nose. Still, the use of this approach in a preliminary design phase shows two main challenges:

- the definition of a geometry that corresponds to the equivalent area distribution;
- the definition of a target ground signature that minimizes a general acoustic metric (e.g. PLdB).

The first point is a critical aspect in the design because of the non uniqueness of the solution, and the designer has to define his preferences. Generating a signature that minimizes a specific acoustic metric is one of the aspect that Hass et al. [76] have suggested to investigate in order to obtain a valuable tool for the design of a low-boom configuration.

Several studies have investigated analytically the definition of a lower bound for the sonic boom. Petty [14] has demonstrated that in order to reach a lower bound for sonic boom, it is necessary to gather the positive area under F near 0, this has been done as in [15] using a variational approach that aims to minimize the F-function considering lift as a constraint as in equation (4.1). Hayes et al. [77] evaluated the minimum aircraft length that completely eliminates the front and the aft shocks. Howell et al. [78] analyzed the application of the theory to real aircraft configurations describing the effects of each aircraft components.

The idea at the basis of the shaped sonic boom theory is to define a parameterization of the F-function in order to obtain a specified ground signature after an analytical optimization. The problem that arises is: how to parameterize the F-function to consider general configurations?
Over the years, different parameterizations have been proposed aiming at the generalization of the methodology for the inverse design of complex configurations.

Jones and Seebass parameterization

The Jones-Seebass parameterization is based on the design of an A_e distribution that can define a ground signature with the minimum shock overpressure, the signature minimum impulse or the minimum shock pressure rise (see Figure 4.1).

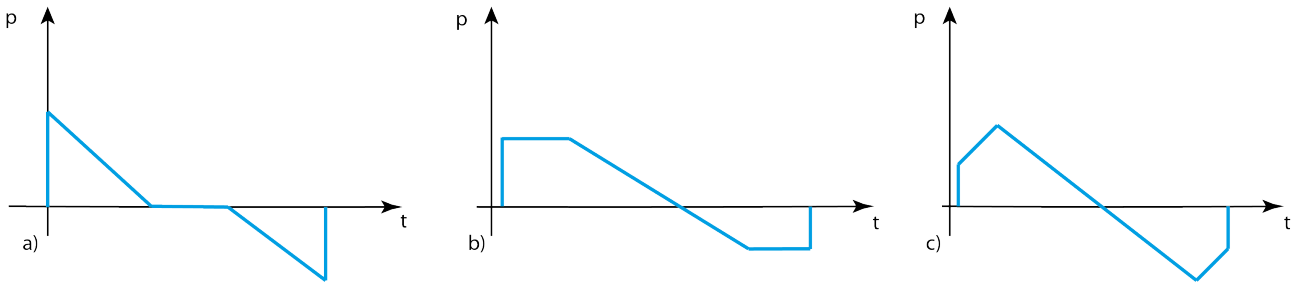

Figure 4.1: Different ground signature that can be obtained using the Jones and Seebass parameterization: a) minimum impulse, b) minimum shock overpressure, c) minimum shock pressure rise.

The boom lower bound limit identified by Petty [14], essentially means to concentrate volume in $x = 0$, thus producing a blunt nose. This peculiarity results in the following F-function parameterization schemed in Figure 4.2:

$$F(x) = \begin{cases} A\delta(x) + Bx + C & 0 \leq x \leq \lambda \\ Bx - D & \lambda \leq x \leq L \end{cases} \tag{4.2}$$

It is possible to distinguish the nose shock region defined using a Dirac's δ, the wing trailing edge

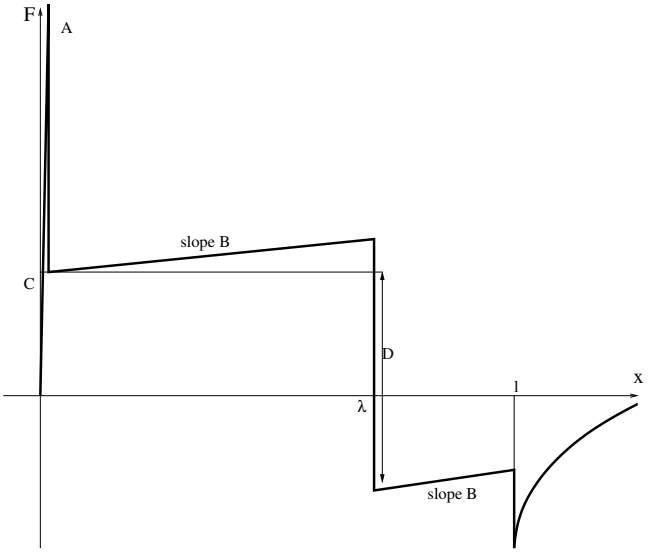

Figure 4.2: F-function for Jones-Seebass parameterization.

discontinuity located at $x = \lambda$ and the fuselage expansion regions. Regions before and after the trailing edge discontinuity are described using the same slope B of the F-function. The aft shock is related to the discontinuity that occurs at $x = L$.

Combining equations (2.5) and (2.4) results in the proportional relationship between the equivalent area and the pressure field far from the body:

$$\pi\sqrt{2\beta h}C_p(\xi, \theta = 0°) = \int_0^{\xi} \frac{A_e''(x, \theta = 0°)}{\sqrt{\xi - x}} dx \tag{4.3}$$

where C_p is the pressure coefficient. The inversion of equation (4.3) using the Abel transform and equation (4.1) leads to the relationship between the equivalent area, the aircraft weight and the Whitham F-function:

$$A_e(L, \theta = 0°) = A_{eng}(L, \theta = 0°) + \frac{\beta W}{\rho V^2} = 4\int_0^{l} F(x, \theta = 0°)\sqrt{L - x}dx \tag{4.4}$$

In the present study the engine stream tube area is always neglected as only glider configurations are considered. The evaluation of equation (4.4) using the F-function parameterization defined in (4.2)

leads to the following A_e distribution:

$$A_e(x,\theta=0^\circ) = 4Ax^{\frac{1}{2}} + \frac{16}{15}Bx^{\frac{5}{2}} + \frac{8}{3}Cx^{\frac{3}{2}} - \mathbf{1}(x-\lambda)\frac{8}{3}(C+D)(x-\lambda)^{\frac{3}{2}} \tag{4.5}$$

where $1(x-\cdot)$ is the Heaviside function[1], and the unknowns are the coefficients A, B, C, D, λ.

Darden nose bluntness relaxation

The F-function defined by George and Seebass describes bodies with a blunt nose resulting in low-boom/high-drag configurations [16]. No trade-off between aerodynamic and acoustic has been taken into account. Darden in [16] introduced a modification in the parametrization in order to consider nose bluntness relaxation allowing configurations with limited downgrading of the aerodynamic performance.
The Darden F-function is defined as:

$$F(x) = \begin{cases} 2xH/y_f & 0 \le x \le y_f/2 \\ C(2x/y_f - 1) - H(2x/y_f - 2) & y_f/2 \le x \le y_f \\ B(x-y_f) + C & y_f \le x \le \lambda \\ B(x-y_f) - D & \lambda \le x \le L \end{cases} \tag{4.6}$$

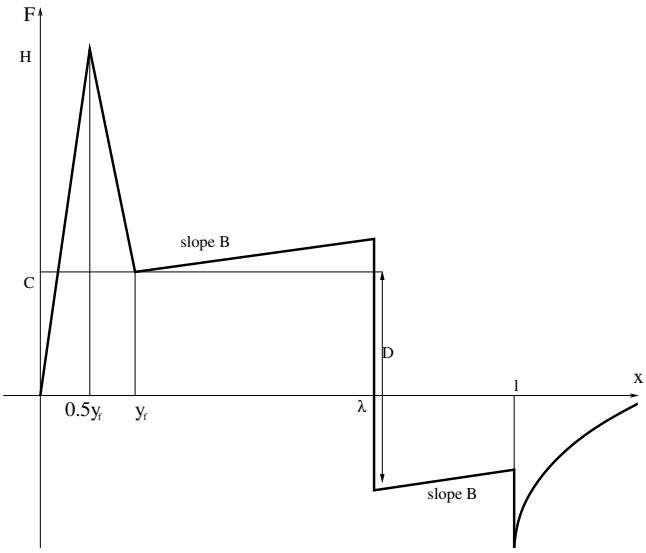

Figure 4.3: F-function for Darden parameterization.

If y_f tends to zero, Darden formulation converges toward the Jones and Seebass F-function. The fuselage nose region corresponds to the first part of the F-function from zero to y_f, while λ always corresponds to the geometrical discontinuity due to the wing trailing edge. Using the Abel transformation defined in equation (4.4) with the F-function parameterization (4.6), it is possible to evaluate the equivalent area as:

$$\begin{aligned} A_e(x,\theta=0^\circ) = {} & \frac{32}{15}\frac{H}{y_f}x^{5/2} + 1(x-\frac{y_f}{2})\frac{8}{15}(x-y_f)^{3/2}\left[\left(\frac{3y_f}{2}+2x\right)\left(\frac{1}{y_f}\right)(2C-4H)+5(2H-C)\right] \\ & +1(x-y_f)4(x-\eta y_f)^{3/2}\left[\left(\frac{2C}{y_f}\right)\left(-\frac{2}{15}\right)(3y_f+2x)+\frac{2}{3}C+\frac{4}{15}\frac{H}{y_f}(3y_f+2x)+\right. \\ & \left.-\frac{4}{3}H+\frac{2}{15}B(3y_f+2x)-\frac{2}{3}By_f+\frac{2}{3}C\right]-1(x-\lambda)\frac{8}{3}(x-\lambda)^{3/2}(C+D) \end{aligned} \tag{4.7}$$

where the unknowns are H, C, D, B, λ. Mack [80], in the context of the High Speed Research (HSR) program, adopted the Jones-Seebass-George-Darden theory to the design of a real supersonic business jet configuration, and showed the advantages and the limitations of the application of this strategy to a complex design process (e.g. generalization of the design geometry).

[1] In shaped sonic boom literature it is common practice to use this notation[16], [79].

Rallabhandi formulation

The results of the studies conducted during the HSR program ([10], [11]) have shown that low-boom signatures are determined using more complex F-functions than those obtained with the Darden parameterization. A first generalization of the parameterization was proposed by Rallabhandi and Mavris [79] aiming at low-boom signatures described in the work of Mack [80]. The F-function is written in equation (4.8) and schemed in Figure 4.4.

$$F(x) = \begin{cases} \dfrac{xH}{\eta y_f} & 0 \le x \le \eta y_f \\ \dfrac{C}{1-\eta}\left(\dfrac{x}{y_f} - \eta\right) - \frac{H}{2(1-\eta)}\left(\dfrac{2x}{y_f} - 2\right) & \eta y_f \le x \le y_f \\ B_1(x - y_f) + C & y_f \le x \le \xi \\ B_2(x - \xi) + C_1 & \xi \le x \le \lambda \\ \dfrac{-(D + C2)}{t}(x - \lambda) + C_2 & \lambda \le x \le \lambda + t \\ B_3(x - \lambda - t) - D & \lambda + t \le x \le L \end{cases} \tag{4.8}$$

The formulation is such that for the case $B_1 = B_3$, $\eta = 0.5$, $\xi = y_f$, $t = 0$, it reduces to the Darden

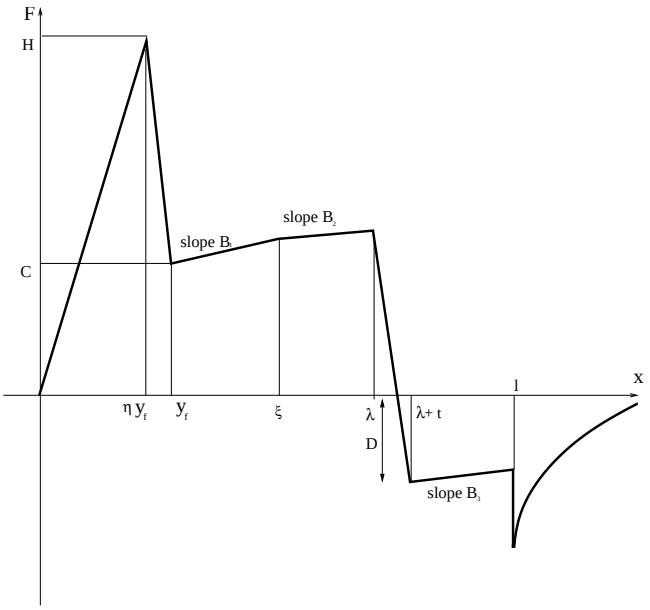

Figure 4.4: Rallabhandi F-function parameterization.

F-function. Using the Abel transform defined in equation (4.4), the equivalent area distribution is written as:

$$\begin{aligned} A_e(x, \theta = 0^\circ) = {} & \frac{16H}{15\eta y_f} x^{5/2} + 1(x - \eta y_f)\left[\frac{8}{15\eta y_f(1-\eta)}(x - \eta y_f)^{3/2}(H - \eta C)(2\eta y_f - 2x)\right] + \\ & + 1(x - y_f)\left[\frac{8}{15 y_f}(x - y_f)^{3/2}\left(B_1 y_f - \frac{C - H}{1 - \eta}\right)(2x - 2y_f)\right] + \\ & + 1(x - \xi)\left[\frac{8}{15}(x - \xi)^{3/2}(B_2 - B_1)(2x - 2\xi)\right] + \\ & + 1(x - \lambda)\left[\frac{8}{15}(x - \lambda)^{3/2}\left(B_2 + \frac{D + C_2}{t}(2\lambda - 2x)\right)\right] + \\ & + 1(x - \lambda - t)\left[\frac{16}{15}(x - \lambda - t)^{5/2}\left(B_3 + \frac{D + C_2}{t}\right)\right] \end{aligned} \tag{4.9}$$

Notice that in [79] the term $(H - \eta C)$ is not reported. However, it is required as result of the integration of the Whitham F-function in the range $\eta y_f \le x \le y_f$.

Generalization to front and aft shaping

The analysis of the wing-body configuration presented in chapter 3 has shown that even simple configurations are related to complex F-functions. Further improvements of the parameterization were proposed by Haas and Kroo [76] and Plotkin et al. [81]. The two methods are very similar, both aim at generalizing the sonic boom minimization theory in order to consider more general ground signature thus increasing the design space in terms of configuration geometries. Haas and Kroo have proposed an interesting revisited version of the classical shaped sonic boom theory able to produce multi-shock signatures. In their work they have also introduced some primordial elements of trade-off between aerodynamics and acoustics.
The formulation proposed by Plotkin is in continuity with the previous developments, and for this reason is adopted and analyzed in this chapter in order to define a complete inverse design approach based on the shaped sonic boom theory.
The generalized parametric F-function presented in Plotkin et al.[81] is one of the most general and embed all the previous formulations. It is schemed in Figure 4.5. and is defined as:

$$F(x) = \begin{cases} \beta_0 x & 0 \le x \le \eta_2 y_f \\ \frac{H-\beta_0\eta_2 y_f}{(\eta-\eta_2)y_f}x - \frac{H-\beta_0\eta y_f}{(\eta-\eta_2)y_f}\eta_2 y_f & \eta_2 y_f \le x \le \eta y_f \\ \beta_2(x-\eta y_f)+H & \eta y_f \le x \le \eta_3 y_f \\ \frac{C-H-\beta_2(\eta_3-\eta)y_f}{(1-\eta_3)y_f}(x-\eta_3 y_f)+H+\beta_2(\eta_3-\eta)y_f & \eta_3 y_f \le x \le y_f \\ B_1(x-y_f)+C & y_f \le x \le \lambda_{1,1} \\ B_2(x-\lambda_{1,1})+C_1 & \lambda_{1,1} \le x \le \lambda_{1,2} \\ ... & \\ B_P(x-\lambda_{1,P-1})+C_{P-1} & \lambda_{1,P-1} \le x \le \lambda \\ -\frac{D+C_P}{t}(x-\lambda)+C_P & \lambda \le x \le \lambda+t \\ B_{P+1}(x-\lambda-t)-D & \lambda+t \le x \le \lambda_{2,1} \\ B_{P+2}(x-\lambda_{2,1})-D_1 & \lambda_{2,1} \le x \le \lambda_{2,2} \\ ... & \\ B_{P+N}(x-\lambda_{2,N-1})-D_{N-1} & \lambda_{2,N-1} \le x \le L \end{cases} \tag{4.10}$$

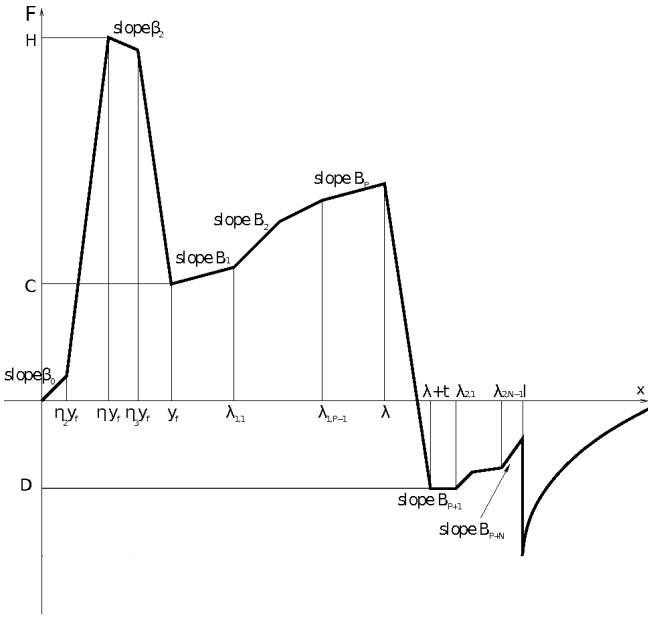

Figure 4.5: Generalized F-function for front and aft shaping.

Applying the Abel transformation on the F-function defined in (4.10) it is possible to obtain the

analytical expression of the equivalent area distribution as:

$$
\begin{aligned}
A_e(x,\theta=0^\circ) = {} & \frac{16}{15}\beta_0 x^{5/2} + 1(x-\eta_2 y_f)\frac{16}{15}(x-\eta_2 y_f)^{5/2}\left[\frac{H-\beta_0\eta_2 y_f}{(\eta-\eta_2)y_f}-\beta_0\right] + \\
& +1(x-\eta y_f)\frac{16}{15}(x-\eta y_f)^{5/2}\left[\beta_2-\frac{H-\beta_0\eta_2 y_f}{(\eta-\eta_2)y_f}\right] + \\
& +1(x-\eta_3 y_f)\frac{16}{15}(x-\eta_3 y_f)^{5/2}\left[\frac{C-H-\beta_2(\eta_3-\eta)y_f}{(1-\eta_3)y_f}-\beta_2\right] + \\
& +1(x-y_f)\frac{16}{15}(x-y_f)^{5/2}\left[B_1-\frac{C-H-\beta_2(\eta_3-\eta)y_f}{(1-\eta_3)y_f}\right] + \\
& +\sum_{i=1}^{P-1} 1(x-\lambda_{1,i})\frac{16}{15}(x-\lambda_{1,i})^{5/2}(B_{i+1}-B_i) + \\
& +1(x-\lambda)\frac{16}{15}(x-\lambda)^{5/2}\left[-\frac{D+C_P}{t}+B_P\right] + \\
& +1(x-(\lambda+t))\frac{16}{15}(x-(\lambda+t))^{5/2}\left[\frac{D+C_P}{t}+B_{P+1}\right] + \\
& +\sum_{i=1}^{N-1} 1(x-\lambda_{2,i})\frac{16}{15}(x-\lambda_{2,i})^{5/2}(B_{P+i+1}-B_{P+i})
\end{aligned}
\tag{4.11}
$$

where N and P are respectively the number of segments before and after λ. No constraints are imposed on their values. The unknowns are $H, C_i, B_i, D, \eta_i, y_f, \beta_i, t, \lambda$. This parameterization is able to describe complex configurations producing multi-shocks signatures that can reduce the sonic boom impact at ground. This formulation embed the previous one, so that for $N = 2$, $P = 1$, $\eta_2 = \beta_0 = \beta_2 = 0$ and $\eta_3 = \eta$, the Rallabhandi formulation is obtained. As a consequence a common approach to the different parameterizations can be identified for the evaluation of the unknowns.

4.2 AIDA: Acoustic Inverse Design Approach

Methodology and algorithm

A Python module called AIDA - Acoustic Inverse Design Approach - has been developed to define low-boom configurations using the shaped sonic boom theory. The main objectives of this module are three fold:

- The evaluation of the F-function coefficients;
- The evaluation of the geometry area distribution starting from the corresponding equivalent area A_e;
- The definition of an F-function that minimizes a user-specified acoustic metric in the far-field.

The input data required are the flight conditions in term of Mach number M_∞ and altitude h, the aircraft weight W and length L, the desired front on rear pressure shocks ratio P_f/P_r, the coefficients B_*, λ_* and y_f. The length L can be replaced by the front shock pressure rise P_f depending on the procedure adopted for the evaluation of the coefficients (this aspect will be discussed later in this section).

To achieve the first objective it is necessary to introduce some theoretical elements of geometrical acoustics. The age parameter Λ defines the steepening of the signal during propagation. Propagation is performed using the non-linear ray-tracing code TRAPS [37] which provides this value. The inverse of Λ represents the slope s of the area balance line (Figure 4.6) defined as in [82]:

$$
s = -\frac{\sqrt{2\beta}}{\gamma M_h^3 \int_0^h \frac{p_h}{p}\sqrt{\frac{\rho a_h}{\rho_h a}}\sqrt{\frac{A_h}{z_h A}}\frac{M}{\beta}dz}
\tag{4.12}
$$

This line is used to evaluate a front and a rear area balance of the F-function, thus obtaining the expression of two unknown coefficients H and C. The front area balance (Figure 4.6a) is expressed as:

$$\frac{1}{2}\Lambda C^2 = \int_0^{y_f} F(x)dx \tag{4.13}$$

If equation (4.13) is satisfied a shock is produced at location y_f at an altitude h below the aircraft. Using the definition of the F-function in equation (4.10) for evaluating equation (4.13), the parameter H is written as:

$$H = \frac{\frac{\Lambda C^2}{y_f} - \beta_0\eta_2\eta y_f - \beta_2 y_f(\eta_3-\eta)^2 + [C + \beta_2(\eta_3-\eta)y_f]\,(\eta_3-1)}{1-\eta-\eta_2+\eta_3} \tag{4.14}$$

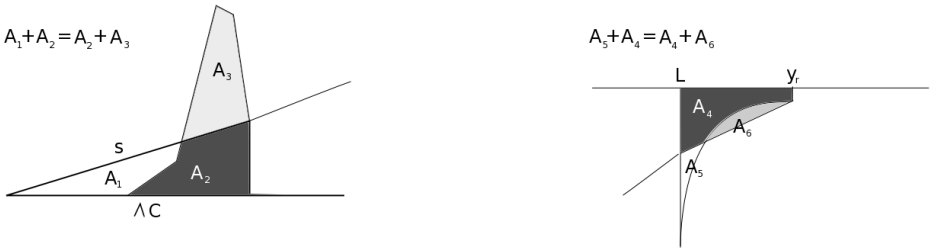

(a) Front area balance.

(b) Rear area balance.

Figure 4.6: Area balance definition.

The rear shock area balance (Figure 4.6b) is defined as:

$$\int_L^{y_r} F(x)dx = \frac{1}{2}[F(L)+F(y_r)](y_r-L) \tag{4.15}$$

where y_r is the total length of the signal, obtained also as the intersection between the area balance line that goes from $F(L)$ to $F(y_r)$:

$$F(y_r) = F(L) + s(y_r - L) \tag{4.16}$$

where $F(L)$ is evaluated using the parameterization defined in (4.10). Combining equation (4.16) and the constraint on the front and rear shock defined as:

$$\frac{P_f}{P_r} = \frac{C}{F(y_r)-F(L)} \tag{4.17}$$

it is possible to obtain the coefficient C as:

$$C = \frac{y_r - L}{\Lambda}\frac{P_f}{P_r} \tag{4.18}$$

A typical value assumed for the shock ratio is 1.

In order to evaluate D it is necessary to use the analytical form of A_e written in equation (4.11) and its definition in equation (4.4). For notation simplicity we define $\hat{D}$ as:

$$\begin{aligned}\hat{D} = A_e(L,0) - \frac{16}{15}\beta_0 L^{5/2} - \frac{16}{15}(L-\eta_2 y_f)^{5/2}\left[\frac{H-\beta_0\eta_2 y_f}{(\eta-\eta_2)y_f} - \beta_0\right] - \frac{16}{15}(L-\eta y_f)^{5/2}\left[\beta_2 - \right.\\ \left.\frac{H-\beta_0\eta_2 y_f}{(\eta-\eta_2)y_f}\right] - \frac{16}{15}(L-\eta_3 y_f)^{5/2}\left[\frac{C-H-\beta_2(\eta_3-\eta)y_f}{(1-\eta_3)y_f} - \beta_2\right] +\\ -\frac{16}{15}(L-y_f)^{5/2}\left[B_1 - \frac{C-H-\beta_2(\eta_3-\eta)y_f}{(1-\eta_3)y_f}\right] +\\ -\sum_{i=1}^{P-1}\frac{16}{15}(L-\lambda_{1,i})^{5/2}(B_{i+1}-B_i) - \frac{16}{15}(L-\lambda)^{5/2}\left[-\frac{C_P}{t} + B_P\right] +\\ -\frac{16}{15}(L-(\lambda+t))^{5/2}\left[\frac{C_P}{t} + B_{P+1}\right] - \sum_{i=1}^{N-1}\frac{16}{15}(L-\lambda_{2,i})^{5/2}(B_{P+i+1}-B_{P+i})\end{aligned} \tag{4.19}$$

and thus obtaining

$$D = \frac{\frac{15}{16}\hat{D}t}{(L-(\lambda+t))^{5/2} - (L-\lambda)^{5/2}} \tag{4.20}$$

The coefficients B_i are user defined parameters. When $B_i = 0$ the maximum pressure behind the front shock is minimized, $0 < B_i < s$ results in a minimized pressure rise signature while $B_i \geq s$ produces a N-wave.
Determining the remaining unknown coefficients requires the introduction of additional equations on the rear part of the signal [16]. $F(y_r)$ is evaluated as:

$$F(y_r) = -\frac{1}{\pi\sqrt{y_r - L}}\int_0^L \frac{\sqrt{L-x}}{y_r - x}F(x)dx \tag{4.21}$$

The area under the F-function between L and y_r can be expressed as:

$$\int_L^{y_r} F(x)dx = -\frac{2}{\pi}\int_0^L F(x)\tan^{-1}\sqrt{\frac{y_r - L}{L-x}}dx \tag{4.22}$$

Two strategies can be adopted to find the coefficients:

- Plotkin et al. [81] show that the equations set can be expressed as a system of two unknown parameters. As a consequence, the problem is reduced to the analytic solution of two transcendental equations. This method avoids numerical errors that can be introduced solving numerical integrals, but as a main drawback changes in the F-function parametrization requires a complete reformulation of the solution;

- equations can be solved numerically and the unknown coefficients evaluated as the result of an optimization loop. The solution becomes independent of the F-function model chosen.

The second choice is adopted to solve the inverse design. Within AIDA, integrals are solved numerically with an adaptive Simpson method with tolerance set at 10^{-10}. The minimization problem is solved using an L-BFGS-B algorithm [83]. The cost function is defined as the absolute value of the difference between equation (4.22) left-hand-side and the right-hand-side terms which are evaluated separately. Two different strategies are proposed depending on the set of design variables of interest: (λ, y_r) or (λ, L). The length of the aircraft is fixed by using the first design variable set, while the second one is useful if no constraints on the geometry are imposed and the designer freezes the amplitude of the front shock. All the remaining unknown coefficients of the F-function are defined as functions of the two design variables adopted.
If the couple (λ, y_r) is adopted, the following process is proposed:

1. INPUT: y_f, flight conditions, aircraft weight, P_f/P_r, B_*, L, t, $\lambda_{1,*}$, $\lambda_{2,*}$;

2. C is directly evaluated using equation (4.18);
3. H is evaluated from equation (4.14);
4. The remaining unknowns have to be determined using an optimization loop with a given initial guess for λ and y_r:
   a) D is evaluated using equation (4.19) and equation (4.20);
   b) $F(y_r)$ is evaluated from equation (4.21);
   c) Evaluation of the right-hand-side of equation (4.22);
   d) Evaluation of the left-hand-side of equation (4.22) using equation (4.15);
   e) The procedure is repeated changing λ and y_r until equation (4.22) is satisfied.

Slight modifications have to be introduced if the couple (λ, L) is considered as design variables. Length L is now an input and C is evaluated as function of the front shock pressure:

$$C = \frac{p_f - p_\infty}{p_\infty} \frac{\sqrt{2\beta r}}{\gamma M_\infty^2} \tag{4.23}$$

Due to the local nature of the optimization algorithm it appears that by changing the starting point it is possible to obtain different combinations of the two design variables that could satisfy the equality (4.22). The bound constraints on the DV set that could be introduced with the algorithm L-BFGS-B aim to reduce the set of final solutions.

Validation of AIDA

The validation test case is based on the work of Darden [16], adopted as validation also in [79] by Rallabhandi and Mavris. The input values are given in Table 4.1. The validation test case consists in an F-function parameterised via the Darden formulation. This formulation is embedded within the generalized one and the corresponding parameter set is: $P = 1$, $N = 1$, $\eta = 0.5$, $\eta_2 = 0$, $\eta_3 = \eta$, $\beta_0 = 0$, $\beta_2 = 0$.

Variable	Value
M	2.7
L	91.46 m (300 ft)
W	272,155.42 kg (600,000 lbs)
B	0 $m^{-0.5}$ (0 $ft^{-0.5}$)
y_f	9.146 m (30 ft)

Table 4.1: Input values for AIDA validation test case.

AIDA is run considering both the variable couple (λ, y_r) with a fixed L as in [16] and [79], and using the modified version fixing the value of the target bow shock at $P_f = 50.86\ Pa$. In the latter case the length obtained at convergence is $L = 91.60$ m (300.46 ft). The results obtained with AIDA (Figure 4.7) are in very good agreement with the ones obtained in the literature as shown in Table 4.2. The signature at ground shows the expected flat-top front shock. The results validate the approach and show the good accuracy of AIDA, which offers in addition the possibility of changing the F-function form and to fix the front shock pressure thus considering the aircraft length as a variable.

4.3 Evaluation of the geometrical area distribution

In the preliminary design phases, the geometrical area distribution $A_g(x)$ or the corresponding section radius distribution is required to define the configuration. The shaped sonic boom theory can become a powerful and efficient time saving approach if it is able to identify a geometry that corresponds to

Variable	Darden [16]	Rallabhandi [79]	AIDA(fixed L)	AIDA (fixed P_f)
H $[m^{0.5}]$	0.191 (0.346)	0.194 (0.351)	0.192 (0.347)	0.192 (0.347)
C $[m^{0.5}]$	0.0303 (0.0549)	0.0305 (0.0553)	0.0304 (0.0551)	0.0304 (0.0551)
D $[m^{0.5}]$	0.0377 (0.0683)	0.0373 (0.0676)	0.0409 (0.0741)	0.0406 (0.0735)
λ $[m]$	82.514 (270.645)	81.743 (268.118)	82.603 (270.938)	82.485 (270.550)
y_r $[m]$	153.627 (503.896)	154.027 (505.209)	153.598 (503.802)	153.747 (504.290)

Table 4.2: Comparison of the AIDA analysis with previous works. (Between brackets values in Imperial units).

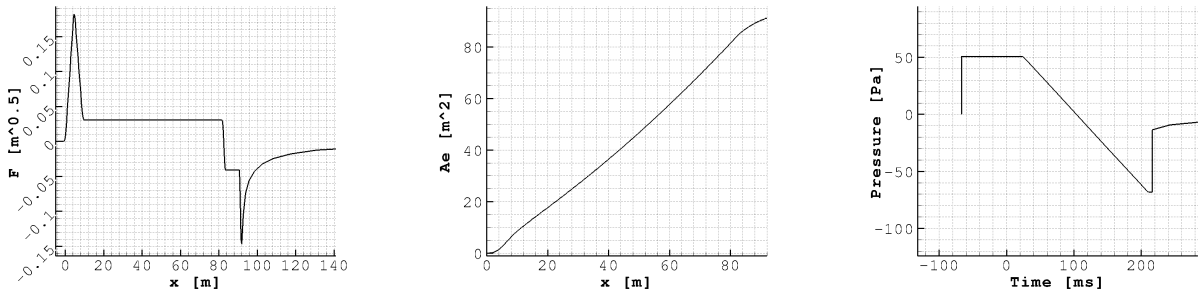

(a) F-function. (b) Equivalent area. (c) Ground signature.

Figure 4.7: Minimum overpressure solution for Darden reference test case.

the equivalent area rule. Numerical algorithms have been developed in the past in order to overcome this main problem of the inverse approach. Barger and Adams [84] have developed two numerical algorithms, but each of them shows problems associated to the non uniqueness of the solution and to convergence problems that occur around real solution local discontinuities. The final solution generally presents undesired oscillations.
An analytical approximated method based on the approximation of slender bodies has been proposed by Mack [85]. The use of this method requires some experience to adjust some correction parameters in order to obtain the expected results. This method essentially consists in tailoring the fuselage in order to obtain the target A_e. Li et al. [86] have proposed an inverse method based on smooth shape modification. The parameterization proposed is based on a spline curve with few control points to describe the fuselage. The optimization aims at modifying the shape without introducing high invasive shape modifications in order to minimize the differences between the actual and the target equivalent area. It emerges from the analysis that this method is inefficient in terms of computational time and final solutions result that are far from the expected results. In fact, using a trial and error strategy, the solution in terms of ground signal succeeds in reaching the target, but with high relative error in terms of equivalent area distribution. The approach also brings evidence that the solution is not unique. Particular attention is required when the geometry shows discontinuities. The solution obtained is generally a wavy configuration. Palacios [87] using an adjoint method succeeded in reducing an objective function based on the difference to a target equivalent area function, but no comparison is proposed between the resulting F-function and ground signature with the target ones.
The identification of the geometrical area distribution must satisfy several requirements:

- a reduced computational cost if the method is based upon an iterative procedure;
- a control on the geometry that avoids oscillating solutions;
- a sufficient accuracy of the target ground signature.

AIDA provides the area distribution of an equivalent axi-symmetric body that corresponds to the desired F-function. However, the formulation of the inverse problem does not guarantee the uniqueness

of the area distribution. In fact, if we assume that for a wing-body configuration, the A_e distribution can be decomposed as follows:

$$A_e = A_v^{fuse} + A_v^{wing} + A_l^{fuse} + A_l^{wing} \tag{4.24}$$

Different combinations of these terms can produce the same result. In addition, acting on the geometry impacts explicitly the volume terms but it has also an indirect influence on the lift terms, in particular when the wing shape is modified. The choice of the fuselage tailoring, based on direct optimization with the CMA-ES algorithm, has been made to achieve the target shaped configuration limiting the impact of shape modification on the lift contributions. The problem can be stated as a minimization problem of a cost function that describes the error between the actual and the target designed configuration. Design variables are radius values at several locations along the fuselage axis. Using these geometrical parameters, the 3D structured mesh is generated automatically using an in-house mesh generation tool and Euler CFD computations are performed using the Onera *elsA* [88] solver to evaluate the lift terms. The equivalent area distribution and the F-function are evaluated using the surface body mesh and the corresponding pressure field solution, while the ground signature is obtained using TRAPS. The fuselage tailoring is a critical and fundamental aspect of the inverse design, as several factors have an impact on the final solution:

- the parameterization of the fuselage (number of DVs, points distribution, interpolation method,..);
- the objective cost function;
- the lift distribution evaluation.

Impact of geometry parameterization

Different aspects are fundamental in the description of the fuselage geometry: the nature of the interpolation method adopted, the number of design variables considered as well as their distribution. The choice of the interpolation method can hardly be defined *a priori*. Two approaches have been considered: Bézier curve and cubic spline. A geometry obtained using Bézier curves is described by control points which do not belong to the real geometry, thus helping in the description of complex geometries but the control on local curvature becomes hard. Due to the fact that the Whitham function is very sensitive to A_e'' [86], the cubic spline has finally been adopted in this study to describe the fuselage geometry.

The choice of the design variables is critical as a compromise has to be achieved between a fine and a coarse parameterization. On one side, a fine parametrization is able to better describe the geometry, but can slow down significantly the shape optimization convergence due to the increased design search space dimension. On the opposite side, a coarse parameterization is unable to produce modifications of the second derivative to achieve a low-boom compliant F-function. A coarse (10 points) and a finer (27 points) parametrization (uniformly distributed points), respectively named A and B, are considered on a non-lifting axi-symmetric body at an altitude of $18,288\ m$ and a Mach number $M_\infty = 1.6$. The design parameters adopted to define a configuration with a flat-top ground signature are defined in Tables 4.3 and 4.4 and shown in Figure 4.8. The parameters have been evaluated using the (λ, y_r) couple approach.

Var.	Value	Var.	Value
W	$0\ kg\ (0\ lbs)$	t	$0\ m\ (0\ ft)$
N, P	1	η_2	0
B_1, B_2	$0\ m^{-0.5}\ (0\ ft^{-0.5})$	η_3	η
η	0.5	y_f	$9.84\ m\ (3\ ft)$
β_0, β_2	$0\ m^{-0.5}\ (0\ ft^{-0.5})$	L	$30\ m\ (9.146\ ft)$

Table 4.3: AIDA input coefficients.

Var.	Value
H	0.00909 $m^{0.5}$ (0.0298 $ft^{0.5}$)
C	0.00270 $m^{0.5}$ (0.00885 $ft^{0.5}$)
D	0.0154 $m^{0.5}$ (0.0506 $ft^{0.5}$)
y_r	33.537 m (110 ft)
λ	21.341 m (70 ft)

Table 4.4: Coefficients evaluated with AIDA.

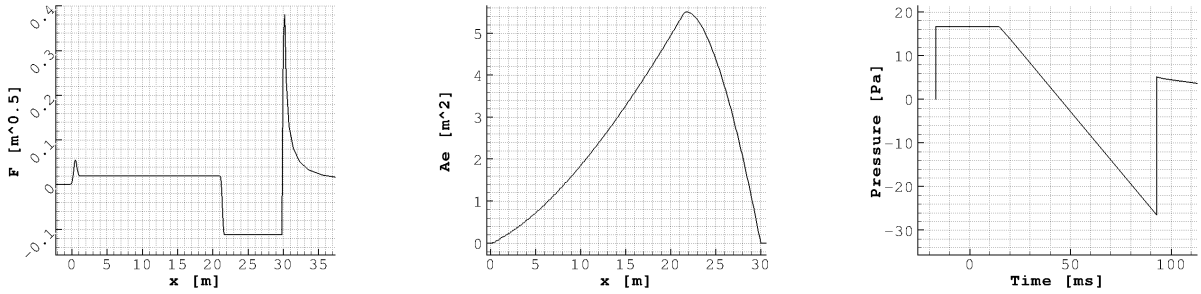

(a) F-function. (b) Equivalent area. (c) Ground signature.

Figure 4.8: Minimum overpressure solution obtained using AIDA for the fuselage non-lifting configuration.

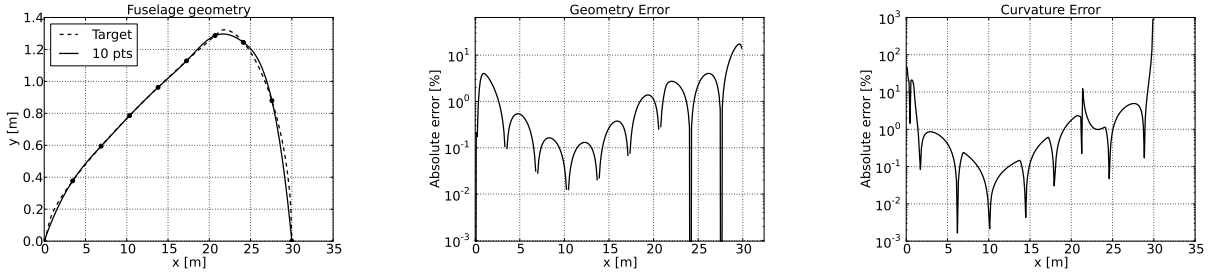

(a) (b) (c)

Figure 4.9: Initial geometry with a 10 points uniformly distributed parameterization. (Param. A).

Due to the fact that a non-lifting configuration is considered, the weight is set to $W = 0$ in order to satisfy the condition $A_e(L) = A_v^{fuse}(L) = 0$. The fuselage being considered as a slender body, a good initial solution is obtained by approximating at the first order the geometrical area distribution $\hat{A}_g$ with the equivalent area, so that $\hat{A}_g(x) \sim A_e(x)$. The ability of the chosen parameterization to fit the geometrical target area distribution is evaluated comparing the absolute errors between the approximated initial area distribution $\hat{A}_g$ and the one obtained using the spline interpolation. Figures 4.9 and 4.10 show the geometrical and the curvature errors respectively for parametrization A and B. Significant errors can be noticed where F' changes its sign: at the nose and rear region, as well as at the discontinuity located $x = \lambda = 21.34\ m$. In these critical regions, multiple variations of the sign of F' occur therefore impacting the curvature of the corresponding A_e distribution. Notice that in weak curvature variation regions, parametrization B provides a more accurate geometry. The comparison between the configuration obtained with the two initial solutions is shown in Figure 4.11. On one hand it is possible to note that parameterization A shows oscillations in the first half of the F-function that result in a multi-shock ground signature response. On the other hand, parameterization B provides a satisfactory detailed description of the configuration as it allows to reproduce the desired flat-top ground signature. Considering these results, parameterization B is retained for the following analysis.

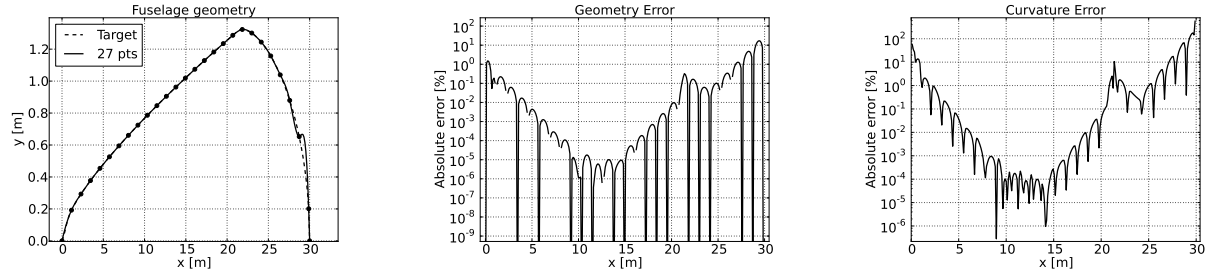

(a) (b) (c)

Figure 4.10: Initial geometry with a 27 points uniformly distributed parameterization. (Param. B).

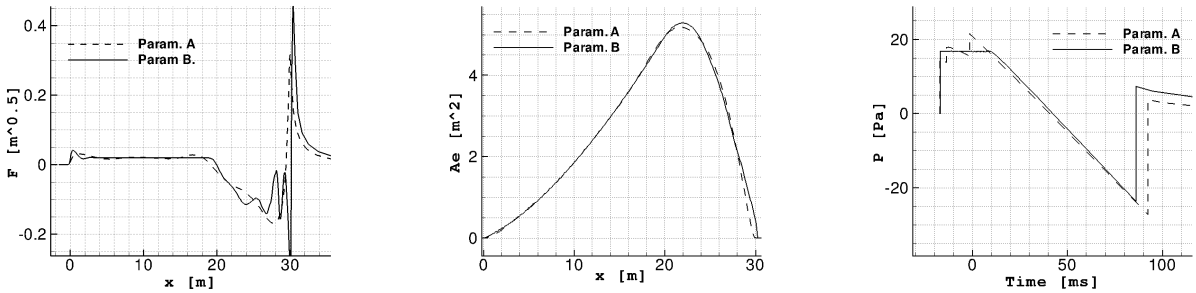

(a) F-function. (b) Equivalent area. (c) Ground signature.

Figure 4.11: Configuration obtained using the two initial approximated geometries.

Impact of objective cost function formulation

The objective function chosen to tailor the geometry has been defined in the present approach as an integral error estimator which general formulation is:

$$J_f = \int_0^L |f(x) - f^{target}(x)|dx \tag{4.25}$$

Three functions $f(x)$ have been considered in the present study: $A_e(x)$, $F(x)$ and $\Delta p(x)$ at ground. The objective is to analyze the impact of the cost function on the final solution and in this way to select the most suitable strategy for future studies. To analyze the impact of each cost function on the final configuration, the initial solution obtained with the fine parameterization is perturbed by the introduction of two bumps in the proximity of the nose. This is due to the fact that, as previously explained, the initial solution is a good approximation of the target configuration (see Figure 4.11). Figures (4.12-4.16) shown the comparison between the different objective functions presented in equation (4.25).

The optimization based on J_{A_e} results in a good matching between the optimized and the target A_e distribution (Figure 4.13a) with a decrease of the objective function by more than 80% (Figure 4.16a). The corresponding F-function (Figure 4.12a) shows some oscillations at the F' discontinuity located around λ. The resulting ground signature (Figure 4.14a) presents multiple shocks instead of a flat-top. The configuration obtained using J_F as objective results in a Whitham F-function (Figure 4.12b) with less oscillations than those obtained with the other two strategies. The A_e distribution is different from the target, but it remains smooth and reduces the initial bumps which has a positive impact on the resulting geometry in terms of curvature fluctuations reduction (Figure 4.15b). The use of the ground signature as cost function J_P is not able to eliminate the initial oscillations of the geometry (Figure 4.15c). The corresponding F-function (Figure 4.12c) shows two peaks after the first one thus producing a ground signature (Figure 4.14c) close to the initial one. Furthermore, two shocks still persist in the bow region.

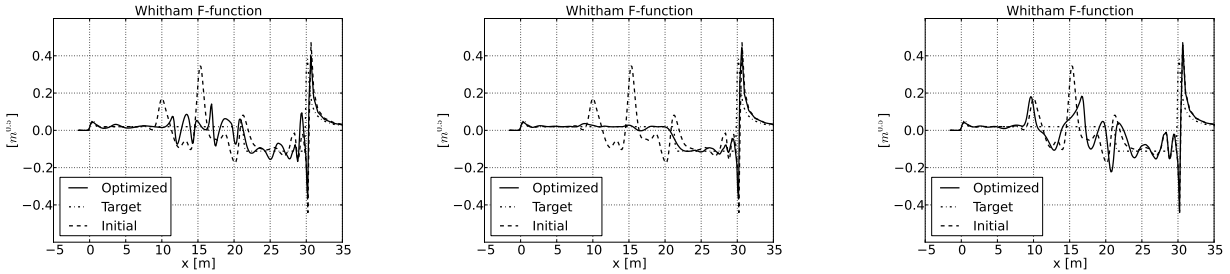

(a) A_e based optimization. (b) F-function based optimization. (c) Signature based optimization.

Figure 4.12: Whitham F-function obtained with the different objectives - Parametrization B: 27 design variables.

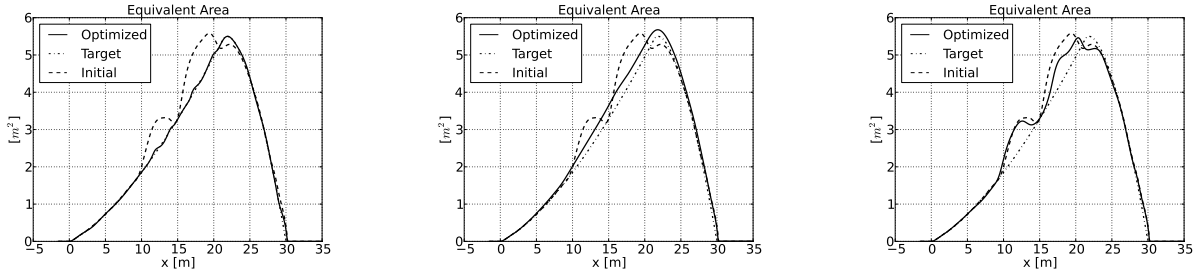

(a) A_e based optimization. (b) F-function based optimization. (c) Signature based optimization.

Figure 4.13: Equivalent area obtained with the different objectives - Parametrization B: 27 design variables.

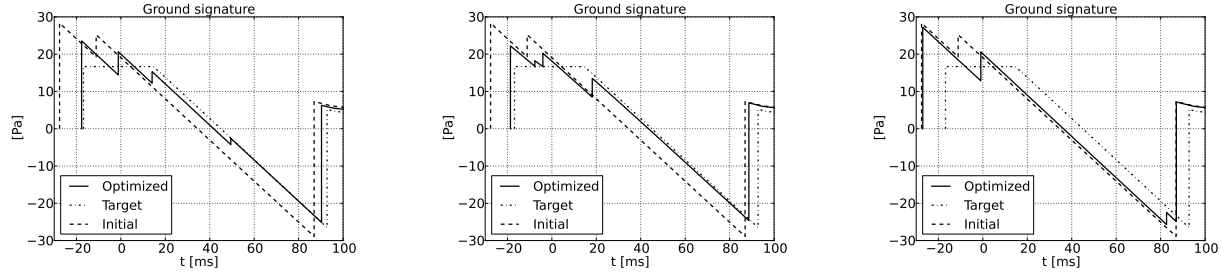

(a) A_e based optimization. (b) F-function based optimization. (c) Signature based optimization.

Figure 4.14: Ground signature obtained with the different objectives - Parametrization B: 27 design variables.

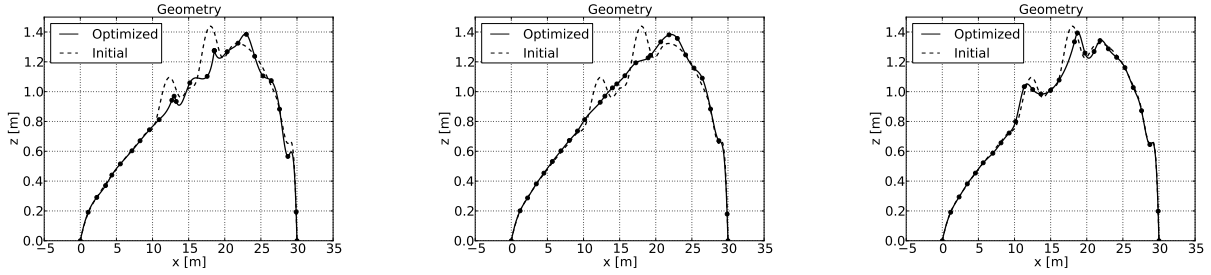

(a) A_e based optimization. (b) F-function based optimization. (c) Signature based optimization.

Figure 4.15: Radius distribution obtained with the different objectives - Parametrization B: 27 design variables.

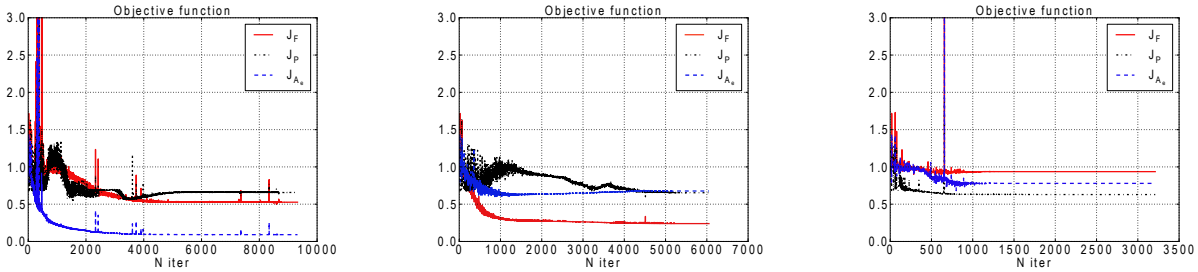

(a) A_e based optimization. (b) F-function based optimization. (c) Signature based optimization.

Figure 4.16: Objectives normalized with respect to their respective initial value.

The analysis shows that the A_e and the F-function based optimizations provide complementary information required to obtain the desired shaped configuration. As a result of this preliminary study, the choice has been oriented to the definition of a cost function as a linear combinations of these two cost functions:

$$J_{comb} = \frac{J_{A_e}}{J^0_{A_e}} + \frac{J_F}{J^0_F} \tag{4.26}$$

where each objective function is normalized with their value at the first iteration of the optimization process $J^0_{(.)}$.

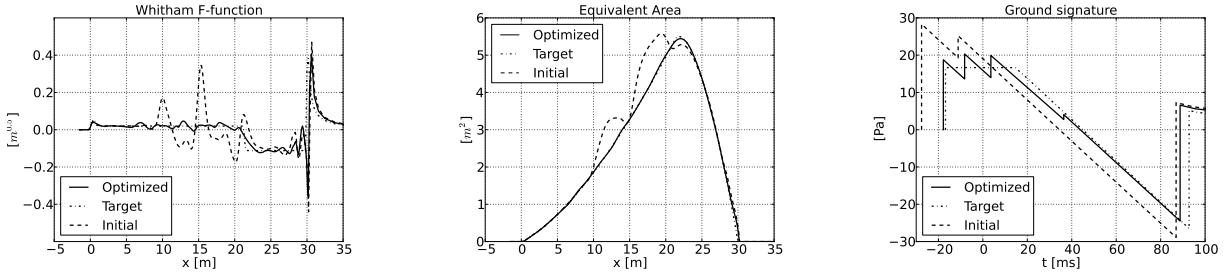

(a) (b) (c)

Figure 4.17: Optimization based on linear combination of objective functions using 27 variables.

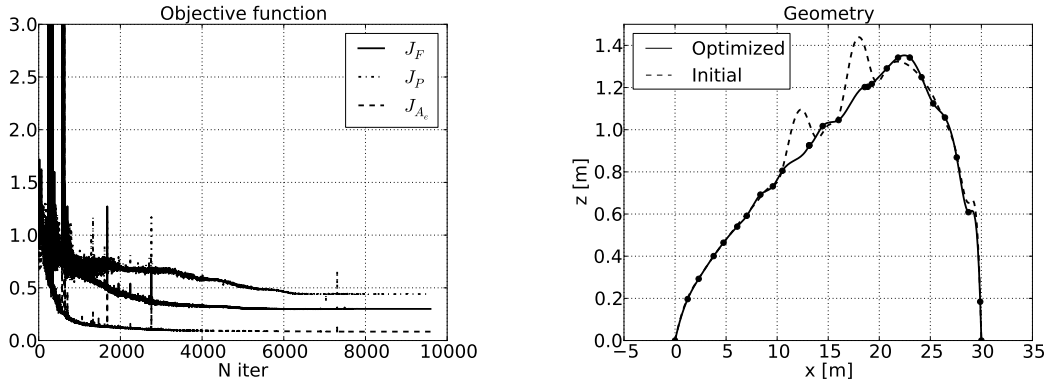

(a) (b)

Figure 4.18: Optimization based on linear combination of objective functions using 27 variables.

The resulting Whitham F-function (Figure 4.17a) obtained with the J_{comb} minimization shows an approximation of the target without the oscillations observed using J_F as cost function when $x \leq \lambda$. In addition the zero slope achieved after the initial peak and the limited angle variation at $F(\lambda)$ allow

to reach a multi-shocks approximation of the flat-top ground signature (Figure 4.17c). The oscillations in the second half of the signal have a limited extent around the discontinuity in $x = L$ resulting in a negligible impact on the ground signature. The equivalent area (Figure 4.17b) approximates the optimal target reducing J_{A_e} (see Figure 4.18a) by more than 80% compared to the initial geometry. Each objective components J_{A_e}, J_F and J_P are reduced using J_{comb} as objective, producing an accurate approximation of the target configuration. An extension results in the application of J_{comb} to more complex configurations.

4.4 Wing-body configuration design

The fuselage tailoring strategy that has been investigated in the previous section is here applied to the low-boom inverse design of the reference wing-body configuration.

Non lifting fuselage tailoring

Considering a non-lifting wing-body configuration with non cambered wing at $AoA = 0^o$, equation (4.24) reduces to: $A_e = A_v^{fuse} + A_v^{wing}$. In an attempt to retrieve the target area distribution, the fuselage is tailored while the wing shape is frozen. The target shaped configuration is the same as the one defined in the previous section (Table 4.4) and is shown in Figure 4.19. The initial approximated geometrical area distribution of the fuselage is obtained by removing the wing volume contribution from the total area distribution :

$$\hat{A}_g^{fuse}(x) \simeq A_v^{fuse}(x) = A_e(x) - A_v^{wing}(x) \tag{4.27}$$

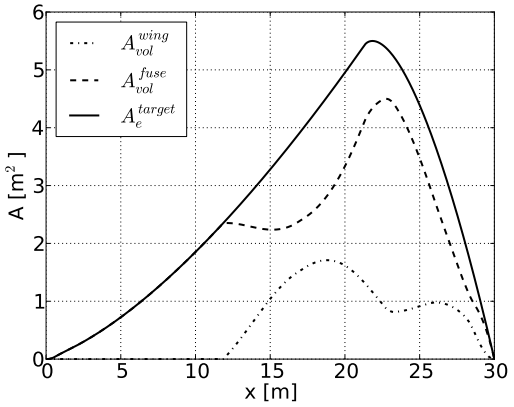

Figure 4.19: Initial tailoring of the fuselage area distribution.

The design variable set selected consists in 41 fuselage section radius equally distributed along the fuselage axis: 13 for the nose region, 15 for the cabin and 13 for the aft part. Figure 4.20 shows the comparison between the target equivalent area distribution and the one evaluated on the tailored fuselage configuration that satisfy equation (4.27). Results show that the approximated configuration is close to the target. This approximated configuration is adopted as initial solution of the optimization based fuselage tailoring. The optimization approach based on the composite objective function defined in equation (4.25) results in a cost function reduction near the 98% of its initial value. The resulting A_e distribution (Figure 4.21b) is in excellent agreement with the target one.
The F-function (Figure 4.21a) obtained shows reduced oscillations, especially in the first part of the signal. As a direct consequence the ground signature (Figure 4.21c) results in a flat-top with the same overpressure amplitude as the target. The oscillations in the aft part of the F-function still persist as in the fuselage design case analyzed previously, but they produce a minor impact on the ground signature. The proposed strategy alleviates the oscillations of the F-function related to

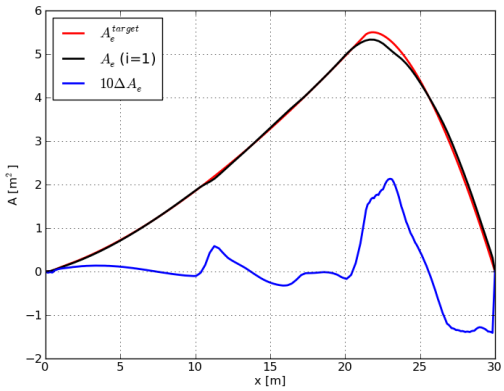

Figure 4.20: Equivalent area distribution of the initial tailored configuration.

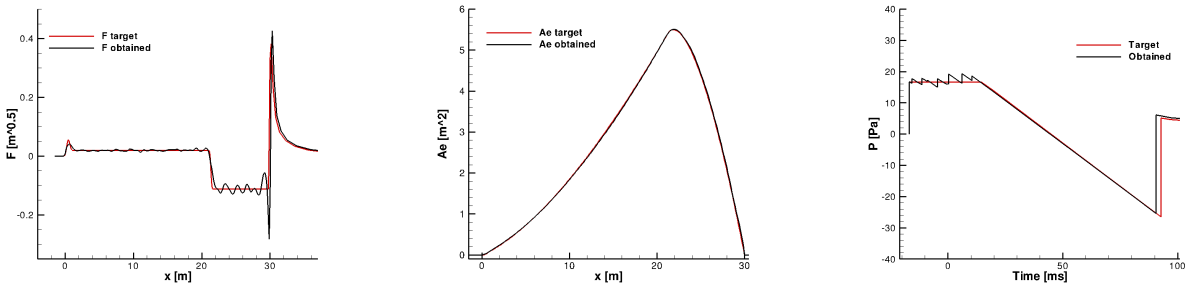

(a) F-function. (b) Equivalent area. (c) Ground signature.

Figure 4.21: Wing-body configuration obtained after fuselage tailoring.

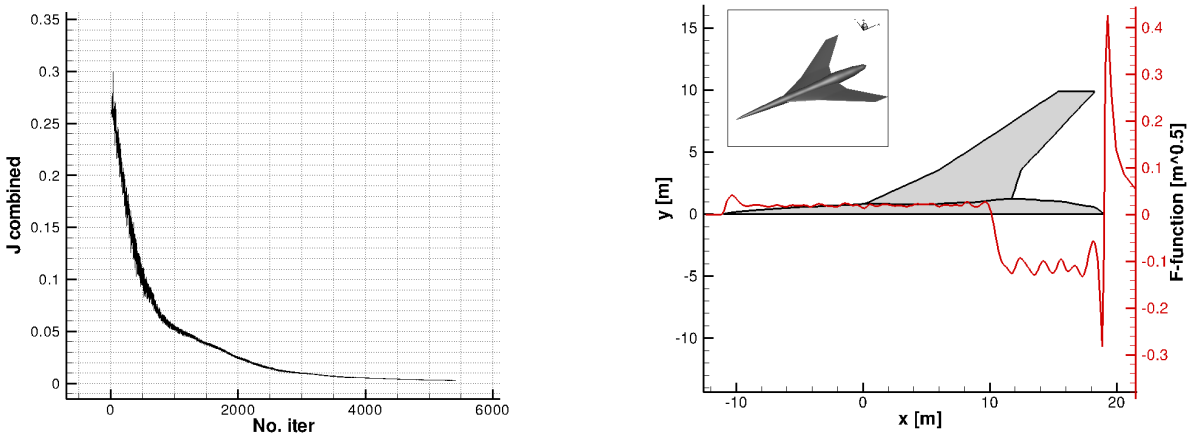

(a) Cost function convergence history.

(b) Shaped configuration. Geometry and corresponding F-function.

Figure 4.22: Shaped non lifting configuration.

the discontinuities of the geometry, like the wing in the present case, and it can be applied without modification in presence of other discontinuities such as engine nacelle and lifting surfaces. Figure 4.22 shows the geometry obtained after the tailoring of the fuselage. The inverse design approach does not introduce any control on the final configuration design, as a consequence the fuselage cabin volume has been extremely reduced with respect to the reference configuration.

Fuselage tailoring of a lifting wing-body configuration

When the configuration is producing lift at a given angle of attack α different from zero, the effective length l_e of the A_e distribution is different from the aircraft length L (see Figure 4.23). The relationship between the flight axis x and the horizontal one ξ is defined as:

$$\xi = x\cos(\alpha) - x\frac{\sin(\alpha)}{\tan(\mu)} \tag{4.28}$$

Furthermore, to take into account the impact of lift in the design of an aircraft all the terms of

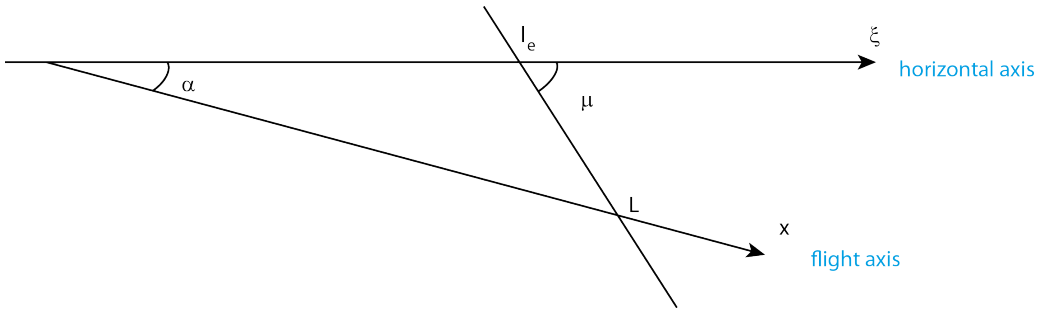

Figure 4.23: Relationship between the flight and the horizontal axis.

equation (4.24) have to be considered, thus meaning that CFD evaluations are needed. In the present approach, to reduce CFD evaluations during the fuselage tailoring, two assumptions are made:

- the lift contribution originates from the wing component;
- the wing lift distribution does not change significantly during fuselage shape modification.

Indeed preliminary CFD studies have shown that the fuselage contribution to the lift can be neglected in non viscous flow conditions. Figure 4.24 shows the pressure distribution over the axi-symmetric fuselage and the corresponding lift area distribution. The magnitude of the A_l term due to the fuselage represents less than one tenth of the value obtained for a wing-body lifting configuration. The second

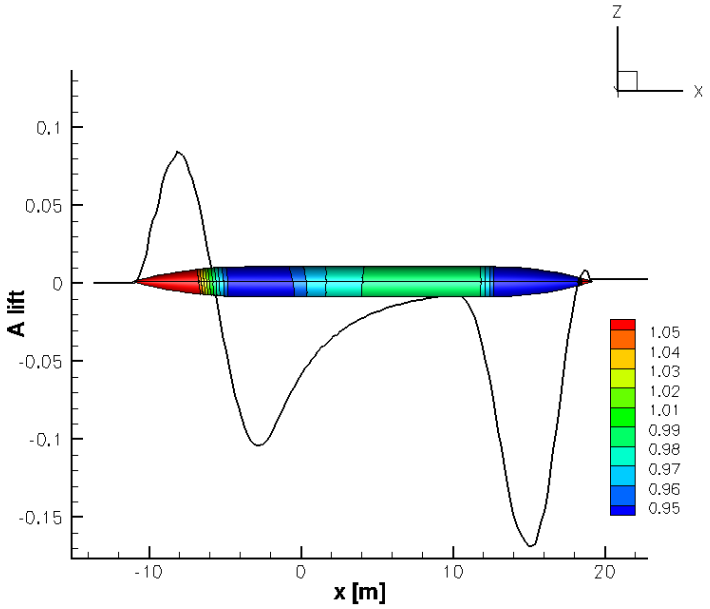

Figure 4.24: Equivalent lift area distribution and its corresponding pressure distribution (p/p_0) due to an axi-symmetric fuselage.

approximation is made as the exposed wing surface may change during the fuselage tailoring but is

assumed to be of limited extent. Furthermore as long as the angle of attack is frozen, and with the fuselage radius modifications foreseen, the wing lift distribution variation should not be significant. The two hypothesis considered valid if the initial configuration geometrical deviation from the target one is small enough.

At this stage, a new target configuration has been designed using AIDA with the input values summarized in Table 4.5. The design flight conditions are: $M_\infty = 1.6$, $\alpha = 2^o$, h =18000 m. The resulting F-function unknown coefficients obtained after the inverse design are summarized in Table 4.6. Using the reference wing-body geometry all the terms of the equation (4.24) are evaluated after

Var.	Value	Var.	Value
W	16000 kg (lbs)	t	0 m (0 ft)
N, P	1	η_2	0
B_1, B_2	0 $m^{0.5}$ 0 $ft^{0.5}$	η_3	η
η	0.5	y_f	1.524 m(5 ft)
β_0, β_2	0	l_e	28.67 m (98.04ft)

Table 4.5: AIDA input coefficients.

Var.	Value
H	0.0756 $m^{0.5}$ (0.248 $ft^{0.5}$)
C	0.0290 $m^{0.5}$ (0.0952 $ft^{0.5}$)
D	0.0473 $m^{0.5}$ (0.1552 $ft^{0.5}$)
y_r	33.419 m (109.614 ft)
λ	21.362 m (70.067 ft)

Table 4.6: Coefficients evaluated with AIDA.

a CFD computation. A new geometry can be defined using the approximation:

$$A_g^{fuse}(x) \simeq A_v^{fuse}(\xi) = A_e^{target}(\xi) - A_v^{wing}(\xi) - A_l^{wing}(\xi) - A_l^{fuse}(\xi) \tag{4.29}$$

The approximated fuselage area distribution is shown in Figure 4.25a. At this point a CFD computation on the new configuration is performed and all the equivalent area terms are re-evaluated. The new $A_l(i = 1)$ distribution is significantly different from the initial one (see Figure 4.25b), so that the second hypothesis at the basis of the optimization-based tailoring without CFD computations is still not verified. For this reason another coupled iteration (tailoring+CFD) is required and, as shown in Figure 4.25b, is sufficient to satisfy all the hypothesis. The A_l distribution, that has been evaluated only for two new configurations, is then frozen during the following optimization based tailoring iterations. The configuration obtained after the two coupled iterations is adopted as initial solution for the minimization problem of the combined objective function J_{comb}. To sum up, generally the strategy to be adopted is the following:

1. $i = 0$;
2. A_g^i, A_v^i, A_l^i evaluated from reference configuration;
3. $i = i + 1$;
4. Define A_g^i using equation (4.29);
5. Perform CFD analysis;
6. Evaluate all the terms of equation (4.29);
7. If $|A_l^i(L) - A_l^{i-1}(L)| < \epsilon$ then go to 8 else go back to 3;

8. $A_l^i = A_l$ is frozen;

9. Fuselage tailoring without CFD.

where ϵ is a tolerance.

The final configuration is obtained after a reduction of J_{comb} by more than 80% in less than 2000

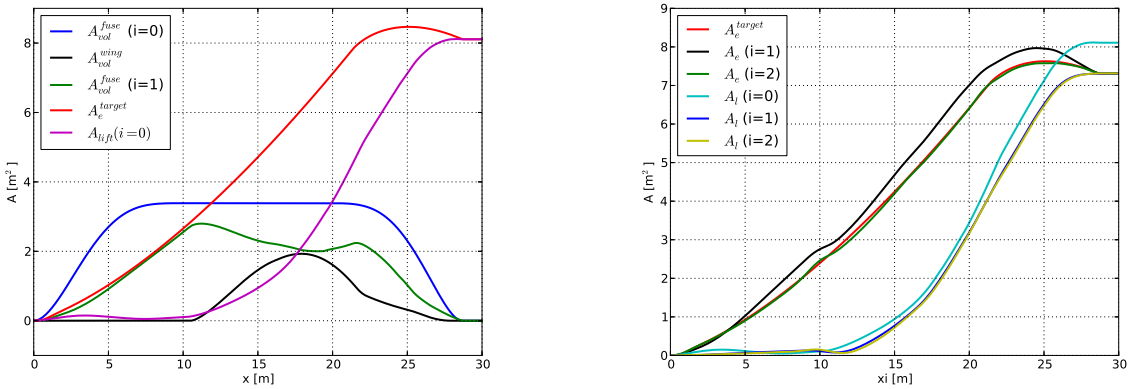

(a) Initial tailoring of the fuselage area distribution.

(b) Fuselage tailoring and CFD computations coupled iterations.

Figure 4.25: CFD-based fuselage tailoring iterations.

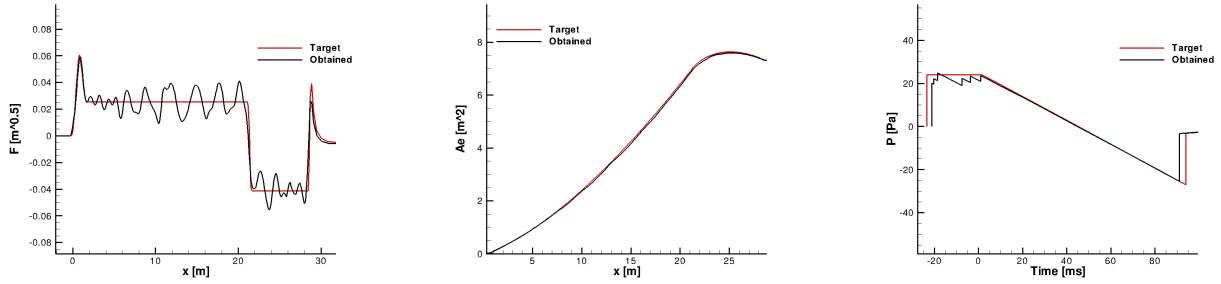

(a) F-function.

(b) Equivalent area.

(c) Ground signature.

Figure 4.26: Wing-body lifting configuration obtained after fuselage tailoring.

iterations (see Figure 4.27a). The F-function (Figure 4.26a) shows an accurate agreement also at the discontinuities. Several oscillations occur in the horizontal zero slope region of the function which are due to variations of curvature in the A_e distribution (Figure 4.26b). Despite this, the obtained equivalent area distribution is in good agreement with the target distribution. The main consequence of these oscillations is a flat-top ground signature (Figure 4.26c) described with several small amplitude shocks. Nevertheless the front shock overpressure has an amplitude near the design value of the target signature. The tailored geometry (Figure 4.27b) is not wavy but shows a considerable reduction of the cabin value. This problem can be overcome with the introduction of a volume constraint during the definition of the target A_e. An application with a volume constraint is presented in Appendix B.

4.5 Definition of a low-boom F-function

The shaped sonic boom theory is not able to take into account the acoustic metrics currently used to evaluate people annoyance due to sonic boom (e.g. PLdB, dBA,..). The generalization of the F-function parametrization has introduced additional coefficients that have to be defined by the designers. These coefficients can be exploited to define a low-PLdB F-function.

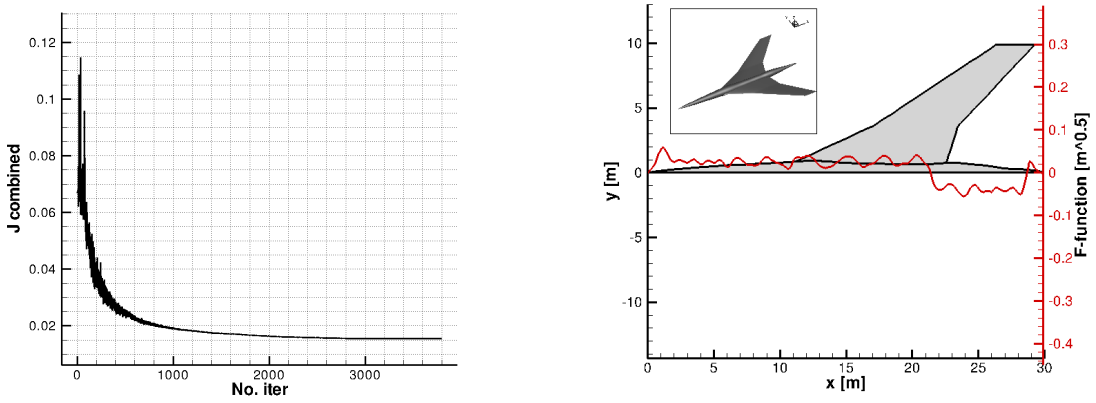

(a) Cost function convergence history.

(b) Shaped configuration. Geometry and corresponding F-function.

Figure 4.27: Shaped lifting configuration.

The strategy proposed is to couple the AIDA module and an external optimization loop as shown in Figure 4.28. The design variables are the AIDA input parameters that defines the F-function (B_*, η_*, t, y_f). At each optimization iteration AIDA evaluates the remaining unknown coefficients (H, C, D, λ, y_r), thus defining the A_e distribution and the F-function. The corresponding ground signature can then be calculated using the TRAPS propagation code. To evaluate PLdB, the zero-thickness signal is post-treated introducing rise time as function of the peak overpressure. The optimization is

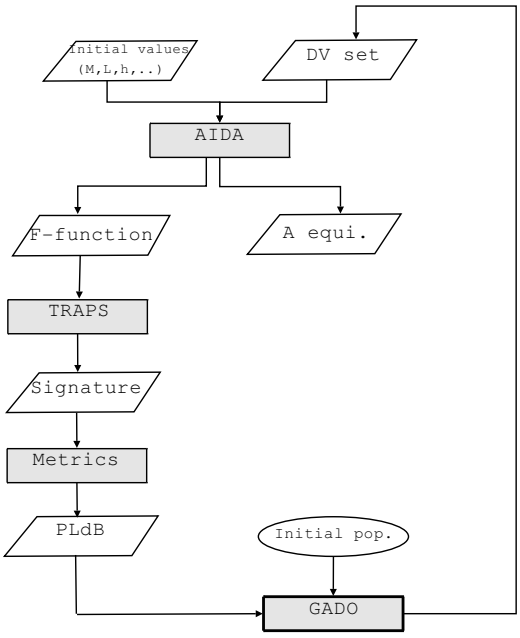

Figure 4.28: Flow-chart of the coupling between AIDA and the genetic algorithm GADO.

performed using GADO [89], a genetic algorithm integrated to the Dakota optimization library [90].

In Table 4.7 are summarized the lower and upper bounds for the design variables. The other input required to solve the problem are summarized in Table 4.8.

The optimized coefficients (Table 4.9) and the other coefficients evaluated by AIDA (Table 4.10) result in a configuration that creates a 88.84 PLdB ground signature. The optimizer reduces by about 2 PLdB the initial value determining a low-PLdB solution shown in Figure 4.30. The initial F-function peak tends to a δ Dirac aiming at reducing the coefficient C and so the front shock amplitude. The first shock is then followed by a ramp-like behavior and a subsequent expansion. The same occurs at

Variable	Lower bound	Upper bound
$B_i \quad \forall i \in [1, N+P]$ $[m^{-0.5}]$	-9.15 x 10^{-5} (-3 x 10^{-4})	2.44 x 10^{-4} (8 x 10^{-4})
β_0 $[m^{-0.5}]$	3.05 x 10^{-6} (1 x 10^{-5})	0.03 (0.1)
β_2 $[m^{-0.5}]$	-0.03 (-0.1)	0.03 (0.1)
t $[m]$	0 (0)	1.524 (5)
η	0.2	0.8
$y_f[m]$	1.524 (5)	4.573 (15)

Table 4.7: Ranges for F-function optimization. (In brackets Imperial system units).

Constant	Value	Constant	Value
M	1.6	$\lambda_{1,1}$	$y_f + 9.146$ (+30)
L	36.58 m (120 ft)	$\lambda_{2,1}$	$\lambda + t + 1.524$ (+5)
W	45,000 kg (99,208.018 lbs)	$\lambda_{1,i} \quad \forall i \in [2, N]$	$\lambda_{1,i-1} + 1.524$ (+5)
N, P	3	$\lambda_{2,i} \quad \forall i \in [2, P]$	$\lambda_{2,i-1} + 1.524$ (+5)
h	18,000 m (59,040 ft)		

Table 4.8: Additional fixed input values. (In brackets Imperial system units).

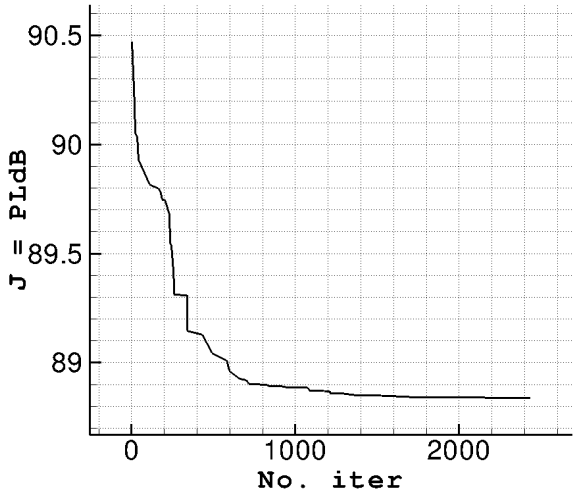

Figure 4.29: F-function input coefficient optimization history.

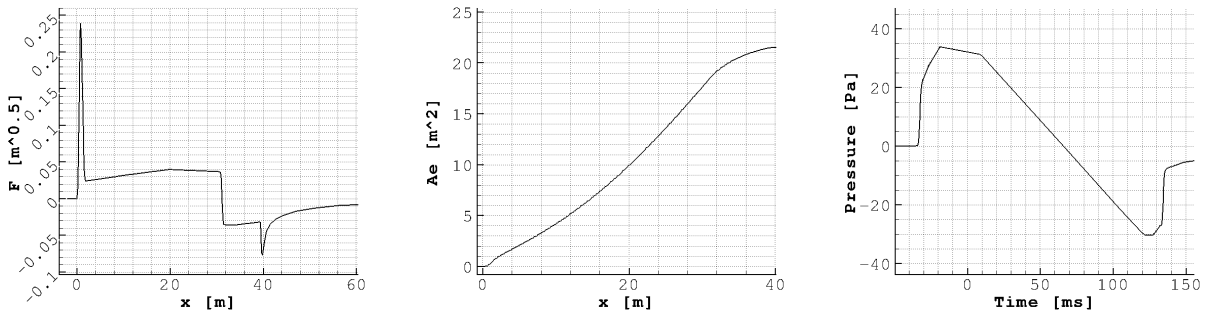

(a) F-function. (b) Equivalent area. (c) Ground signature.

Figure 4.30: Low-PLdB configuration.

the rear part of the acoustic signal. The result shows that the ground signature has the tendency to become a sinusoidal signal thus avoiding any shocks. Obviously the result is depending on the DV

Variable	Value	Variable	Value
B_1 $[m^{-0.5}]$	9.426 x 10^{-4} (5.205 x 10^{-4})	B_4 $[m^{-0.5}]$	-8.313 x 10^{-5} (-4.590 x 10^{-5})
B_2 $[m^{-0.5}]$	8.237 x 10^{-4} (4.548 x 10^{-4})	B_5 $[m^{-0.5}]$	-2.660 x 10^{-5} (-1.469 x 10^{-5})
B_3 $[m^{-0.5}]$	-2.798 x 10^{-4} (-1.545 x 10^{-4})	B_6 $[m^{-0.5}]$	7.416 x 10^{-4} (4.0951 x 10^{-4})
η	0.415	y_f $[m]$	1.524 (5)
β_0 $[m^{-0.5}]$	0.00498 (0.00275)	t $[m]$	0.0643 (0.211)
β_2 $[m^{-0.5}]$	-0.180 (-0.0993)		

Table 4.9: Optimized value of the coefficients. (In brackets Imperial system units).

Variable	Value
H $[m^{0.5}]$	2.874x 10^{-4} (5.205 x 10^{-4})
C $[m^{0.5}]$	-2.511x 10^{-4} (-4.548 x 10^{-4})
D $[m^{0.5}]$	-8.531x 10^{-5} (-1.545x 10^{-4})
y_r $[m]$	48.216 (158.148)
λ $[m]$	25.736 (84.415)

Table 4.10: Coefficients evaluated with AIDA. (In brackets Imperial system units).

set adopted and on the range of variation selected for each variables. Nevertheless it could be applied to any problem for which it is required to define a specific F-function.

4.6 Conclusions

Despite the increasing interest in direct shape optimization methods, the inverse design approach is useful in preliminary design of low-boom configuration if three main requirements are satisfied:

- the procedure that defines the F-function coefficients has to be robust enough to solve for different parameterizations;
- a geometrical area distribution is obtained at the end of the design;
- the approach is able to consider acoustic metrics in the design.

A module called AIDA (Acoustic Inverse Design Approach) has been developed to overcome the drawbacks of the classical shaped sonic boom minimization. An optimization based procedure has been adopted to evaluate the coefficients of the F-function. The approach has the property, in contrast with other methods of the literature, to be applicable to different F-function parameterizations without analytical reformulation of the problem. It enables also the introduction of a constraint on the front shock overpressure if the aircraft length constraint is relaxed.

A fuselage tailoring based on shape optimization is adopted with success on different test cases of increasing complexity to evaluate the geometrical area distribution that corresponds to a target equivalent area. Results show that the geometry parametrization has to describe in detail the regions that corresponds to the F' discontinuities. Furthermore a suitably chosen combination of the cost functions, based on the F-function and the equivalent area, provides an accurate approximation of the target ground signature obtained with the final tailored configuration.

The definition of a low-PLdB target function using an optimization process shows that it is possible to introduce with limited effort relevant up-to-date acoustic metrics in the inverse design. The proposed approach based on optimization and an enriched F-function parametrization may also improve the possible applications of the shaped sonic boom theory introducing new metrics or trade-off with other disciplines such as aerodynamic performance.

An extension of the present work would be to focus on the sensitivity of the functions of interest with respect to the design variables aiming at performing robust design at a single or multiple flight conditions.

Chapter 5

The optimization scenario and direct single objective optimization

Everyone by now presumably knows about the danger of premature optimization. I think we should be just as worried about premature design - designing too early what a program should do.
Paul Graham

Contents

In the last years the availability of high fidelity models coupled with the increase of the computational power has permitted the growth of numerical shape optimization techniques for the design of innovative configurations since early design phases. The ultimate objective of such approaches is to exploit the information provided by high-fidelity models (e.g. CFD, structural finite elements,..) for the design of new systems with improved performance. The way the information is used and the strategy adopted clearly distinguish unintelligent methods, like random search and the so-called numerical optimization. The designer experience and intuition is used to define targets, analysis tools and optimization strategies. Different choices necessary mean different final results. Analysis tools have been already introduced in the previous chapters, and are here coupled together with the optimization algorithms in an optimization chain. Parameterization is defined and the sensitivities of the geometrical variables to the aero-acoustic performance are evaluated. Then the aerodynamics and the

acoustics shape optimization are performed separately and the resulting configurations are analyzed and compared. Concerning low-boom optimization, in chapter 4 the inverse design method has been developed and its effectiveness but also its limitations pointed out. The final section of the chapter aims at the definition of an hybrid approach where the inverse design and the direct optimization are considered together. The objectives are to combine the advantages of the two methods avoiding their respective limitations and to define a strategy that can enable the designer to introduce a trade-off between low-boom and low-drag configurations.

5.1 The optimization chain

A direct optimization requires to couple together the evaluation of the cost functions, the optimization algorithm, and the shape parameterization. Each of these three elements are required and strictly depends upon the problem considered, but a general optimization scenario can be identified (see Figure 5.1). In this scenario the modules can be used as black-box or not. Furthermore, it is solely the engineer experience on the problem analyzed that drives the definition of a complete scenario.

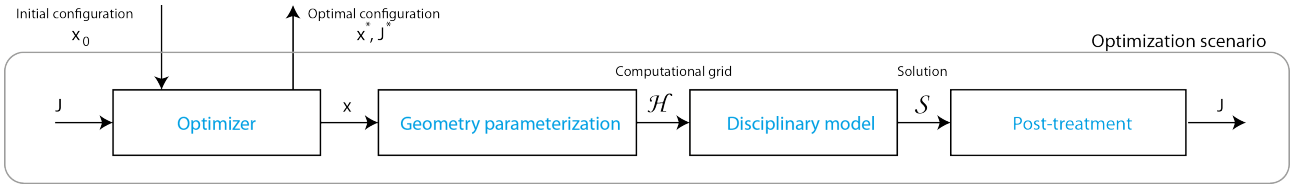

Figure 5.1: Generic shape optimization scenario.

In the case of shape optimization, the scenario begins with an initial reference configuration, meaning an initial design variables set x_0. The parameterization module adopts this information to define the geometry and to associate the corresponding computational grid $\mathcal{H}$ that is used in the disciplinary model. More than one model can be used as more than one discipline can be considered in the optimization. These models can belong to the category of low-fidelity models or to the high-fidelity one. Cost function(s) are then generally computed after some post-processing of the solution $\mathcal{S}$. The optimizer using the information provided by the cost functions, proposes a new design variables set that is given to the parameterization module. A new optimization iteration begins. The process is repeated until convergence is reached. The convergence can be reached when the maximum number of iterations is achieved or when a particular criteria on the cost function is satisfied (e.g. gradient value, function values unchanged during the last iterations, ...).

Optimizer

The optimizer consists essentially in a software implementation of an optimization algorithm that tries to minimize a given cost function repeatively proposing new sets of design variables, thus defining new configurations that are evaluated by the disciplinary model. Looking at the optimizer algorithms, a large number are available in literature and generally belongs to two categories: local optimizers or global optimizers.

Local algorithms have the tendency to converge to a local optimum while convergence to global optimum is not ensured. They are very efficient tools for local optimization. When the initial guess is sufficiently close to the optimum solution, and the gradient available, they usually result in fast convergence to the desired optimum. However these methods are usually not very robust, since they rely on the local convexity of the problem. The solution obtained at convergence strictly depends upon the initial solution. Different starting points generally result in different final optimal solution if multiple local minima exist. Gradient based algorithm or the gradient-free Nealder-Mead simplex algorithm belong to this class of algorithm. Gradient based algorithms requires the evaluation of the cost function gradient. In PDE-constrained optimization, developing the exact or approximate expression for the functional gradient is always a complex task. This difficulty is even more severe in multi-objective problems when the convexity or even the continuity of the Pareto front is not

guaranteed. Gradient can be provided with additional computational efforts by finite differences, by complex-step method [91] or using the adjoint method [92].
Furthermore local optimization algorithms suffer from the fact that when the function analyzed is non smooth, multimodal or even discontinuous, convergence to a minimum is hard to achieve. In this case global optimization algorithms are preferable. They are generally based on genetic algorithms. Several exists. In their principle, operators that mimic evolution (e.g. natural selection, cross-over, and mutation) are constructed to let a population of design-points evolve according to successive generations. In general, these methods are less accurate, very demanding in computational effort, but greatly superior in robustness. Furthermore they suffers from the problem of curse of dimensionality as the number of design variables increases. Indeed as the number of design variables increases the number of function evaluations required to achieve the convergence increases exponentially. For this reason an efficient algorithm is required in order to reduce the number of function evaluations. At the same time it is required to use a minimal parameterization able to accurately describes the relevant geometry properties of the configuration with a reduced number of variables.

Among the global optimizer class, CMA-ES [93] represents an efficient optimization algorithm based on evolutionary strategies. The CMA-ES algorithm is well suited for non-linear optimization problems in continuous domain. It is a second order approach estimating a positive definite matrix within an iterative procedure (more precisely: a covariance matrix, that is, on convex-quadratic functions, closely related to the inverse Hessian). This makes the method feasible on badly conditioned problems. In contrast to quasi-Newton methods, CMA-ES does not use or approximate gradients and does not even presume or require their existence. This makes the method feasible on non-smooth and even non-continuous problems, as well as on multimodal and/or noisy problems. The key aspects of the method are here summarized. New search points are sampled normally distributed as perturbation of the mean $m \in \mathbb{R}^N$:

$$x_i \sim m + \sigma \mathcal{N}_i(0, C) \tag{5.1}$$

where $\sigma \in \mathbb{R}_+$ is the step-size and $C \in \mathbb{R}^{N \times N}$ is the covariance matrix that defines the shape of the distribution ellipsoid. The normal distribution $\mathcal{N}$ is adopted because, in addition to stability properties, is the most convenient way to generate isotropic search points, thus not encouraging any direction. $\mathcal{N}_i(0, C)$ is uniquely defined by the covariance matrix C. The mean determines the displacement of the search region. The distribution is symmetric about its mean value. Taking μ parents that generates λ offspring individuals and let $x_{i,\lambda}$ the i-th ranked solution, the new mean is evaluated as

$$m = \sum_{i=1}^{\mu} w_i x_{i,\lambda} \tag{5.2}$$

where $w_1 \geq ... \geq w_\mu > 0$, and $\sum_{i=1}^{\mu} w_i = 1$, $\frac{1}{\sum_{i=1}^{\mu} w_i^2} \approx \frac{\lambda}{4}$. The best μ points are selected from the new solutions. The covariance C determines the shape of the search region. Geometrically it is identified by the iso-density ellipsoid:

$$x \in \mathbb{R} \mid (x - m)^T C^{-1} (x - m) = 1 \tag{5.3}$$

The adaptation at each iteration of the step-size and covariance matrix, as described in [93], results in an improvement of the method performance by orders of magnitude with respect to other algorithms that belong to the class of ES, thus providing an efficient optimization algorithm. The CMA-ES has several invariance properties. Two of them, inherited from the plain evolution strategy, are invariance to order preserving (i.e. strictly monotonic) transformations of the objective function value, and invariance to angle preserving (rigid) transformations of the search space (including rotation, reflection, and translation), if the initial search point is transformed accordingly. The CMA-ES does not require a tedious parameter tuning for its application. In fact, the choice of the strategy internal parameters is not left to the user with exception of the population size. For these reasons in this work it is used for single-objective optimizations. In addition due to its robustness properties, it is well suited for the sonic boom minimization. Indeed the acoustic function is generally noisy and multimodal.

Parameterization

To minimize the sonic boom and improve the aerodynamic performance an accurate description of the geometry is required. Often little or not sufficient importance is given to this aspect, but the choice of the parameterization may have a strong impact on the problem formulation, implementation and final solution. The objective is to identify a set of parameters that can describe the reference configuration and that will be used in the optimization problem. In other words parameterization is the process of deciding and defining the parameters necessary for a complete or relevant specification of a geometric object. The parameterization module has to fulfill two requirements:

- To be able to deform or re-generate the geometry;
- To ensure the relationship between the design variables and the geometry.

Concerning the first requirement, geometry deformation and re-generation are both retained. Firstly, if a structured mesh is considered, an analytic Fortran volume mesh generator developed at Onera is adopted. At the origin, the code has been associated to high-fidelity design of wing-body supersonic configurations with the possibility to introduce canard and horizontal tail plane. The code has been modified in order to be integrated into an optimization framework. Furthermore the fuselage geometry configuration that can be treated by the code has been generalized. Instead of a classic cylindrical cabin, the actual code can consider a generic cabin that can assume any shape. This aspect is fundamental for the fuselage tailoring approach. Mesh is completely re-generated at each optimization iteration due to the reduced wall clock time required (less than one minute). Secondly, in the case of unstructured mesh, the deformation of the initial mesh is retained. An application based on the free-form-deformation approach is described in details in Appendix B.

A parameterization has to satisfy several requirements, according to the problem considered, to ensure the relationship between geometry and design variables [94]. The set of parameters has to be an effective set in the sense that the objective functions are sensitive to variation of the parameters. In addition when considering a multi-objective optimization the parameterization has to be effective and consistent across multiple disciplines. A compact set or a modulable set where it is possible to add or remove parameters is generally preferred when each function evaluation is costly. In fact, the speed of convergence of the optimization algorithms (global or local) depends on the size of the design variables set. Not only because in some cases it is necessary to evaluate the gradient or the Hessian of the cost function, but also because the search space is increased. Furthermore the parameters directly related with airplane shape design variables (e.g. dihedral angle, sweep angle, fuselage radius, camber, twist,...) are generally preferred for the set up of the problem, but also for the post-processing and analysis of the results. Another condition that the parameterization has to satisfy is related to the impact of variables modification on the shape. Shape perturbations have to maintain a smooth geometry, thus avoiding "wavy" geometries and at the same time have a local control on the geometry. Other conditions related to the compability between the CAD model and the geometry are presently not considered. Satisfying all the conditions is not an easy task, and a discrimination based on their relative importance for the problem considered is required but not sufficient. In fact the parameters chosen are usually a direct consequence of the methods available to generate or deform the geometry (e.g free-form deformation).

For the problem considered in this work, due to the fact that the mesh is created analytically, aircraft shape design parameters are adopted. The fuselage is defined using three tension spline [95] in order to better describe the nose, the cabin and the aft part. Each spline can be described using a variable number of fuselage radius as shown in Figure 5.2. An increase of the number of control sections for the fuselage generally increase the degree of freedom and oscillations. A compromise has to be defined in order to increase the exploration space of the optimization algorithm and at the same time preserve shape properties such as monotonicity and convexity. The three-dimensionality is achieved with a revolution of the control line along the longitudinal axis. The result is an axi-symmetric fuselage. This parameterization has been modified in order to suppress the axi-symmetry limitation. The vertical coordinate of the nose apex can be modified and the tension spline that defines the nose re-generated. The volume is then built up using circular sections centered on the new mean

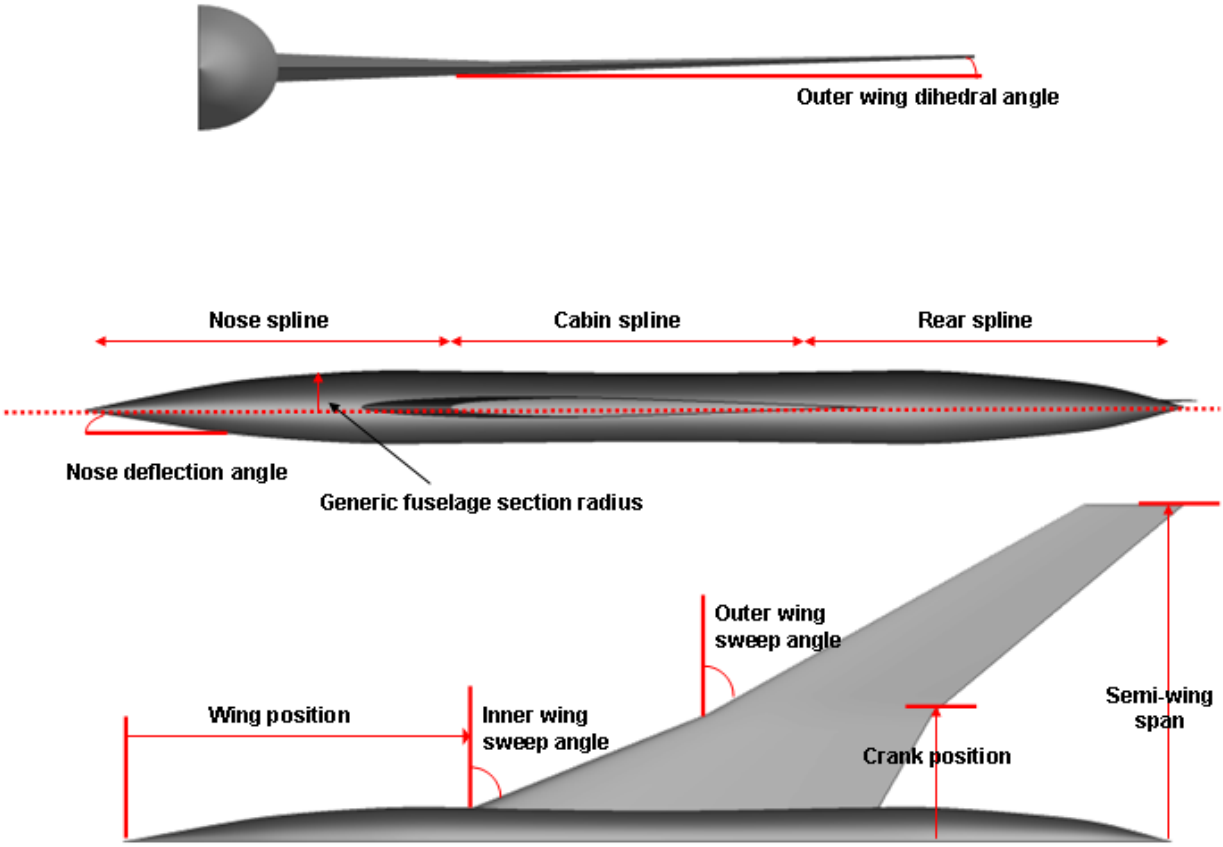

Figure 5.2: Generic shape parameterization adopted for the optimization problems.

line.
Concerning wing-geometry, the wing planform is described using aircraft shape design variables such as wing sweep angle, dihedral angle, root, tip and crank chords and thickness over chord ratio. Wing parameterization is shown in Figure 5.2. Only the wing planform is modified, keeping fixed the wing airfoil shape and twist distribution. The position of the wing with respect to the fuselage main axis is also a design variable. The wing leading edge is described by linear segments, thus introducing non-$\mathcal{C}^1$ junctions at the wing root with the fuselage and at crank. This actually represents a limitation of the meshing tool adopted.

Once the geometry is described and a set of design variables is defined, the following step has to be defined how to modify the reference configuration. A design variables set generally contains lengths, angles, dimensionless quantities with different ranges of variation. To avoid undesired convergence of the optimization algorithm into local optima thus providing a better conditioning of the problem, a non-dimensional optimization variables set $\mathbf{x}$ is adopted . The optimization variables $\mathbf{x}$ are related to the geometry design variables set (DV) using the following equation:

$$DV_i = \bar{DV}_i(1 + x_i\delta_i) \quad \forall i > 1 \quad (\text{for } \bar{DV}_i \neq 0) \tag{5.4}$$

where $\bar{DV}_i$ represents the geometrical variable of the reference configuration, δ_i is the maximum percentage modification allowed to each variable. δ_i can take different values depending on which variable is considered, in this way it is possible to define different range of variations, thus keeping the optimization variables set defined in the range:

$$\forall i \quad x_i \in [-1, 1] \tag{5.5}$$

The design perturbation δ_i generally depends upon the sensitivity of the objective function to a specific variable DV_i. An analysis of sensitivities can provide a qualitative idea of the relative importance of each variable on the objective function considered.

Disciplinary model

Disciplinary models are required to evaluate the cost functions during the optimization process. Taking as input a computational grid $\mathcal{H}$ fitting the actual geometry, the model provides as output the cost function(s) evaluated for the current design variables set. The evaluation can be associated to high-fidelity or low-fidelity models. High-fidelity models used for the aero-acoustic prediction of the sonic boom have been described in chapter 2. For the aero-acoustic problem they are generally based on the solution of PDE. Low-fidelity models are based on approximated models, where the behavior of the real model is mimed using a surrogate model [96]. The surrogate model is constructed using a database of high-fidelity solutions. Different surrogates exist, among these the most adopted are kriging, response surfaces and neural networks. Although surrogate models enable faster analyses than the high-fidelity disciplinary models, the meta-model approximation introduces a new element of uncertainty that must be managed: how accurate is the value predicted by the surrogate model? Different methods provide an uncertainty quantification and a methodology to improve the quality of the meta-model [97] and they are strictly required when complex problems are analyzed. When a disciplinary model is described by PDE, the solution of such system at each optimization iteration requires a considerable computational effort. For this reason low-fidelity models or mixed-fidelity approaches are well suited for optimization [97]. Mixed-fidelity approaches consists in the adoption during the optimization process of both low and high-fidelity models. Generally optimization convergence, that requires many function evaluations is performed upon the low-fidelity model. The optimal solutions are then evaluated using the high-fidelity model. Low-fidelity models can then be updated and several mixed-fidelity iterations can be performed. In the following studies both approaches are adopted, depending on the problem and on the optimization algorithm considered.

5.2 Analysis of sensitivities

To define an optimization scenario that is well suited for the problem considered a sensitivity analysis is required. Sensitivity analysis consists in computing the impact on one or more quantities (outputs) with respect to one or several independent variables (inputs) modification. The result of the analysis provides indications about the variables that have to be retained for the following optimization process and several information that can be exploited in the analysis of the optimal final solutions.

Several methods are available in literature for the evaluation of the function sensitivity to variations of design variables [98]. Due to their simplicity and implementation easiness, finite differences are commonly used to estimate sensitivities. Despite the fact that approximations are neither accurate nor efficient and their lack of robustness, the finite difference analysis can provide a qualitative idea of function sensitivities.

When estimating sensitivities using finite difference formula, we have to face to the step-size dilemma. On one hand if a too large step size is selected the truncation error becomes dominant on the exact values. On the other hand a too small step size will result in a value biased by the round-off error due to the machine precision. To overcome this problem, several function evaluations are required for the identification of the step size associated to each variable.

The scheme adopted in this analysis is the centered finite difference. For each variable and each cost function considered 2 evaluations are required but not sufficient. For a problem with n variables, m functions at least $2nm$ function evaluations are required. Due to the step-size problem generally more evaluations are required. In fact for each variable x_i the evaluation of $\frac{\partial f_j}{\partial x_i}$ is repeated with different step-size in order to converge to a value of the derivative for a specific value of h.

A configuration defined with ten design variables ($n = 10$) configuration is considered to evaluate the sensitivity of c_l, c_d and $\sum \Delta p$ ($m = 3$), thus resulting in at least 60 function evaluations. The list of the design variables considered is summarized in Table 5.1.

Figure 5.3 shows the finite difference analysis of sensitivity. Drag is considered first. The following

Variable	Description
x_1	Nose fuselage section x-coordinate
x_2	Nose fuselage section radius
x_3	Rear fuselage section x-coordinate
x_4	Rear fuselage section radius
x_5	Inboard wing sweep angle
x_6	Cabin fuselage section radius
x_7	Wing position along the fuselage
x_8	Nose angle deflection
x_9	Dihedral angle
x_{10}	Outboard wing sweep angle

Table 5.1: Design variables adopted for the sensitivity analysis.

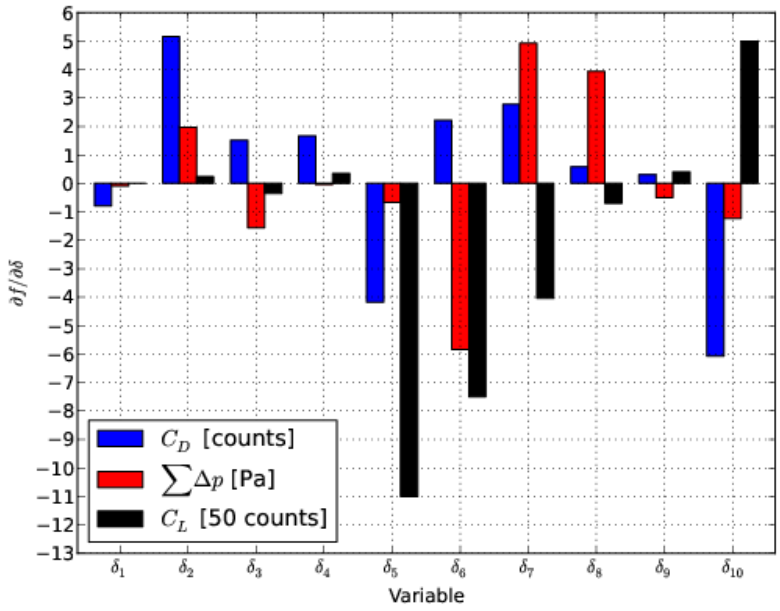

Figure 5.3: Finite difference sensitivity analysis.

terms define the total drag in the supersonic regime:

$$C_D = C_{D_f} + C_{D_{wv}} + C_{D_{wl}} + C_{D_l} \tag{5.6}$$

where the C_{D_f} is the skin friction drag coefficient, $C_{D_{wv}}$ is the supersonic volume wave drag coefficient, $C_{D_{wl}}$ is the lift dependent wave drag coefficient and C_{D_l} is the induced drag coefficient. Using CFD we are not able to discriminate the different terms that define the total drag, nevertheless it can be useful for the sensitivity analysis the estimation of the different terms as:

$$C_D = \frac{A}{S} C_f + K_V \frac{128V^2}{\pi S L^4} + K_L \frac{\beta^2 S C_L^2}{2\pi l^2} + K_I \frac{S C_L^2}{\pi b^2} \tag{5.7}$$

where:
A: total surface
S: reference surface
C_f: friction coefficient
K_I: shape parameter for induced drag
K_L: shape parameter for lift dependent wave drag

K_V: shape parameter for volume wave drag
l: lifting length
L: total aircraft length
V: total aircraft volume
Volume drag depends mainly on volume and slenderness V/L^2. The lift dependent wave drag increases with speed as a difference from induced drag and decreases quadratically with lifting length l^2. This term is so reduced in the case of slender wing with high sweep and small span. K_L is reduced for smooth elliptical lift distribution along lifting length l. Induced drag decreases with aspect ratio b^2/S and it depends also from K_I, that is the Oswald factor equal to 1 for elliptical lift distribution along span. Skin friction drag term depends upon the wetted surface, but it is neglected as unviscous computations are performed.

Considering the impact of the fuselage variables on the drag coefficient in Figure 5.3, the displacement of x_1 closer to the nose means an increase of the nose bluntness thus an increase of the nose wave drag. The same effect can be obtained with an increase of the value of x_2. An analogue behavior is shown in the aft-body part of the fuselage with respectively x_3 and x_4 that define the x and z-coordinate of the rear control point. Modifications of the cabin section radius (x_6) act on the aft-body interference drag due to central fuselage, in particular an increase of the section radius increases the drag coefficient. In addition all the reductions of the fuselage cross section not only reduce the fuselage wave drag due to volume, but also the wave drag due to lift that strongly depends on cross section [99]. The increase of the nose slope (x_8) introduces an increase of the effective angle of attack seen by the nose of the fuselage, increasing in this way the fuselage drag, but at the same time increasing the lift produced. The sweep angles defined by x_5 and x_{10} respectively for the inner and the outer wing determine the nature of the wing leading edge: subsonic or supersonic. The tendency is that as the sweep angle is reduced, thus defining a supersonic leading edge, the drag is increased as also shown by Roskam in [99]. A decrease in the inner wing sweep angle corresponds also to an increase of the lift coefficient. The skin pressure distribution for modification of the outer wing sweep angle is shown in Figure 5.4. As x_{10} is increased, the outer wing leading edge becomes subsonic, while on the contrary as x_{10} is reduced the leading edge is supersonic and the shock region over the outer wing intrados extends to 30% of the chord resulting in an increase of the drag coefficient.

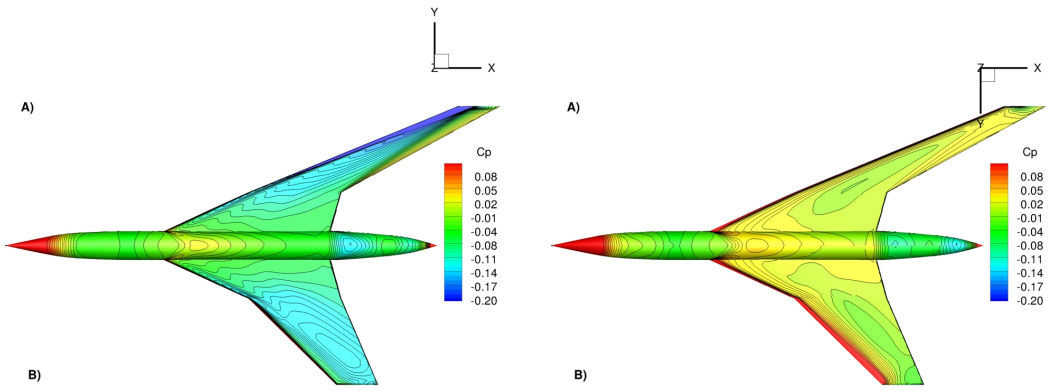

(a) Upper. (b) Bottom.

Figure 5.4: Pressure coefficient. A) Increased sweep angle of the outer wing. B) Decreased dihedral angle of the outer wing.

Modifications of the dihedral angle (x_9) impact the angle of attack of the wing α only if sideslip occurs. For the case analyzed, Figure 5.3 shows that an anhedral configuration reduces the drag coefficient and at the same time the lift coefficient.

Modifications of the wing position (x_7) directly act on the cross-sectional area rule. Whitcomb in [100] identifies the area distribution that corresponds to the minimum wave drag due to the volume.

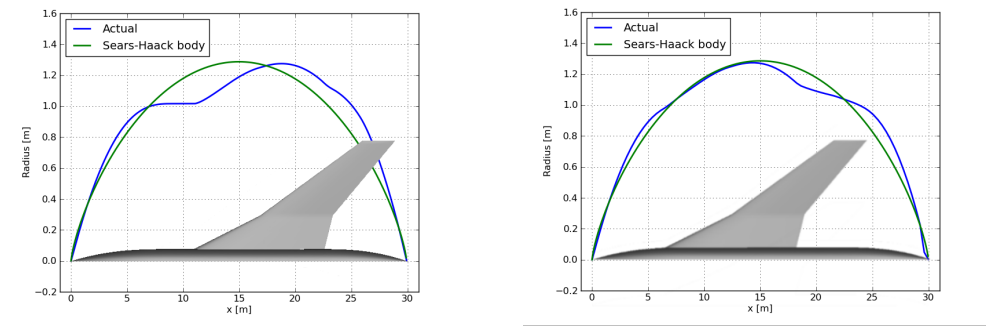

(a) Reference configuration. $C_D = 0.005636$

(b) Forward wing configuration. $C_D = 0.005150$

Figure 5.5: Comparison of the radius rule with the Sears-Haack body.

The body with the minimum wave drag is identified as the Sears-Haack body described by the following area distribution:

$$A_{sh}(x) = \frac{16V}{3L\pi}[4x(1-x)]^{3/2} \tag{5.8}$$

where V is the volume of the configuration and L its length.
In order to reduce the drag profile of an aircraft, a smooth distribution of area in the proximities of the wing structure must be maintained, thus reducing the profile drag of the aircraft. Modifications of the wing position have a strong impact on the volume wave drag, in particular a forward displacement of the wing results in a reduction of this term. Nevertheless the reduction of drag due to the Whitcomb area rule tends to become less effective for Mach number superior to 1.5 [101]. In Figure 5.5 is shown the comparison between the radius distribution for the reference configuration and for a configuration with a wing closer to the nose with a Sears-Haack body with an equivalent volume and length.

Adopting the Karman formula defined in equation (3.2) for an estimation of wave drag, we obtain a $C_{D_{wv}}$ for the reference configuration equal to 0.005636, while the second one shows a value of 0.005150. A wing closer to the nose is closer to the Sears-Haack configuration than the reference one thus reducing the wave drag term.

Considering the acoustic cost function, the variables that defines the fuselage nose x_{1-2} clearly show that a sharp slanted nose instead of a blunt one provides a reduction of the acoustic cost function. The radius of the cabin (x_6) plays a primary role in defining the magnitude of the acoustic cost function. Modifications of the cabin geometry have an impact on the middle-aft part of the acoustic

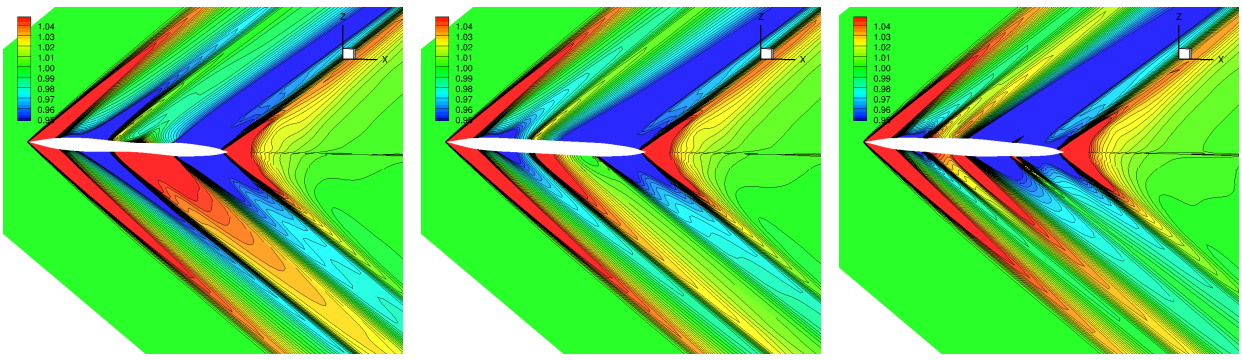

(a) Decreased cabin radius. (b) Reference cabin radius. (c) Increased cabin radius.

Figure 5.6: Impact of cabin radius modifications on pressure near-field (p/p_0).

signal. On one hand a decreased cabin radius (Figure 5.6a) produces a more extended expansion zone before the wing shock. On the other hand an increase of the cabin radius (Figure 5.6c) limits the flow

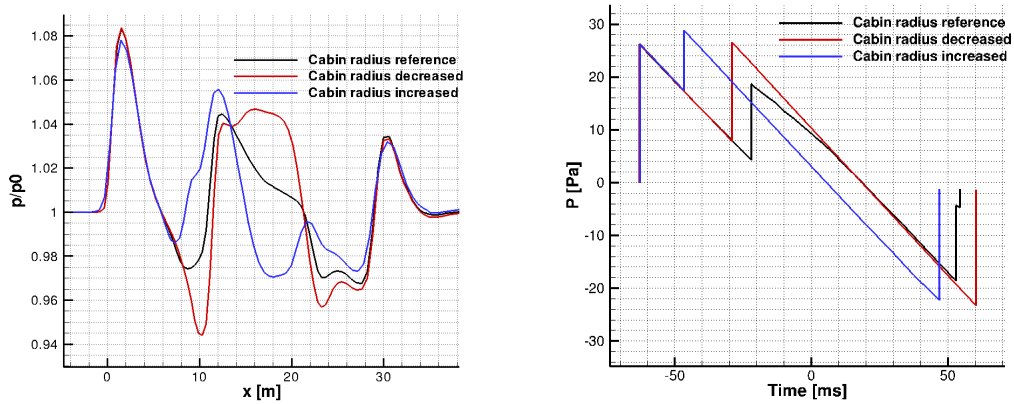

(a) Near-field pressure signature ($h = h_z - 10$ m). (b) Ground signature.

Figure 5.7: Impact of cabin radius modifications on acoustic signature.

acceleration after the front shock, an additional shock occurs just before the wing leading edge shock. This trend is clearly shown by the under-track acoustic signature in the near-field (Figure 5.7a). The dip after the first peak is exaggerated as the cabin radius is decreased, while an increase of the cabin radius limits pressure expansion. In the region that follows the wing shock the opposite situation occurs. For the decreased radius configuration, in the wing region the fuselage section increases thus producing a new shock, while on the contrary for the increased radius configuration a strong expansion occurs. As expected the front shock at ground (Figure 5.7b) remains unchanged among the different configurations, while the wing shock magnitude is reduced for the configuration with the largest fuselage cabin due essentially to the reduced expansion after the front shock. Rear shock is increased for both configuration with respect to the reference one. The analysis confirms the indication provided by finite differences: as the cabin radius increases, the sum of the shock overpressure in the ground signature reduces. Wing horizontal position along the fuselage has a strong impact on both near-

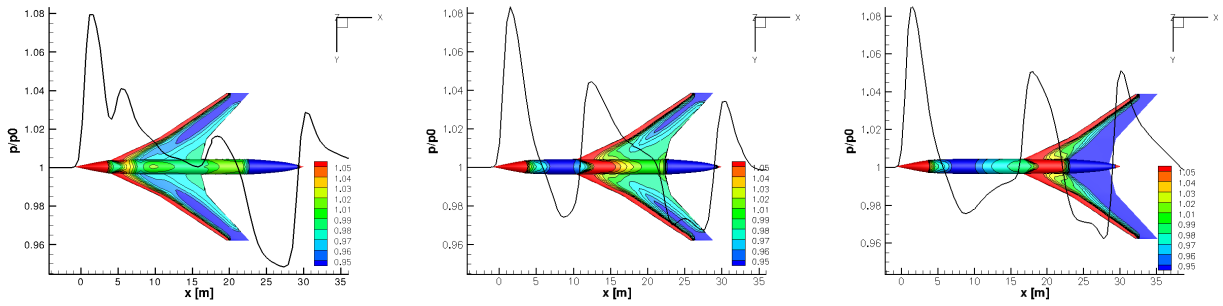

(a) Fore wing. (b) Reference wing. (c) Rear wing.

Figure 5.8: Effects of wing position on near field pressure (p/p_0) (Bottom skin pressure). Near-field signatures are extracted 10 m below the aircraft.

field (Figure 5.8) and ground signature (Figure 5.9). As the wing is displaced towards the front part of the aircraft, the related pressure peak in the near-field signature approaches to the nose pressure peak. During the propagation the two shocks tend to coalesce resulting in a N-wave signature. The front shock overpressure is so increased compared to the reference configuration. A rear wing, due to the interference with the rear fuselage, results in a configuration with increased lift. The acoustic performance is not improved due to the creation of an additional rear shock. A compromise solution has to be identified if the reduction of the acoustic performance is envisaged.

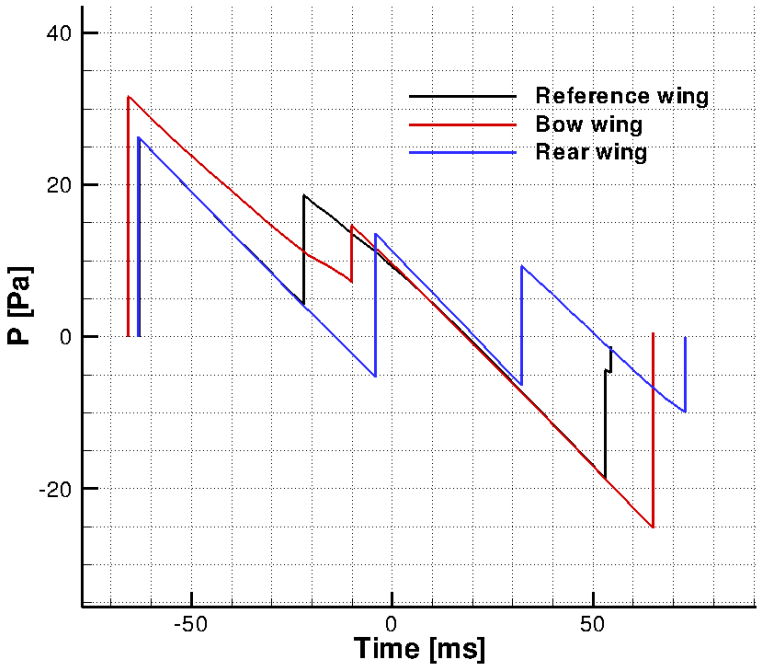

Figure 5.9: Effects of wing position on ground signature.

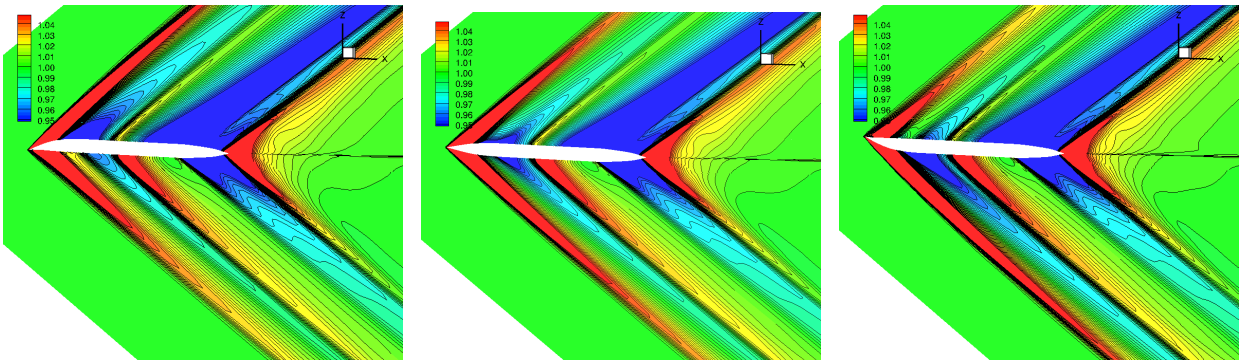

(a) Nose deflected downward. (b) Reference configuration. (c) Nose deflected upward.

Figure 5.10: Effects of nose deflection on near field pressure (p/p_0).

The other parameter that has a strong effect on the acoustic performance is the nose deflection. This parameter affects the near-field, in particular the region that extends from the nose to the wing as shown in Figures 5.10 and 5.11a. A nose deflection downward deviates the flow-field in the region above the aircraft thus reducing the nose shock wave directed towards the ground with a beneficial effect on the ground signature front overpressure (Figure 5.11b). Furthermore the expansion wave just before the wing is reduced. As a consequence the configuration with a nose deflected downward shows a reduction also of the wing shock magnitude thus providing a considerable improvement of the acoustic performance. The contrary occurs for an upward nose deflection.

The analysis provided by finite differences is local, because derivatives are evaluated at a specific reference point. A global analysis can be performed evaluating the sensitivity index. The sensitivity index (SI) [102] is defined as:

$$SI = \frac{D_{max} - D_{min}}{D_{max}} \tag{5.9}$$

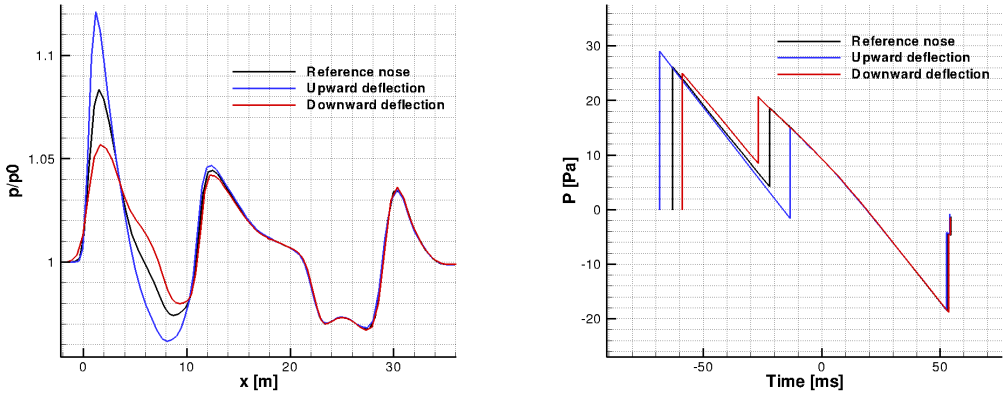

(a) Near-field pressure signature.

(b) Ground signature.

Figure 5.11: Effects of nose deflection on the acoustic signatures.

where D_{min} and D_{max} are respectively the minimum and maximum output values, resulting from varying the input over its entire allowable range. This figure-of-merit provides a global indication of parameters and model variability. Table 5.2 summarizes the sensitivity index for the aero-acoustic functions. In addition ranking provides an indicator of which parameter impact the most each function.

	SI_{C_D}	$SI_{\sum \Delta p}$	SI_{C_L}	Rank_{C_D}	$\text{Rank}_{\sum \Delta p}$	Rank_{C_L}
x_1	0.01783	0.006489	-7.3218e-5	8	10	10
x_2	0.10995	0.071208	-0.0014986	3	4	8
x_3	0.03677	-0.033381	0.0012835	7	7	9
x_4	0.0371735	-0.0360376	0.00154376	6	5	7
x_5	-0.1114509	0.0350624	-0.047527	2	6	1
x_6	0.049551	-0.1730625	-0.03053995	5	1	2
x_7	0.070465	0.032882	-0.0207928	4	8	3
x_8	0.014445	0.08490	-0.001796	9	3	5
x_9	0.007067	-0.0198549	0.0016	10	9	6
x_{10}	-0.149338	-0.093734	0.02006	1	2	4

Table 5.2: Sensitivity Index.

Considering the sensitivity indices related to drag for each variable, the values are in perfect agreement with the indication provided by finite difference analysis. The most influencing parameters when considering drag are the two wing sweep angles followed by the radius of the nose and the longitudinal wing position. Ground signature is impacted mainly by the modification of the cabin radius, outer wing sweep angle and nose deflection. SI shows also if the parameter acts mainly only on one discipline and not on the others. This aspect is interesting in multi-objective optimization where local disciplinary subsets of the parameters have to be identified. To this class of parameters belong the inner sweep angle that impact mainly aerodynamics and the cabin radius that impact mainly acoustics.

Finite difference and sensitivity index are methods that belong to the once-at-time (OAT) class. In OAT analysis the impact of the variation of a single input parameter on the output function is evaluated keeping all the other parameters fixed. Second order effects due to the coupled modification of more than one parameter are not taken into account by these methods. Sobol indices [103] or the Morris screening method [104] provide information due to multiple variables influence on the output function. These methods are computationally expensive because they require several function

evaluations for accurate estimation of the sensitivity. For this reason they are not taken into account in this work.

5.3 Single objective aerodynamic optimization

Aerodynamic numerical optimization over the years has gained popularity in design procedures [105]. Its application to the analysis of complete three-dimensional configurations has become relevant in all design phases.
The aerodynamic shape optimization problem can be stated as follows:
Find the design variables set $\mathbf{x}$ *that*

$$\begin{array}{lllll} \text{Minimize} & J_{aero}(\mathbf{x}) & := & c_D & \\ \text{subject to} & g(\mathbf{x}) & := & c_L - c_L^{target} & \geq 0 \end{array} \tag{5.10}$$

where c_L^{target} is taken equal to 0.116 and the design variables $\mathbf{x}$ are defined as perturbation of the reference configuration as in equation (5.4). The variables are shown on the geometry in Figure 5.12 and summarized in Table 5.3.

Variable	Specification	$\bar{DV}_i$	δ_i
x_1	radius nose section [m] $x = 1$ m	0.265	10%
x_2	radius nose section [m] $x = 2$ m	0.486	10%
x_3	radius nose section [m] $x = 3$ m	0.663	10%
x_4	radius nose section [m] $x = 4$ m	0.800	10%
x_5	radius nose section [m] $x = 5$ m	0.899	10%
x_6	radius nose section [m] $x = 6$ m	0.963	10%
x_7	radius nose section [m] $x = 7$ m	0.998	10%
x_8	wing root chord [m]	11.584	10%
x_9	wing crank chord [m]	6.430	10%
x_{10}	wing tip chord [m]	2.896	10%
x_{11}	crank position along wing span [adim]	0.31	10%
x_{12}	inner wing sweep angle [deg]	65	10%
x_{13}	outer wing sweep angle [deg]	56	10%
x_{14}	relative wing position [adim]	0.45	10%
x_{15}	aspect ratio [adim]	3	10%
x_{16}	nose deflection [deg]	0	-%
x_{17}	dihedral angle [deg]	3	100%
x_{18}	angle of attack [deg]	2	100%

Table 5.3: Design variables set definition.

Concerning nose deflection, the following relationship is adopted: $DV_{16} = 0.15x_{16}$, because the reference value is equal to zero. The angle of attack is considered in this case as an optimization variable in order to satisfy the lift constraint.

The convergence history of the minimization problem (5.10) using a modified version of the CMA-ES algorithm capable to deal with non linear constraints [106] as optimizer is shown in Figure 5.13.

After a reduction of nearly 19% of the cost function with respect to the initial configuration achieved with less than 2000 iterations, the optimal configuration shows a drag coefficient equal to 88.43 drag counts with the constraint that is satisfied and active. This performance is closer to the one of the initial configuration (89 drag counts). Table 5.4 summarizes the properties of the optimal configuration. The optimizer acts mainly on the wing planform (see Figure 5.14). The wing is displaced close towards the nose so that the volume wave drag is reduced. The inner wing of the optimal configuration is almost unmodified with respect to the reference one so that the pressure distribution in a wing section located at $y = 4$ m is mostly unchanged from the two configurations (see Figure 5.16). At the same time the

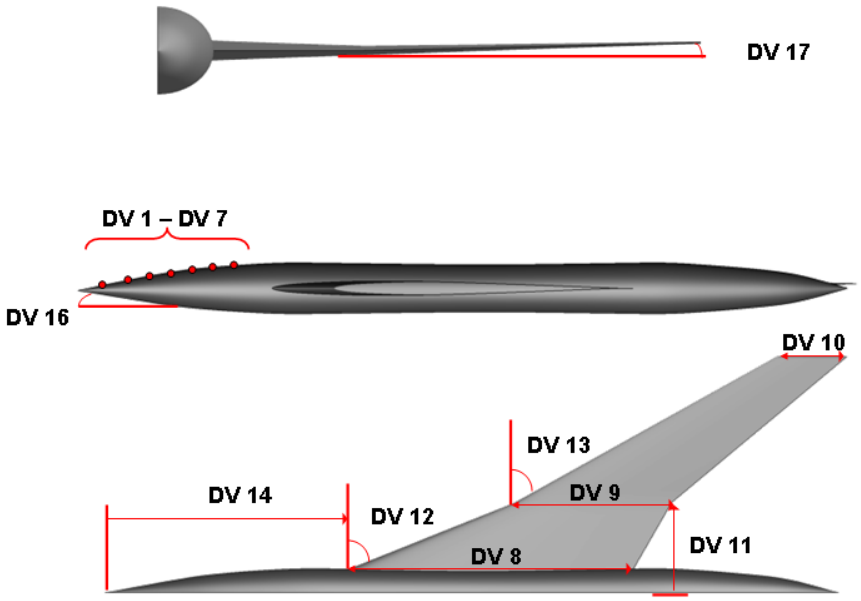

Figure 5.12: Parameterization set adopted for the single-discipline optimization.

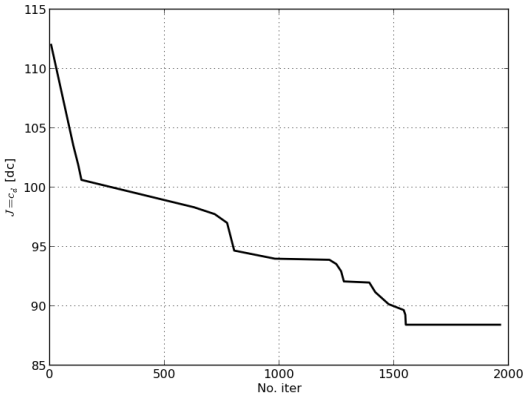

Figure 5.13: Aerodynamic cost function convergence history.

$\alpha[deg]$	c_D [drag counts]	c_L	Δp [Pa]
2.258	88.438	0.1165	60.29

Table 5.4: Properties of the low-drag configuration.

sweep angle of the outer wing is increased. This parameter, as shown by the sensitivity analysis (see Figure 5.3), has a strong impact on the aerodynamic performance. In fact, swept wings with subsonic leading edge have the advantage of reducing the wave drag component at supersonic flight speeds that generally represents 60% of the total drag in the supersonic regime. Dihedral angle is slightly reduced while the aspect ratio is slightly increased. These modifications result in a outer wing that produces more lift (see pressure coefficient distribution in a wing section located at $y = 8$ m). The nose is deflected upward (see Figure 5.15). The flow deviates downward so that the magnitude of the nose shock directed to the ground is increased. At the same time the nose shock on the upper part of the nose is reduced. Another consequence is an increase of the fuselage contribution to lift.

The acoustic signature of the optimal configuration evaluated in the near-field and at ground is shown in Figure 5.17. The comparison with the initial configuration shows that the front shock is

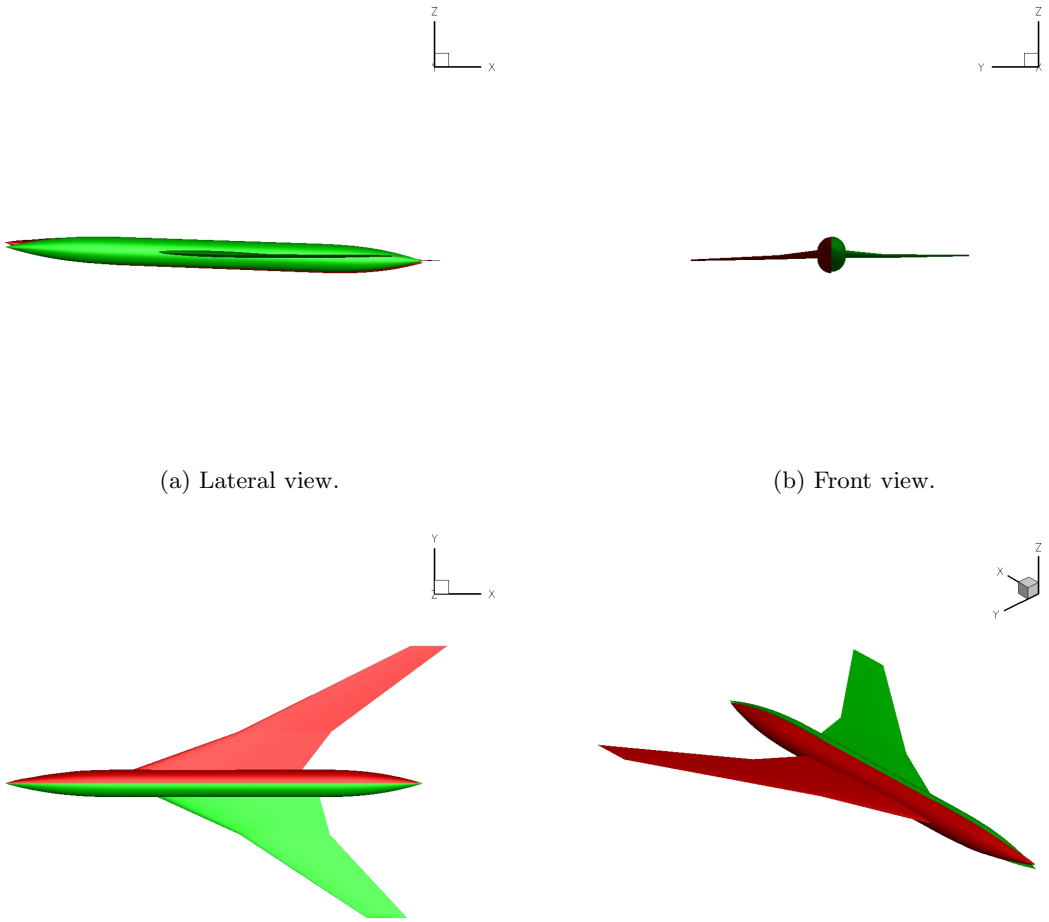

(a) Lateral view.

(b) Front view.

(c) Top view.

(d) 3D view.

Figure 5.14: Comparison between the initial configuration (green) and the optimized one (red).

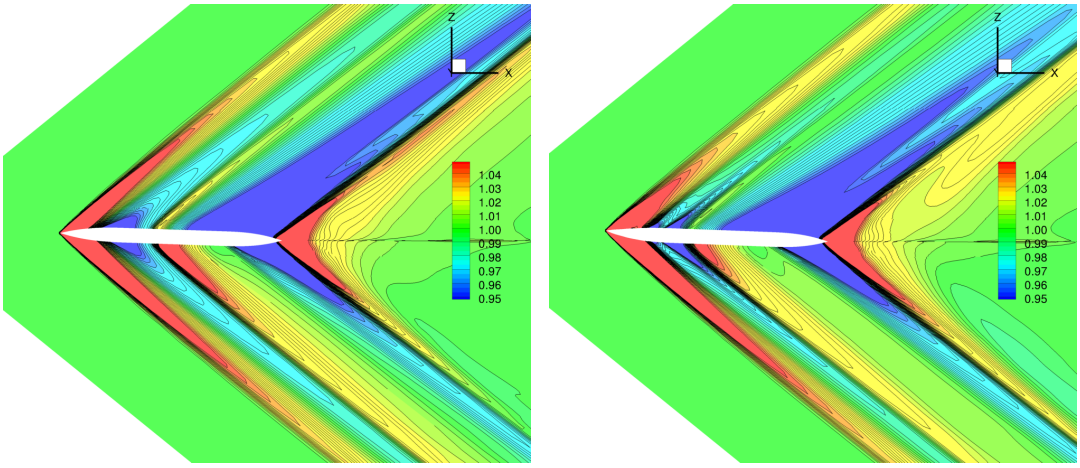

(a) Initial configuration.

(b) Optimized configuration.

Figure 5.15: Comparison between the near pressure field (p/p_0) of the initial and optimized configuration.

almost unchanged, while the modification that occurs at the wing planform has a beneficial effect reducing the related shock in the near-field and at ground. Wing shock is reduced as a consequence to the wing displacement close to the nose. The modification of the outer wing that in the optimal

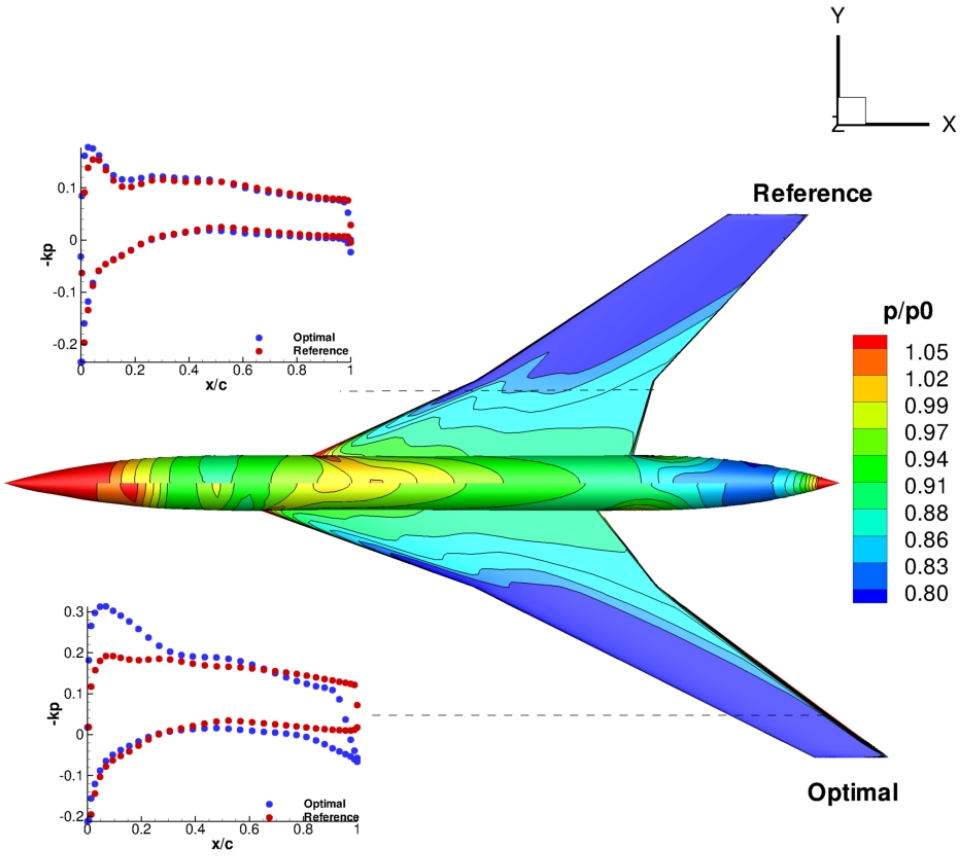

Figure 5.16: Upper skin pressure distribution and pressure coefficient at different wing sections ($y = 4$ m and $y = 8$ m).

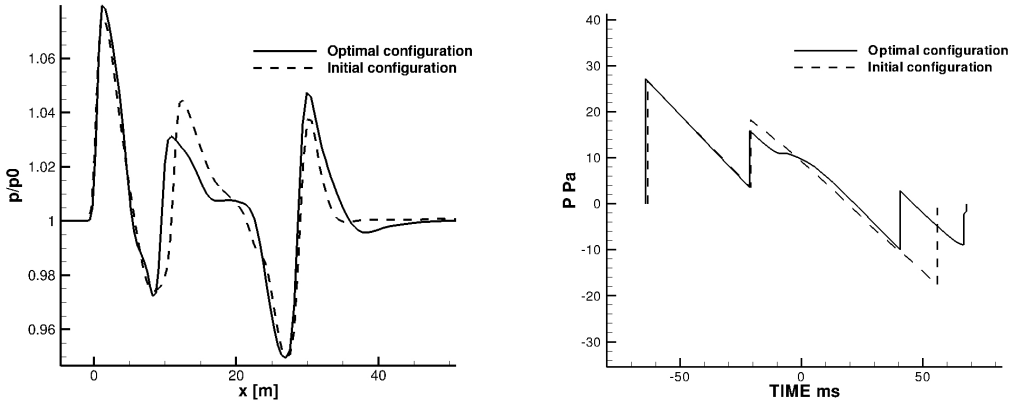

(a) Near-field signature ($h_z = h - 10$ m).

(b) Ground sonic boom signature.

Figure 5.17: Under-track signature extracted in the near-field and at ground for the initial and the low-drag configurations.

geometry increases the effective length of the configuration, results in the creation of an additional shock in the aft part of the ground signature. The sum of the shocks amplitude is close to the one of the initial configuration.

5.4 Single objective acoustic optimization

The same optimization scenario can be easily adapted to minimize the acoustic function alone. The optimization algorithm and the parameterization used for the aerodynamic shape optimization introduced in section 5.3 are here adopted. The acoustic minimization problem can be stated as follows: *Find the design variables set* $\mathbf{x}$ *that*

$$\begin{array}{lllll} \text{Minimize} & J_{acou}(\mathbf{x}) & := & \sum \Delta p & \\ \text{subject to} & g(\mathbf{x}) & := & c_L - c_L^{target} & \geq 0 \end{array} \tag{5.11}$$

where c_L^{target} is taken equal to 0.116. The sum of the under-track ground signature shocks is the acoustic function to be minimized. As already introduced in chapter 2 this choice is motivated by the fact that pressure based metrics are more related to the design variables instead of loudness based metrics so that the optimization algorithm can converge more easily. The convergence of the objective J_{acou} using the modified version of CMA-ES is shown in Figure 5.18. The algorithm converges in about

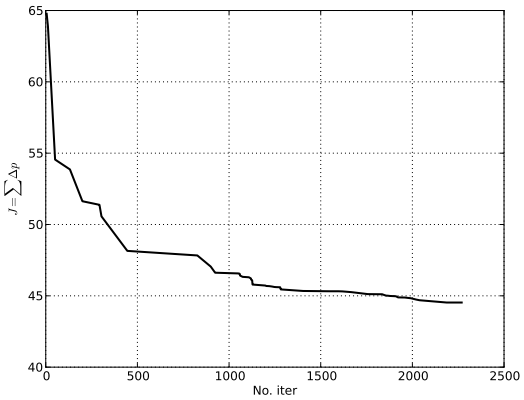

Figure 5.18: Acoustic objective function convergence history.

2200 iterations, resulting in a decrease of the cost function of more than 30% with respect to the initial configuration from 64.9 Pa to 44.7 Pa. The low-boom configuration degrades the drag coefficient by 2 drag counts with respect to the low-drag configuration and by 1.5 drag counts compared to the reference configuration.

The optimal geometry is shown in Figure 5.19 and its main properties are summarized in Table 5.5. The nose is shifted downward, this aims to modify the intensity of the front shock, in particular

α	c_D [drag counts]	c_L	Δp [Pa]
2.155	90.515	0.1161	44.53

Table 5.5: Properties of the low-boom configuration.

(see Figure 5.20b) the pressure perturbation that propagates downward is reduced , while its upward counterpart is increased. Further small shocks are created with nose curvature changing in the nose region. At ground the nose modifications produce a reduction of the front shock overpressure by 4 Pa. The flow expansion before the wing leading edge shock maintains the same magnitude of the initial configuration but occurs in a less extended region. This trend is clearly shown by the under-track near-field signature (Figure 5.21a). The first peak is reduced by near 20 % and is followed by an additional smaller peak. The expansion due to the fuselage radius increases is more localized than the initial one, but it has the same amplitude. The wing peak is reduced and at the same time a pressure plateau is created. The result at ground is a secondary shock closer to the nose shock, with an amplitude that is half of the initial one. Wing is slightly moved upward, while the wing dihedral angle is strongly increased in the optimal configuration, and as a consequence the footprint ground signal

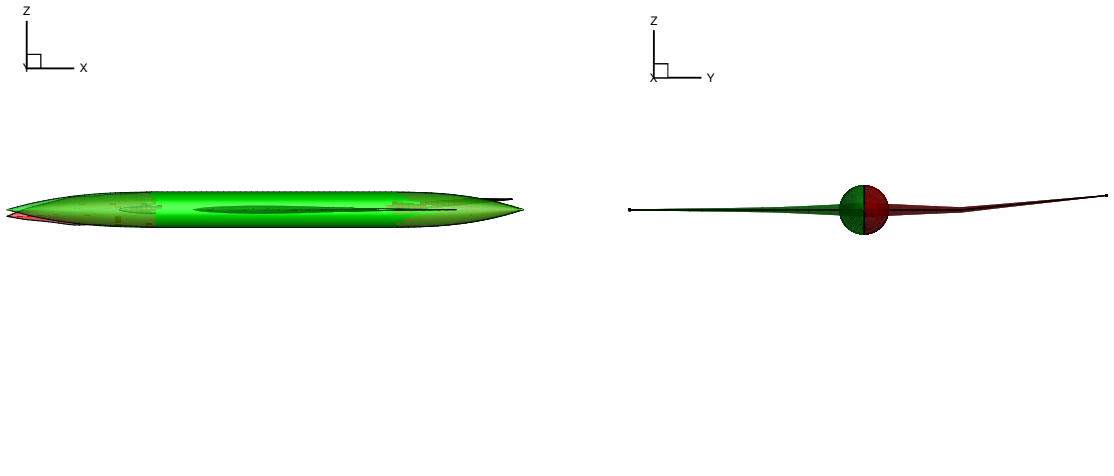

(a) Lateral view.

(b) Front view.

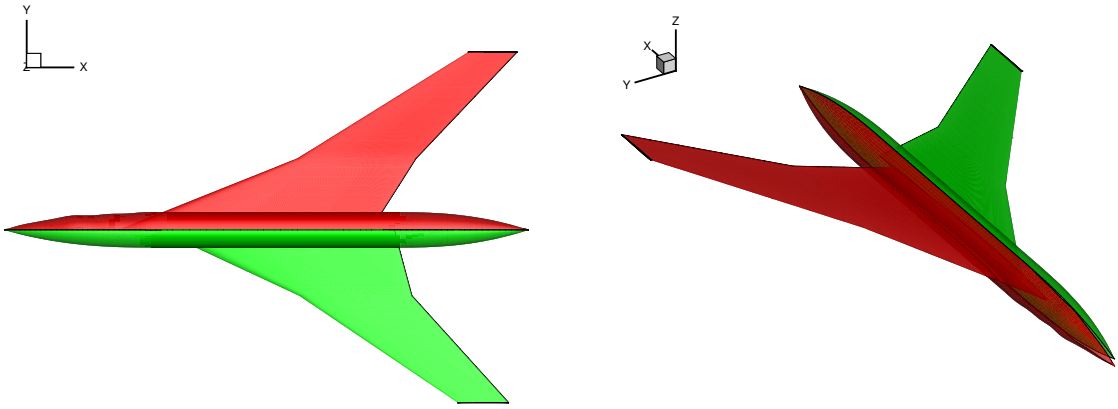

(c) Top view.

(d) 3D view.

Figure 5.19: Comparison between the initial configuration (green) and the optimized one (red).

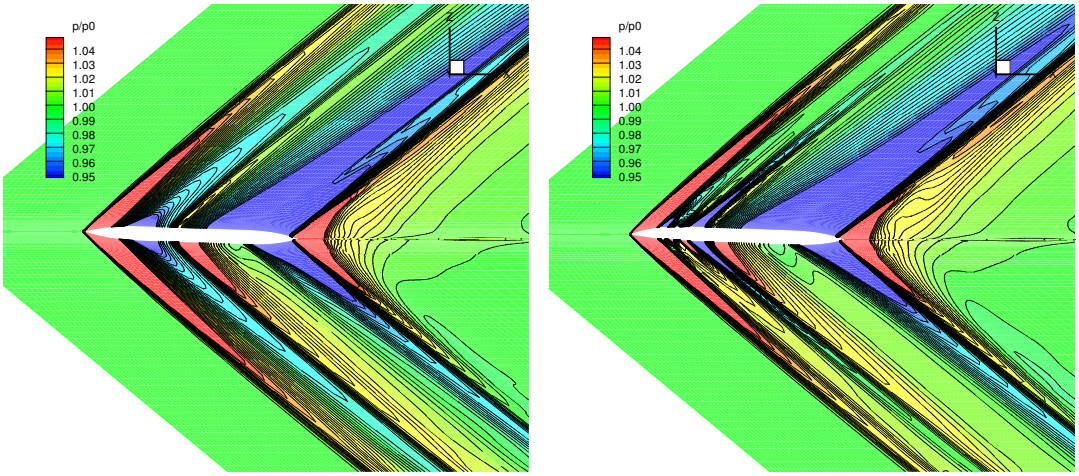

(a) Initial configuration.

(b) Optimized configuration.

Figure 5.20: Comparison between the near pressure field of the initial and optimized configurations.

duration is reduced (Figure 5.21b). The total signal length created by the low-boom configuration is 110 ms.

The tendency of the solution is to obtain a flat-top signature with an initial pressure rise followed by a

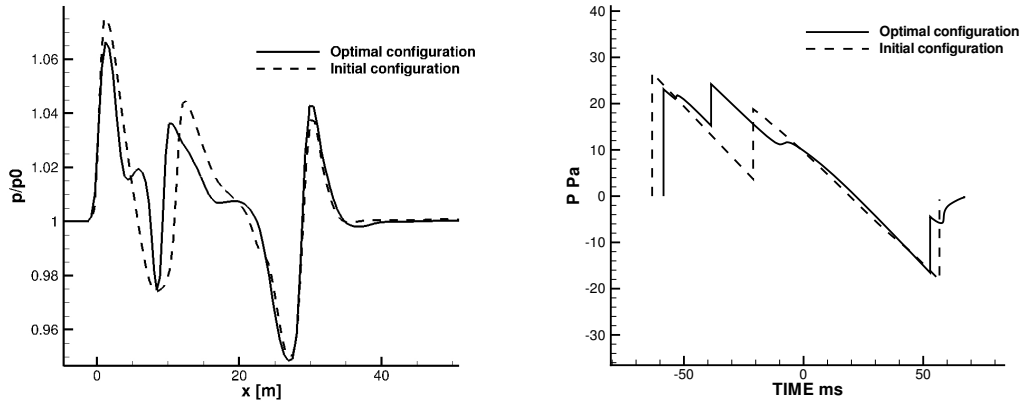

(a) Near-field signature ($h_z = h - 10$ m). (b) Ground sonic boom signature.

Figure 5.21: Acoustic under-track signatures.

pressure plateau. If the wing-fuselage junction will be designed to avoid the creation of a geometrical slope discontinuity (e.g. curvilinear leading edge), the flat-top signature can be achieved more easily.

Modification of the shock-expansion pattern in the aft part of signal are limited due to the lack of a corresponding fuselage parameterization. The rear shock reduction could be due to several aspects such as angle of attack modification, the wing planform shape, and in particular the increase of the dihedral angle. The low-boom configuration shows at ground a reduction of all the three shocks of the reference configuration signature.

5.5 Hybrid approach

Direct shape optimization requires a considerable amount of function evaluations to reach convergence, in particular when adopting a global optimization algorithm. Despite this, the approach can take into account different disciplines solving single or multi-objective optimizations. Furthermore it can provide the designer with a direct control on the configuration geometry.

The inverse design approach provides low-boom configurations in a limited amount of time, but experience and several counter-measures are required to overcome the method limitations. The main drawbacks already observed in chapter 4 are here summarized:

- introduction of another discipline in the design is not straight forward;
- identification of the geometrical area distribution that corresponds to the A_e distribution.

The idea is to combine the advantages of the two approaches for the identification of a low-boom configuration using an hybrid approach that takes inspiration from the physics.
Considering the reference flight conditions, if the wing is sufficiently far from the nose apex the two shocks do not coalesce during propagation. In this case the sole modifications of the fuselage nose geometry will shape and modify the front shock. As a consequence fuselage nose and wing design can be considered independently. We proceed in two phases. First, the fuselage nose is designed using the inverse design approach. The fuselage considered is an axi-symmetric body so that the identification of the geometrical area distribution that corresponds to A_e is relatively easy. Secondly, the wing is introduced in the shaped fuselage and a direct acoustic wing shape optimization is performed.

Fuselage nose inverse design and wing direct optimization

The inverse design of an axi-symmetric low-boom fuselage at zero incidence is first considered. The objective is to design a flat-top fuselage that generates a flat-top ground signature satisfying some

cabin volume constraints. The weight parameter W associated to a non-lifting configuration is taken equal to zero. Indeed, in this case equation (4.24) reduces to $A_e = A_{vol}^{fuse}$. The input values used in the

Variable	Value	Variable	Value
M	1.6	N	1
l	30 m (98.4 ft)	P	1
W	0 kg (0 lb)	t	0
B_*	0	η	0.5
y_f	2 m (6.56 m)	η_*	0
β_*	0		

Table 5.6: Input values for shaped nose.

module AIDA are summarized in Table 5.6, while the output of the module is shown in Figure 5.22 and summarized in Table 5.7. The ground signature shows the desired flat-top with an amplitude of only 14 Pa that is below the criteria fixed by the HISAC and the DARPA projects (see Table 2.7).

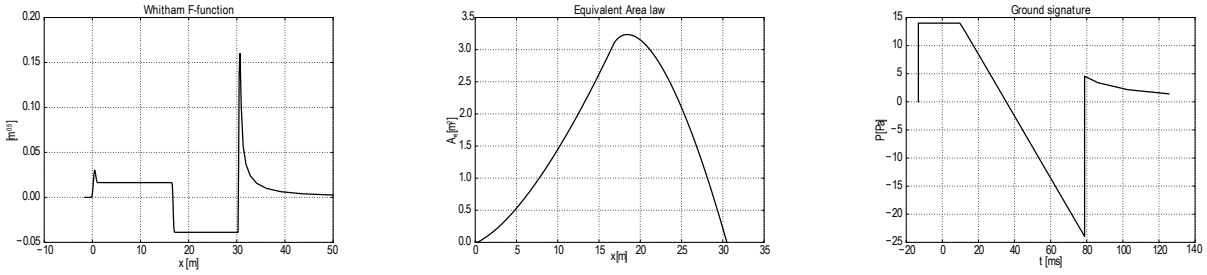

(a) (b) (c)

Figure 5.22: Flat-top configuration obtained using AIDA.

Variable	Value
H $[m^{0.5}]$	0.00743 (0.01345)
C $[m^{0.5}]$	0.00337 (0.0061)
D $[m^{0.5}]$	0.00795 (0.0144)
λ $[m]$	16.77 (55)
y_r $[m]$	32.93 (108)

Table 5.7: AIDA results for a flat-top signature. (Between brackets values in Imperial units).

The geometrical area distribution can be easily approximated by the equivalent area, due to the fact that the fuselage is a slender body of revolution so that:

$$A_g^{fuse}(x) \sim A_e(x) \tag{5.12}$$

One can directly use the equivalent area distribution for the definition of a shaped low-boom fuselage, but some problems arise if this strategy is pursued:

- no volume constraints are considered;
- the design of the middle and aft part of the fuselage will be impacted by the introduction of the wing.

For these reasons the idea is to design only the nose and keep the cabin fixed and equal to the one defined in chapter 3 for the reference initial configuration.

It is assumed that the first part of the signature, in this case the flat-top, is described by the F-function from 0 to λ. Looking at Figure 5.22b it can be seen that the equivalent area reaches its maximum at a distance λ from the nose and then decreases to satisfy the condition $A_e(L) = 0$. A new shaped nose configuration will be defined considering the distribution of the equivalent area solution of the generalized shaped sonic boom theory from 0 to λ to describe the nose, while the middle and the rear part will be described using the equivalent area distribution of the conventional fuselage. The expectation is to obtain a flat-top ground signature with the corresponding geometry that satisfies the cabin volume requirements.
The continuity between the two equivalent area distributions has to be assured. It is possible to scale

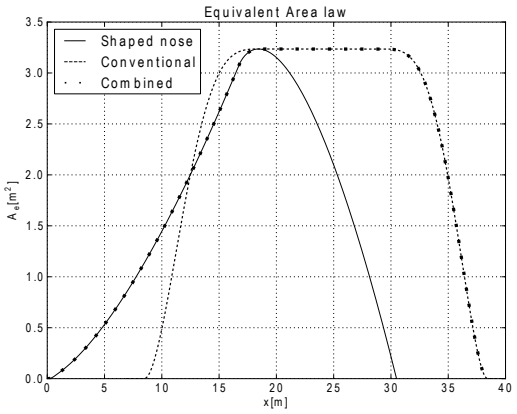

Figure 5.23: Equivalent area for a conventional fuselage with a shaped nose.

the A_e distribution using a scaling factor sf. The scaling factor $sf \in \mathbb{R}$ is defined as:

$$sf = \frac{A_e^C(x_c)}{A_e^S(\lambda)} \tag{5.13}$$

where S means shaped nose, C conventional fuselage and x_c is the beginning of the cabin for the conventional fuselage. This merging procedure determines an increase of the fuselage length of $\lambda - x_c$ with in general $\lambda > x_c$. Figure 5.23 shows the equivalent area distribution of the conventional fuselage with shaped nose: A_e^C describes the second part of the fuselage, while the nose is shaped by the A_e^S distribution obtained from the generalized shaped sonic boom theory. The fuselage with the shaped nose and the conventional one are shown in Figure 5.24. Figure 5.25 shows the ground signatures for the conventional and for the shaped nose fuselage. The shaped configuration shows the flat-top behavior as expected, with a reduction of the front shock overpressure of nearly 50% from 25.9 Pa to 14.2 Pa. Such a strong reduction may be influenced by the introduction of the wing.

In the second phase of the hybrid approach, a wing is added to the shaped fuselage (solution of the inverse design) and then optimized using the direct shape optimization to reduce its impact on the ground signature. The objective is to maintain the flat-top region of the ground signature obtained using the inverse design. The optimizer must be able to move and decrease the amplitude of the wing shock. The wing planform design variables set $\mathbf{x} \in \mathbb{R}^{11}$ is summarized in Table 5.8. Concerning nose deflection, the following relationship is adopted: $DV_9 = 0.15x_9$, because the reference value is equal to zero. The optimizer adopted is the modified CMA-ES and the optimization problem, based on the minimization of the sum of the shocks overpressure, is defined as in equation (5.11).
One could expect that due to the set of optimization variables that describes only the wing shape, the algorithm acts only on the reduction of the wing shock and the result is equivalent if adopting an objective function based only on the overpressure of the ground signature middle shock. In practice different shapes and positions of the wing may result not only in a different amplitude of the wing shock at ground, but also they could drive the coalescence or not with the front shock. In the hypothetical case that one adopt as objective function only the amplitude of the middle shock, if the leading edge shock melts with the front shock the optimizer converges to zero, but the result is a N-wave instead of the desired flat-top signature.

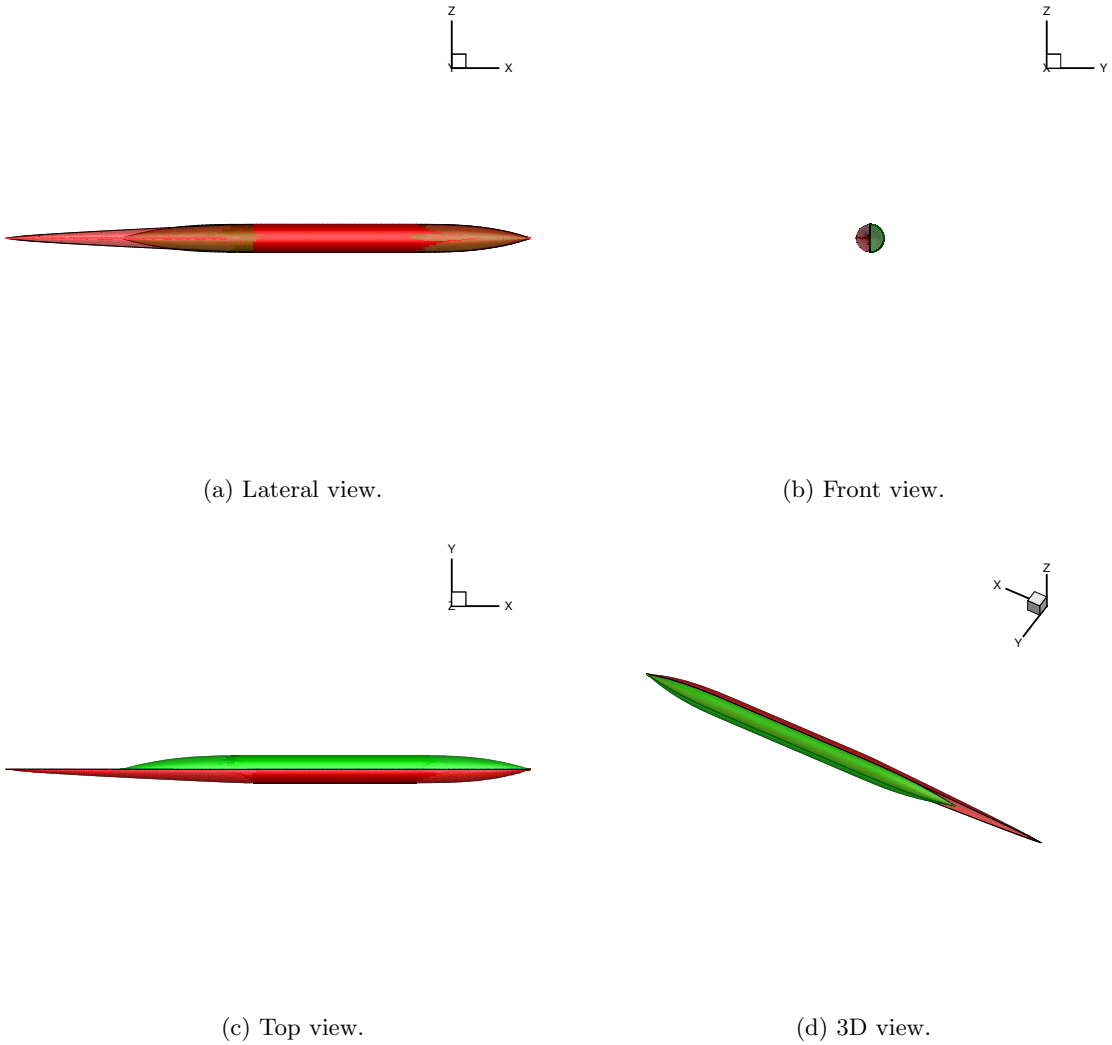

(a) Lateral view.

(b) Front view.

(c) Top view.

(d) 3D view.

Figure 5.24: Comparison between the conventional axi-symmetric fuselage (green) and the shaped nose fuselage (red).

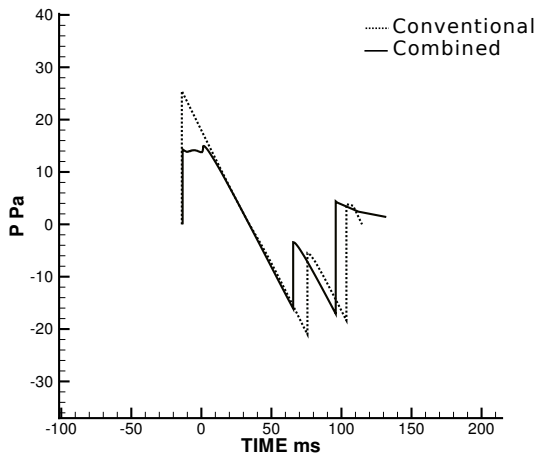

Figure 5.25: Under-track ground signatures; Comparison between the combined shaped nose fuselage and the conventional fuselage.

Variable	Specification	$\bar{DV}_i$	δ_i
x_1	wing root chord [m]	11.584	10%
x_2	wing crank chord [m]	6.430	10%
x_3	wing tip chord [m]	2.896	10%
x_4	crank position along wing span [adim]	0.31	10%
x_5	inner wing sweep angle [deg]	65	10%
x_6	outer wing sweep angle [deg]	56	10%
x_7	relative wing position [adim]	0.45	10%
x_8	aspect ratio [adim]	3	10%
x_9	nose deflection [deg]	0	-%
x_{10}	dihedral angle [deg]	3	100%
x_{11}	angle of attack [deg]	2	100%

Table 5.8: Design variables set definition for the wing optimization.

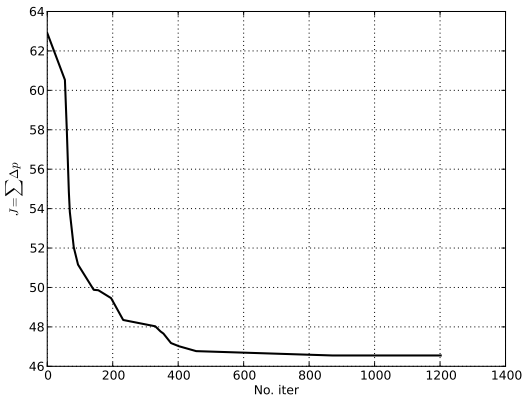

Figure 5.26: Objective function ($\sum \Delta p$) for the wing optimization adopting a shaped nose fuselage.

Figure 5.26 shows the history of the acoustic minimization: after 600 iterations the algorithm is almost converged with a reduction around 16 Pa. More interesting is the comparison between the initial geometry and the two configurations with the shaped nose: the first one with the conventional wing and the second one with the optimized wing.

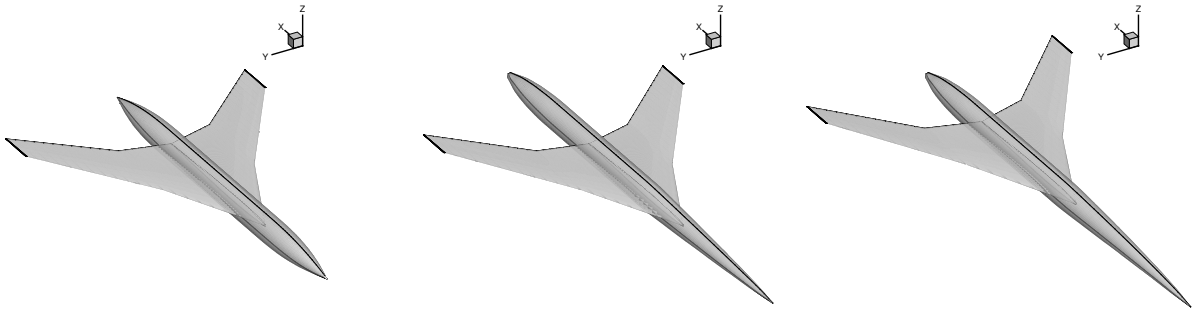

(a) Initial configuration with conventional fuselage.

(b) Initial configuration with shaped nose fuselage.

(c) Optimal configuration.

Figure 5.27: Comparison of geometries.

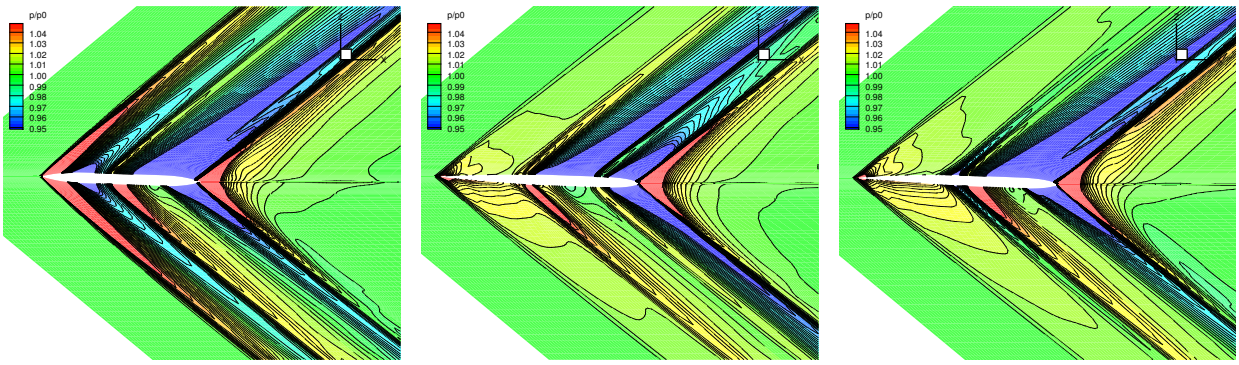

(a) Initial configuration with conventional fuselage.

(b) Initial configuration with shaped nose fuselage.

(c) Optimal configuration.

Figure 5.28: Comparison of the near field pressure (p/p_0) in the symmetry plan ($h = h_z - 10$ m).

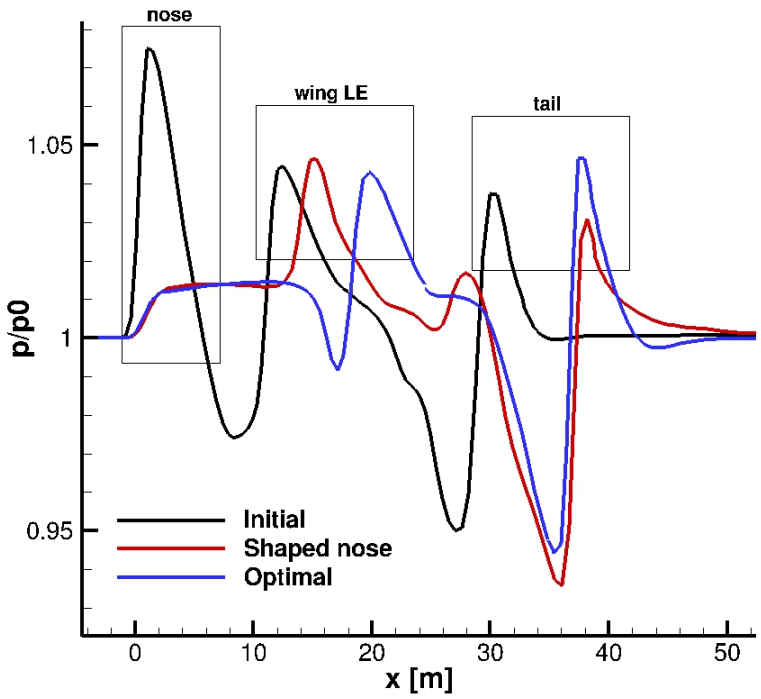

Figure 5.29: Comparison of the near-field signatures.

In Figure 5.27 and in Figure 5.28 are shown respectively the geometry and the near field pressure disturbance for the three configurations. The two shaped nose configurations show the same typical behavior in terms of near-field pressure in the nose region. The nose shock is strongly reduced and in the following nose region the isopressure curves are almost parallel to the fuselage main axis. This is the physical representation of what happens during the inverse design when it is required to impose the slope after the first peak of the F-function equal to zero in order to obtain the flat-top. This pressure plateau replaces the front shock in the near-field signature of the two shaped nose configurations (Figure 5.29). The near-field signatures obtained by the conventional and the optimal wing configuration show important differences, in particular in the wing region. The shaped-nose-conventional-wing configuration shows no expansion after the first shock as in the initial configuration, but another compression due to the leading edge of the wing. The optimizer acts to modify the shape preserving the expansion region before the wing and at the same time reducing the amplitude of the following shock (Figure 5.28c). Furthermore, the wing planform modifications have avoided a

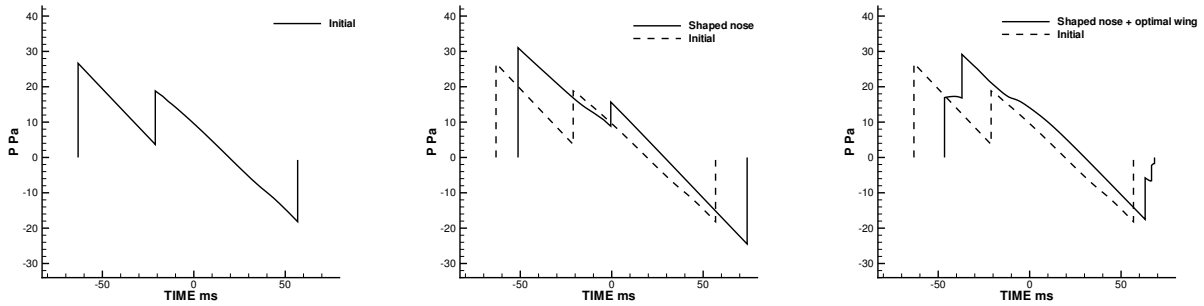

(a) Initial configuration with conventional fuselage.

(b) Initial configuration with shaped nose fuselage.

(c) Optimal configuration.

Figure 5.30: Ground signature.

secondary pressure peak in the wing region. This one appears in the shaped nose configuration with conventional wing due to the interactions between the wing trailing edge and the fuselage. The resulting ground signatures are shown in Figure 5.30. The optimal configuration reduces by almost one third the front shock overpressure of the reference configuration avoiding the wing shock coalescence shown in the shaped nose configuration with the conventional wing. The hybrid designed configuration (shown with the corresponding pressure field in Figure 5.31) produces at ground a flat-top followed by the wing shock which is independent from the front one (the distance is superior to 10 ms). The maximum pressure is comparable to that of the front shock for the initial configuration. In addition the optimal wing has also a beneficial effect on the aft shock that is slightly reduced with respect to the initial configuration.

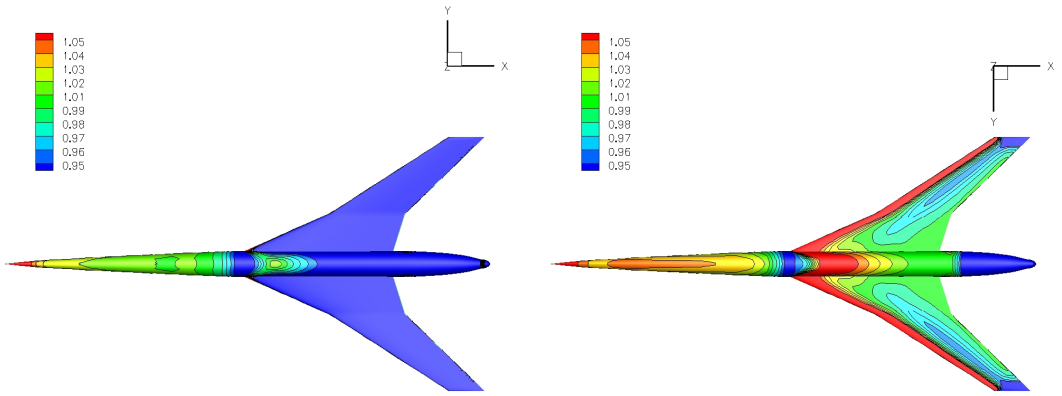

(a) Top.

(b) Bottom.

Figure 5.31: Pressure skin distribution (p/p_0) for the optimal configuration.

5.6 Conclusions

A complete optimization scenario has been defined and applied for the direct shape optimization of the wing-body SSBJ configuration. The shape optimization chain is a robust and versatile tool that can be adopted to solve both single and multi-objective optimizations. The scenario identified consists in an analytical mesh generation tool that completely regenerates the volume mesh at each optimization iteration. A modulable, effective design variables set directly related to aircraft shape parameters has

been selected. Due to the properties of the acoustic cost function, a modified version of the CMA-ES algorithm is associated to the mono-objective optimizations (under lift constraint).

Results obtained from the sensitivity analysis and the single-objective optimizations have shown that the low-boom (LB) configuration geometry shows several contrasting features compared to the low-drag (LD) configuration. The LB configuration shows a nose deflected downward so that the flow is deviated in the opposite direction thus reducing the wing front shock and variations of the nose curvature that produce several small amplitude shocks, while the LD configuration presents a nose directed upward that aims to increase the aerodynamic efficiency of the fuselage. At the same time both configurations show the forward displacement of the wing thus reducing the volume wave drag and at the same time preventing the coalescence of the wing shock with the nose one. The aerodynamic and the acoustic optimal configurations differ only by 2 drag counts and by more than 15 Pa. It is notable that the reference initial configuration has an aerodynamic cost function (J_{aero} = 89 drag count) already close to the optimality (J_{aero} = 88.4 drag count), but with a violation of the lift constraint. The initial configuration evaluated at constant lift coefficient of the optimal geometry results in 108.6 drag count.

A hybrid approach has provided a methodology to design low-boom configuration combining the inverse approach with shape optimization. Inverse design acts on the definition of a simple fuselage configuration, thus reducing the impact of the front shock overpressure, while the design of the wing is taken into account by numerical optimization. In this way the results of the inverse design can be preserved when the wing is introduced. The hybrid approach has permitted to reduce the front shock overpressure more than using the direct shape optimization and at the same time the fuselage cabin volume has been maintained. When the designer has a limited number of constraints on the configuration geometry it appears a valuable tool for the definition of an initial configuration. The method has succeeded to reduce the front shock more than the acoustic optimization, because of the limited number of design variables that describe the fuselage nose in the direct approach. A future extension consists in the coupling of the low-boom inverse design with the aerodynamic optimization of the wing. This represents a first extension of the acoustic optimization to consider aerodynamics.

Chapter 6

Multi-objective optimization strategies applied to the aero-acoustic problem

20 percent of focused effort results in 80 percent out come of results!
Vilfredo Pareto

Contents

An engineering design usually requires the analysis of a multi-physics/multi-objective problem. The design of a real aircraft in practice, always has to take into account several disciplines at the same time and results in a compromise solution. For example bi-plane wings were the concession of the aerodynamicist to the need of structural stiffness. Only after progress in materials and structural stiffness design of monoplanes with enough wing were built.

A systematic approach [107] is required in order to define an optimization scenario that takes into account different disciplines, constraints and variables. In aircraft shape design the common practice is to perform first an aerodynamic optimization which is considered a primary discipline. Then, if one is interested to optimize other disciplines such as structure, noise, range performance, fuel consumption

or others, the solution usually adopted is a single-discipline, sequential (or not in the case of function scalarization) analysis. Generally optimizing a particular solution with respect to a single objective can result in unacceptable results with respect to the other objectives. It is when more than one discipline is considered in the design, that shape optimization techniques could introduce a significant advantage with respect to traditional engineering design strategies providing a set of optimal solutions. Two are the main objectives of this chapter:

- to define a trade-off between low-drag and low-boom configurations;
- to adopt innovative algorithms in the aero-acoustic shape optimization problem.

In the first part of the chapter multi-objective optimization is introduced as well as a literature short survey on the aero-acoustic multi-disciplinary problem. The second part investigates different algorithms from the most traditional approach based on the scalarization of the cost functions to evolutionary based algorithm. In the last part we analyze more innovative algorithms based on cooperation and competition that will be finally adopted for the exploration of the complete set of optimal solutions.

6.1 Multi-disciplinary optimization

Multi-disciplinary optimization (MDO) is the study of the application of numerical optimization techniques to the design of engineering systems involving multiple disciplines or components [107]. If the multi-disciplinarity occurs at the analysis level, like structural optimization of an aircraft wing to prevent flutter, the optimization problem is not considered multi-disciplinary [108]. The terms multi-disciplinary and multi-objective optimization are used in this work with the same meaning: an optimization problem that takes into account more than one criterion, at least one for each discipline considered. A minimization multi-objective problem is defined as follows:

Definition 6.1.1 *Given a design variable set* $\mathbf{x} \in \mathbb{R}^n$*, find a vector* $\mathbf{x}^\star$ *that minimizes a set of objective functions* $\boldsymbol{J} \in \mathbb{R}^N$*. Usually the solution is restricted to satisfy* K *constraints* $g_k(\mathbf{x})$*.*

A multi-objective problem involves inseparable objectives and does not result in a unique optimum, but a set of compromised individuals known as Pareto optimal solutions.

Definition 6.1.2 *A point* $\mathbf{x}^\star$ *is Pareto optimal if there does not exist another point* $\mathbf{x}$ *such that* $\boldsymbol{J}(\mathbf{x}) \leq \mathbf{J}(\mathbf{x}^\star)$ *and* $J_i(\mathbf{x}) < J_i(\mathbf{x}^\star)$ *for at least one function. For any problem there may be an infinite number of Pareto optimal points that define the Pareto optimal set. Any point* $\mathbf{x}^\star$ *that belongs to the Pareto set dominates any other point* $\mathbf{x}$ *(that does not belong to the Pareto set) in the solution space* $(\mathbf{x}^\star \succ \mathbf{x})$*. The image of the Pareto set in the function space is referred as the Pareto front.*

The optimization scenario has to be able to affect more than one discipline, taking into account the interactions between them. Different algorithms are available in the literature and several surveys propose an overview of the different methods [109],[110]. It is possible to classify multi-objective algorithms according to the optimizer (gradient based or not), the cost function (scalar or vector), or the preference articulation. As in the case of single-objective optimization, gradient based and genetic algorithms exist for the solution of multi-objective problems. On one hand gradient based algorithms aim at the identification of a common descent direction for all the criteria. Indeed, the antagonism between the different objectives cannot prevent to use cooperation to simultaneously optimize each cost function. This is the main idea of the Multiple Gradient Descent Algorithm developed by Désidéri in [111]. It is a natural extension of the steepest-descent method for multiple discipline optimization using a descent direction common to all the objectives. Gradient based algorithms in general provide a single solution that belongs to the Pareto front. On the other hand, multi-objective evolutionary algorithms are based on the identification of non-dominated set of solutions that defines a Pareto front as accurately as possible. The size of the non-dominated set is not known *a priori*, and it can be extremely variable ranging from zero to infinity so that the entire identification is practically impossible. They differ from traditional single-objective algorithms by using particular fitness functions

and promoting individual diversity. Multi-objective algorithms based on evolutionary strategies have acquired a wide diffusion because of their ability to capture a set of distributed solutions on the Pareto front [112], [113]. This is the result of the population based mechanisms that distinguish this category of algorithms. In addition these algorithms are very robust, they are less sensitive to the shape and continuity of the Pareto front [114]. For these reasons, actually some 70% of the approaches to multi-objective problems are based on evolutionary strategies [115].

Considering the objective functions, it is possible to discriminate algorithms that consider scalar cost functions from others that adopt vector cost functions. To the first category belong algorithms where one searches to optimize a single functional agglomerating all the other objectives. The scalarization reduces a multi-objective problem to a single-objective one. In this way any multi-objective algorithm can be adopted to solve the scalarized problem. As for gradient-based algorithms, scalar multi-objective optimizations are in general able to identify only one point that belongs to the Pareto front. Vector cost functions are adopted by optimization algorithms able to consider independently the contribution of each discipline (e.g. multi-objective GA).

Preferences are defined as decision-maker's opinions concerning points in the criterion space. Indeed, MDO is not a "push-button" design, human interface is important to inject judgment and creativity into the process. Multi-objective algorithms generally belong to three categories if preferences are used as discrimination factor:

- *a priori* articulation of preferences, in which the user indicates the relative importance of the objectives before performing the optimization (e.g. the weight of each cost function in the weighted sum approach);
- *a posteriori* articulation, made after the optimization. Solutions are selected from a set (e.g. non dominated solutions obtained using multi-objective genetic algorithms);
- progressive articulation provided during the optimization (efficient technique adopted to the solution of many-objectives optimization problems [116]). Preferences may change along the optimization due to some user-defined criteria.

The most adopted algorithms for bi-objective optimizations are based on the first two categories of preferences. With the *a priori* articulation the decision-maker has to express his decision before the optimization process so he needs to quantify the preference. The setting of this kind of parameter is not an easy task, some preliminary experience on the problem is in fact required. The main advantage is that the *a priori* preferences definition is CPU time efficient due to the fact that one wants a single solution. On the contrary, algorithms based on *a posteriori* decision typically provide a Pareto set of solutions. It is up to the designer at the end to identify his optimal solution among the Pareto-optimal solutions.

The computational cost required to solve a MDO problem is generally higher than a classical single discipline problem. A compromise between the accuracy of the cost function prediction and computational cost has to be achieved. For this reason, multi-disciplinary shape optimization problems are usually coupled with low-fidelity surrogate models and occasionally with mixed low-high fidelity models.

6.2 Trade-off between aerodynamic performance and sonic boom

In chapters 4 and 5, aerodynamics and acoustics have been analyzed independently, but in the definition of a feasible SSBJ configuration, due to their strong interaction, they must be considered together since the initial design phases. The antagonism between sonic boom and drag reduction is a well-known fact. Indeed the definition of a low-boom/low-drag configuration is a paradox [117]. A low-boom configuration generally presents a blunt nose, the F-function has a Dirac's δ at the nose that corresponds to an equivalent area with infinite slope at the nose. This result in a configuration penalized in terms of drag, in particular the volume wave drag undergoes a severe increase. On the contrary a supersonic low-drag configuration generally presents a sharp nose with the shock attached at the nose. Paradoxically in the near-field the low-drag configuration has several weaker shocks instead of

a stronger shock that occurs when considering the low-boom configuration. During the propagation the weak shocks of the sharp nose configuration tend to coalesce thus producing a stronger shock at ground. In general this configuration shows the typical N-wave. Concerning the low-boom configuration, no further shocks are created by coalescence so that during the propagation the shock amplitudes reduces. The mono-disciplinary analysis performed in chapter 4 have shown that the two optimal configurations for aerodynamics and acoustics show different geometry not only at the nose, but also in the wing region.

Over the years, several multi-objective optimizations have analyzed the solution of the aero-acoustic problem for boom and drag reduction, some of them are summarized in Table 6.1. Models, parameterizations and optimization methods have evolved together throughout the years. The simplest method that does not take into account any optimization algorithm, but only the engineer experience, is based on the design of experiments, where a database of different configurations is analyzed and the best configuration selected [122]. Optimization algorithms based on aggregating cost function have been introduced together with the analysis of more complex configurations with a limited amount of design variables ([123], [126]). When a vector objective function is considered adopting more sophisticated multi-objective algorithms, two are the solutions that have been considered to reduce the total computational time: to use low-fidelity surrogate models for each discipline ([125], [118], [120]) or to consider only single aspect of the geometry (e.g. wing optimization [119], [24]).

Recently, the tendency is to adopt multi-fidelity methods, where the multi-objective algorithm acts on the surrogate models and then the solution is re-evaluated using the high-fidelity models. In some cases ([118],[24]) some of the solutions are used to build a new low-fidelity model so improving progressively its accuracy. Nevertheless this technique can introduce oscillations in the surrogate model if too localized solutions are injected. Adjoint strategies have also been adopted to investigate the aero-acoustic problem ([124], [87]), but several additional developments are still required to generalize the formulation.

Some of the studies have more than two objectives. In Sato [118] a three-objective shape optimization problem is analyzed where sonic-boom is evaluated by two functions: the front shock and the rear shock amplitude. The choice is motivated by the fact that in general it is possible to shape the front shock, but it is hard to reduce the rear shock. The optimization result shows that the two sonic-boom objectives cooperate. In fact, if one wants to reduce the front shock, the rear shock is not increased because the two phenomena are produced by two different regions of the aircraft.

Structure represents another important discipline that has been introduced in the low-boom/low-drag trade off in the study of a supersonic wing [24]. As already outlined, the design of a supersonic business jet is necessary multi-point due to the difference between the flight in the supersonic and in the subsonic regime. Chiba et al. [119] consider at the same time aerodynamics in the subsonic and supersonic regime, structures and boom noise using high-fidelity models. This is the most complex study that has been found in literature that brings together a multi-disciplinary, multi-point shape optimization with an innovative hybrid multi-objective algorithm. Despite these aspects, the optimization considers only modifications of the wing-shape. As outlined in a recent survey [4], MDO using high fidelity models for each discipline, considering complete configurations and advanced and/or innovative multi-objective optimization algorithms for the solution of the low-drag/low-boom problem has never been performed. The following sections will introduce new insights to this problem.

6.3 Weighted sum approach

The weighted sum approach (WSA) is a special case of the global criterion method [127], where all the objective functions are combined in order to define a scalar global cost function. Despite deficiencies in the definition of the Pareto set, the weighted sum method for multi-objective optimization is extensively adopted because of its simplicity and because the result at convergence belongs to the non-dominated set. Zadeh demonstrates in [128] that using a global cost function it is possible to define a Pareto optimal point towards the simultaneous reduction of all the criteria. The main problem consists in the definition of the weights that do not have any physical meaning. In [109] there is a complete overview of the different methods to define the weights and an analysis of the impact on the

Study	Objectives	Algorithm	DVs	Model
Two engine SSBJ (Sato [118])	$J_A = C_D$,$g : C_L$,$J_B = \Delta p$,$J_C = \Delta p$	MOGA	< 20	Kriging
Supersonic wing (Seto [24])	$J_A = -e$,target C_L, $J_B = p_{max} - p_{min}$,$J_C = W$	MOGA	14	Kriging
SSBJ (Choi et al. [23])	$J_A = C_D$,$J_B = dBA$	Nealder-Mead simplex	17	Quadratic fit
S^3TD wing(Chiba et al. [119])	$J_A = C_p@M > 1$, $J_B = C_f@M > 1$, $J_C = I_b@M > 1$ $J_D = W@M < 1$, $J_E = -C_L@M < 1$	Hybrid MO-PSO ARMOGA	58	High fidelity
SSBJ (Chung et al.[120])	$J_A = C_D$,$g : C_L$,$J_B = \Delta p_{init}$	MOGA	15	Kriging
SSBJ (Rallabhandi et al.[121])	$J_A = -e$,$g : geometry, volume$,$J_B = PLdB$	NSGA-II	> 31	Whitham
Delta wing (Khasdeo et al.[122])	$J_A = -e$,$J_B = \Delta p_{init}$	Design of experiments	4	High fidelity
HSST (Chattopadhyay et al.[123])	$J_A = -e$,$g : C_L, geometry$,$J_B = \Delta p_{1+}$,$J_C = \Delta p_{2+}$	Function aggregation and gradient based alg.	6	High fidelity
Wing profile (Nadarayah et al. [124])	$J_A = C_D$,$g : C_L$,$J_B =$target p	Adjoint	-	High fidelity
SSBJ (Chan [125])	$J_A = D$,$J_B = dBA$	MOGA	11	Low-fidelity
SSBJ (Chan [125])	$J_A = D$,$J_B = max\Delta p$	MOGA	11	Low-fidelity
Fuselage (Chan [125])	$J_A = D$,$J_B = max\Delta p$	MOGA	12	Low-fidelity
SSBJ (Vazquez [126])	$J_A = C_d$,$J_B = C_L$,J_C target p	Function aggregation and gradient based alg.	11	High-fidelity
SSBJ (Palacios [87])	$J_A =$target A_e,$g : C_L$	Adjoint	-	High fidelity

Table 6.1: Multi-disciplinary studies related to the mitigation of the sonic boom and the improvement of the aerodynamic performance.

solution. In the weighted sum method a composite scalar objective function is defined as:

$$J_U = \sum_{i=1}^{n} w_i J_i(\mathbf{x}) \tag{6.1}$$

If all the weights are positive, then the minimization of equation (6.1) is a sufficient condition for Pareto optimality. In addition, generally $\sum_{i=1}^{n} w_i = 1$. The relative value of the weights reflects the relative importance of the objectives made *a priori* by the designer. To prevent that one objective dominates the others, the first step is to transform each cost function as:

$$\bar{J}_i = \frac{J_i}{J_i^o} \tag{6.2}$$

For a two-objective problem, the WSA cost function is then defined as:

$$J_U = \alpha_1 \bar{J}_1 + \alpha_2 \bar{J}_2 \tag{6.3}$$

Simple and easy to use, the weighted sum method is a benchmark for the other methods. Varying weights continuously may not necessarily result in a complete representation of the Pareto set [129]. Well known is the clustering phenomenon in some region of the Pareto set and the problems related to the presence of non convex part of the front. The method is not able to determine non-convex region of the Pareto front. Furthermore, it is quite impossible to know correct weights needed to generate particular points on the Pareto curve without knowing the shape of the curve itself.

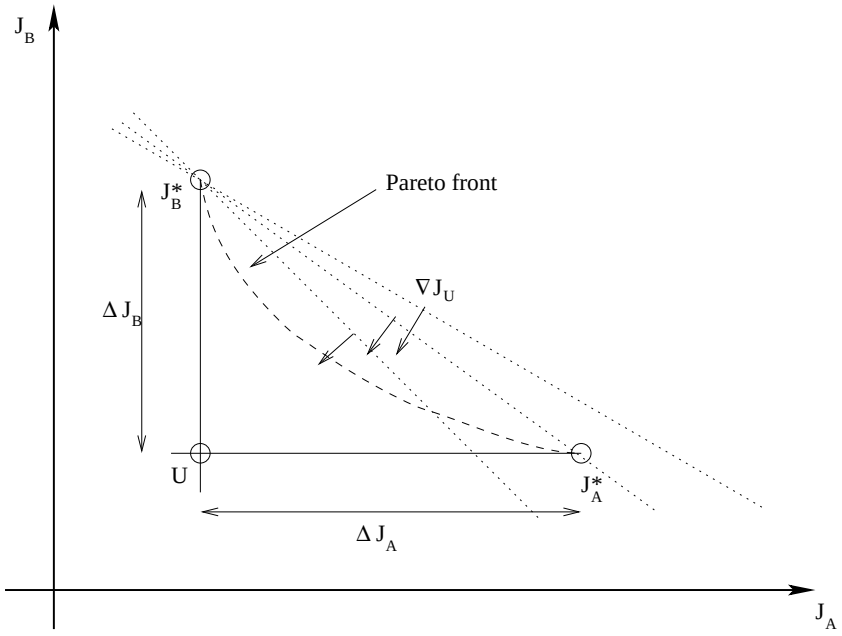

Figure 6.1: Descent directions for the adaptive weighted sum method.

Weights represent the gradient of the agglomerated cost function J_U:

$$\nabla J_U \left\{ \begin{array}{rcl} \frac{\partial J_U}{\partial J_1} & = & \alpha_1 \\ \frac{\partial J_U}{\partial J_2} & = & \alpha_2 \end{array} \right.$$

The slope of the Pareto front shown in Figure 6.1 is defined as:

$$\frac{dJ_2}{dJ_1} \simeq \frac{\Delta J_2}{\Delta J_1} = -\frac{\alpha_1}{\alpha_2} \tag{6.4}$$

where ΔJ is considered as the distance between the point considered and the utopia point U_J.

Definition 6.4 *The utopia point U_J is in general an unfeasible point that corresponds to the minimum of all the objective functions.*

If the mono-disciplinary minima are known the weights can be evaluated using:

$$\begin{array}{rcl} \Delta J_1 & = & J_1(\mathbf{x}_2^\star) - J_1(U_J) \\ \Delta J_2 & = & J_2(\mathbf{x}_1^\star) - J_2(U_J) \end{array} \tag{6.5}$$

Generally J_1 is considered as the reference function so that $\alpha_1 = 1$, and the descent direction is defined changing α_2. To analyze the weighted sum approach, the test case proposed in [109] is here analyzed.

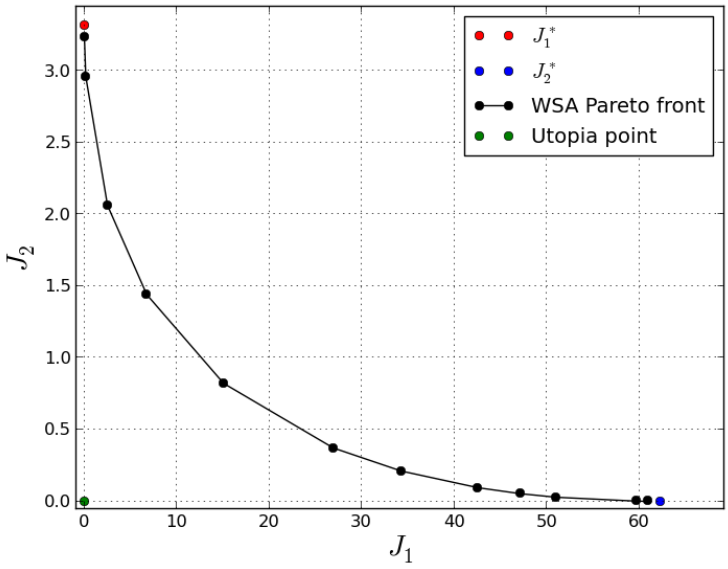

Figure 6.2: Pareto front of the analytic problem obtained using the WSA approach.

The problem consists in the minimization of the following objectives:

$$\left\{ \begin{array}{rcl} J_1(\mathbf{x}) & = & 20(x-0.75)^2 + (2y-2)^2 \\ J_2(\mathbf{x}) & = & (x-2.5)^2 + (y-1.5)^2 \end{array} \right. \tag{6.6}$$

The minima of J_1 and J_2 are both equal to zero, so that the utopia point is located at $U = (0, 0)$. If α_1 is fixed at 1, as α_2 tends to zero the non dominated solutions are located in proximity to the J_1 minimum, while if the weight α_2 tends to infinity the solutions obtained are in proximity of the J_2 minimum.

Application of the weighted sum approach to the aero-acoustic problem

This method has been adopted to perform an aero-acoustic shape optimization of a SSBJ fuselage and reported in Minelli et al. [130]. The same procedure is performed here considering the reference wing-body configuration. The aero-acoustic shape optimization problem can be stated as follows:

$$\text{Minimize} \left\{ \begin{array}{lll} J_1(\mathbf{x}) = c_D & \text{subject to :} & g : c_L - c_{L_0} \geq 0 \quad \text{with } c_{L_0} = 0.116 \\ J_2(\mathbf{x}) = \sum \Delta p & \text{subject to :} & \text{no constraints} \end{array} \right. \tag{6.7}$$

so that the WSA cost function is defined as:

$$J_U = \alpha_1 \bar{J}_1 + \alpha_2 \bar{J}_2 \tag{6.8}$$

J_1 and J_2 are normalized respectively by 100 dc and 60 Pa. From the results of single-discipline optimization, the utopia point considered is $U = (88, 44)$. This value is associated to the mono-disciplinary optimizations presented in chapter 5. The mono-disciplinary problems represent particular

cases of the WSA approach. Indeed taking α_1 equal to 1, $\alpha_2 = 0$ is associated to the aerodynamic optimization while if $\alpha_1 = 0$ and $\alpha_2 = 1$ the problem solution tends to the acoustic optimum. The two solutions represent extreme points of the Pareto front.

Considering $\alpha_2 = 1$ two non-dominated solutions are added to the Pareto front discretization taking $\alpha_1 = 1$ and $\alpha_1 = 0.5$ that, as demonstrated by the results, assure the description of different Pareto front regions. The different problems considered are summarized in Table 6.2. This approach

Configuration	α_1	α_2	Specification
A	1	0	Low-drag
B	1	1	Trade-off 1
C	0.5	1	Trade-off 2
D	0	1	Low-boom

Table 6.2: Optimization problems considered in the WSA.

requires the complete convergence of the minimization problem for each combination of cost function weights and as a consequence it results in a computationally expensive approach as shown in Figure 6.3. The Pareto front obtained with two mono-disciplinary problems and with the two additional

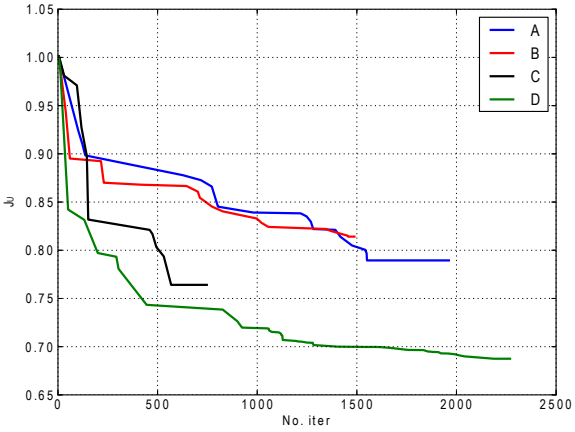

Figure 6.3: Convergence history for different J_U. The curves are normalized with respect to the initial value of each cost function.

solutions of the WSA approach is shown in Figure 6.4. The two trade-off solutions differ by 2 drag counts and about 4 Pa. The solution B favors the reduction of drag as a contrast to solution C that has a smaller α_1 and emphasizes the reduction of the sonic boom performance.

Figure 6.5 shows the symmetry plane near-field pressure of the two trade-off configurations, while Figure 6.6 shows the comparison of the near and far-field signature for the different configurations. Configuration B is associated to a near field signature close to the one obtained for the low-drag configuration A. A reduced near-field first peak area determines a reduction of the front shock overpressure at ground with respect to configuration A. Furthermore also the wing and the rear shocks generated by configuration B are reduced. Considering the near-field pressure of configuration C, a shock is created just before the wing due to nose curvature. The main difference between configurations C and D occurs at the wing region where the shock amplitude is increased by some 2 Pa.

Despite the easiness of its implementation, the computational cost of this approach appears too important if one wants several non dominated solutions. Furthermore, it illustrates the difficulty to choose *apriori* the right α coefficients when a particular region of the Pareto front is targeted.

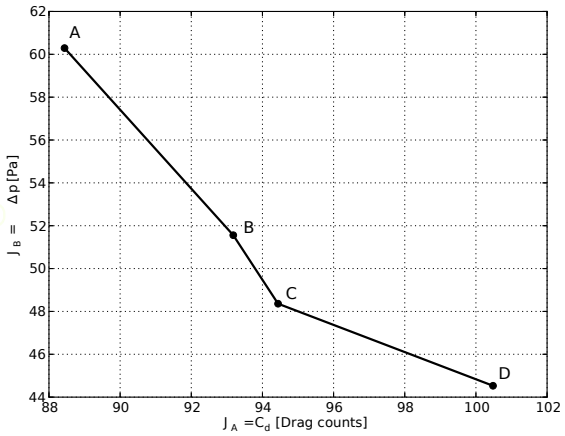

Figure 6.4: Pareto front obtained using the weighted sum approach.

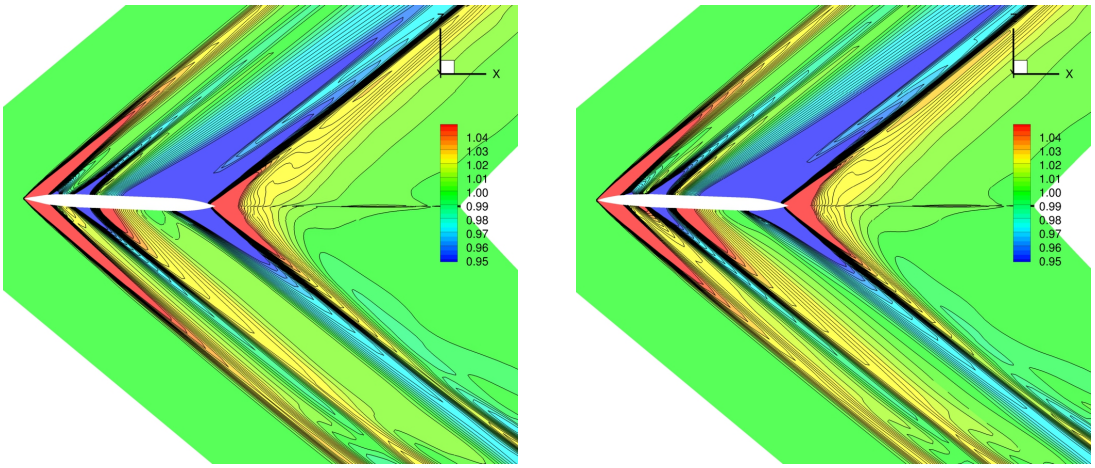

(a) Configuration B. (b) Configuration C.

Figure 6.5: Symmetry plane near-field pressure.

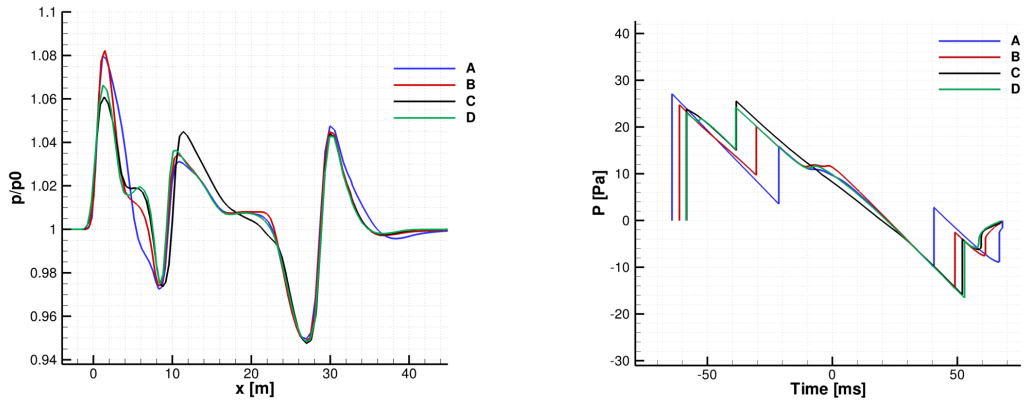

(a) Near-field signature ($h_z = h - 10$ m). (b) Ground signature.

Figure 6.6: Acoustic signature of the non-dominated solutions obtained using the weighted sum approach.

6.5 NSGA-II

A discretization of the Pareto front using the WSA requires at least a number of optimizations with different weights equal to the number of the desired points on the front. A direct extension is the WBGA-MO algorithm proposed by Hayela et al. [131]. In the WBGA-MO algorithm (Weight Based Genetic Algorithm - Multi Objective) the weight vector is embedded in the design variables that define an individual. Therefore multiple solutions can be obtained in a single run, but problems with non-convex fronts still persist.
Vector cost functions can be treated by multi-objective genetic algorithms. Genetic algorithms already in the case of mono-objective optimization work with a population of individuals, their extension to multi-objective problems can thus easily provide multiple solutions on the Pareto set in a single run. Indeed the population evolves toward a non-dominated set. Among the available algorithms (SPEA-II [132], DMOEA [133], PESA-II [134], PAES [135], RDGA [136], NPGA [137], MOGA [138], VEGA [139],...), NSGA-II [140] has been tested on several academical and industrial test case and represents today the state-of-the-art of the multi-objective genetic algorithms due to its efficiency and fast convergence [115]. The NSGA-II algorithm description and implementation in an in-house Python version as well as its application to analytical test cases are presented and analyzed in details in appendix C.

Application of NSGA-II to the aero-acoustic problem

NSGA-II is applied here to solve the aero-acoustic shape optimization problem using high-fidelity models. The optimization scenario adopted in the previous section, with the exception of the optimization algorithm, is here adopted: the problem is stated in equation (6.7), while the 18 design variables are summarized in Table 5.3. Ten generations of the algorithm are performed considering a population made up of 24 individuals. After 240 individual evaluations, the Pareto optimal set composed of 27

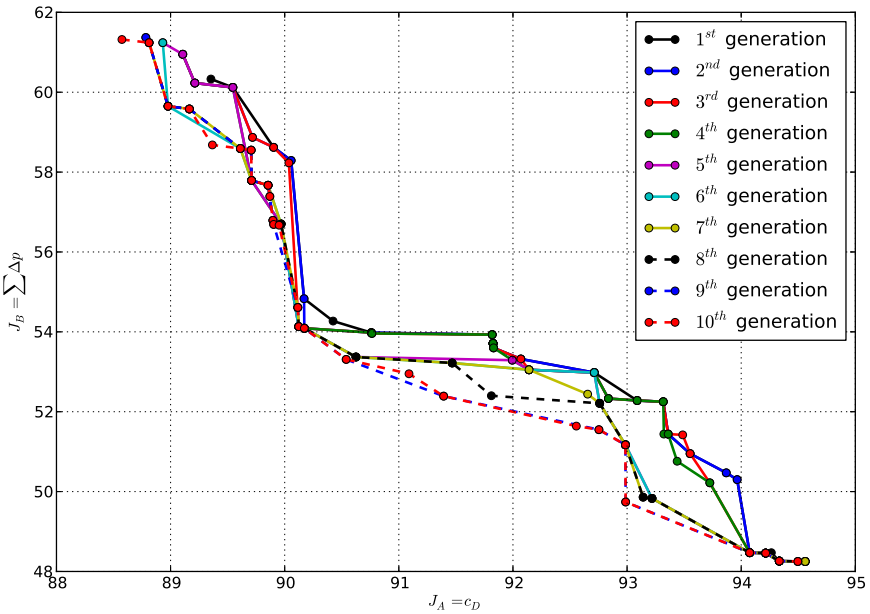

Figure 6.7: History of the non-dominated set during ten generations.

solutions is shown in Figure 6.7. The set of ndividuals shows a considerable diversity, drag ranges from 88 to 94 drag counts, while the sonic boom performance ranges from 48 to 61 Pa. Since the first generation the algorithm is able to obtain a Pareto set that is close to the final one showing a considerable diversity among individuals. The extreme individuals of the front with a reduce drag are

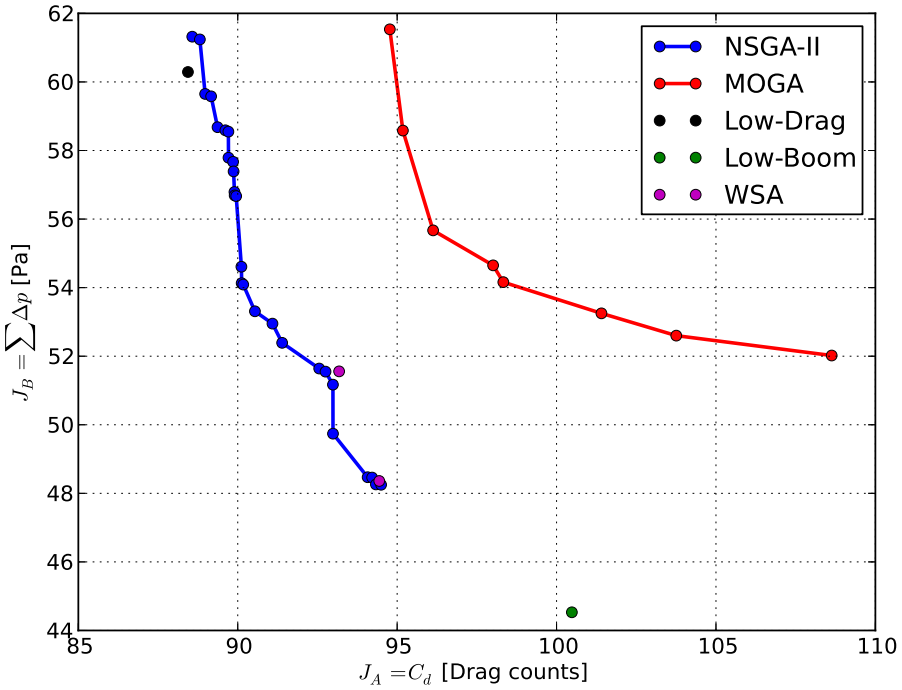

Figure 6.8: Comparison between the Pareto front obtained using NSGA-II, the one obtained using MOGA, the WSA trade-off solutions and the mono-disciplinary optimizations.

in proximity of the minimum obtained in chapter 5 for the aerodynamic optimization. This is due to the strategy of NSGA-II that favors the exploration of the extreme parts of the Pareto front giving to those individuals a better fitness (crowding distance equal to infinity).

To compare the performance of NSGA-II with other multi-objective algorithms, the optimization has been performed also adopting the algorithm MOGA [138] implemented in Dakota. The front obtained with NSGA-II completely dominates the MOGA front (see Figure 6.8) despite the fact that some 2000 function evaluations are performed (8 times more than the iterations required by NSGA-II). NSGA-II is able to reduce drag with more efficiency satisfying the lift constraint. For an equal level of the acoustic cost function NSGA-II non-dominated solutions have a drag at least 5 count less than MOGA solutions.

Three configurations that belong to different regions of the non-dominated set, have been selected for further analysis. Their performance are summarized in Table 6.3. All the three configurations

Configuration	J_A [dc]	J_B[Pa]	$g = c_L - c_{L_0} \geq 0$
A	94.5	48.25	0.0012
B	88.58	61.32	0
C	89.96	56.67	0.0008

Table 6.3: Selected configurations on the NSGA-II Pareto front. Individual A is a lowest-boom configuration, B is a lowest-drag configuration, while C is a compromise solution.

satisfy the lift constraint with a positive margin. The only exception is the low-drag configuration that activates the constraint. The main geometrical differences between the three configurations occur in the wing planform (see Figure 6.9). The low-boom configuration (A) shows a reduced out-wing sweep angle and a trailing edge that does not show discontinuity at crank. Two are the main consequences: the wing leading edge shock is increased (see Figures 6.10 and 6.11) and the flow expansion that occurs downstream is reduced in amplitude. The increase of the shocks in the near-field has beneficial effects

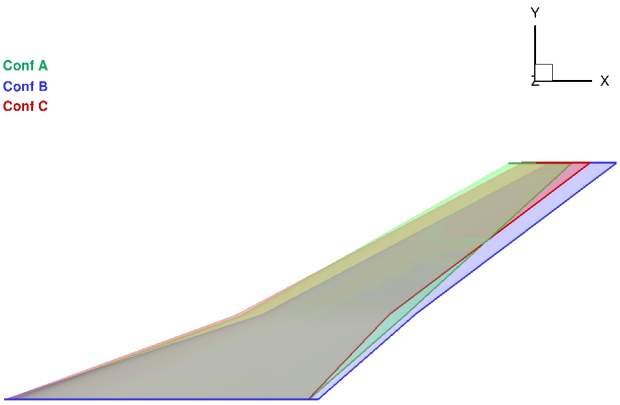

Figure 6.9: Wing planform shape modifications for the non-dominated solutions.

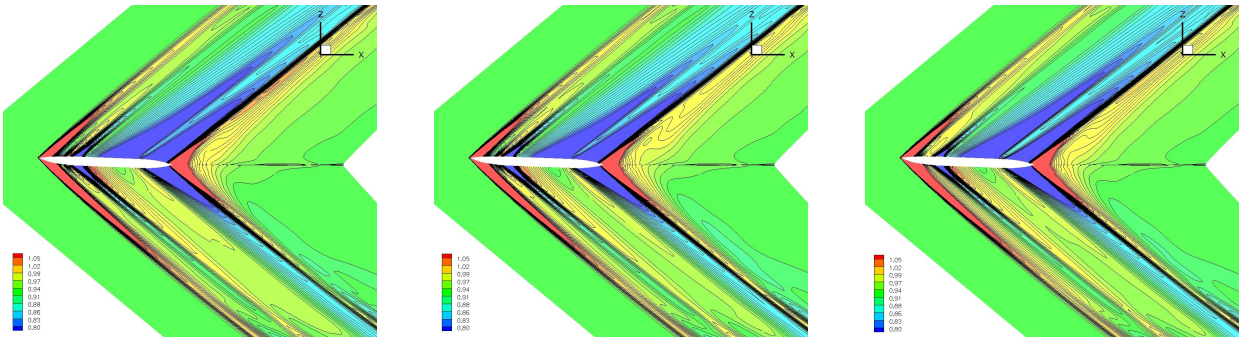

(a) Configuration A. (b) Configuration B. (c) Configuration C.

Figure 6.10: Symmetry plane near-field pressure.

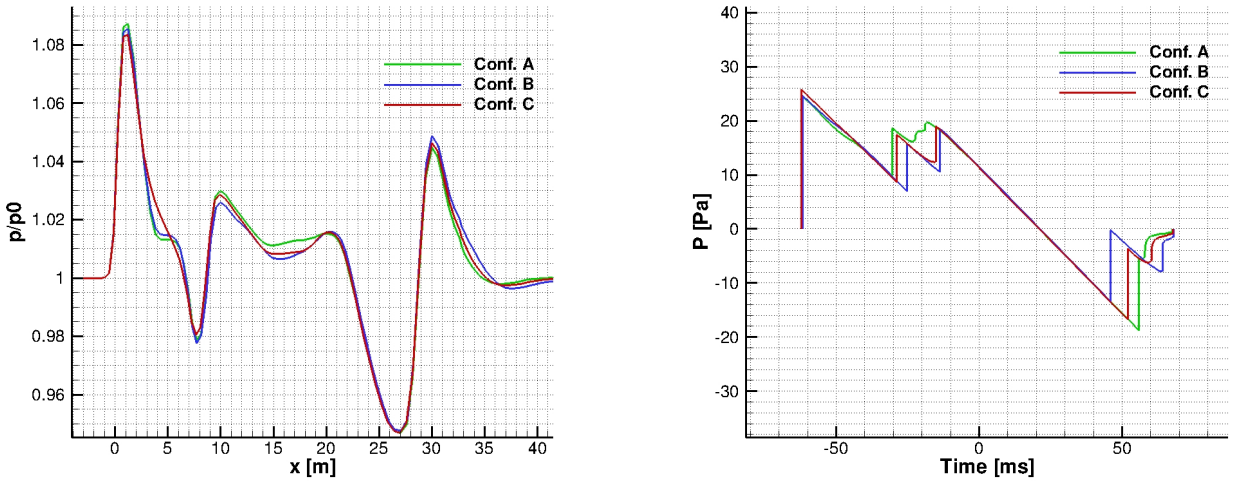

Figure 6.11: Under-track near field ($h_z = 10$ m) and ground pressure signature.

on the ground signature. Indeed the expansion after the nose shock is reduced and so the following wing leading edge shock overpressure. The second shock related to the wing is also strongly reduced and splitted in two small shocks. The low-drag configuration (B) shows larger values of the root chord and sweep angles compared to the other two configurations. This configuration results in a reduction of the maximum pressure peak achieved by the wing shock and, as already shown in the sensitivity analysis, the increased sweep angles determine a sensible reduction of the drag coefficient. The wing generates at ground two shocks with similar amplitude. Two are the shocks that distinguish also the aft part of the ground signature, thus resulting in a strong deterioration of the sonic boom performance of this configuration. The compromise solution (C) presents a leading edge similar to the one of the low-boom configuration thus resulting in a similar wing leading edge shock in the near-field and at ground. Geometry shows more differences in the outward wing with respect to configuration A. The crank chord is reduced and at the same time the tip chord is increased. The outward trailing edge results similar to the one of the low-drag configuration. Indeed it shows the same sweep angle. This similarity results in a second wing shock that presents nearly the same amplitude to the one produced by configuration B.

NSGA-II is demonstrated to be effective in the identification of the Pareto front outperforming the majority of the other multi-objective algorithms.

6.6 Cooperation and competition strategies

Competition and cooperation are two natural laws that regulate several aspects of nature, economy, human society, ... As already performed for genetic algorithm, ant-colony, simulated annealing, etc., optimization algorithms take inspiration from natural law. In this section competition and cooperation are exploited in two multi-objective algorithms: a multiple descent gradient algorithm and a Nash game strategy. In order to introduce their main features, the two are first described and analyzed on analytical test cases.

Multiple Gradient Descent Algorithm

In current evolutionary algorithms, cooperative interactions between population members are not always modeled, when no evolutionary pressure or mechanisms that exploit cooperation in the form of co-adaptation exist. Potter et al. [141] proposed a multi-objective evolutionary algorithm that exploits the cooperation co-evolution. In cooperative co-evolution a number of species is evolved together. The cooperation among the individuals is encouraged by rewarding the individuals based on how well they cooperate to solve a target problem. However, the assignment of fitness to the subcomponents is very complex, and remains mainly an open task, as it is difficult to measure how much credit must a subcomponent receive from the performance of the individual where it is a constitutive part.

Cooperation can be more easily considered in gradient based algorithms. The simultaneous improvement of the disciplines is possible following Pareto descent directions. They consist in directions to which no other descent directions are superior in improving all objective functions. A generalization of the classical steepest-descent method [142] is MGDA that stands for Multiple-Gradient Descent Algorithm [111]. It applies to cases in which an arbitrary number of criteria, of known gradients, have to be minimized.

MGDA principle

We consider the problem of simultaneous (unconstrained) minimization of n objective functions of N design variables, $J_i(\mathbf{x})$ $(i = 1, \ldots, n;\ \mathbf{x} \in \mathbb{R}^N$, design vector). Scalarization of the cost functions is not considered. The dimensions n and N are arbitrary, although in many applications $n \leq N$. Let $\mathbf{x}^0$ be a particular design-point about which the objective functions are smooth (say $\mathcal{C}^2$ in practice) and locally convex. Denote $u_i^0 = \nabla J_i(\mathbf{x}^0)$ $(i = 1, \ldots, n)$ the gradients, and define the following convex hull:

$$\bar{U} = \left\{ w \in \mathbb{R}^N, \quad w = \sum_{i=1}^{n} \alpha_i u_i, \quad \alpha_i \geq 0, \forall i \quad \sum_{i=1}^{n} \alpha_i = 1 \right\}. \tag{6.9}$$

$\bar{U}$ is a closed, bounded and convex set associated in the affine space $\mathbb{R}^N$ with a polyhedron of at most n vertices. Hence $\bar{U}$ admits a unique element of minimum norm, say ω [111]. The Pareto stationarity condition is then defined as:

Definition 6.6.1 *A point* $\mathbf{x}$ *is said to be Pareto-stationary if there exists a convex combination of the gradients,* $\nabla J_i(\mathbf{x})$*, equal to 0:*

$$\exists \alpha \in \mathbb{R}^n / \alpha_i > 0 \, \forall i; \quad \sum_{i=1}^{n} \alpha_i = 1; \quad \sum_{i=1}^{n} \alpha_i \nabla J_i(\mathbf{x}) = 0$$

Two cases are possible when the descent direction ω is evaluated:

1. $\omega = 0$, and we say that $\mathbf{x}^0$ is a point of Pareto-stationarity, a necessary condition for Pareto-optimality;

2. or $\omega \neq 0$, and the directional derivatives of the objective functions satisfy the inequalities:

$$\left(u_i^0, \omega\right) \geq ||\omega||^2 . \tag{6.10}$$

   hence, $-\omega$ is a descent direction common to all the objective functions.

In the latter case, we define MGDA as the iteration that uses $-\omega$ as the direction of search, and a step-size adjusted to maximize the smallest absolute decrease of the criteria. In the particular case of two criteria, the minimum-norm vector is known analytically. Figure 6.12 shows the vector ω in the three different possible cases that can occur in a bi-objective problem.

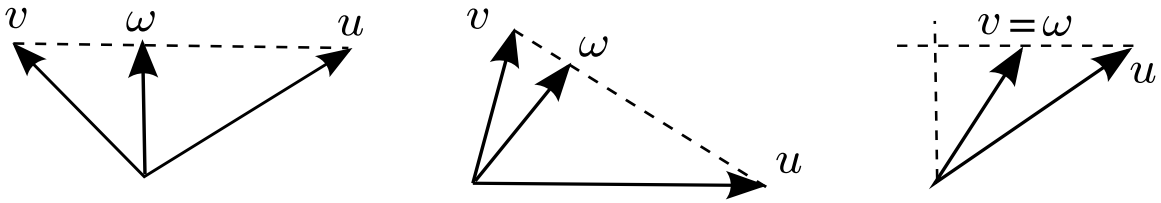

Figure 6.12: Various possible configurations of the two gradients-vectors $u = u_1$ and $v = u_2$ and the minimal-norm element ω.

The descent iterations is then written as:

$$\mathbf{x}_{new} = \mathbf{x}_{old} - \rho\omega(\mathbf{x}_{old}) \tag{6.11}$$

where $\mathbf{x}_{old}$ is the solution at the i^{th} iteration and $\mathbf{x}_{new}$ at the next iteration. In single objective optimization, when the optimal value is neither known nor estimated *a priori*, the norm of the gradient of the objective function is frequently used as a stopping criterion. The MGDA algorithm in use should terminate as soon as all the gradients norm are small enough. This, however, is not possible in multi-criteria optimization since the gradients of the objective functions may not vanish at a Pareto optimal point where the Pareto-stationarity condition is satisfied to some tolerance. For this reason, iterations are performed until the condition of Pareto stationarity is satisfied.

Accumulation points of this method are Pareto-optimal designs [111]. MGDA is a gradient based algorithm thus belonging to the class of local optimization algorithm. Several optimizations, starting from different points, are required to define a Pareto set of solutions.

Analytical validation

In [111] the ability of MGDA to converge and identify the Pareto optimal set has been proven. As a first illustration of the method, several analytical multi-objective optimization test-cases proposed in [143] have been solved by MGDA and compared with evolutionary strategies [144]. Here a simple test-case is considered in order to validate and introduce the method.
The test-case corresponds to the two-objective unconstrained minimization of the following functions:

$$\begin{cases} f_1(\mathbf{x}) = 1 - \exp\left(-\sum_{i=1}^{3}\left(x_i - \frac{1}{\sqrt{3}}\right)^2\right) \\ f_2(\mathbf{x}) = 1 - \exp\left(-\sum_{i=1}^{3}\left(x_i + \frac{1}{\sqrt{3}}\right)^2\right) \end{cases} \tag{6.12}$$

The design variable is $\mathbf{x} = (x_1, x_2, x_3) \in \mathbb{R}^3$. This test-case is known to yield a continuous but non convex Pareto set in function space and it has been adopted also by Deb for the validation of the algorithm NSGA-II. From a given starting point, MGDA converges quickly (6 steps in this example)

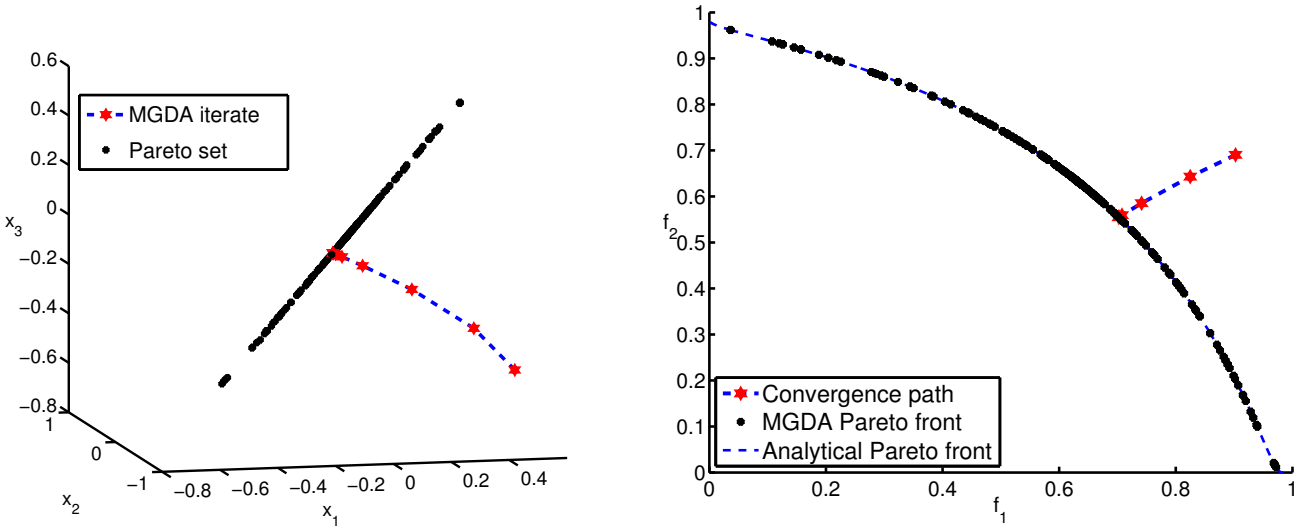

Figure 6.13: Convergence of MGDA from an initial design point to the non dominated set.

and provides an accurately-defined design-point on the Pareto set (see Figure 6.13). In order to identify a set of solutions that belong to the Pareto front, a set of 60 initial design-points distributed over a sphere in the design space $\mathbf{x} \in \mathbb{R}^3 | x_i \in [-1, 1]$ (see Figure 6.14) has been considered.

Due to the local nature of the algorithm each initial point has the tendency to converge to a different point on the Pareto front. The result is an accurate discretization of the analytically-known Pareto front with a reduced computational cost. Indeed the convergence for each initial design solution requires at maximum 11 iterations.

Evolution of the MGDA strategy for engineering problems

Two main aspects have to be taken into account when complex shape optimization problems are analyzed: computational time and constraints handling. Objective functions computations are generally based on high-fidelity models and each function evaluation is costly. If finite difference evaluations of the gradients are required, the computational time tends to increase dramatically. To overcome this difficulty a meta-model assisted version of MGDA has been developed and applied to an engineering shape optimization problem in [145]. Concerning the second aspect, engineering problems have always to face up with several constraints for this reason the algorithm has to be able to solve for multi-objective constrained problems. Three versions of MGDA have been considered in this work and are described in the following sections. Table 6.4 summarizes the main features of each of them.

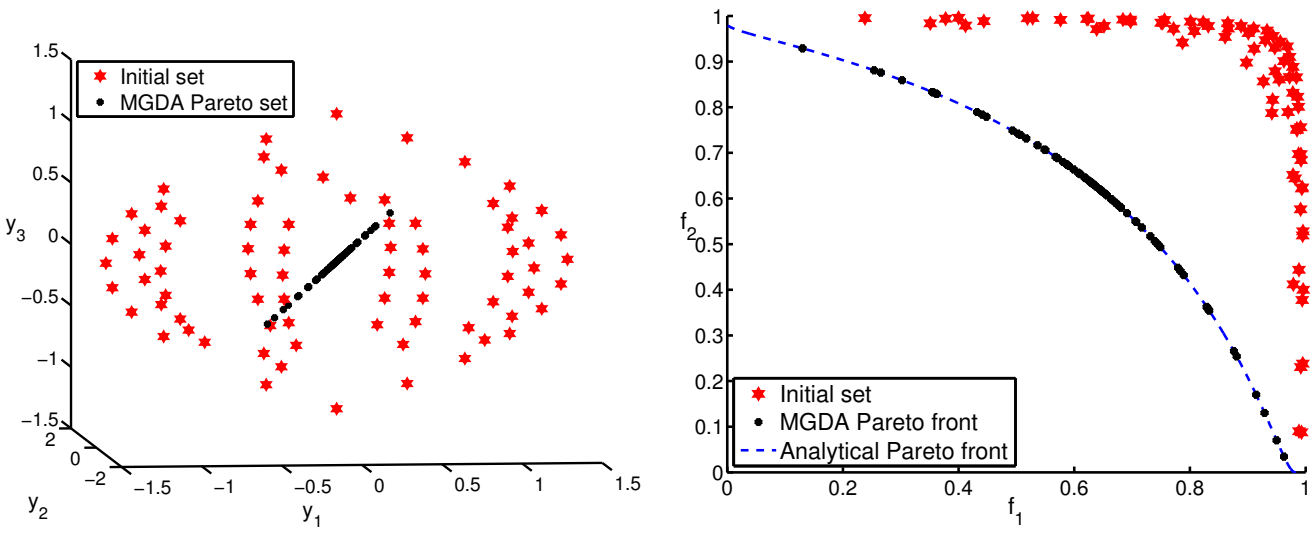

Figure 6.14: Convergence of MGDA from initial design points around Pareto front, for a classical test case proposed by Fonseca, in design space (left), in function space (right).

Version	Model	Gradient evaluation	Constraints handling
MGDA	high or low fidelity	model provided	penalty functions
MA-MGDA	mixed	low-fidelity model	penalty functions
MGDA-CM	high or low fidelity	model provided	method of feasible directions

Table 6.4: Differences between MGDA versions.

Metamodel-assisted MGDA (MA-MGDA)

In PDE-constrained optimization, and in particular in optimum-shape design in aerodynamics, the calculation of function values and their gradients can be very computationally demanding, and usually requires substantial methodological developments. To alleviate this task we have investigated the possibility of calculating approximate gradients from a surrogate model, or meta-model, devised from a database of high-fidelity function values [145]. In the applications considered presently, the high-fidelity models are associated with 3D compressible flows governed by the Euler equations.

We proceed as follows (see flowchart in Figure 6.15). An initial set of design points is generated using of a Latin hypercube sampling in $\mathbb{R}^N$. The sampling serves two purposes. Firstly, the function values corresponding to the sampling form a database supporting Kriging metamodels, surrogate of the actual objective functions. Secondly, some of these sampling points are used to initiate independent MGDA iterations applied to the multi-objective minimization of the meta-models, and converging to Pareto-stationary points (associated with the meta-models). These Pareto-stationary points are then evaluated according to the high-fidelity models to enrich the database and proceed with the next update. A filtering method is used additionally to remove points found too close to an existing design-point, in order to avoid redundancy. At each complete step of this mixed-fidelity approach the solutions tend to the non dominated set of the high-fidelity model.

MGDA coupling with CONMIN (MGDA-CM)

When a constrained problem is considered two approaches are possible:

- consider an equivalent unconstrained problem using penalty functions;
- project the descent direction in the direction tangent to the constraint surface, eventually taking care of push-off factors in order to descend into a feasible region.

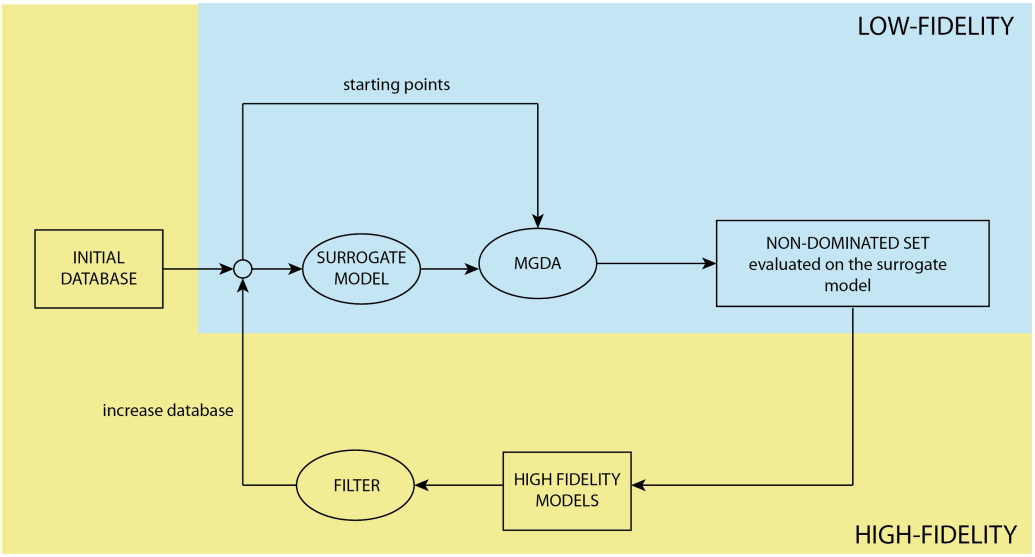

Figure 6.15: MGDA with surrogate model scheme. A surrogate model based on an initial database is trained. Then, MGDA [111] is applied from each database point using surrogate models. Thus a non dominated set on the surrogate model is obtained.

The first methodology is easy-to-use and does not require particular care with the important exception of the choice of the weight for the penalty functions and will be applied in the aero-acoustic shape optimization problem. The second strategy requires modifications of the original algorithm. MGDA has been coupled with the algorithm CONMIN [146] to exploit its features when constrained problems are considered in a MGDA-CM version. The descent direction ω is provided by MGDA, the line-search is performed on the two functions and then the minimum step between the two is adopted. The constraints handling technique based on the method of feasible directions is performed by CONMIN and the convergence to the Pareto front is assured when the condition of Pareto stationarity is satisfied.

Consider the following multi-objective constrained problem:

$$\text{Minimize} \begin{cases} J_1(\mathbf{x}) &= (x_1-2)^2+(x_2-2)^2+2 \\ J_2(\mathbf{x}) &= 9x_1-(x_2-1)^2 \end{cases} \tag{6.13}$$

subject to the following constraints:

$$\begin{cases} g_1(\mathbf{x}) &: x_1^2+x_2^2-225 \leq 0 \\ g_2(\mathbf{x}) &: x_1-3x_2+10 \leq 0 \end{cases} \tag{6.14}$$

where $x_i \in [-20, 20]$. Figure 6.16 shows the comparison between the Pareto front obtained using MGDA-CM starting from 200 initial design points, and the one obtained using NSGA-II with a 12 individuals population and 100 generations performed. MGDA-CM is able to provide a discretized Pareto front as well as the NSGA-II algorithm, but requiring less function evaluations.

Meta-model-assisted MGDA application to the aero-acoustic problem

The objective in this section is to solve the aero-acoustic optimization using the MA-MGDA algorithm. The application case consists in the reference wing body configuration presented in chapter 3 at the following flight conditions: Mach number equal to M_∞=1.6, flight altitude of 18,000 m and an AoA equal to 2 degrees.

Figure 6.17 shows the set of design variables adopted to describe the complete geometry. The first six design variables (DVs) define the fuselage and consist in the nose deflection angle α_n, a control point at the nose, one at the middle that has a fixed x-coordinate and another control point that describes the aft part of the fuselage. The wing planform geometry is defined using the leading edge

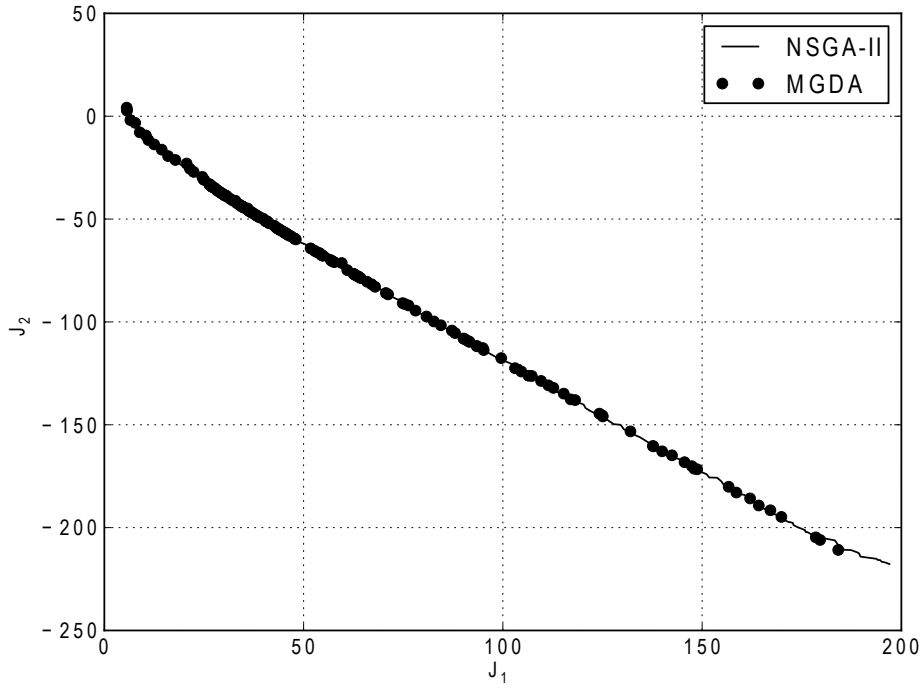

Figure 6.16: Pareto front obtained with MGDA-CONMIN compared with the result obtained using NSGA-II.

sweep angle of the inboard and the outboard wing respectively ϕ^1_{BA} and ϕ^2_{BA}, the longitudinal position of the wing x_w and the dihedral angle Λ of the external wing. The set of design variables is then written as :

$$DV = (\alpha_n, x_1, z_1, z_2, x_3, z_3, \Lambda, x_w, \phi^1_{BA}, \phi^2_{BA}) \tag{6.15}$$

The reduced number of variables is an implicit requirement to the construction of a surrogate model with a limited number of individuals in the starting database. The initial database consists of 50 individuals and it has been created using a classical LHS method. The DV set represents different geometrical entities: angles, relative distances and coordinates. Instead of their direct use in the optimization problem, to provide a better conditioning of the problem, a non-dimensional optimization variables set $\mathbf{x}$ is defined as in equation (5.4). An exception is made for the nose deflection variable because $\bar{DV_1}$ is equal to 0, the following relation is adopted: $DV_1 = 0.5\ x_1$. The design variables set $\mathbf{x}$ can take values between -1 and 1. Table 6.5 shows the geometrical variables and their respective modification allowed.

Variable	Specification	$\bar{DV_i}$	δ_i
DV1	nose deflection [deg]	0	-
DV2	x-coordinate nose section [m]	4	2%
DV3	radius nose section [m]	0.8	10%
DV4	radius cabin section [m]	1.015	10%
DV5	x-coordinate rear section [m]	28	2%
DV6	radius rear section [m]	0.535	10%
DV7	dihedral angle [deg]	3	100%
DV8	relative wing position [adim]	0.367	10%
DV9	inner wing sweep angle [deg]	65	10%
DV10	outer wing sweep angle [deg]	56	10%

Table 6.5: Design variables set definition.

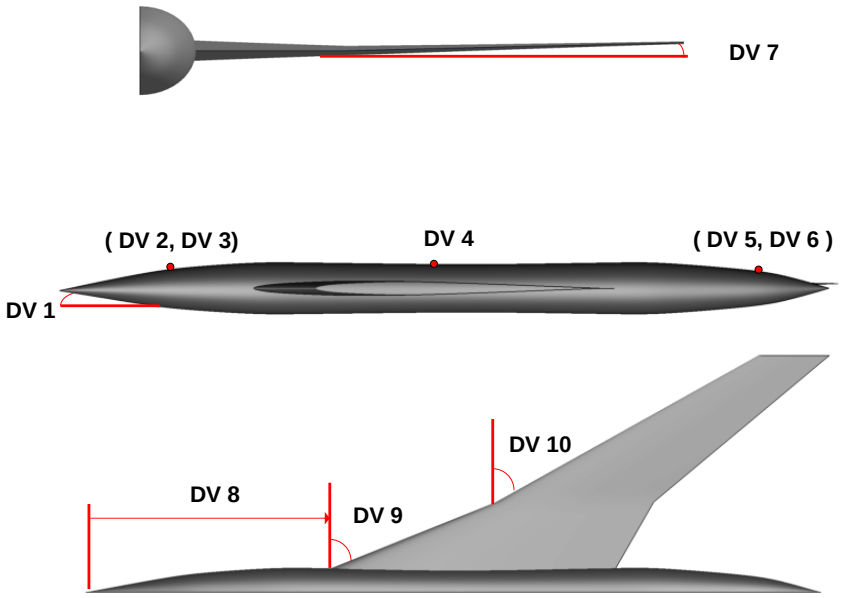

Figure 6.17: Supersonic glider parameterization.

The objective function for aerodynamics and acoustics are respectively the drag coefficient with lift constraint, and the sum of the shock overpressure of the under-track ground signature. The problem can be stated as follows:

$$\text{Minimize} \begin{cases} J_1(\mathbf{x}) = c_D & \text{subject to :} \quad g : c_L - c_{L_0} \geq 0 \quad \text{with } c_{L_0} = 0.1 \\ J_2(\mathbf{x}) = \sum \Delta p & \text{subject to =} \quad \text{no constraints} \end{cases} \tag{6.16}$$

As a difference from the problems previously treated, the target lift coefficient has been reduced because the angle of attack, that has a strong importance to satisfy the constraint, does not belong anymore to the design variables set.

The meta-model-assisted MGDA is applied to solve the aeroacoustic optimization problem (6.16) using a penalty function to take into account the constraint. At each step, the algorithm tends to converge toward the optimal front of the two objectives optimization problem based on the surrogate models. This set of solutions is then evaluated using the high fidelity CFD-based three-layer approach. These new points, in addition with the database at the i^{th} iteration, are then used to create a new surrogate model at the iteration $i+1$. In this application all the training points of the low-fidelity model are used as MGDA starting points. This aims to increase the set of non dominant points identified, thus reducing the number of required MGDA cycles. The algorithm does not take into account bound constraints on the variable ranges. Solutions that do not respect the variables ranges at the end of each MGDA convergence on the surrogate model are removed before the high-fidelity evaluations. Furthermore, an adequate initial step choice of the descent iteration prevents the convergence outside the feasible domain. Figure 6.18 shows the convergence of MGDA toward the Pareto front. After the first step of MGDA, each new set brings improvement in the Pareto optimal set thus increasing the number of non-dominated points. The first step is applied to a surrogate model made only of 50 points, this could explain the sparsity of the different solutions. Six steps of the meta-model assisted MGDA are sufficient for an accurate definition of the Pareto front.

The Pareto front obtained using the NSGA-II algorithm applied to the high fidelity model is used as comparison with the solution evaluated using MGDA. The total number of evaluations on the high fidelity model used for MGDA convergence is used as stop criterion for NSGA-II. This means that the comparison is made at an identical computational cost. Figure 6.18 clearly shows that the Pareto front evaluated using MGDA completely dominates the solution of NSGA-II, thus identifying the efficiency of MGDA. The meta-model assisted MGDA requires less function evaluations during the convergence

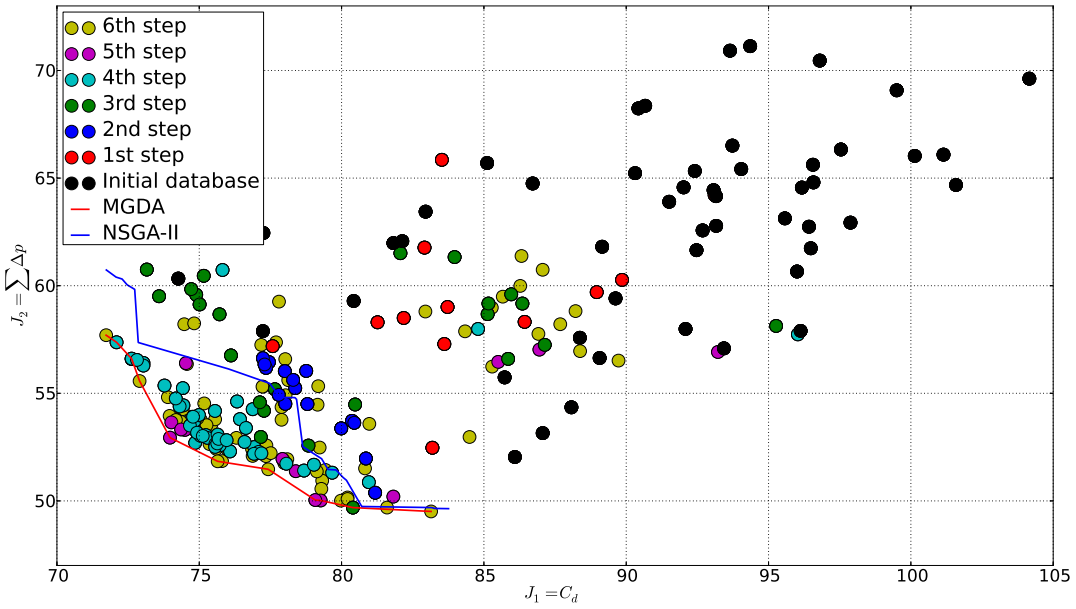

Figure 6.18: Convergence history of MA-MGDA. The comparison with NSGA-II is made at an identical number of high-fidelity function evaluation calls. (Data plotted are results from CFD analysis)

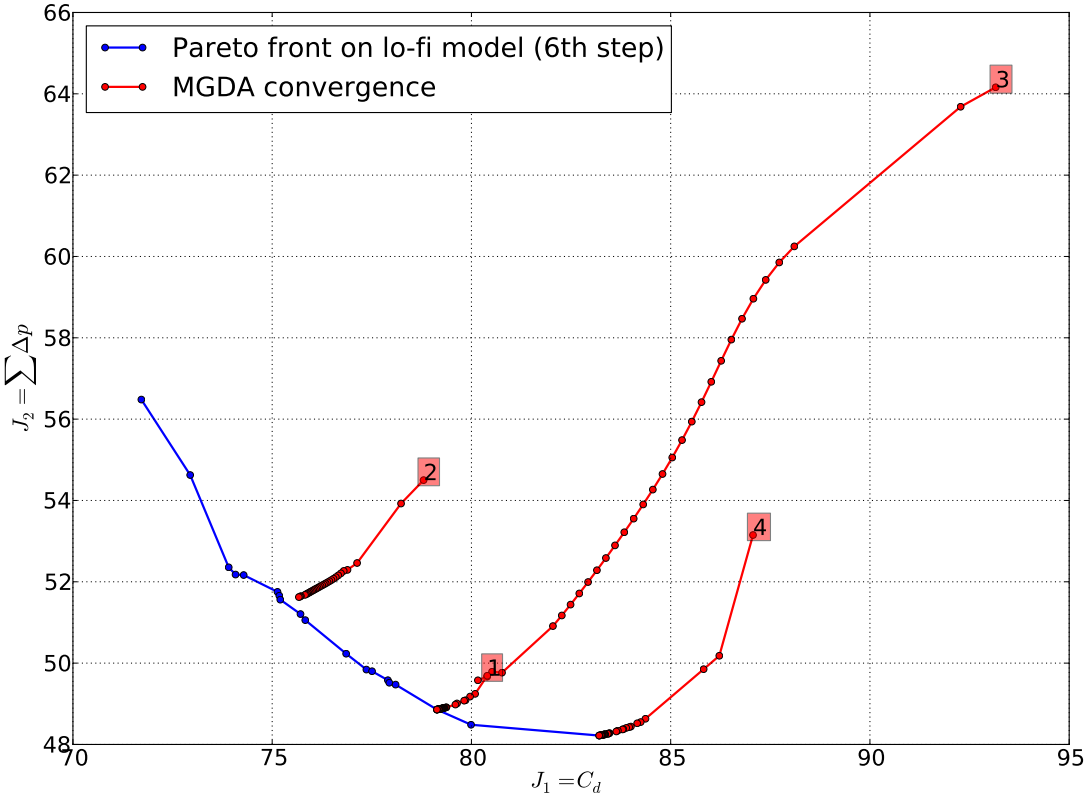

Figure 6.19: MGDA convergence to the Pareto front of the low-fidelity model starting from 4 initial points of the database.

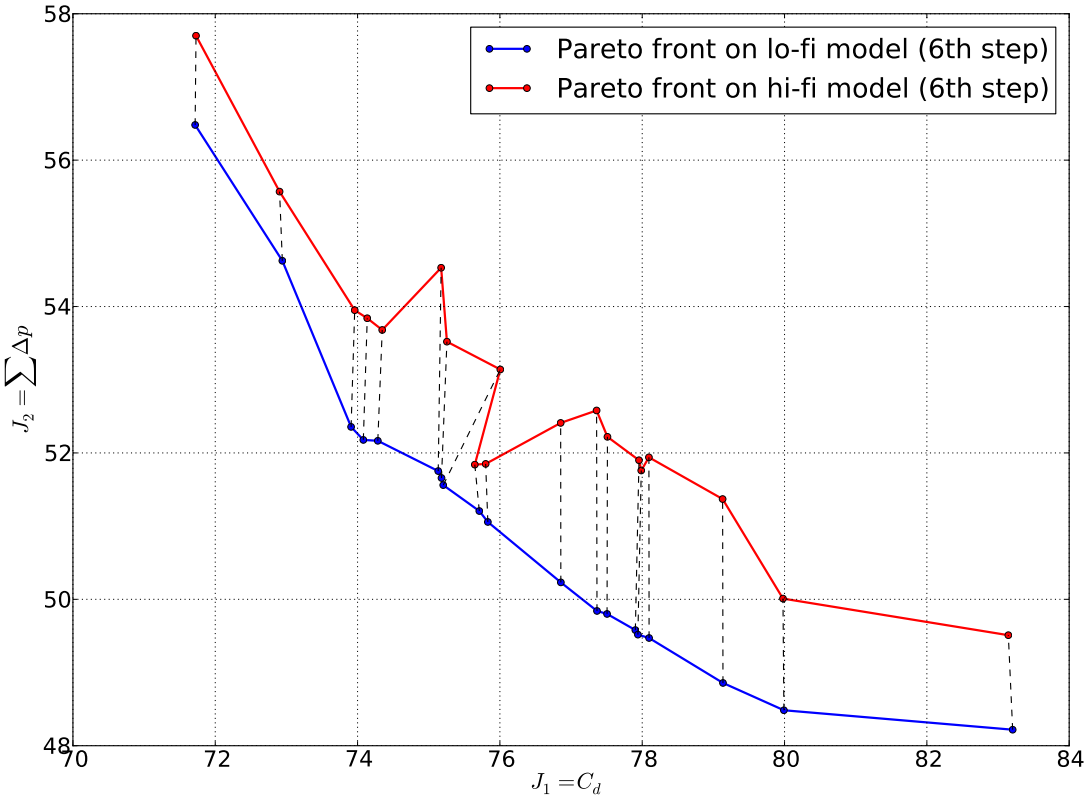

Figure 6.20: Comparison between the Pareto front of the MGDA 6th step and the values after high-fidelity evaluations.

to the real Pareto front and is suited to computationally expensive problems. Furthermore, the diversity of the solutions is comparable between the two algorithms.

The convergence of MGDA on the low-fidelity model is shown in Figure 6.19. Four points are used as starting points to show the limited amount of function evaluations required by this gradient based algorithm to converge to the Pareto front. In addition, the mixed-fidelity approach based on the continuous update of the surrogate model ensures an accurate description of the real model, despite the well known difficulties encountered with a noisy, non smooth, multimodal cost function such as the sonic boom. Figure 6.20 shows the comparison between the points evaluated using the surrogate model at the last step of the algorithm and the corresponding set obtained after the high-fidelity model evaluations. As expected the surrogate model of the acoustic function shows more discrepancies between the predicted and the actual values. The surrogate model prediction of the acoustic function is on average 1 Pa lower than the actual value.

Three different configurations (see Table 6.6) that belong to the Pareto front are compared in Figures 6.21 and 6.22. The low drag configuration (A) and the trade-off configuration (B) show

Configuration	J_1	J_2
A	71.72 dc	57.7 Pa
B	73.98 dc	52.94 Pa
C	83.14 dc	49.51 Pa

Table 6.6: Selected configurations that belong to the high-fidelity Pareto front in Figure 6.18.

minor modifications on the fuselage geometry. The modification impacts mainly the wing planform. Configuration (B) shows a reduction of the dihedral angle with respect to the configuration (A) that

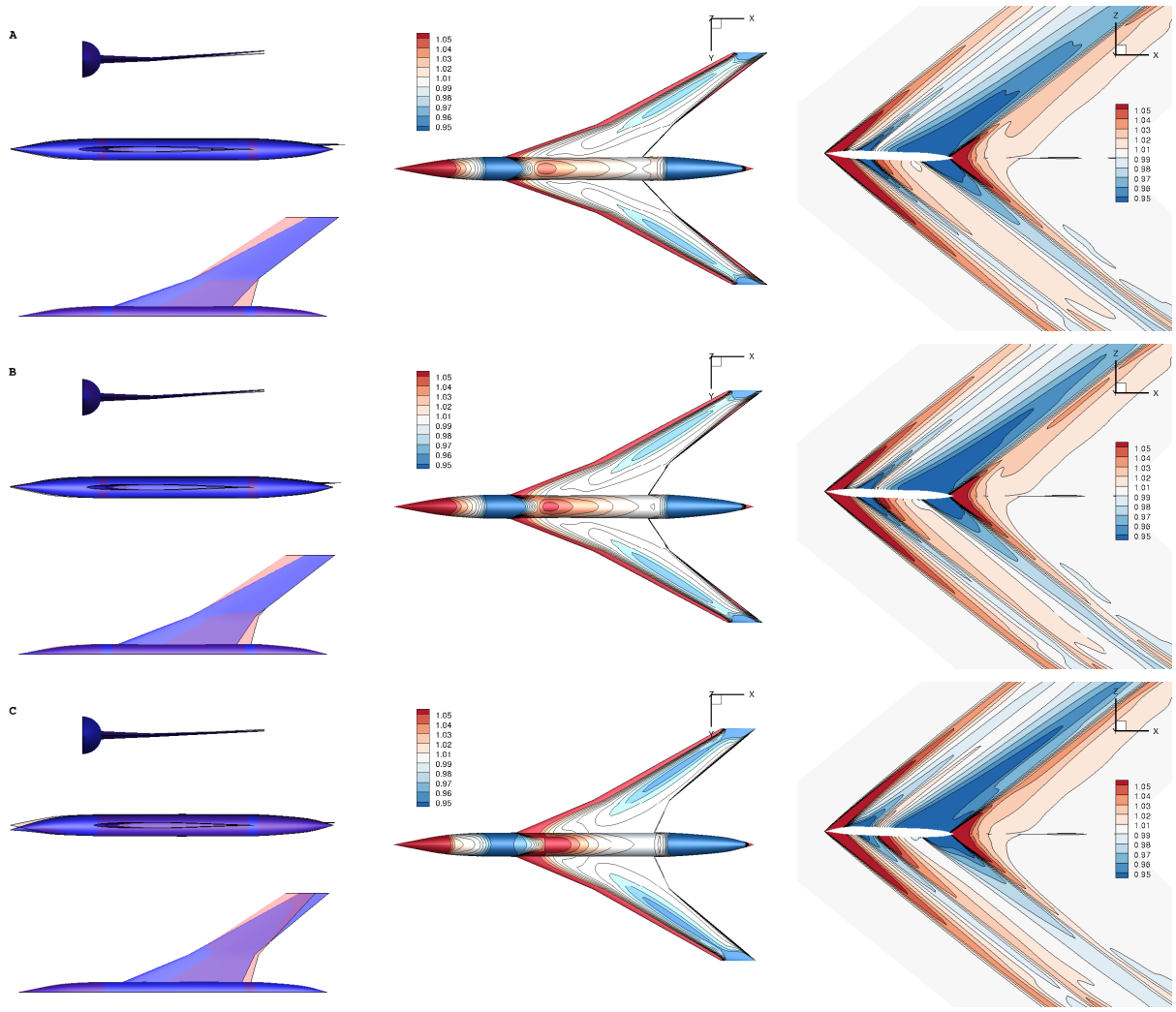

Figure 6.21: Geometry configuration, bottom skin pressure (p/p_0) and symmetry plane pressure (p/p_0) in near field for configuration A, B and C on the Pareto front (In red the initial geometry).

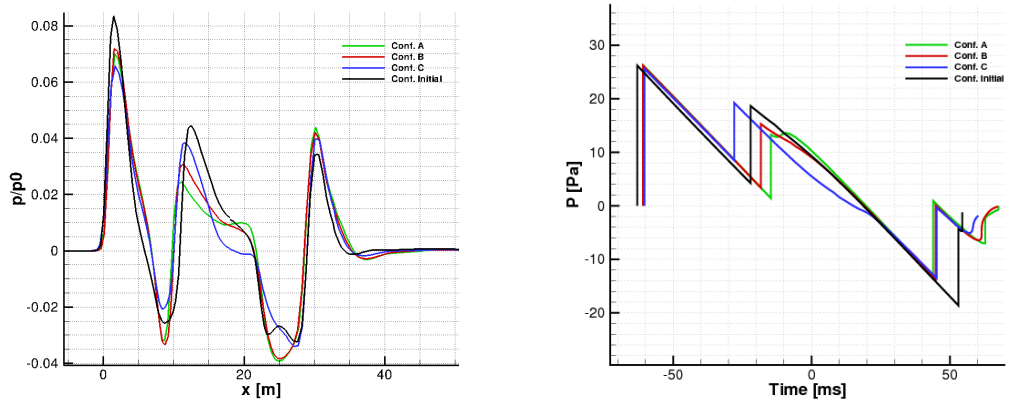

(a) Near field $p/p0$ (z=h-10m).

(b) Ground signature.

Figure 6.22: Near-field and ground pressure signal for different configurations on the Pareto front

is beneficial for the rear shock of the ground signature (see Figure 6.22b) with a limited deterioration

of the aerodynamic performance. Indeed, the dihedral angle acts modifying the acoustic footprint at ground, in particular the duration of the signature. The low boom configuration (C) shows a strong downward displacement of the nose angle, which determines a modification of the flow conditions that reaches the wing leading edge. The front shock is almost not modified in any of the selected geometries. As the sonic boom is reduced from (A) to (C), the expansion after the first shock is reduced.

Looking at the pressure signal just below the aircraft in Figure 6.22a it is possible to note that the design variables are able to act and shape all the shock and expansion waves. In particular all the configurations show a split of the rear shock due to the combined wing planform and the rear fuselage modifications. The initial peak in the near field p/p_0 is reduced by some 20% with respect to the initial configuration, but this does not correspond to an analogue reduction of the front shock overpressure (Figure 6.22b). In contrast, wing and aft fuselage modifications produce changes in the middle and ending part of the near-field signature, that correspond to strong modifications on the ground signature. A better parameterisation of the nose shape with more design variables, can improve the ability of the algorithm to reduce the front shock amplitude. The algorithm has identified the wing and the rear shock reductions as the most promising regions to improve the functions of interest with respect to the chosen parameterization.

Competition: Nash game and splitting of territories

The competition due to the antagonism between different objective functions can be solved using a problem decomposition technique. If one is able to decompose the initial problem into several simpler design problems with their own objective and search space, the solution can be more easily evaluated. Concurrent Subspace Optimization [147] allocates the design variables to subspace corresponding to engineering discipline or subsystems. Each subspace performs a separate optimization, operating only on its own unique subset of design variables. A problem arise in the extreme case when everything influence everything else directly, so each subspace have to include all design variables. A strategy is so required to split the variables set.

An engineering multi-objective problem can be seen also as a concurrent game where different designers (players) are responsible for one or more objectives [148]. The design problem is decomposed into several simpler design problems and each virtual player represents a discipline. Competitive games combined with genetic algorithms have been already adopted to perform shape optimization of a wing airfoil in Periaux et al.[149].

Competitive games, also called Nash games or non-cooperative games, has been defined by Nash [150]. A game is a model that captures the interaction between different players. Each player separately tries to improve or optimize his "pay-off" function performing an action under the constraint of the others decisions. The game is simultaneous because each player optimizes his criterion with the others considered as fixed. When one of the player is the leader and the others have to made their decision after the first, the game is called Stackelberg game [151]. This kind of game is not considered in this work.

We are considering optimization problems involving two objective functions $J_A(\mathbf{x})$ and $J_B(\mathbf{x})$ to be minimized. By an appropriate change of variables (to be defined later) the design vector $\mathbf{x}$ is made a function of two sub-vectors U and V:

$$\mathbf{x} = \mathbf{x}(U, V) \tag{6.17}$$

where $\dim U + \dim V = \dim \mathbf{x}$. In this way $J_A(\mathbf{x}) = J_A(U, V)$ and $J_B(\mathbf{x}) = J_B(U, V)$. Then following Tang et al. [152] and Désidéri [153], the subvectors U and V are used as strategies in a symmetrical Nash game to improve J_A and J_B respectively.

In a symmetrical Nash game, an equilibrium point is found when each player's set of action parameters realize a local optimum of one's own pay-off subject to the action parameters decided by the other players. For two players, this can be reformulated as follows:

Definition 6.6.1 (Nash equilibrium) *Consider a symmetrical Nash game with two players A and B. The strategy pair $\bar{\mathbf{x}} = (\bar{U}, \bar{V})$ represents the Nash equilibrium for the two players iff :*

$$\begin{cases} \bar{U} &= \arg\min_U J_A(U, \bar{V}) \\ \bar{V} &= \arg\min_V J_B(\bar{U}, V) \end{cases} \tag{6.18}$$

Each player uses a subset of $\mathbf{x}$, respectively $U \in \mathbb{R}^{n-p}$ and $V \in \mathbb{R}^p$,to minimize their discipline functional. In our method, an $n \times n$ splitting matrix Ω_H is defined and the following change of variables is adopted:

$$\mathbf{x} = \mathbf{x}_A^\star + \Omega_H \begin{pmatrix} U \\ V \end{pmatrix} \tag{6.19}$$

The definition of the splitting matrix becomes a crucial aspect in the optimization process. In general, the choice of the Ω_H matrix requires an *a priori* knowledge of the physics of the phenomenon [152]. In Désidéri [154],[153] a method to define an adequate split of territories is proposed with a complete mathematical formulation. For this purpose we proceed as follows.

1. Identify the optimum solution associated with the single-objective problem related to the primary discipline:
$$\begin{array}{l} \mathbf{x}^\star = \arg\min J_A(\mathbf{x}) \\ \text{subject to } g(\mathbf{x}) = 0 \end{array} \tag{6.20}$$

2. Assume that the approximations of the gradient $\nabla J_A(\mathbf{x}_A^\star)$, the Hessian matrix $H_A^\star = H_A(\mathbf{x}_A^\star)$ and the gradient of the constraints $\nabla g(\mathbf{x}^\star)$ are available. If it is not the case it is possible to compute an approximation adopting a surrogate model of discipline A and associated constraints. Considering a constrained problem, if $K \geq 1$ constraints are active, the Gram-Schmidt orthogonalization process is applied to the constraint gradients $\{\nabla g_k\}$. This results in a set of orthogonal unit vectors $\{\omega_k\}$, spanning the same subspace. Then, a projection matrix P is defined as follows:
$$P = I - \sum_{k=1}^{K} [\omega_k] [\omega_k]^T \tag{6.21}$$
where $[\omega_k]$ denotes the $n \times 1$ column-vector, and the superscript ^{T} stands for transposition. The projected Hessian is then written as follows:
$$H'_A = P H_A^\star P \tag{6.22}$$
Applying a spectral decomposition:
$$H'_A = \Omega_H \Lambda_H \Omega_H^T \tag{6.23}$$
where the split matrix Ω_H is fully defined after the ordering of the eigenmodes is chosen such that the eigenvalues $\{h_i\}$ of the projected Hessian H'_A satisfy: $h_i = 0$ for $i = 1, \ldots, K$, and $h_{K+1} \geq h_{K+2} \geq \cdots \geq h_n$. For an unconstrained problem the projection matrix P is the identity matrix and the spectral decomposition is performed directly on $H_A^\star$.

If the objective of the optimization is to optimize two different disciplines where one is considered primary or "fragile", the interest is to introduce the optimization of the second discipline as a small perturbation from the original optimum of the primary cost function $J_A^\star$. The definition (6.6.1) could be applied directly to a multi-objective problem [149], but a more interesting revisited formulation of the concurrent optimization problem proposed by Désidéri [154] defines this new multi-objective problem as:

$$\begin{cases} \min_U J_A(U,V) \\ \text{subject to} \qquad g = 0 \end{cases} \tag{6.24}$$

$$\begin{cases} \min_V J_{AB}(U,V) \;=\; \frac{J_A}{J_A^\star} + \epsilon \left(\theta \frac{J_B}{J_B^\star} - \frac{J_A}{J_A^\star} \right) \\ \text{subject to} \qquad\qquad \text{no constraints} \end{cases} \tag{6.25}$$

where ϵ is a continuation parameter that allows to smoothly introduce the antagonism between disciplines varying from 0 to 1 and θ is a relaxation factor usually set to 1.
The complete procedure is sketched in Figure 6.23.

The main theoretical result (cf. Désidéri [153]) is that when $\epsilon = 0$, the Nash equilibrium exists and it corresponds precisely to $\mathbf{x}_A^\star$ independently of the dimensions n, p and K, thus guaranteeing the

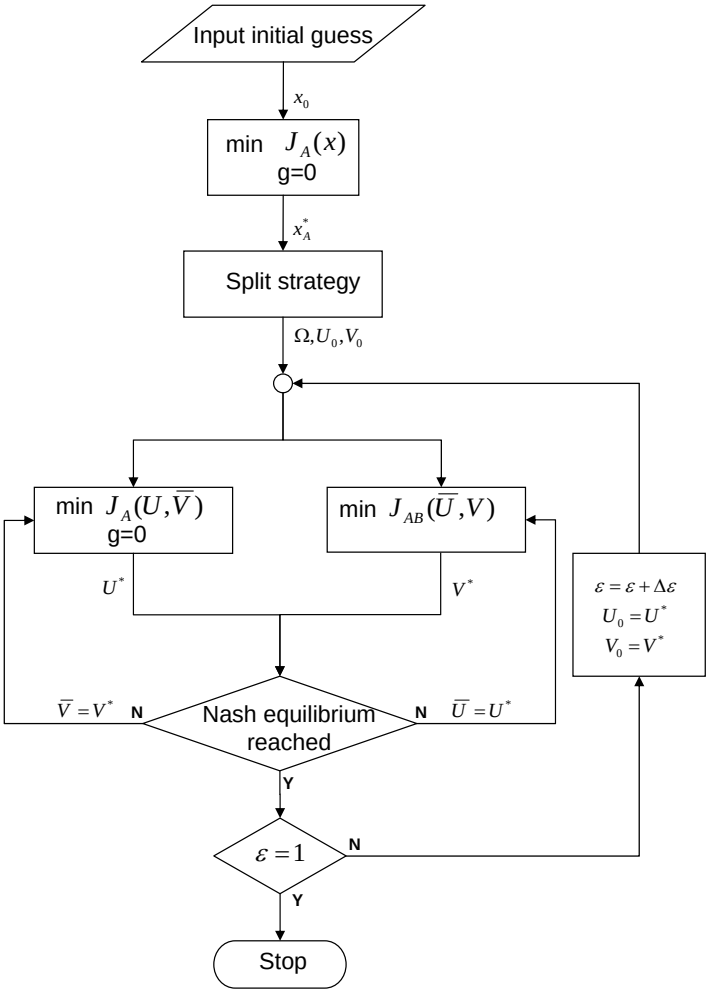

Figure 6.23: Flow-chart for the continuum Nash equilibrium in multi-objective optimization.

consistency of the Nash game for $\epsilon = 0$ with the single-discipline optimization of discipline A alone. As ϵ increases, the continuum of Nash equilibrium is found $\bar{\mathbf{x}} = \bar{\mathbf{x}}_\epsilon = \mathbf{x}(\bar{U}_\epsilon, \bar{V}_\epsilon)$. The Nash equilibrium evolves smoothly from the optimum $J_A^\star$ solution of the problem for $\epsilon = 0$ to the solution of the problem minimization of J_B when ϵ progressively varies from 0 to 1. Infinitesimal perturbations of the parameters lying on the secondary functional territory potentially cause the least possible degradation to the value of the primary functional so that $J_A(\bar{\mathbf{x}}_\epsilon) = J_A^\star + \mathcal{O}(\epsilon^2)$.

When a constrained problem is considered, usually the constraint functions are considered using a penalty function that deteriorates the cost function if any constraint violations occur. The new augmented functional is written as:

$$\bar{J}_A = J_A + \frac{1}{2\varepsilon}\mathbf{g}^T\mathbf{g} \tag{6.26}$$

where $\varepsilon \in \mathbb{R}^+$ is a penalty coefficient. In this case to properly identify the split of the design variables, the initial functional J_A has to be considered. The calculation and diagonalization of the Hessian matrix associated with the augmented criterion, would instead yield an erroneous result, only reflecting the constraints.

We want to demonstrate that using the augmented functional an Hessian-based split is not required to satisfy the initial equilibrium at $\epsilon = 0$. Consider $\mathbf{x}_A^*$ as the Nash equilibrium of the eigensplit-based

formulation for $\epsilon = 0$. To demonstrate this property it is required to prove that for $\epsilon = 0$, $U = V = 0$, $\mathbf{x} = \mathbf{x}_A^\star$ is the Nash equilibrium of (6.24) and (6.25). For $V = 0$, $U = 0$ is solution of (6.24), because the definition of $\mathbf{x}$ includes the optimum $\mathbf{x} = \mathbf{x}_A^\star$ when $U = 0$. The condition of optimality for the unconstrained criterion J_{AB} is the stationarity condition

$$\left(\frac{\partial J_{AB}}{\partial V}\right)_{U=0} = \frac{1}{J_A^\star}\nabla J_A^\star \left(\frac{\partial x}{\partial V}\right)_{U=0} = 0 \tag{6.27}$$

where $\nabla J_A^\star \in Sp(\omega^1, \omega^2, ..., \omega^k)$ and $\left(\frac{\partial x}{\partial V}\right)_{U=0}$ is a linear combination of the last p column vectors of the splitting matrix Ω_H. To satisfy equation (6.27) it is necessary to split variables using the orthogonal basis Ω_H. Otherwise at $\epsilon = 0$ it is not guarantee that $\mathbf{x}_A^*$ is the Nash equilibrium and so that $\frac{J_{AB}}{J_{AB}^\star} = 1$. In general this is not the case for the primitive split, nevertheless this property is assured if the following problem for the functional J_{AB} is considered:
find V solution of

$$\left\{ \begin{array}{lcc} \min_{V \in R^p} & : & J_{AB}[x(U,V)] \\ g[\mathbf{x}(U,V)] & = & 0 \end{array} \right. \tag{6.28}$$

This situation can typically occurs when the augmented functional $\bar{J_A}$ is considered. Considering the problem defined as in (6.28) the condition of optimality of the constrained criterion J_{AB} is the stationarity condition:

$$\left(\frac{\partial J_{AB}}{\partial V}\right)_{U=0} = \left(\frac{1}{J_A^\star}\nabla J_A^\star + \sum_{k=1}^{K} \lambda_k \nabla g_k^\star\right) \left(\frac{\partial x}{\partial V}\right)_{U=0} = 0 \tag{6.29}$$

but $\frac{1}{J_A^\star}\nabla J_A^\star + \sum_{k=1}^{K} \lambda_k \nabla g_k^\star = 0$ is the stationarity condition for the constrained problem. So in this case we do not need to satisfy the requirements of an orthogonal basis. In the implemented algorithm that solves for the Nash equilibrium continuum, no aggregated functional are considered, because the optimization algorithms are able to take into account constraints.

Consider the following multi-objective constrained problem:

$$\text{Minimize} \left\{ \begin{array}{lll} J_A(\mathbf{x}) = \sum_{k=0}^{3} \frac{x_k^2}{3^k} & \text{subject to :} & g = x_0^4 x_1^3 x_2^2 x_3 - 96\sqrt{3} \\ J_B(\mathbf{x}) = \sum_{k=0}^{3} x_k^2 & \text{subject to :} & \text{no constraints} \end{array} \right. \tag{6.30}$$

The minimum of the primary discipline A is $J_A^\star = 3.\bar{3}$ located at $\mathbf{x}^\star = (2/\sqrt{3}, \sqrt{3}, \sqrt{6}, 3)$. and the corresponding $J_B(\mathbf{x}^\star) = 19.\bar{3}$.
The Hessian, the gradient and the projected Hessian are respectively:

$$H(\mathbf{x}^\star) = \begin{bmatrix} 2 & 0 & 0 & 0 \\ 0 & 0.\bar{6} & 0 & 0 \\ 0 & 0 & 0.\bar{2} & 0 \\ 0 & 0 & 0 & 0.0741 \end{bmatrix}, \qquad \nabla g(\mathbf{x}^\star) = \begin{bmatrix} 576 \\ 288 \\ 135.77 \\ 55.43 \end{bmatrix},$$

$$H' = \begin{bmatrix} 0.2186 & -0.3837 & -0.1012 & -0.0305 \\ -0.3837 & 0.7284 & 0.0689 & 0.0336 \\ -0.1012 & 0.0689 & 0.2735 & 0.0235 \\ -0.0305 & 0.0337 & 0.0235 & 0.0847 \end{bmatrix},$$

The splitting matrix Ω_H obtained after the spectral decomposition and the reordering is so defined as:

$$\Omega_H = \begin{bmatrix} 0.8721 & 0.4748 & -0.1124 & -0.037 \\ 0.4361 & -0.8637 & -0.2452 & -0.0607 \\ 0.2056 & -0.1599 & 0.9582 & -0.1186 \\ 0.0839 & -0.0543 & 0.0955 & 0.9904 \end{bmatrix}$$

The algorithms adopted for J_A and J_B are respectively Cobyla [155] (Constrained problems by linear approximation of the constraints) and a Nelder-Mead simplex algorithm implemented in the

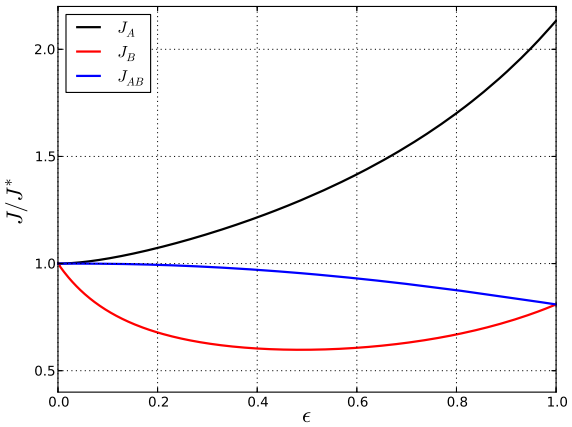

Figure 6.24: The continuum of Nash equilibrium points as ϵ varies. The ϵ step is taken equal to 0.001, the Hessian based split is adopted to perform the (2+2) Nash games.

Scipy.optimize [156] Python library. The continuity parameter ϵ varies from 0 to 1 with a step size of 0.001 and the relaxation parameter θ is set to 1. For each ϵ we perform several iterations in order to satisfy the Nash equilibrium or reach the maximum number of iterations set to 20. Figure 6.24 shows the continuum of the Nash equilibrium as the continuity parameter ϵ varies. It is possible to note that J_A increases monotonically while J_B is convex. The minimum of J_B is achieved at $\epsilon = 0.487$. Further increases of ϵ is counter-productive. The Nash game coupled with the split of territories based on the Hessian is able to reduce a second discipline without strong deterioration of the fragile one, satisfying at the same time the constraints.

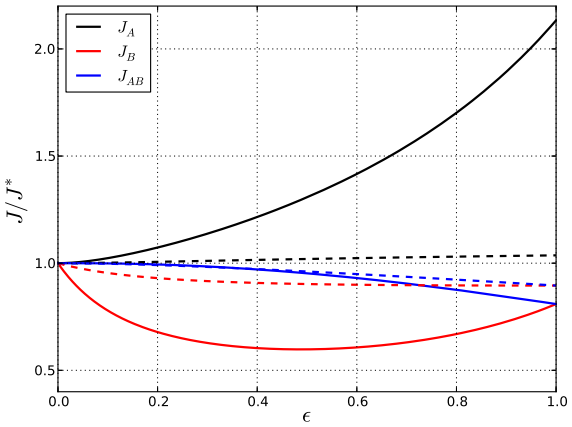

Figure 6.25: Comparison between the primitive based 2+2 split (dotted lines) and the Hessian based 2+2 split (continuous lines).

Figure 6.25 shows the continuum of the Nash equilibria for the primitive and the Hessian based (2+2) split of territories. The primitive split gives the first two variables to the J_A problem and the remaining to the J_{AB} problem. Furthermore the minimization of J_{AB} using the primitive split has to take into account the constraint as in (6.28), otherwise the algorithm is unable to find an equilibrium point that satisfies the constraint. This is one of the problem related to the primitive split that does not take into account any constraint information.
Along the Nash equilibria continuum it is possible to evaluate an index I_s to classify two different split taking into account the improvement of J_B and the degradation of J_A defined as:

$$I_s(\epsilon) := \frac{1}{J_A(\epsilon)J_B(\epsilon)} \tag{6.31}$$

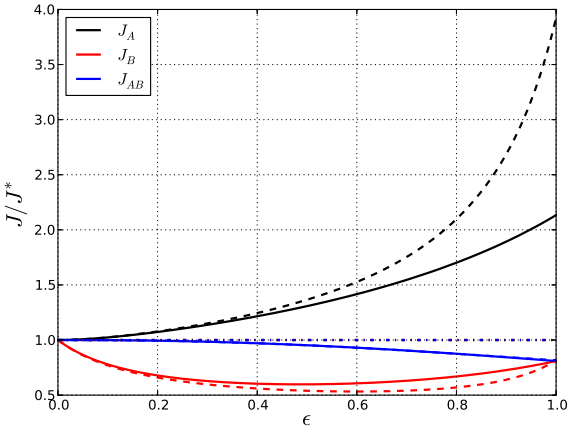

Figure 6.26: Comparison between different Hessian based split: (2+2) continuous lines, (1+3) dotted lines, (3+1) dash-dot lines.

with $J_A \geq 1$ and $J_B \leq 1$. For the same split consider two Nash equilibria at ϵ_1 and ϵ_2, if $I_s(\epsilon_1) > I_s(\epsilon_2)$ the Nash equilibrium at ϵ_1 is more interesting from a design point of view than the one at ϵ_2 because is closer to the Pareto front. The best point is obtained at $\epsilon^\star$ and this solution has the maximum value of the index $I_s^\star$. Considering two different splits s_1 and s_2, it is possible to classify the effectiveness of the split comparing their respective maximum split index $I_s^\star$: if $I_{s_1}^\star > I_{s_2}^\star$ the split s_1 performs better than the split s_2. The maximum I_s associated to the primitive split is 1.08 obtained for the J_A, J_B couple (1.02, 0.9), while considering the Hessian one is 1.34, obtained for the couple (1.26, 0.59). The Hessian split degrades more the primary discipline but at the same time ameliorating more the secondary one.

Different Hessian splits have been tested on the same problem: (2+2), (1+3) and (3+1). Figure 6.26 shows the Hessian based split for different size of territory given at the two discipline. The 3+1 split is unable to ameliorate the acoustic discipline, the territory assigned to the acoustic discipline is too small to change the initial equilibrium. On the contrary the 1+3 split is able to satisfy the constraints of the primary discipline and at the same time ameliorates more the secondary one. The maximum split index $I_s^\star$ for the 1+3, 2+2 and 3+3 splits are respectively: 1.28, 1.34, 1. From a designer point of view the 2+2 split appears more interesting for the analytical test case considered.

Application of Nash games to the aero-acoustic problem

The low-boom/low-drag shape design problem is treated in this section as a competitive game. Instead of a family of configurations that belong to the Pareto set, the result of the Nash game is a single configuration. The choice is to consider aerodynamics as preponderant and progressively introduce the sonic boom performance. The objective is to obtain a configuration where sonic boom is minimized and at the same time aerodynamics is not too degraded. The problem can be stated as follows

$$\begin{cases} \min J_A = c_D \\ \text{subject to} \quad g : c_L - c_{L_0} \geq 0 \end{cases} \tag{6.32}$$

$$\begin{cases} \min J_{AB} = \frac{J_A}{J_A^\star} + \epsilon \left(\theta \frac{J_B}{J_B^\star} - \frac{J_A}{J_A^\star} \right) \\ \text{subject to} \quad \text{no constraints} \end{cases} \tag{6.33}$$

where $J_B = \sum \Delta p$ and c_{L_0} is the target lift coefficient equal to 0.1.

Concerning the model adopted, the choice is to consider a mixed approach, where the Nash game iterations are performed on a surrogate model and are finally evaluated using the high-fidelity CFD based model. This approach is chosen for two main reasons:

- the Hessian based split of territories requires the evaluation of the Hessian at the optimum point of the primary discipline $H_A^\star$ and the gradient of the constraints $\nabla g_A^\star$. A surrogate model can provide these values without any additional function evaluations. Furthermore Hessian and gradient accuracy problems related to finite differences errors are completely avoided;

- Nash game iterations require many function evaluations for local disciplinary minimization of the two cost functionals that have to be repeated for several Nash game equilibrium iterations. In addition if the continuum of the Nash equilibrium is the goal of the analysis, the process has to be repeated several times at each continuity iteration.

As a main difference with the approach adopted for the Metamodel Assisted MGDA, the surrogate model adopted is not updated along the iterations. In addition the surrogate model has to be sufficiently accurate to predict the Hessian of the aerodynamic discipline. For this reason the construction of the surrogate models of each discipline requires particular care and the number of design variables considered has to be limited. The number of design variables considered is reduced to 5: nose deflection (x_1), nose radius (x_2), cabin radius (x_3), wing position along the fuselage (x_4), and the dihedral angle (x_5). Design variables $\mathbf{x}$ are related to geometrical variables as in equation (5.4). Table 6.7 shows the geometrical variables and the corresponding variation allowed. Concerning nose deflection,

Variable	Specification	$\bar{g}_i$	δ_i
DV1	nose deflection [deg]	0	-
DV2	radius nose section [m]	0.8	20%
DV3	radius cabin section [m]	1.015	15%
DV4	relative wing position [adim]	0.367	20%
DV5	dihedral angle [deg]	3	100%

Table 6.7: Design variables set definition.

the following relationship is adopted: $g_1 = 0.7x_1$. The Kriging models of each discipline and of the constraint function are created using a LHS database made up of 40 individuals. Five improvement iterations are performed to introduce points where the aerodynamic drag Kriging model expected improvement is maximum. This procedure determines a final database that consists in 45 points. Finally, cross-validation has been used to validate the final low-fidelity models.
To evaluate the Nash equilibrium continuum the following steps are then performed:

- The minimization of the drag coefficient with constraint on lift $g = c_l - 0.1 \geq 0$ is obtained using the CMA-ES algorithm applied to the previously constructed surrogate model for c_D and c_L. After some 1200 iterations the optimum is found at $J_A^\star = 81.458$ Pa with $g = 0.002$. The corresponding design vector is $\mathbf{x} = [-0.558, -0.836, -0.506, -0.434, -1]$;

- The Hessian-based split matrix Ω is evaluated using the procedure defined in section 6.6. A split 2+3 is adopted, where 2 variables are assigned to aerodynamics and the remaining ones to acoustics:

$$\Omega = \begin{bmatrix} -0.1967 & -0.1839 & 0.0944 & -0.8251 & -0.4876 \\ -0.1257 & -0.4079 & -0.9042 & 0.0107 & 0.0114 \\ -0.6606 & -0.5744 & 0.3548 & 0.3282 & -0.0037 \\ -0.7055 & 0.6776 & -0.2077 & -0.0095 & 0.0049 \\ 0.1070 & 0.1036 & -0.0672 & 0.4596 & -0.8730 \end{bmatrix};$$

- Nash game iterations are performed using an SQP optimizer [142] for J_A and a Nelder-Mead simplex algorithm for J_{AB}. Each single optimization is performed until convergence;

- Concerning continuity iterations, a step of 0.05 is considered for ϵ.

Figure 6.27 shows the history of the Nash equilibrium continuum. For $\epsilon = 0$ all the three curves initiate at the value 1. J_A and J_B have zero slope due to the problem formulation defined in equation (6.24) and (6.25) which is consistent with the original optimum. As ϵ increases, drag degrades monotonically, while J_{AB} and J_B diminish. During the first iterations, the nose is deflected downward (x_1) (see Figure 6.28b). At ϵ close to 0.25, x_1 reaches its low-bound constraint. A new equilibrium point is obtained at the next iteration increasing the cabin radius (x_3) and keeping the wing closer to the nose (x_5). This new configuration causes an abrupt decrease of J_B and g. The constraints function g is

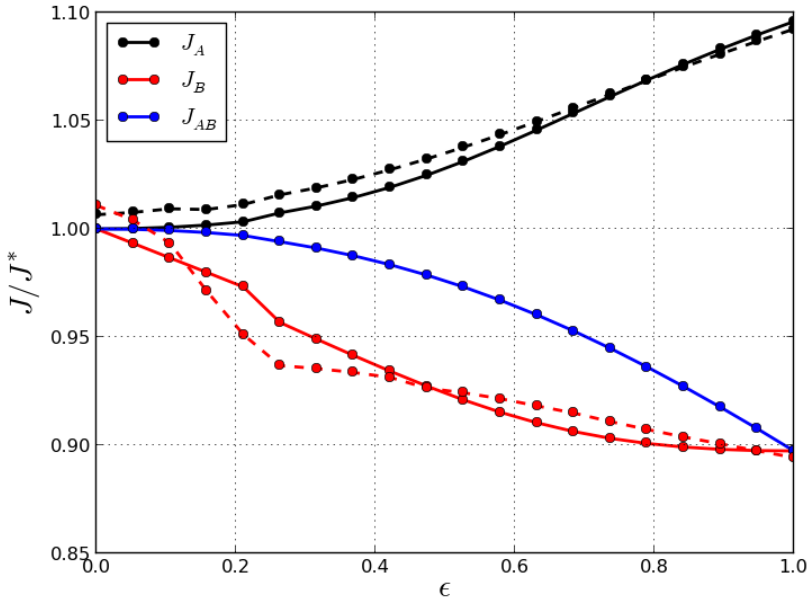

Figure 6.27: Continuum of the Nash equilibrium. Continuous lines represent evaluations using surrogate models, while dotted lines represent evaluations using high-fidelity models.

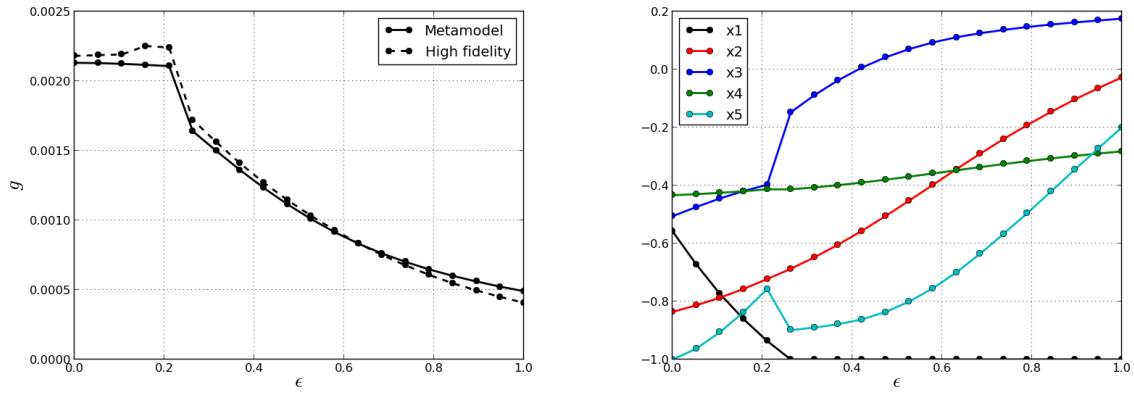

(a) Constraints function.

(b) Variables.

Figure 6.28: Evolution of constraint function and variables during Nash game iterations.

satisfied along the iterations (see Figure 6.28a), but reducing the margin to the constraints activation when we are moving away from the aerodynamic optimum $\mathbf{x}_A^\star$. The low drag configuration has a dihedral angle (x_5) equal to zero, while as shown in Figure 6.31c when $\epsilon \geq 0.5$ the dihedral angle is almost equal to 3 degree.

The equilibrium points evaluated using the Kriging model are re-evaluated using the high fidelity models. The new curves shown in dotted lines in Figures (6.27) and (6.28) are in agreement with the results obtained using the low-fidelity model. The accurate definition of the Kriging models has permitted to obtain the high correlation between low and high-fidelity models. From a design point of view the solution at the point $\epsilon = 0.25$ is the most interesting. Indeed considering the high-fidelity prediction drag is degraded by only 1%, while the acoustic function is reduced by more than 7%.

To understand trade-offs visualization is essential. Self-organizing maps (SOM) [157] are adopted to produce two-dimensional maps. SOM consists in an artificial neural network that preserves the topological properties of the input space and aims at analyzing the different configurations obtained. The unified distance matrix, sometimes referred as U-matrix, is a representation of a self-organizing

map where the Euclidean distance between different neuron is depicted. Cluster regions that have the same color code mean neurons with similar topological properties. The U-matrix for the problem analyzed (Figure 6.29a) shows four cluster regions that are labeled respectively: low-boom (LB), high-antagonism (HA), low-antagonism (LA) and low-drag (LD). The discrimination is based upon the continuity parameter: LB ($\epsilon > 0.75$), HA ($0.5 < \epsilon \leq 0.75$), LA ($0.25 < \epsilon \leq 0.5$) and LD ($\epsilon \leq 0.25$).

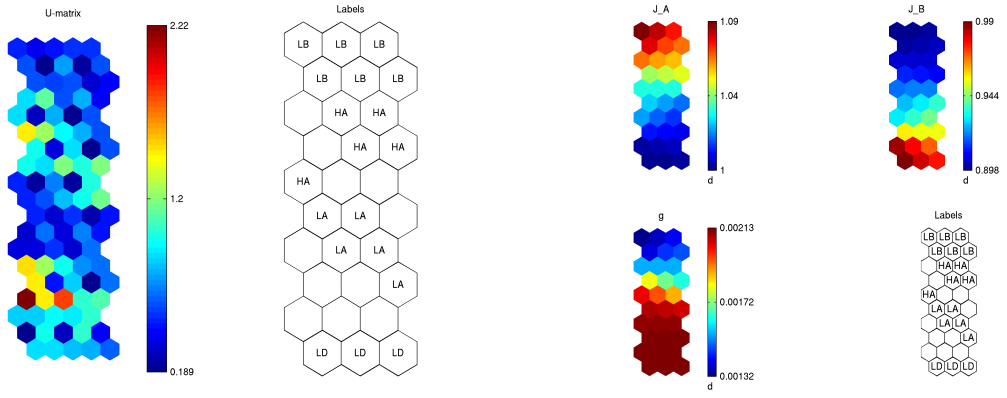

(a) U matrix SOM. (b) Cost functions SOMs.

Figure 6.29: SOM of the competitive game.

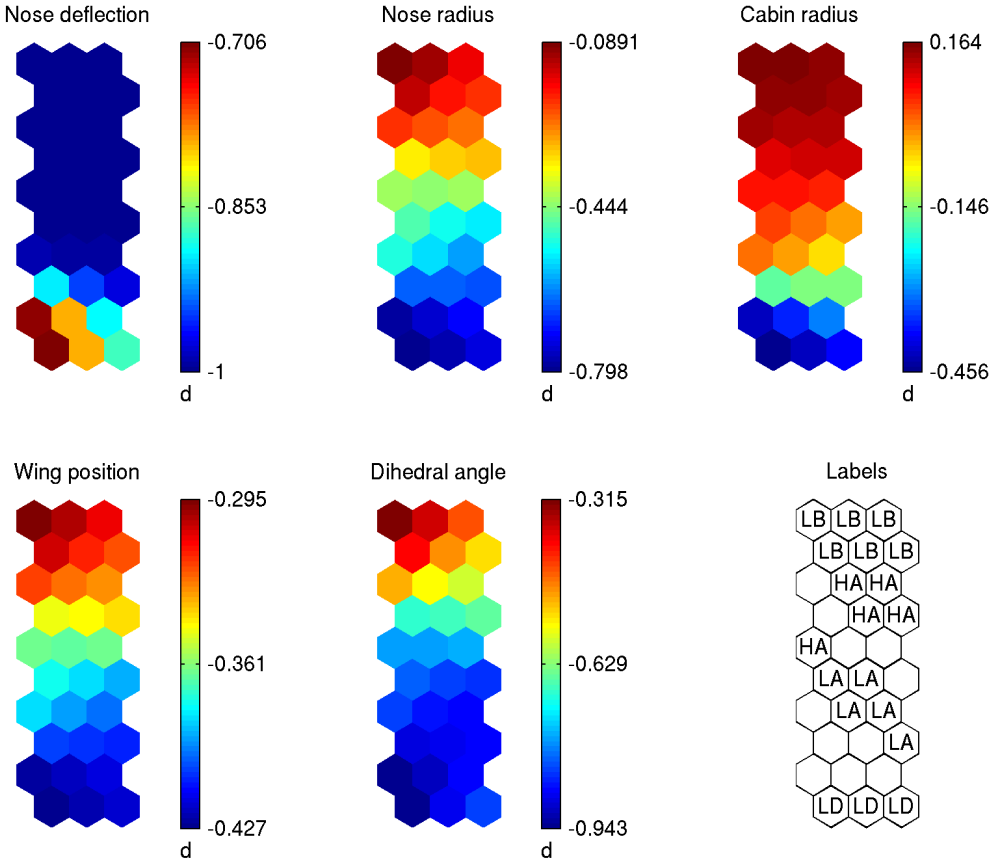

Figure 6.30: Variables SOM.

Cost functions SOMs (Figure 6.29b) highlight the strong antagonism between drag and sonic boom, but also the existence of a region across LA and HA configurations that provides an interesting trade-off between the two disciplines. Low-boom and high antagonism configurations show a strong nose deflection and an increase of the cabin radius. The acoustic function shows a strong influence of the nose deflection. As the antagonism is introduced by increasing ϵ, the nose is rapidly deflected downward. At the same time the aerodynamic function is not impacted by this variable (at bottom in the x_1 SOM in Figure 6.30). For this reason it is the variable that shows the maximum rate of change since the beginning until the activation of the constraint. Low-drag configurations show a strong decrease of the dihedral angle, while HA and LB configurations have very different values ranging from -0.6 to -0.3. Wing position and nose radius show a SOM strictly similar to that of the drag function. A low-drag configuration shows a smaller nose and a wing closer to the nose than other configurations.

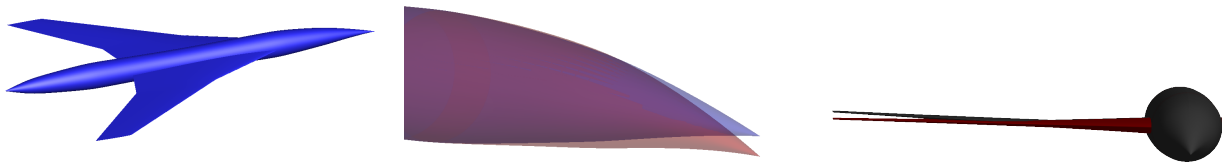

(a) Initial low-drag configuration. (b) Nose deflection from $\epsilon = 0$ to $\epsilon = 0.5$. (c) Dihedral angle increases from $\epsilon = 0.5$ to $\epsilon = 1$.

Figure 6.31: Main geometry modifications during Nash game convergence. In blue the initial low-drag configuration ($\epsilon = 0$), in red the configuration at $\epsilon = 0.5$, in black the configuration at $\epsilon = 1$.

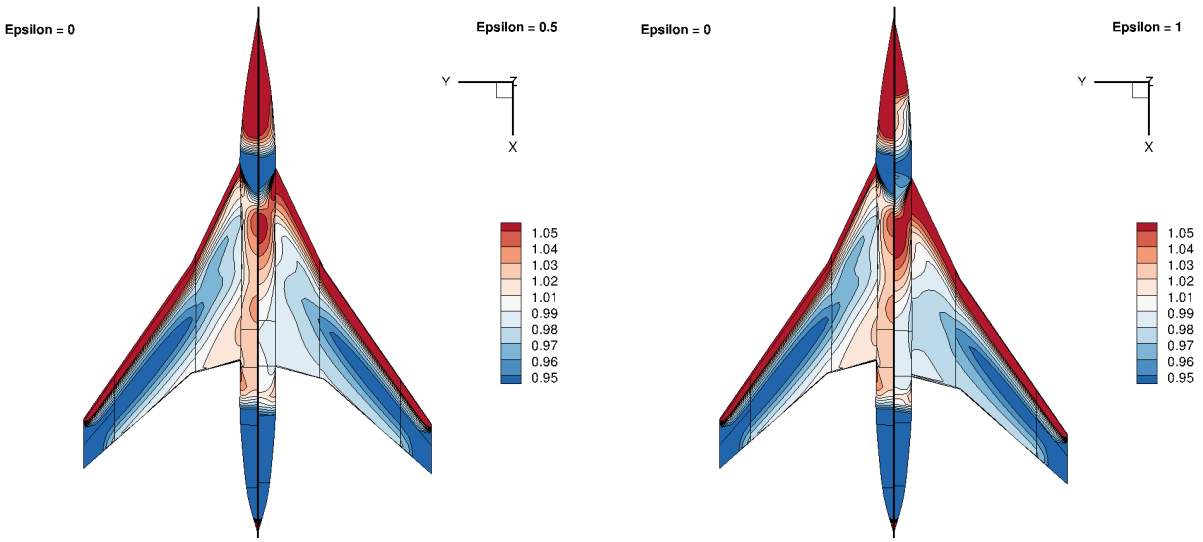

(a) Comparison between $\epsilon = 0$ and $\epsilon = 0.5$. (b) Comparison between $\epsilon = 0$ and $\epsilon = 1$.

Figure 6.32: Bottom skin pressure field (p/p_0) along the Nash equilibrium continuum.

Three configurations are retained for comparative analysis at different ϵ equal to: 0, 0.5 and 1. The main geometry modifications are shown in Figure 6.31. As ϵ increases, the nose shock is bounded in a region close to the nose top. The consequence is an increased nose shock amplitude, but more localized. The area under the first peak of the near field pressure signature is reduced as ϵ tends to 1. This signature is directly related to the Whitham F-function, and in particular the first peak area is

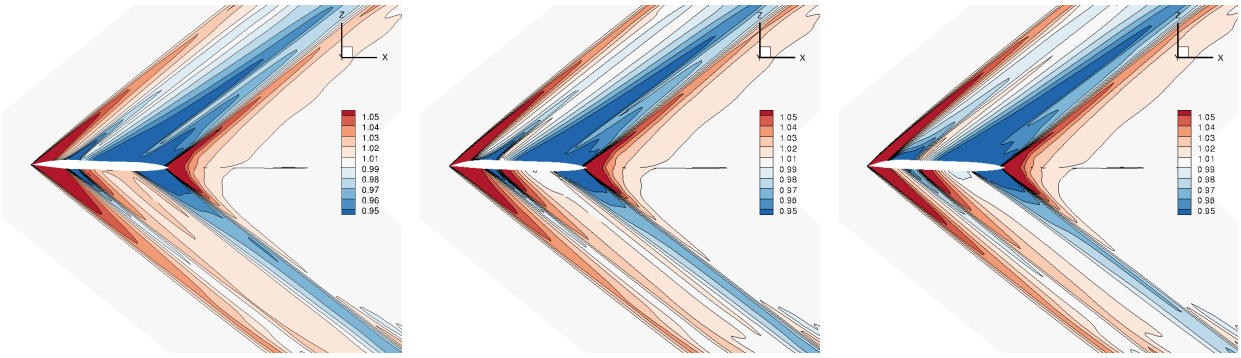

(a) $\epsilon = 0$. (b) $\epsilon = 0.5$. (c) $\epsilon = 1$.

Figure 6.33: Near-field pressure (p/p_0) in the symmetry plane.

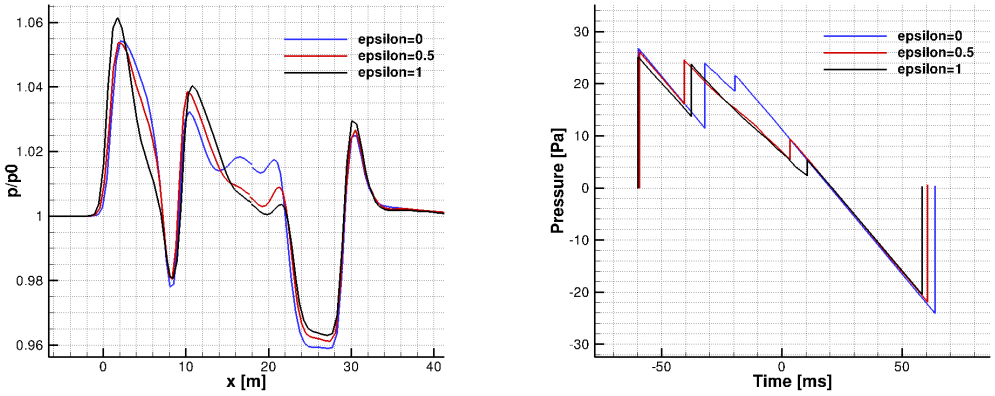

(a) Pressure signature ($p/p0$) extracted under-track at z = h_Z-10 m.

(b) Under-track ground signature.

Figure 6.34: Near-field and ground pressure signal for different ϵ along the Nash equilibrium continuum.

related to the nose shock amplitude and position. A reduced area results in a reduced front shock for the ground signature (Figure 6.34b).

The shock related to the wing leading edge is progressively increased as ϵ tends to 1. The consequence is a reduction of the pressure expansion after the first peak of the ground signature as already seen in the analysis of the Pareto front obtained using the cooperative strategy. The low-pressure region on the bottom skin (Figure 6.32) at the trailing edge of the wing and at the corresponding junction with the fuselage is increased. The interaction with the aft shock pattern results at ground in a reduced amplitude of the rear shock. All the shocks of the ground signature contributes to the reduction of J_B. Nose shock overpressure is reduced by 2 Pa as well as the wing shock, while the aft shock shows a reduction by more than 4% from $\epsilon = 0$ to $\epsilon = 1$.

Coupling cooperation and competition

A natural extension of the previous work consists in combining the cooperation and the competition phases for the exploration of the Pareto front. Consider two cost functions J_1 and J_2 that represent two antagonist disciplines. The starting point of the process is the optimum of the first objective $J_1^\star$. This solution is a Pareto-stationary point that satisfies the definition 6.6.1 when $\alpha_1 = 1$ and $\alpha_2 = 0$. Using the Hessian based split of territories it is possible to perform a Nash game moving in the tangent direction at $x_1^\star$ to the Pareto front. The Nash game can be formulated as:

$$\begin{cases} \min J_A & = & \alpha J_1 + (1-\alpha) J_2 \\ \text{subject to} & & g = 0 \end{cases} \quad (6.34) \qquad \begin{cases} \min J_{AB} & = & \frac{J_A}{J_A^\star} + \epsilon \left(\theta \frac{J_B}{J_B^\star} - \frac{J_A}{J_A^\star} \right) \\ \text{subject to} & & \text{no constraints} \end{cases} \quad (6.35)$$

where $J_B = J_2$.
When $\alpha = 1$ equations (6.34) and (6.35) are coincident with the formulation proposed in equations (6.24) and (6.25). At the end of the competitive phase it exists at least one point that dominates the Nash equilibrium point and that belongs to the Pareto front. From a Nash equilibrium point, it is therefore necessary to perform a cooperative phase using MGDA and to obtain a Pareto stationary point that satisfies definition (6.6.1) for a different α with respect to the initial one.

A simple test case is here analyzed to introduce the procedure. The two criteria minimization problem adopted for this study is written as:

$$\begin{cases} J_1(\mathbf{x}) & = & 4x^2 + y^2 + xy \\ J_2(\mathbf{x}) & = & (x-1)^2 + 3(y-1)^2 \end{cases} \quad (6.36)$$

The Pareto front can be described using the parametric form $J_1(\mathbf{x}(\alpha)), J_2(\mathbf{x}(\alpha))$ and evaluating the Pareto set of solutions $\mathcal{S}^*$. Each solution that belongs to $\mathcal{S}^*$ satisfy the Pareto-stationarity condition for a given α.

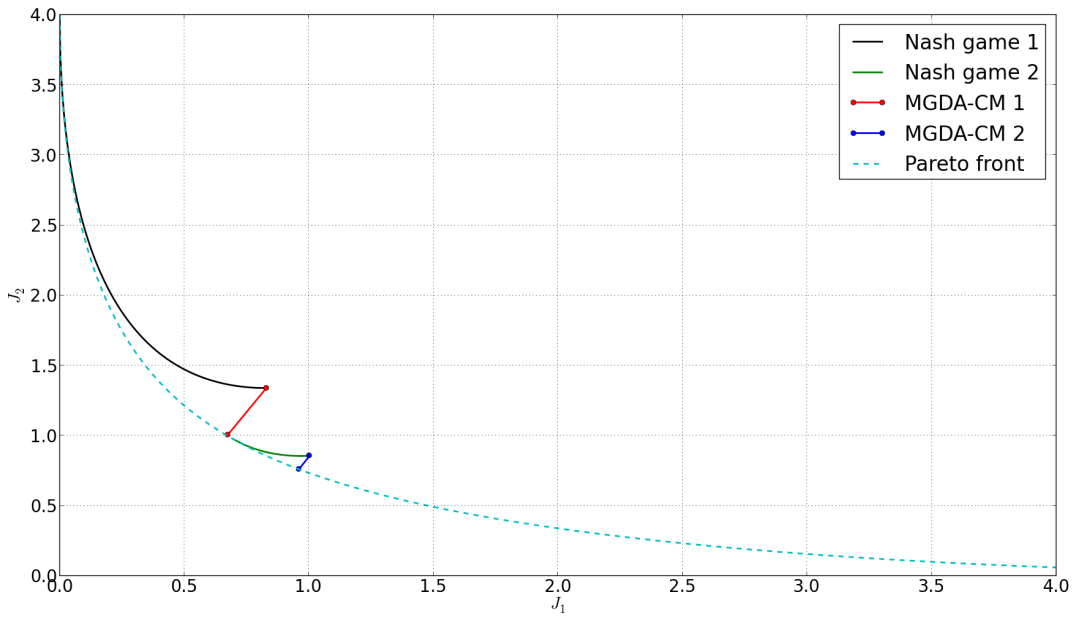

Figure 6.35: Coupling Nash games and MGDA iterations for the Pareto front exploration.

Summing up, the following steps are necessary for the cooperation/competition coupling of the problem (6.36):

1. From the optimum of $J_A^\star(\alpha = 1)$ located at $\mathbf{x}^\star = (0, 0)$ the Hessian based split of territories is evaluated and a Nash game 1+1 is performed with $\alpha = 1$ and a ϵ step size of 0.01;

2. From a Nash equilibrium point $\mathbf{x}_n$ a cooperation phase using MGDA-CM is performed to obtain a solution $\mathbf{x}_s$ that belongs to the Pareto front;

3. A new α is evaluated in order to satisfy the Pareto-stationarity condition at $\mathbf{x}_s$;

4. A new split matrix is evaluated using the Hessian of the function $J_A(\alpha)$ where α has been evaluated at the previous point of the process;

5. A Nash game starting from $\mathbf{x}_s$ is performed using the new split matrix;

6. Points from 2 to 5 can be repeated to explore other regions of the Pareto front.

The procedure, repeated two times on the test problem (6.36), is shown in Figure 6.35. To enrich the discretization of the Pareto front it is possible to couple several cooperation-competition iterations. Furthermore, if Nash games are terminated before the complete antagonism ($\epsilon < 1$), each Nash equilibrium results closer to the Pareto front so that the number of iterations required by MGDA to achieve the Pareto front is reduced.

Coupling cooperation and competition on the aero-acoustic problem

The competitive phase provides a Nash equilibrium point that does not satisfy the Pareto-stationary condition. Considering the aero-acoustic problem, this means that it exists at least one point that shows the same acoustic performance but with a reduced drag. The coupling between a Nash game and a successive MGDA-CM phase will provide a solution that belongs to the Pareto front as shown in the previous test case. The same surrogate models and parameterizations adopted for the competitive phase are considered here. The following steps are performed on Figure 6.36:

- The minimization of the drag coefficient with constraint on lift and the competitive phase as in section 6.6 are performed providing respectively point 1 and 2;
- A cooperative MGDA-CM optimization is performed providing point 3 on the Pareto front;
- A new α is evaluated in order to satisfy the Pareto-stationarity condition at 3;
- A new split matrix is evaluated using the Hessian of the function $J_A(\alpha)$ where α has been evaluated at the previous point of the process;
- Nash game is performed starting from the Pareto front in 3. The formulation adopted is written respectively in equations (6.34) and (6.35);
- From point 4 a cooperative optimization is performed obtaining the point 5 on the Pareto front close to the acoustic optimum.

In Figure 6.36 is shown also the Pareto front obtained using NSGA-II on a population of 24 individuals for 500 generations meaning approximatively ten times the total number of function evaluations required by the cooperative-competitive phase. In addition, the results clearly show that the Hessian based split provides Nash continuum curves that are tangent to the Pareto front at the starting Pareto-stationary point.

In general it is useless to starts from a Nash equilibrium point too far from the Pareto front if the exploration of this one is envisaged. Starting the cooperative phase from point 2 requires more iterations to achieve convergence and in addition will result in a poor discretization of the Pareto front. We then decided to begin each cooperation phase when the primary discipline cost function is degraded by at least 2% with respect to the initial equilibrium point of the competitive phase. In the test case three couplings are performed (see Figure 6.37) providing a better discretization of the Pareto front and requiring less function evaluation.

6.7 Conclusions

In this chapter several algorithms for the solution of a multi-objective problem have been introduced and applied to the low-boom/low-drag design of the SSBJ configuration.

The weighted sum approach is easy to implement because is associated to the same algorithms adopted in single-objective optimizations. The main drawbacks consist in the choice of the cost function weights that have little physical meaning and the computational cost that is important if the complete Pareto set is to be identified.

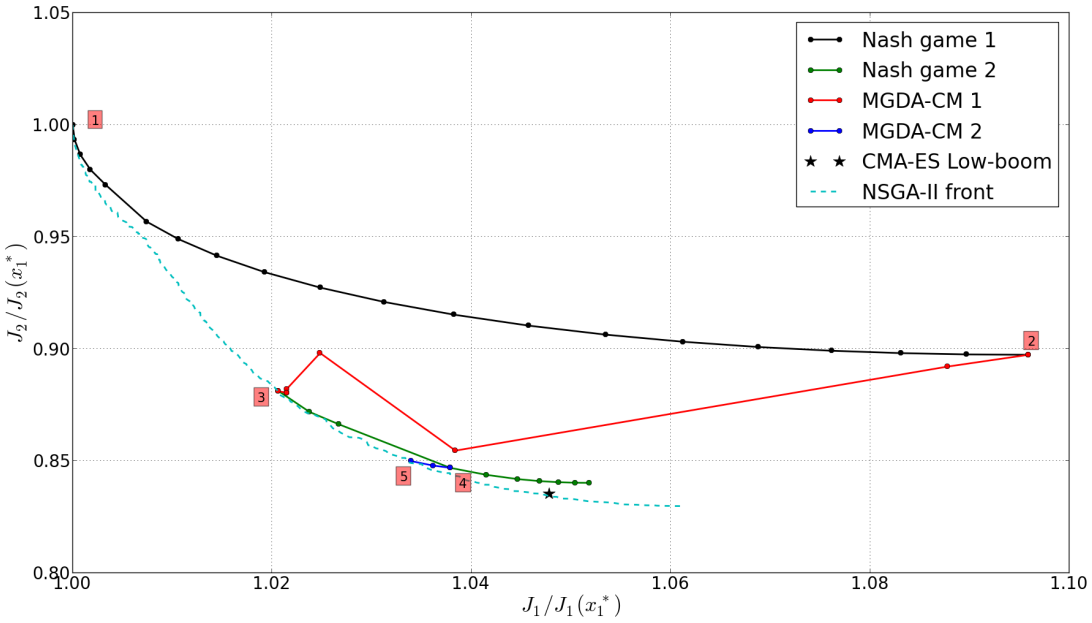

Figure 6.36: Coupling Nash games and MGDA iterations for the Pareto front exploration of the aero-acoustics problem (1/2).

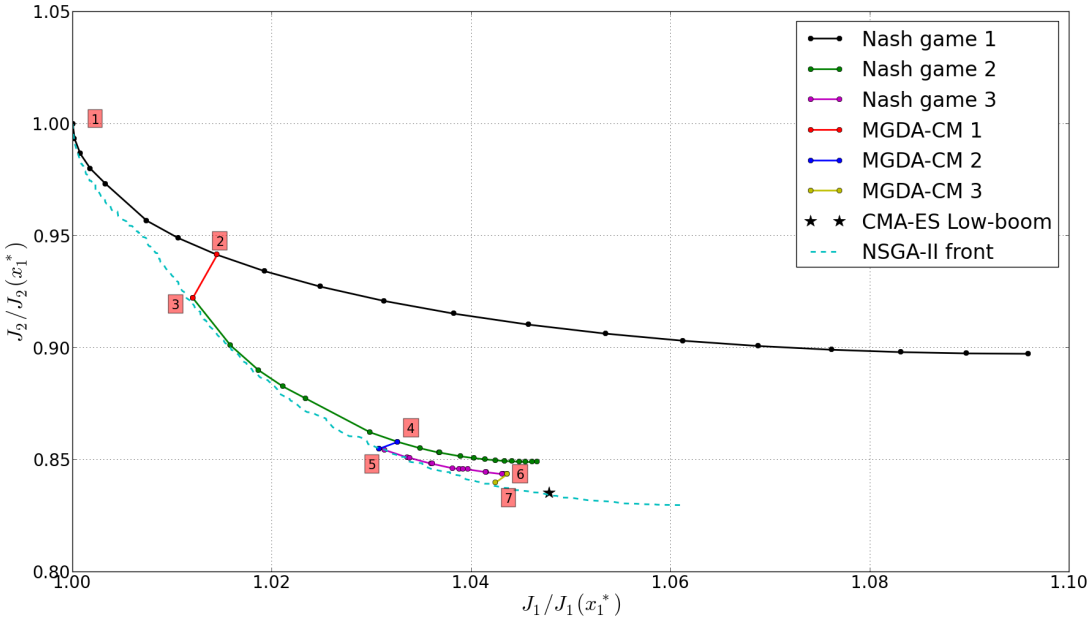

Figure 6.37: Coupling Nash games and MGDA iterations for the Pareto front exploration of the aero-acoustics problem (2/2).

Genetic multi-objective algorithms can provide multiple solutions that belong to the Pareto front and work with vector cost functions. Among the different algorithms available, NSGA-II is proven to be effective for the definition of the Pareto front of the aero-acoustic shape optimization problem.

Two innovative multi-objective optimization algorithms based on cooperation and competition have been described and applied to a low-boom/low-drag shape optimization problem of a SSBJ using either high-fidelity and low-fidelity models. The cooperation strategy is able to provide solutions

that belong to the Pareto front, still avoiding an excessive number of function evaluations required by a classical multi-objective algorithm based on evolutionary strategies and it converges with the usual accuracy of gradient-based methods. Our competitive algorithm is able to introduce a trade-off between disciplines that is not associated with an excessively severe deterioration of aerodynamics which is considered as the primary or fragile discipline. The coupling of the two strategies provides a promising methodology to explore the Pareto-set of optimal solutions at reduced computational cost compared to multi-objective stochastic optimization methods.

The application of these strategies to the aero-acoustic shape optimization of a supersonic business jet has provided the identification of several configurations thus defining a trade-off between the two discipline.

Future work aims to improve both the model, the parameterizations and the algorithms adopted. Concerning the model, the mixed-fidelity approach can be replaced by an high-fidelity approach where the gradients and Hessian are provided to the optimization algorithms using the adjoint method. As a consequence the curse of dimensionality problem of surrogate models can be avoided. An increase of the number of design variables can then provide other sets of possible configurations. Furthermore, the MGDA algorithm can be modified introducing a scaling of the gradients, e.g. inspired from Newton's method, using Hessians. This will improve the efficiency of the algorithm, in fact in single-objective optimization, when both gradient and Hessian are known, Newton's method is the most effective unless additional information is provided.

Chapter 7

Conclusions and perspectives

For years politicians have promised the Moon. I'm the first one to be able to deliver it.
Richard Nixon

7.1 Conclusions

The aero-acoustic shape optimization of a supersonic business jet has been investigated in detail in this research. The study is focused on three main objectives. The first one is the analysis of the numerical up-to-date methods for sonic boom prediction. Secondly the reduction of the sonic boom of a supersonic business jet configuration without degrading at the same time the aerodynamic performance. The third objective consists in the evaluation of innovative algorithms for the solution of the aero-acoustic multi-objective problem.

As an answer to each objective, several elements are required. The logical process followed in this analysis starts from the introduction of the physical phenomenon and the definition of the numerical models for aerodynamics and acoustics and goes to the evaluation of the performance, the analysis and the design of a supersonic business jet. Once the performance is evaluated, the reduction of the acoustic performance has been first visited through an inverse approach. To improve also the aerodynamic performance the direct shape optimization has been applied to the same configuration thus leading to the solution of a multi-disciplinary problem. The aero-acoustic problem has been first solved using "classical algorithms" (WSA, NSGA-II,...) and then considering more innovative algorithms based on cooperation and competition among disciplines. One of the outcomes is an innovative strategy to explore the Pareto front. The designer is able to "surf" over the front of non dominated solutions using Nash games and exploiting cooperation among objectives, enabling the identification of several trade-off configurations.

Novel elements have been introduced in several areas: the sonic boom prediction, the inverse design of low-boom configurations, the hybrid approach, the multi-objective optimization algorithms.

To analyze the sonic boom phenomenon, we have investigated the approaches currently adopted for the prediction of the acoustic signature at ground. The analysis has been associated with the evaluation of the sonic boom performance of a supersonic business jet. The results show that the two-layer approach, despite its limitations is a valuable tool for the early design phases. The three-layer approach has reached a sufficient maturity for the application to real aircraft configurations, in particular if it is combined with the multipole decomposition method and/or the anisotropic mesh adaptation. Mesh adaptation based on the Mach solution has improved the near-field prediction. The application of different metrics for the adaptation is an immediate perspective. The last approach analyzed, based on the direct boom prediction, requires further investigation and studies. Its application on the design of low-boom supersonic configurations is actually a perspective to be investigated.

The inverse design, which is the classical approach for the design of low-boom configuration, has been investigated as a first method to reduce the ground signature. The result is a software module called AIDA. Starting from a desired target ground signature, this module is able to identify the corresponding F-function and the area distribution of an equivalent body of revolution. The generalization of the F-function parameterization and the strategy adopted to solve for the unknown coefficients permit to consider any kind of configuration without any re-formulation of the problem. A fuselage tailoring strategy is then able to shape the real aircraft configuration. Using this method the wing-body configuration has been designed to shape the signature at ground with a flat-top. The results show that low-boom configurations can be obtained with a reduced computational time. This has permitted the submission of [25].

The single-discipline shape optimizations have demonstrated the antagonism between aerodynamic performance and sonic boom. Allowing more drastic modifications to the reference geometry, the antagonism is increased as shown by the finite difference analysis. The reference configuration shows properties close to the aerodynamic optimal configuration. The low-boom configuration slightly degrades the aerodynamic performance but at the same time obtaining a considerable decrease of the acoustic one. An innovative hybrid approach that couples inverse design and direct shape optimization is proposed to combine the two strategies. The front shock of the configuration obtained with the hybrid approach consists in a flat-top with half the amplitude of the front shock overpressure of the reference configuration.

Novel algorithms based on cooperation and competition have been previously associated with academic unconstrained applications. The aero-acoustic shape optimization is one of the first industrial test case solved with such category of algorithms. The multiple gradient descent algorithm, based on the cooperation among disciplines, has permitted to reduce the number of function evaluations, compared to a multi-objective genetic algorithm. Furthermore the adoption of a mixed-fidelity approach has reduced the number of the high-fidelity evaluations and at the same time improved the surrogate model with an update strategy. The Nash game has permitted to define a configuration close the aerodynamic optimality (1% of drag degradation) with an improvement of the acoustic performance (up to 7%). The competitive phase provides a Nash equilibrium point that does not satisfy the Pareto-stationary condition. This means that it exists at least one point that shows the same acoustic performance but with a reduced drag (or *vice versa*), and belongs to the Pareto front. The coupling between a Nash game and a subsequent cooperative gradient descent provides a solution that belongs to the non-dominated set, thus enhancing at the same time the two disciplines.

7.2 Perspectives

The result of this work does not represent the ending point for the definition of a low-boom/low-drag configuration but a starting point for further investigations.

Experimental studies have shown that the variability of the atmosphere, such as temperature gradient, wind distribution with altitude, atmospheric turbulence, etc., have an impact on the sonic boom propagation. Such non-deterministic variations impact the signature at ground leading to variations in the sonic boom overpressure and to distortions of the signature. The low-boom configurations obtained with the inverse design or with the shape optimization approach are designed at specific flight conditions taking into account the standard atmosphere without wind gradients and turbulence. The robustness of the optimized configuration to off-design conditions is a fundamental aspect that has to be investigated. Off-track sonic boom should also be investigated to ensure that the low-boom designs do not create louder booms on either side of the flight path.

In the present study only steady level flight has been considered. This flight condition represents only a phase of a complete flight mission. Maneuvers and accelerations/decelerations are included in typical missions and can yield to complex phenomenon such as caustics. From a physical point of view, a caustic is a region where sound is amplified. In terms of geometrical acoustics, it is the locus

where the ray-tube area vanishes and where the geometrical approximation breaks down. It results in a so-called "superboom" with a characteristic U-wave shaped signature. This signature is loudest with respect to the one produced during a steady level flight. The analysis of the current methods for the analysis of superboom is required. Investigations on the reference and on the steady level flight optimal configuration can identify if the design of the low-boom configuration in the reference conditions is favorable also in these off-design conditions.

In this work we have investigated independently the mesh adaptation technique and the optimization process. We have seen that mesh adaptation has a strong impact on the solution evaluated using CFD. How the mesh adaptation can impact the optimization if the two are considered all together? The ability to control the objective function discretization error will improve the confidence on the obtained optimization designs. Indeed non physical improvements of the performance due to discretization errors could be alleviated. During an optimization, a user-specified number of mesh adaptation cycles can be performed on the same configuration and the cost function evaluated on the final adapted mesh. At each iteration not only the mesh is deformed or regenerated to be compliant with the new design variables set but also adapted to the phenomenon analyzed. This fascinating perspective leads to another one. If the gradients of the aerodynamic field are available through the adjoint system, this information can be exploited not only for an aerodynamic optimization, but also for a goal oriented mesh adaptation. The adjoint solution can be used to drive the mesh adaptation. However the time required for each design iteration will increase with respect to a fixed grid approach. Further extensions consist in the use of coarse mesh at the beginning of the optimization with a progressively increasing number of mesh adaptations as we are close to the optimal solution. This procedure will reduce the number of function evaluations on the finest mesh thus reducing the total required time.

Error-based anisotropic mesh adaptation undoubtedly provides an improvement of the CFD solution. Its application to the direct sonic boom prediction from the flying altitude to the ground over a computational domain with the same size of the physical domain is a perspective to be investigated. From a computational point of view investigations are required to reduce the computational time required for each evaluation and to improve the robustness of the numerical schemes in the CFD solver when grids present high anisotropic elements. From a physical point of view, the relevant phenomena that occur during the propagation through the atmosphere have to be taken into account in the CFD simulation (e.g. molecular relaxation).

Particular phenomena can occur when two aircraft flying at the supersonic regime are sufficiently close so that the two Mach cones intersect. How they interact? Is it possible to exploit the formation flight to reduce the sonic boom at ground? Future studies aim at investigating the formation flight to reduce fuel consumption and thus effectively increasing the range of a formation by exploiting the wingtip vortices generated by the lead aircraft, thus decreasing the induced drag on the trail aircraft. Particular positions of the aircraft in the formation could be used to suppress or alleviate the impact at ground of a single aircraft with an equivalent payload of the formation.

This study focuses on a wing-body configuration. Obviously an increase of the design variables and of the geometry complexity of the configuration analyzed will be needed and could provide additional insight in the definition of a low-boom configuration. An interesting analysis is related to the engine integration and its impact on the sonic boom. The volume of the nacelle is a small contribution to the total equivalent area of the aircraft but the presence of the nacelle introduces an abrupt jump in the area distribution and consequently on the F-function. The under-the-wing engines configuration is the arrangement that is considered as conventional for a supersonic aircraft. In fact the shock losses from the nacelles can be recovered through nacelle-wing interference lift. For the reduction of the sonic boom at ground one can imagine that it is the over-the-wing engines configuration that may achieve a reduced boom. The wing can act as a shield against nacelle shock waves that are in this way reflected upward. An interesting concept to maintain the engine nacelle below the wing is to design a gull dihedral wing that forms a partial shroud around the nacelle. In addition if the nacelles

are mounted on the aft portion of the wing, the wing and nacelle wave drag tend to decrease. An engine integration solution that could be investigated is to consider engine nacelles under the wing constraining the pressure under a reflexed airfoil portion of the wing to generate positive interactions.

Finally, introduction of additional disciplines in the multi-disciplinary optimization is an obvious improvement of the design methodology of the supersonic business jet configuration as well as the multi-point optimization. Mostly interesting appears to be the introduction of an additional discipline in the cooperative phase to evaluate the efficiency of the algorithm in the identification of a common descent direction. A perspective is to consider at the same time cooperation between two or more disciplines that compete in a Nash game with another discipline.

Appendix **A**

D-SEND database analysis

Life is an experiment in which you may fail or succeed. Explore more, expect least.
Santosh Kalwar

Contents

A.1 Introduction

In the framework of an ONERA-JAXA collaboration project, the D-SEND project experimental database, provided by JAXA, has been analysed. Two axisymmetric models designed by JAXA have been dropped at high altitude and their far-field pressure signature measured during the D-SEND1 test campaign. The objective within task 1.1 is to assess numerically these pressure signatures using different approaches and tools available at Onera for sonic boom prediction. The present section describes the first part of the work in preparation of numerical CFD computations. First, the test conditions and model geometrical properties are recalled. Then the method used to find the flight conditions, which are mandatory for CFD computations achievement, corresponding to each drop test and pressure signature measurements is presented. An inverse ray-path based approach is used to find the flight conditions which are summarized in the last section. The results are compared to the ones obtained and partially published by JAXA.

A.2 The outdoor experiment

The models

The D-SEND project activities gather around two drop tests: D-SEND1-1 and D-SEND1-2. In the D-SEND1 drop test, two different axisymmetric bodies are dropped from an aerial balloon. Their pressure signatures corresponding to an equivalent sonic boom signature pattern are measured and analysed. The first one is an N-wave model (NWM), the second one is a low-boom model (LBM) for which the shape has been designed using the JSGD theory [15][16]. Some views of the available CAD models are shown in Figures A.1 and A.2. As it can be observed, the models are not completely axisymmetric, only the front part is. The rear part is equipped with stabilizers in the form of 4 fins in order to limit the impact of roll, pitch and slip momentum. The main model geometry specifications are given in Table A.1 and shown in Figure A.1 and A.2.

Configuration	Length $[m]$	Axisymmetric body radius $[m]$	Front-aft junction distance $[m]$
N-Wave	5.6	0.613	2.8
Low-boom	8	0.613	5.6

Table A.1: D-SEND model main geometrical characteristics.

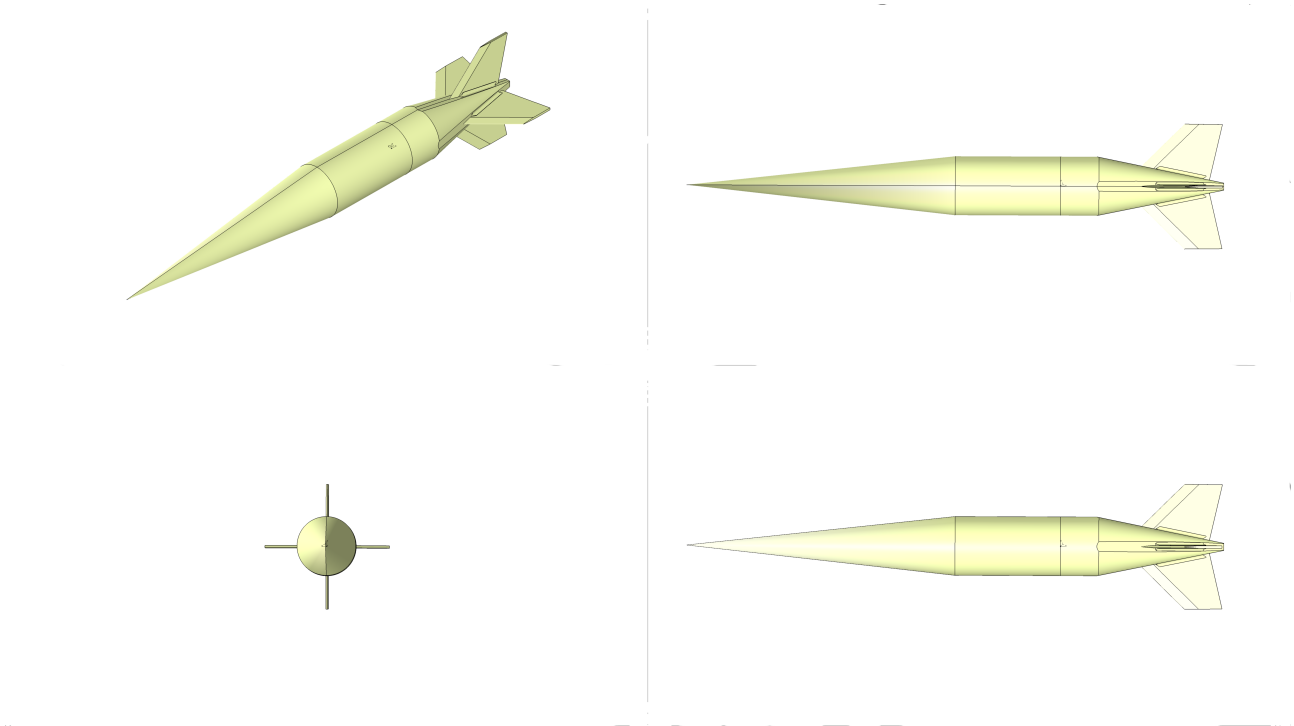

Figure A.1: D-SEND1 N-wave model.

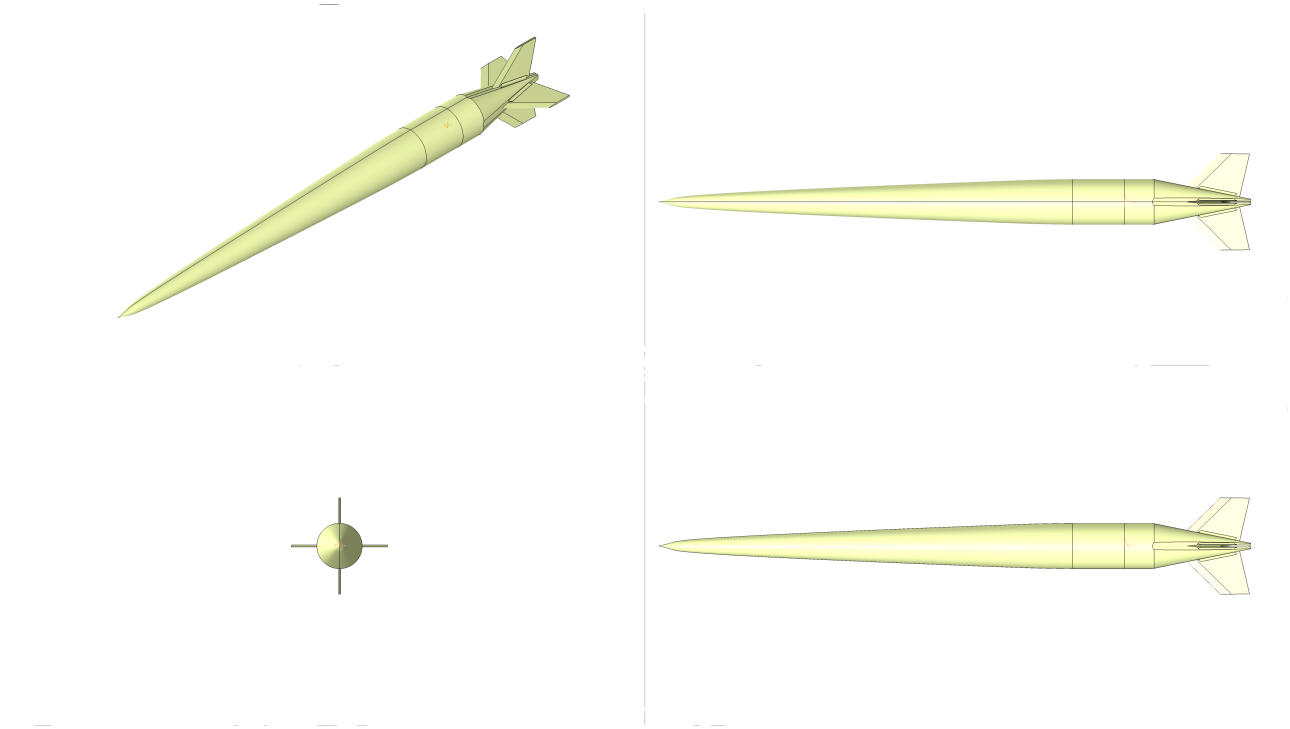

Figure A.2: D-SEND Low-boom model.

Experimental database

Database set description

The experimental database provides the atmospheric conditions from ground up to 50 km altitude, a complete set of measurements given by sensors installed on the models and the pressure signatures at two locations. The content of this database as well as some relevant plots are provided in the following sections.

Drop test set-up

Two tests have been performed at different locations and with different weather and drop conditions. The demonstrators have been elevated through the atmosphere using an aerial balloon at a measured launching altitude $\{z_{launch_i}\}_{i=1,2}$. For each test, two microphones have been placed at a distance $\{d_{mic_i}\}_{i=1,2}$ and altitude $\{z_{mic_i}\}_{i=1,2}$. The experimental set-up is schemed in Figure A.3. The available data set includes :

- the time t;
- the model Mach number M;
- the model trajectory (x, y, z);
- the altitude (z_{model}) at each time step;
- the model speed v_{model};
- the model velocity components (v_x, v_y, v_z);
- the model global drag forces and the pressure and friction trade-off (C_D, C_{D_p}, C_{Df});
- the model acceleration g;
- the atmospheric south and west wind velocities (v_{south}, v_{west});

- the model x and y pitching angles $(\theta_x, \theta y)$;
- the atmospheric pressure p_{atm};
- the atmospheric temperature T_{atm};
- the atmospheric local speed of sound a.

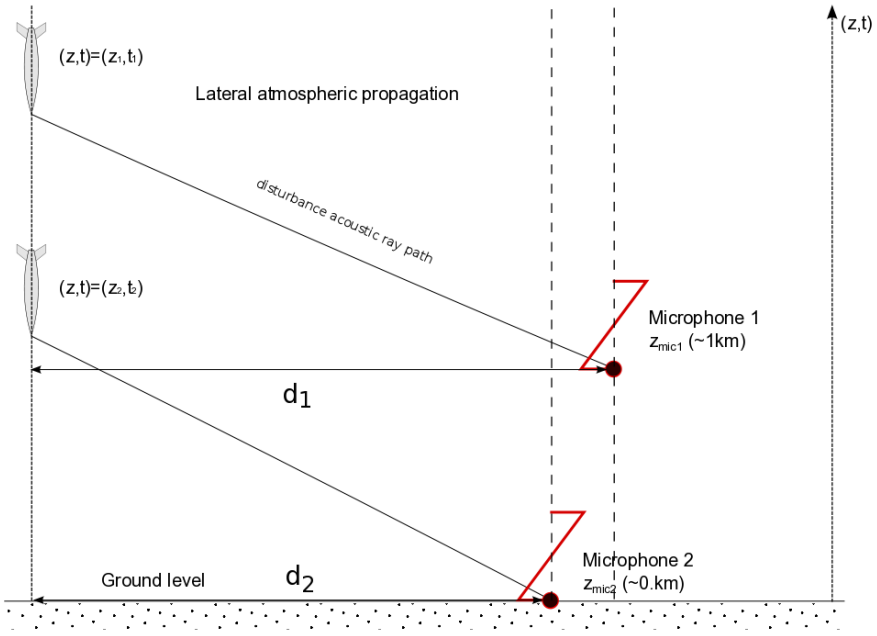

Figure A.3: Scheme of D-SEND outdoor experimental set-up.

We assume that, according to the small discrepancies in their values (around 2 m with regard to 5 km propagation distances), the altitude chosen for the present study is taken from z variable. The main experimental set-up conditions for the different drop tests and configurations are summarized in Table A.2.

D-SEND model	Test number	z_{launch} $[m]$	(z_{mic_2}, d_{mic_2}) $[m]$	(z_{mic_1}, d_{mic_1}) $[m]$
N-Wave	1	$20,935.64$	$(0; 4,176.87)$	$(954.23; 4,050.66)$
N-Wave	2	N/A (first data at :$18,853m$)	$(0; 4,459.31)$	$(1,059.46; 4,346.25)$
Low-boom	1	$20,872.7$	$(0; 4,089.82)$	$(954.23; 4,138.52)$
Low-boom	2	N/A (first data at :$15,822m$)	$(0; 4,332.84)$	$(1,059.46; 4,478.1)$

Table A.2: D-SEND1 test configurations.

Drop test measurements

The atmospheric data analysis, in terms of pressure and temperature (see Figure A.4), shows that between the two drop test campaigns, at a given altitude, there are small variations of pressure whereas strong temperature fluctuations appear (up to 12 K, corresponding to 5% variation). What must be kept in mind is that the measurements provided by the sensors installed on the model are given from ground up to 20 km, where the greatest discrepancies are observed (c.f. Figure A.5). The comparison to the US 1976 standard atmosphere model [158] shows the relevance of using real condition data

for propagation to reproduce accurate pressure signatures, especially considering the gap between the temperature curves evolutions in the Tropopause (between 11 and 21 km).

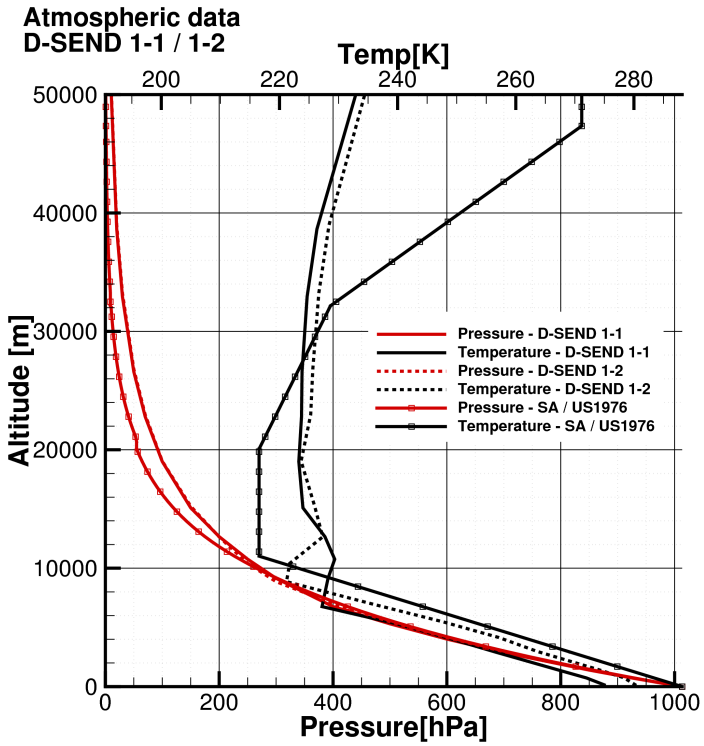

Figure A.4: Measured distribution of static pressure and temperature with respect to the altitude for D-SEND1-1 and D-SEND1-2 tests - comparison with standard US atmosphere model (1976).

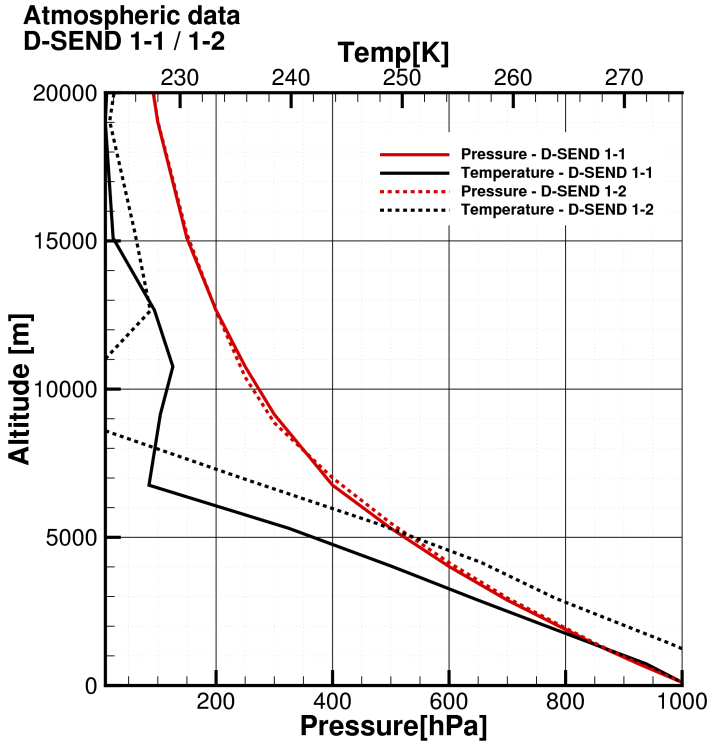

Figure A.5: Measured distribution of static pressure and temperature with respect to the altitude for D-SEND1-1 and D-SEND1-2 tests - Zoom between 20 km to ground level.

These fluctuations have a direct impact on variables such as the local speed of sound, as shown in Figure A.6, but are much less visible on the model Mach number (see Figure A.7). An inflection of the Mach number occurs as the model reaches the region of temperature rise, as shown in Figure A.8, due to the local speed rise (positive temperature gradient) and vertical speed drop. Three other variables are available: the vertical and cross wind velocities as well as the humidity level (from ground up to 9 km only for the latest). The cross wind velocity data shows a deviation from the vertical axis (slightly more than 1 km over a 20 km drop) of the models trajectories.

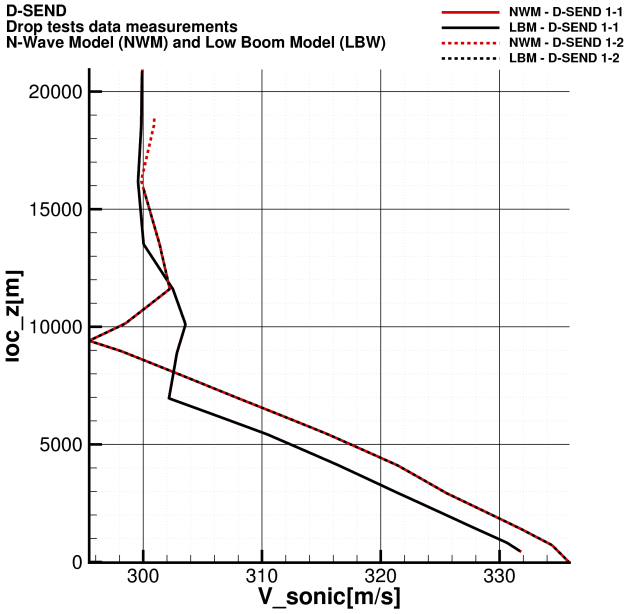

Figure A.6: Local speed of sound distribution with respect to the altitude for D-SEND1-1 and D-SEND1-2 tests.

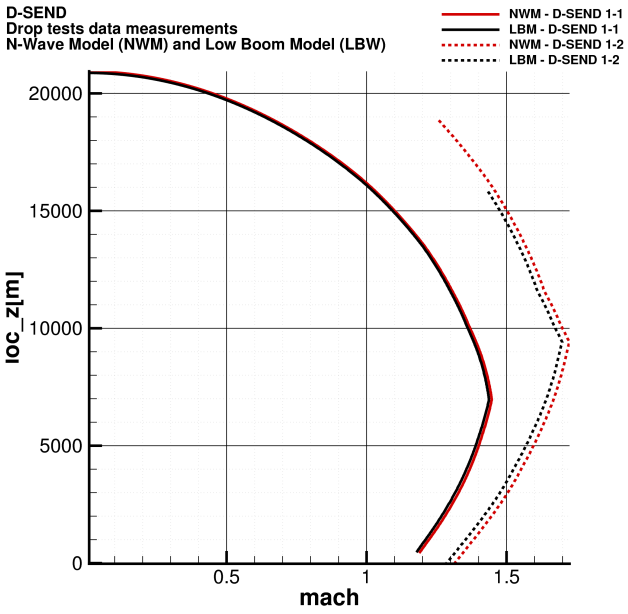

Figure A.7: Mach number distribution with respect to the altitude for D-SEND1-1 and D-SEND1-2 tests.

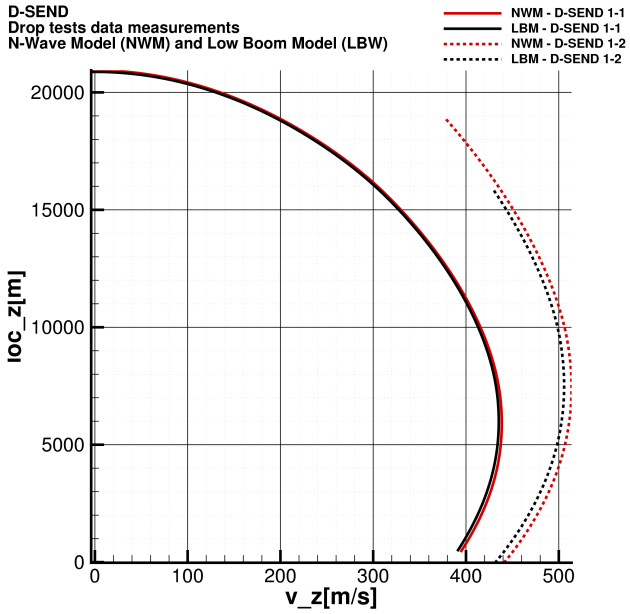

Figure A.8: Vertical velocity distribution with respect to the altitude for D-SEND1-1 and D-SEND1-2 tests.

The measured pressure signatures at the different probe locations and for both test campaigns are given in Figure A.9 for the N-wave model and Figure A.10 for the low boom model. The raw data provides the overpressure distribution over relative time scale, where the origin is shifted to fit with the nose shock wave. The ground signature data has been rescaled considering the shock wave reflection on the ground which yields doubled overpressure level measurements. Comparing the NWM with the LBM distributions, we can state that the shaping has been efficient to decrease the nose shock pressure rise, which is cut by half. The LBM signature follows also a flat-top pattern instead of the typical N-wave one, which was aimed by the JAXA LBM design. The rear shock wave is also reduced by 30% and the signal length shortened. The atmospheric condition variations have a visible impact on both signal lengths and overpressure amplitudes (difference between the D-SEND 1-1 and 1-2 tests), whatever the model. Another general remark is that the ground signatures, for all tests, show more oscillating distributions, which most probably originate from the atmospheric turbulences that the signal crosses within the last kilometer before reaching the ground. Notice that the pressure signatures initial conditions (Mach and atmosphere) differ between the two test campaigns which can also explain the small discrepancies on measurements regarding the same configuration.

A.3 Evaluation of the flight and atmospheric conditions

The first step to prepare the comparison between experiments and CFD results is to determine the right flight conditions which have resulted in the measured sonic boom signature distributions. This means that the altitude, the Mach number and the atmospheric conditions must be identified knowing that the propagation direction of the source of disturbances is assumed vertical, the pressure waves propagating laterally, contrary to usual configurations.

Approach description

To find the correlation between the ground and 1 km probes and the model disturbance emissions, a two-step approach has been used:

- Definition of the source position using a linear acoustic ray tracing technique and no-wind approximations;

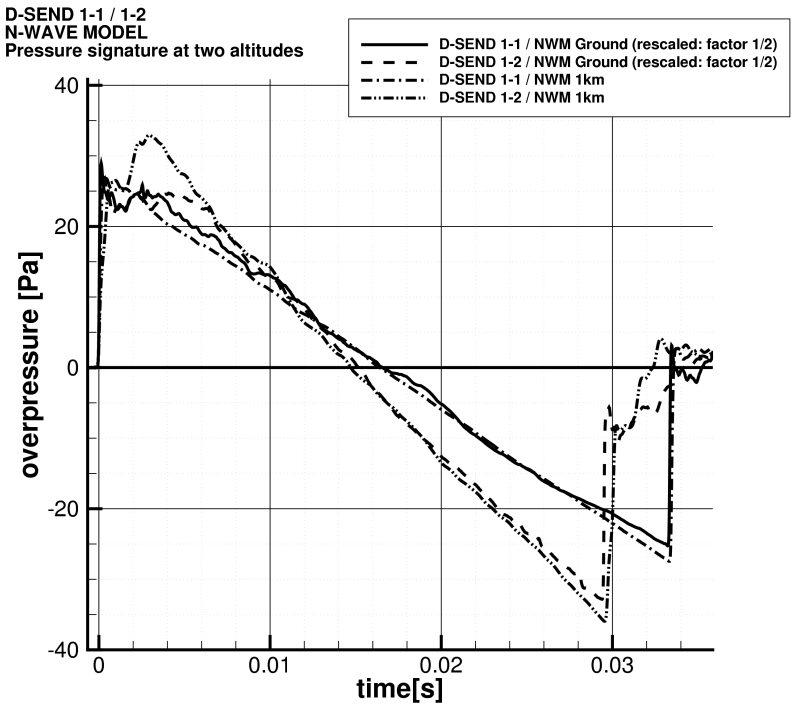

Figure A.9: Pressure signatures of N-Wave model at two altitudes for D-SEND1-1 and D-SEND1-2 tests.

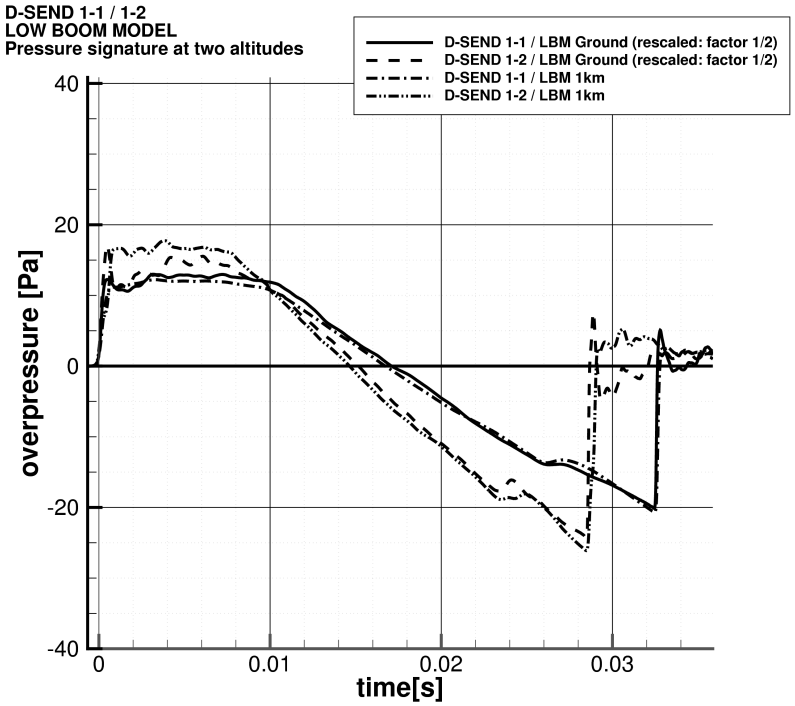

Figure A.10: Pressure signatures of Low boom model at two altitudes for D-SEND1-1 and D-SEND1-2 tests.

- Use the previous coordinates as a starting point for an iterative search algorithm using non linear acoustic ray tracing technique taking into account the atmosphere stratification as well as the cross wind.

The specificity of the present test is that the trajectory is vertical, which means that standard theory considering horizontal-like trajectories can not be used straight-forwardly. This is taken into account in the first step for the height location formulation and the methodology used for the second step is detailed in the dedicated paragraph.

Step one - Linear search

We consider the microphone location and make the first order assumption that the acoustic waves propagate normally to the Mach cone at the source. In addition the Mach cone generator is linear, which means that the propagation is independent from the atmospheric stratification. No wind correction is applied here as only a rough estimation of the source location is needed. To correlate the probe measurement with the disturbance source location, the following iterative process is considered:

- an initial guess of the Mach number M_0 is freezed;
- the corresponding Mach angle μ_0 is computed following the theoretical relationship recalled in equation (A.1):

$$\mu = \sin^{-1}(\frac{1}{M}) \tag{A.1}$$

- assuming an initial value of the distance d_{xy} (projected in (x, y) plane) between the model and the probe, compute the altitude $H = z_{mic} + \frac{d_{xy}}{\tan(\frac{\pi}{2}-\mu)}$;
- compare the assumed Mach number and the measured Mach number at the previously found altitude;
- correction of the distance from source and Mach number;
- iterate until a convergence on the Mach number is found, that is $M_{corrected} = M_{computed}$.

Step two - Ray tracing

The first step is meant to find a preliminary fair approximation of the source location using a very efficient approach. However, considering the very rich information supplied by the measurements, it has been decided to use enhanced techniques to evaluate more precisely the source location.

A classical approach in the sonic boom propagation community is the ray tracing, based on geometrical refraction law. The equations provided by Hayes (see chapter 2) are the base of our ray tracing problem but must undergo a slight adaptation. Indeed, when the aircraft moves with an almost-horizontal trajectory, the disturbances propagates downward and upward within an acceptable angular range: if the azimuthal angle $\theta = 0^o$ is set for the under track plane, then the usual range is $\pm 50^o$ for downward propagation and the symmetrical sector for the upward configuration. The continuous ray tracing generates a surface of ray paths, part of which intersects the ground, the remaining rays being completely refracted.

This approach must be adapted to vertical propagation. As the model propagates downward normally to the atmosphere stratification direction, we can consider that locally the flow conditions are uniform and that the disturbances can propagate spherically in a completely symmetrical way. This means that the ray paths are emitted in all the azimuthal directions without restriction. The refraction occurs downward and, in an atmosphere without wind, the resulting surface is axi-symmetric. From a practical point of view, the analogy with the original approach is that each ray path behaves as an under-track ray path which is not impacted by the azimuthal effects. Therefore for each azimuthal plane, the ray has been built as an equivalent under-track path. The cross wind correction has also been taken into account in the formulation with velocity coordinates projected to be consistent for each azimuth.

In the vertical trajectory case, the approach does not consider the acceleration and deceleration aspects. However, around the first estimation of the source location, it has been checked that the ray paths emitted at different times do not intersect. The locally non-accelerated model assumption is considered valid. Furthermore, the secondary carpet which can usually be observed in standard trajectory conditions is not considered here.

The standard ray equations, expressed in the fixed Cartesian coordinates (x, y, z) in the *(east,north,above ground)* reference, introduced by Hayes and *al.* are reported here for the sake of completeness:

$$\frac{dx}{d(-z)} = \frac{a(z)cos(\xi)sin(\nu) - u_x}{a(z)sin(\xi)} \tag{A.2}$$

$$\frac{dy}{d(-z)} = \frac{a(z)cos(\xi)cos(\nu) - u_y}{a(z)sin(\xi)} \tag{A.3}$$

$$\frac{dt}{d(-z)} = \frac{1}{a(z)sin(\xi)} \tag{A.4}$$

where

$a(z)$ is the local sound velocity
u_x is the x component of the cross wind
u_y is the y component of the cross wind
θ is the azimuth angle
ξ is the angle between the wave front normal **n** and its projection in the horizontal plane **n'**
γ is the angle between the aircraft velocity and its projection in the horizontal plane
ψ is the complementary angle of the velocity in the horizontal plane
$\nu = \psi - tan^{-1}\left\{\frac{cos(\mu)sin(\xi)}{sin(\mu)cos(\gamma)+cos(\mu)sin(\gamma)cos(\theta)}\right\}$

The ξ angle can be obtained through the formulation of Snell's law stating that horizontal vector component of the inverse phase velocity vector $\frac{cos(\xi)\mathbf{n'}}{c_n}$ is constant along each ray. The velocity $c_0 = \frac{c_n}{cos(\xi)}$ is invariant along the horizontal vector **n'**. The ray emitted at the source provides the ξ_0 angle which, in a horizontal trajectory is given by equation A.5.

$$\xi_0 = -sin(\mu)sin(\gamma) + cos(\mu)cos(\gamma)cos(\theta) \tag{A.5}$$

Knowing that the normal velocity is defined by $c_n = a + \mathbf{n} \cdot \mathbf{u}$, we can deduce $cos(\xi)$ as in equation (A.6).

$$cos(\xi) = \frac{a(z)}{c_0 + u_n(z)} \tag{A.6}$$

with

$$c_0 = \frac{a_0}{cos(\xi_0)} - u_{n_0} \tag{A.7}$$

The previous formulation needs slight corrections to be applied to vertical propagation. As explained previously, each ray path will be considered as an under track ray, which means that its dependence on the azimuth is strictly limited to the wind velocity vector formulation and to the geometrical rotation from the under track to the azimuthal plane (which is made in the end). To find more accurately the source of the disturbances measured by the probes, we use the following iterative process:

- freeze an initial guess of the altitude and the Mach number M_0 to the value found in step one;
- the ray paths are computed from this source for all θ considering the atmospheric conditions and the cross wind velocity;
- the intersecting curve between the the ray paths surface and the horizontal plane at the probe height is computed;

- the distance of the probe to the source is compared to the distance of the source from the primary carpet curve;
- while the discrepancy is above the convergence criteria (0.1 m in our case), the source altitude is updated by linear interpolation;
- the process iterates until the convergence criteria is reached thus providing z_{source} and M_{source}.

Results

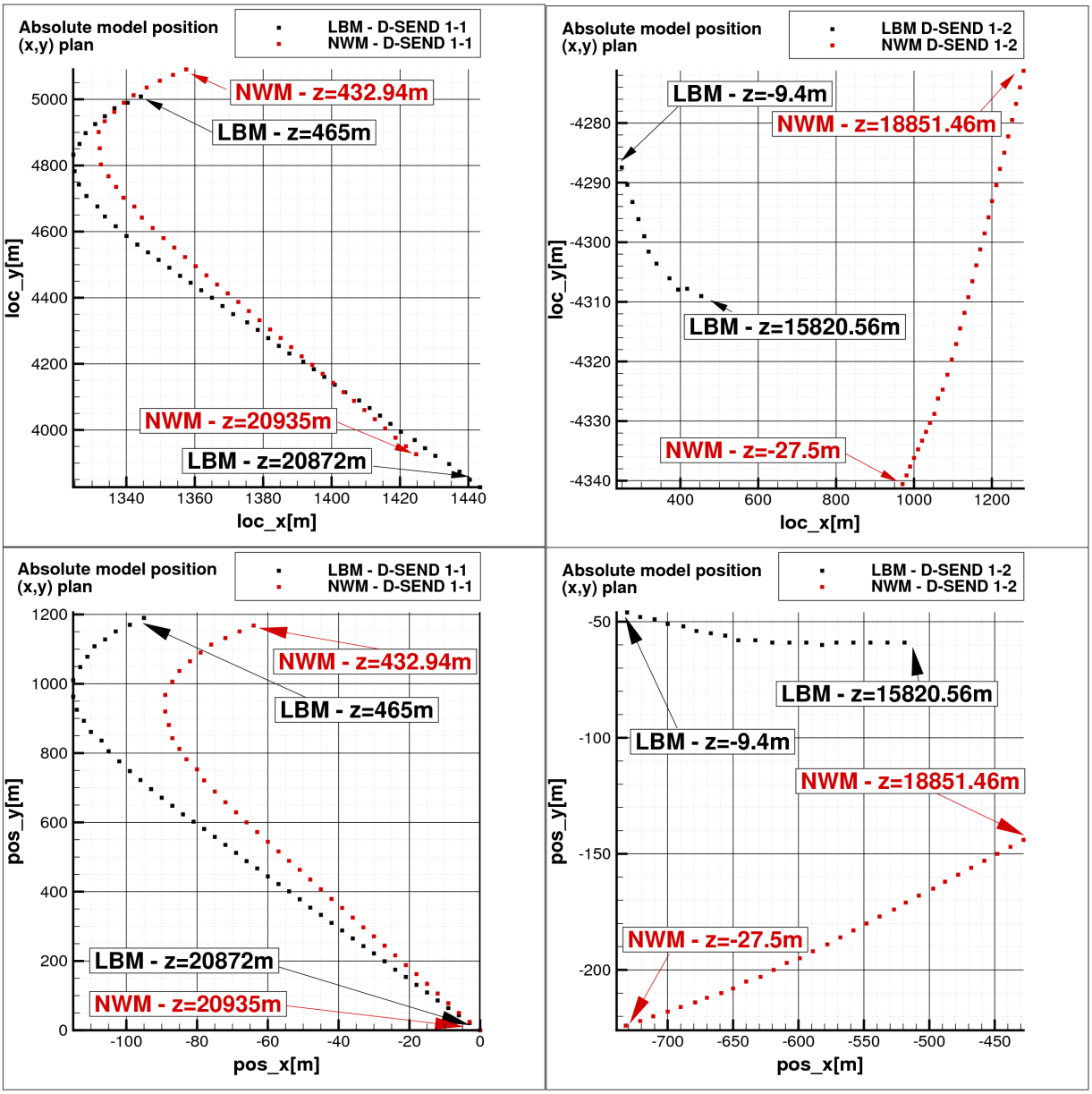

Figure A.11: Models (x, y) positions through D-SEND1-1 and D-SEND1-2 tests.

The previous two-step approach has been applied to the whole test data set and the results are summarised in Table A.3 for the ground probe measurements and Table A.4 for the probe at 1 km from ground level. The (x, y) displacement of the models measured during the drop tests campaign are summarized in Figure A.11. Through their 20 km long drop trajectory, the models deviations reach at most 1.2 km and at least 13 m. The results using the linear approach show significant differences in the Mach number values and up to 1 km shift in the source positioning. The values presented here are also compared to the one provided for the probe at altitude in [18] by Honda and Yoshida. The flight conditions are very similar except for the second test LBM data.

	NWM D-SEND 1-1	NWM D-SEND 1-2	LBM D-SEND 1-1	LBM D-SEND 1-2
Altitude (lin) (m)	5,017.532	4,361.825	4,948.685	4,216.544
Mach number (lin)	1.401	1.568	1.388	1.534
Altitude (m)	4,576.796	3,617.709	4,593.371	3,634.394
Mach number	1.388	1.535	1.377	1.508

Table A.3: Correspondence of flight condition with the pressure measurements of ground level probe.

	NWM D-SEND 1-1	NWM D-SEND 1-2	LBM D-SEND 1-1	LBM D-SEND 1-2
Altitude (lin) (m)	5,942.246	5,422.054	5,873.354	5,278.420
Mach number (lin)	1.426	1.613	1.414	1.581
Altitude (m)	5,261.085	4,542.610	5,278.446	4,550.524
Mach number	1.408	1.577	1.397	1.550
Altitude JAXA (m)	6,015	4,652	6,039	4,552
Mach number JAXA	1.43	1.58	1.42	1.59

Table A.4: Correspondence of flight condition with the pressure measurements of 1 km probe.

A.4 Conclusion and future work

The chapter summarizes the work performed until now within Task 1.1 of the ONERA-JAXA cooperation framework (Task C-14) dedicated to Low-Boom / Low-Drag Small Size Supersonic Aircraft design. The experimental database provided by JAXA on the D-SEND 1 test campaign has been post-processed. The CAD format geometries have been retrieved and analysed. The correlation between the model mounted and the ground and 1 km altitude probe measurements has been performed using an inverse ray-tracing technique. The next step will be dedicated to the cross-validation between CFD and the pressure signature measurements using a recent capability of sonic boom assessment based on unstructured CFD computations with CEDRE Onera solver and the standard multi-zone approaches.

Appendix B

Inverse design of the JAXA glider configuration

Be a part of the innovation that leads the wave. Don't wait for technology to catch up to you or you'll end up sliding down the back side of that wave. If you choose to be a part of it happening, you can ride on top.
John Landau

Contents

In the framework of the ONERA-JAXA collaboration on the low-boom/low-drag research program (Task - C14), sonic boom prediction and inverse design methods in use at ONERA have been used on a JAXA supersonic wing-body configuration and their results are reported here. The present analysis targets different objectives:

- To evaluate the aero-acoustic performance of a supersonic wing-body configuration provided by JAXA using an unstructured mesh strategy;
- To identify the potential improvements of the geometry in terms of boom annoyance using an inverse design approach.

In the first part, the CFD evaluation is performed on an unstructured grid using the Onera solver CEDRE. The pressure disturbances extracted from the CFD near-field are then propagated to the ground using the nonlinear acoustic code TRAPS in order to evaluate the under-track ground pressure signature and the associated acoustic metrics. In the second part an optimal area distribution is designed using the Onera inverse design module AIDA based on the shaped sonic boom theory.

A volume constraint has been introduced in the shaped sonic boom formulation in order to consider cabin constraints. Finally a low-PLdB configuration is proposed. An approach based on free-form deformation of the fuselage is proposed in order to obtain the geometry that corresponds to an equivalent area distribution. The different aspects concerning the sonic boom prediction and the design of a complex 3D configuration are analyzed highlighting limitations and future perspectives of research. This work constitutes the first step of the design activities of the project. Future activities will be devoted to integrate more design constraints and parameters in the design process.

B.1 Reference JAXA configuration

CFD calculation

The wing-body reference configuration provided by JAXA is shown in Figure B.1.

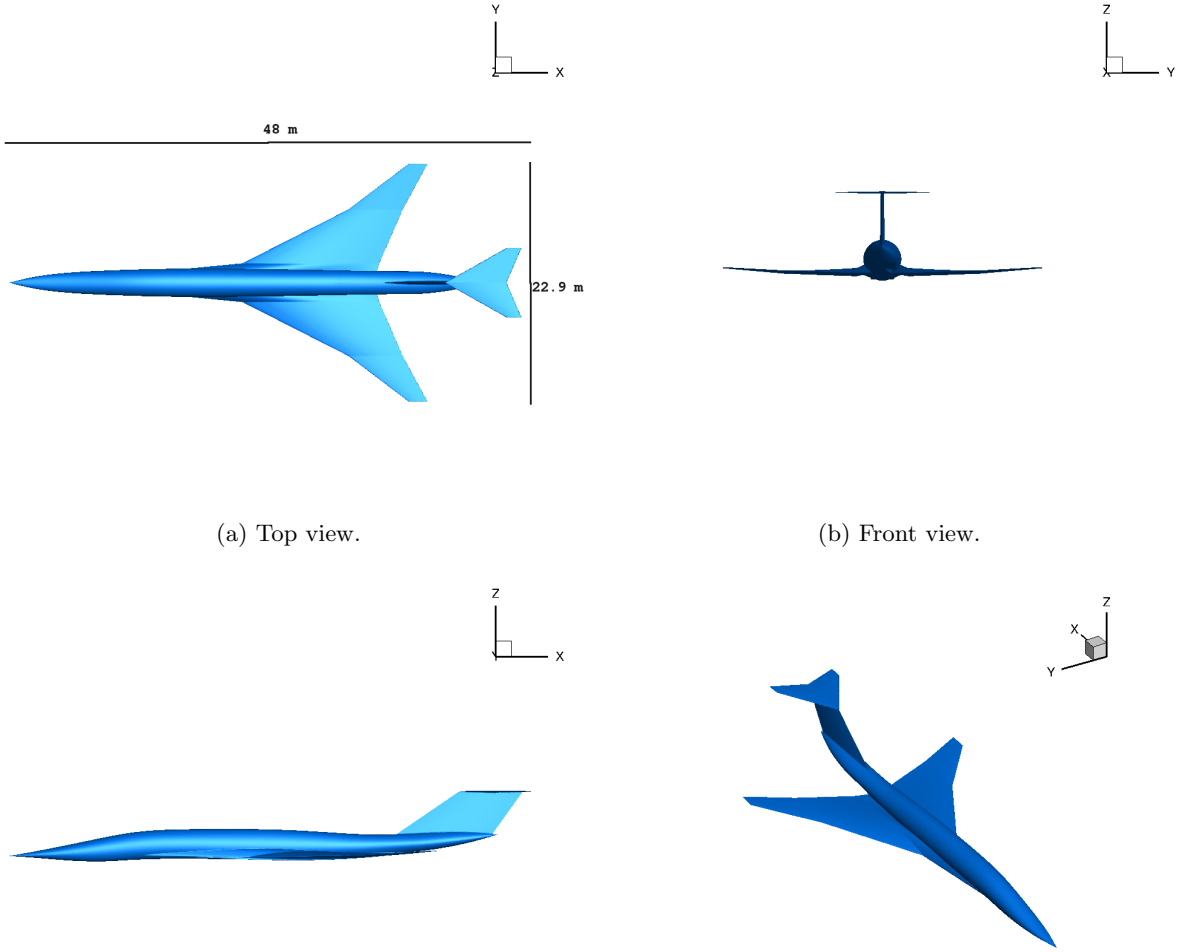

(a) Top view.

(b) Front view.

(c) Lateral view.

(d) 3D view.

Figure B.1: Reference JAXA configuration.

It is a classic supersonic business jet configuration with a sharp nose and a cranked wing. The configuration presents a T-tail plane. The unstructured mesh has been created using the Ansys ICEM Tetra mesh software [159]. The region near the aircraft where the shocks propagate has been refined as in Figure B.2b. The final mesh consists in 6,472,731 vertices, 76,608,359 faces, 287,462 faces at boundaries (214,710 on the body, 62,351 in the symmetry plane, 10,401 in the far-field).

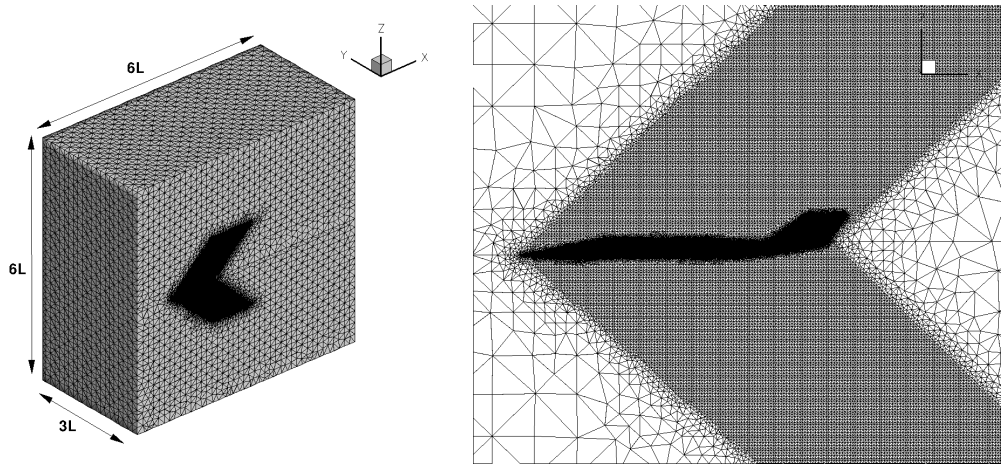

(a) Computational domain. (b) Mesh refinement near the shocks region.

Figure B.2: Unstructured mesh on the JAXA reference configuration.

An Euler CFD computation is performed using the Onera CFD code CEDRE [72] using parallel calculations on 64 cores on Altix ICE 8200 EX cluster. The flight conditions for the reference configuration are provided in Table B.1. The same numerical parameters used in chapter 4 are here applied.

Mach	Altitude	AoA	S_{REF} (wing)
1.6	15 km	3.5 deg	175 m^2

Table B.1: Reference configuration. CFD computation input.

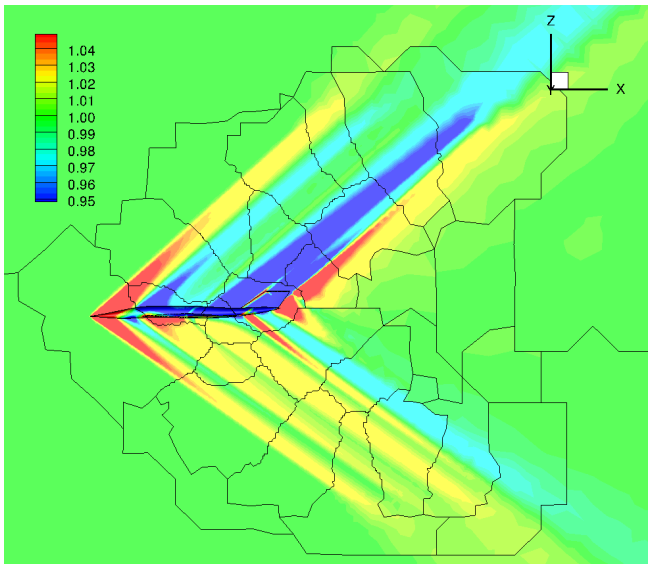

Figure B.3: Symmetry plane pressure field (p/p_∞). Reference configuration.

The resulting aerodynamic coefficients obtained from this CFD calculation are summed up in Table

c_D (3.5 deg)	c_L (3.5 deg)	c_L (3.5 deg) JAXA
0.0143	0.146	0.15

Table B.2: Reference configuration. Aerodynamic coefficients.

B.2. The lift coefficient evaluated using CEDRE appears in good agreement with the value provided by JAXA. At the present time, due to the boundary conditions specified for the computation, the solver is not able to provide the moment coefficients. The non-dimension near-field pressure on the symmetry plane is shown in Figure B.3.

A five shock pattern can be observed when the under-track signal is extracted. Among these shocks that propagate toward the ground, the nose shock has the largest amplitude followed by the shock due to the particular geometry of the rear wing-fuselage junction. This suggests that a specific re-design in these regions will improve the under-track low-boom properties of the configuration.

B.2 Sonic Boom Assessment

The CFD solution is used to feed the two and three-layer approach for sonic boom prediction. Figure B.4 shows the pressure on the aircraft skin. On the wing pressure side, compression occurs along a considerable region with amplitude less stronger than the nose region. The in-house Onera tool

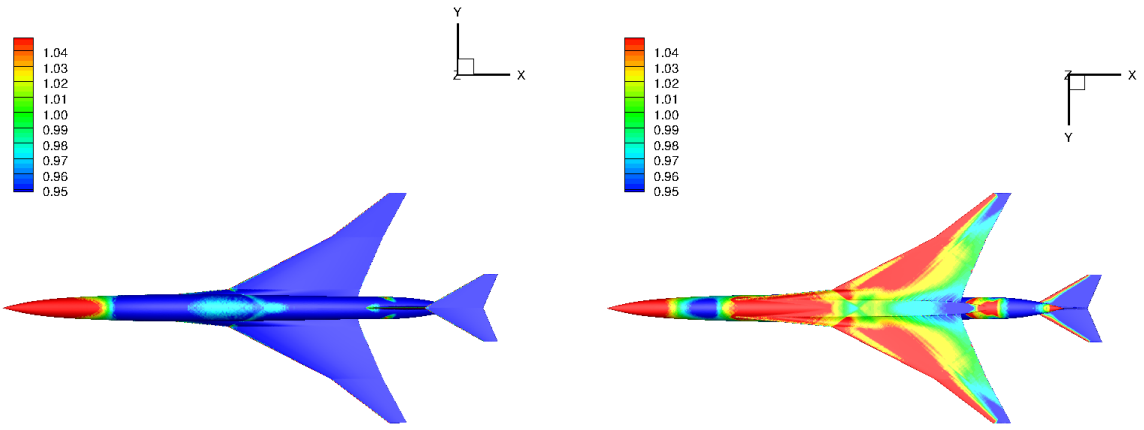

(a) Top view (b) Bottom view

Figure B.4: Skin Pressure (p/p_∞). Reference configuration.

FEsurfcut [160], acting directly on the unstructured skin mesh and the corresponding solution is able to evaluate the different contributions to the equivalent area and the F-function which is defined as:

$$F(\tau,\theta) = \frac{1}{2\pi}\int_0^\tau \frac{A_v''(x)}{\sqrt{\tau - x}}dx + \frac{\beta\cos\theta}{\rho_\infty U_\infty^2}\frac{1}{2\pi}\int_0^\tau \frac{l'(x,\theta)}{\sqrt{\tau - x}}dx \tag{B.1}$$

where A_v is the volume term, that represents the cross-sectional area distribution obtained using a cutting plane inclined at the Mach angle with respect to the flying trajectory and then projected normal to the fuselage axis, l is the longitudinal lift distribution per unit length, U_∞ and ρ_∞ are respectively the free stream velocity and density, β is the Prandtl-Glauert factor, x and τ are x-axis coordinates and θ is the azimuthal angle. Lift contribution is accounted for an equivalent area distribution A_l defined as:

$$A_l(\tau,\theta) = \frac{\beta\cos\theta}{\rho_\infty U_\infty^2}\int_0^\tau l(x,\theta)dx \tag{B.2}$$

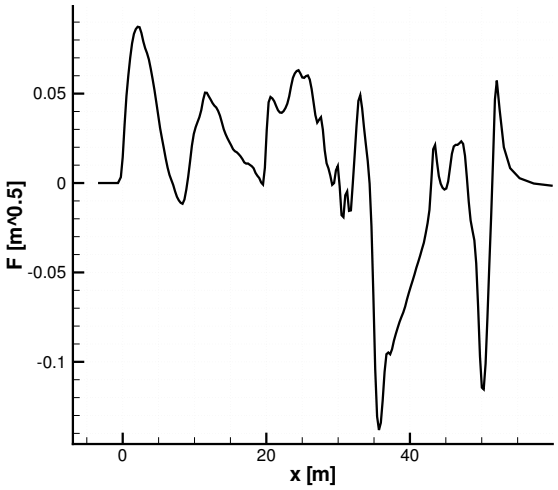

Figure B.5: Whitham F-function. Reference configuration.

The equivalent area distribution is defined as $A_e = A_v + A_l$ so that the F-function can be simply re-written as:

$$F(\tau,\theta) = \frac{1}{2\pi}\int_0^\tau \frac{A_e''(x,\theta)}{\sqrt{\tau - x}}dx \tag{B.3}$$

FEsurfcut using the unstructured skin mesh evaluates the volume distribution directly cutting the geometry with planes inclined at the Mach angle. The lift term is evaluated using the pressure distribution on the body skin obtained from CFD. FEsurfcut evaluates numerically the F-function from equation (B.3) using a finite difference approximation of the second derivative of the equivalent area distribution. The JAXA supersonic configuration F-function and A_e distribution are respectively shown in Figures B.5 and B.6.

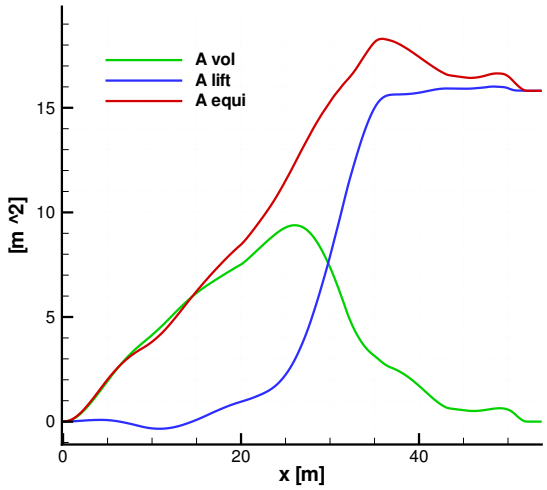

Figure B.6: Equivalent area. Reference configuration.

The configuration shows six main F-function peaks. The nose is responsible of the first peak that represents also the maximum positive value. The wing and its junction with the fuselage are responsible for the next three peaks, while the tail plane causes the remaing peaks. Looking at the area distribution, the volume and the lift term, due to the size of the glider configuration, have the same impact on the equivalent area and no one dominates the other. The pressure signature in the near

field evaluated using the CFD solution is shown in Figure B.7 at two distances beneath the aircraft. Its trend is similar to that of the F-function for the positive part, while the strong negative peaks of the F-function rapidly coalesce into a single depression.

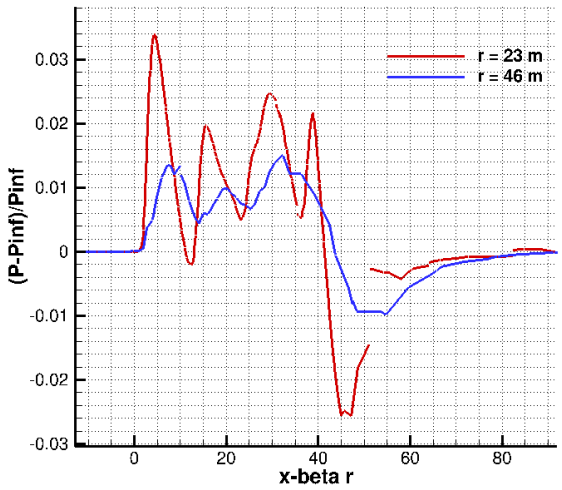

Figure B.7: Under-track pressure perturbation in near-field. Reference configuration.

To evaluate the under-track ground signature the three-layer approach introduced in chapter 2 is first adopted. The pressure near-field is extrapolated on a cylinder aligned with the flow direction. The cylinder, discretized with a structured mesh, has a ratio $R/L = 1$ where R is the cylinder radius and L is the reference configuration length equal to 48 m. The information is used as input for the nonlinear propagation using the acoustic code TRAPS.

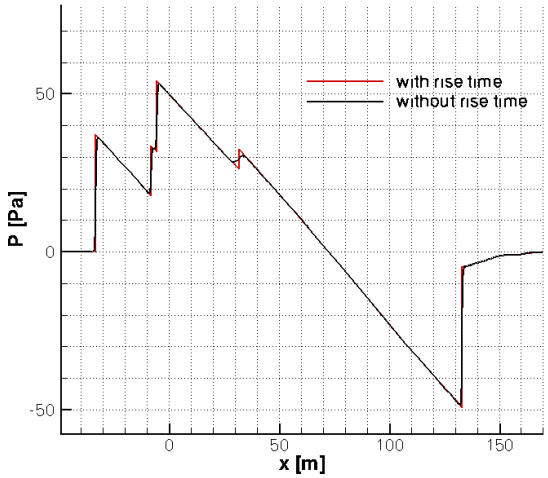

Figure B.8: Ground signature. Reference configuration.

Figure B.8 shows the undertrack signature after a post-processing on the signal that aims to introduce a Taylor shock structure with rise time in [ms] equal to $1/\Delta p[psf]$. The signature shows two independent shocks at the front, with a similar amplitude (around 35 Pa) and an aft shock. The acoustic deciBel metrics evaluated on this signal show high values in particular for the Perceived Loudness deciBel (PLdB) (see Table B.3). The ground signature is compared with the one obtained via the two-layer approach. The propagation code is able to use directly the F-function and to perform the propagation to the ground.

dB	dBA	dBC	PLdB
115.73	85.17	102.84	99.39

Table B.3: Acoustics metrics on ground signature. Reference configuration.

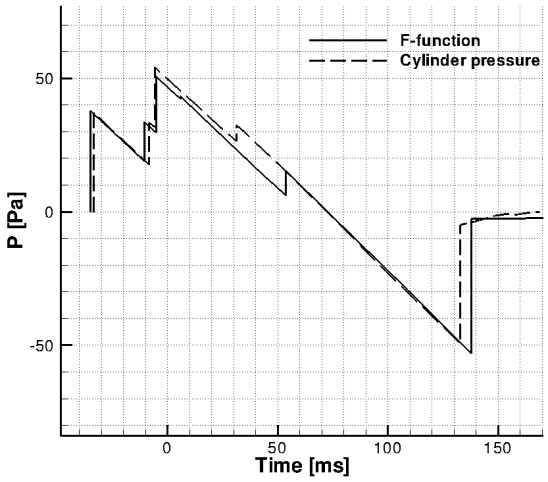

Figure B.9: Ground signature. Comparison between F-function method and pressure extrapolation.

Figure B.9 shows the comparison between the two methodologies for evaluating the ground signature. Results shows good agreement, the discrepancies are mainly due to two aspects that occur in the CFD based methodology:

- numerical dissipation in the near-field;
- non axi-symmetrical effects that still persists at $R/L = 1$.

Considering the first point, pressure can be evaluated also directly from the F-function using the following equation:

$$\Delta P(\tau, \theta, r) = p_\infty \frac{\gamma M_\infty^2}{\sqrt{2\beta r}} F(\tau, \theta) \tag{B.4}$$

The pressure distributions shown in Figure B.7 are used to evaluate the F-function compared to the one provided by FEsurfcut (see Figure B.10). In the first part of the signal, numerical dissipation and non axi-symmetrical effects reduce the peaks amplitude, but it is still possible to recognize a common pattern. The second part of the F-function shows more differences mainly due to two aspects:

- Mesh is not well adapted to take into account vertical T-tail shock;
- The rear part of the pressure field shows more non axi-symmetrical effects due to geometry complexity.

Considering the impact of non axi-symmetrical effects and using as reference the work of Plotkin [2], the methodology based on F-function multipole decomposition developed at Onera (see chapter 2) is here adopted. The objective of this method is to take into account non axi-symmetries of the flow field over the extrapolation cylinder, thus enabling the cylinder R/L reduction. Figure B.11 shows the pressure field over the extrapolation cylinder with no multipole matching and considering multipole decompostition. The pressure under-track using different multipole decomposition (n= 0, 10, 20, 25) is shown in Figure B.12. Results show limited modifications of the shock amplitude in the first part of the signal. The rear part is characterized by an increase of the flow non axi-symmetries, and as

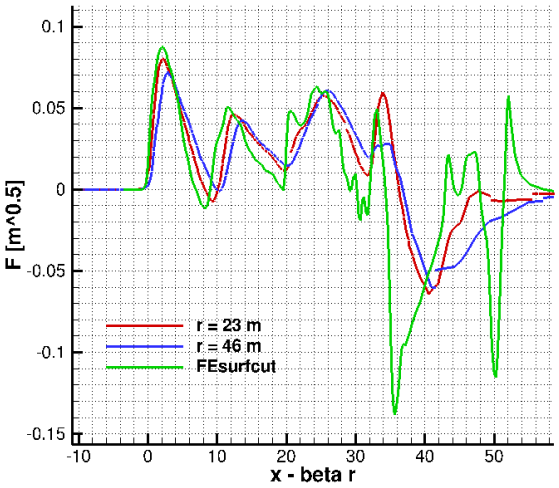

Figure B.10: Comparison of F-function obtained from pressure signal and FEsurfcut.

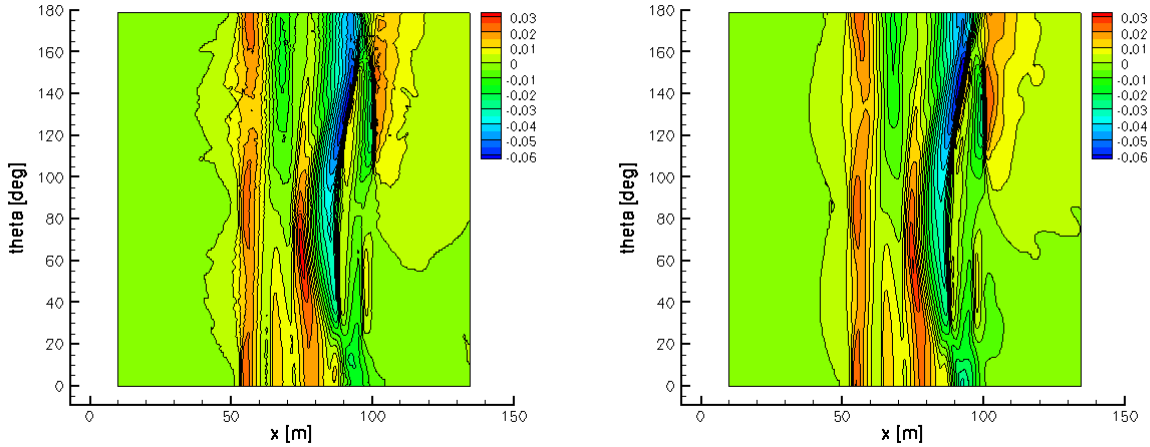

(a) No matching.

(b) Multipole matching with n=20.

Figure B.11: Pressure $((p - p_\infty)/p_\infty)$ extrapolated over a cylinder (R/L=1).

a consequence the result is strongly affected by the multipole decomposition. The decomposition shows convergence for n around 20. Increasing the number of multipoles results in oscillations of the solution as already highlighted in [9]. The pressure field decomposed with $n = 20$ multipoles is used to perform atmospheric propagation. Figure B.13 shows the ground signature using or not the multipole matching. The two signatures have the same shape, but with significative amplitude differences in the rear part of the signal. Multipole decomposition is a suggested operation to be performed when complex non axi-symmetric configurations are analyzed.

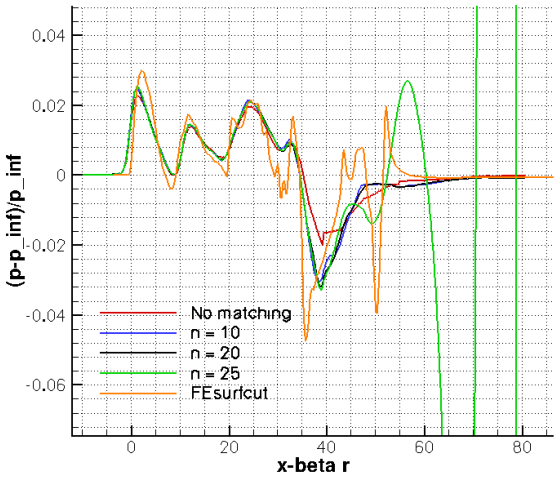

Figure B.12: Pressure undertrack on the cylinder (azimuthal angle $\theta = 0$ deg).

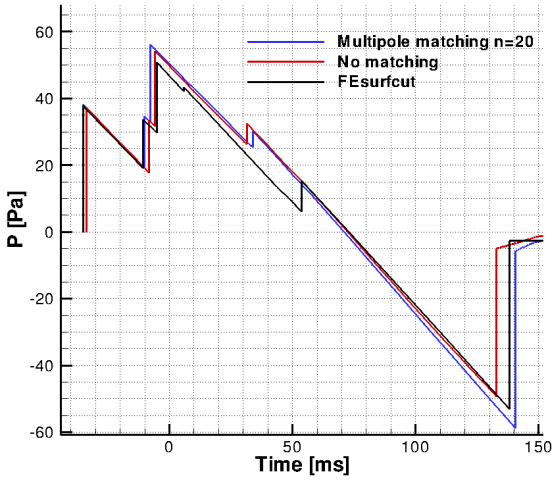

Figure B.13: Ground signature. Comparison between multipole decomposition matching, simple matching and FEsurfcut.

B.3 Inverse design approach

In this section we aim at defining a relevant target equivalent area compliant with the flying conditions and volume constraints of the JAXA reference configuration analyzed in the previous section. Several phases are required in the design process:

- Definition of a shaped ground signature;
- Identification of the equivalent area distribution, F-function and loudness level;
- Introduction of a volume constraint if required;
- Evaluation of a low-boom configuration;
- Identification of the corresponding geometrical area distribution using a fuselage tailoring based on direct shape optimization.

The inverse design approach, based on the Whitham theory, aims to define the geometry of an equivalent body of revolution that corresponds to a shaped ground signature. The JAXA configuration is reshaped using the inverse design module AIDA described in details in chapter 4 in order to obtain a low-boom configuration with a shaped ground signature. At the end of the design, several equivalent area distributions will be available for further investigations. The F-function parameterization is based on the generalization proposed by Plotkin et al. [81] already schemed in Figure 4.5. The corresponding F-function and A_e are respectively written in equations (4.10) and (4.11).

The input values provided to AIDA for the present application are summarized in Table B.4. The

Variable	Value	Variable	Value
M	1.6	η	0.5
L	52.096 m (170.92 ft)	η_2	0
W	33,300 kg (73413.9 lbs)	η_3	η
B	0	β_0	0
y_f	3 m (9.84 ft)	β_2	0
t	0		

Table B.4: Input values for design test case.

weight is evaluated in order to satisfy the following equation:

$$W = \frac{\rho V^2}{\beta} \left[A_e(L, \theta = 0^\circ) - A_{eng}(L, \theta = 0^\circ) \right] \tag{B.5}$$

In the present study the engine stream tube area A_{eng} is neglected as only glider configurations are considered. The length adopted is based on the effective length defined as:

$$l_e = L\cos(\alpha) - L\frac{\sin(\alpha)}{\tan(\mu)} \tag{B.6}$$

where L is the aircraft length, μ is the Mach angle and α is the angle of attack equal to 3.5 degrees. AIDA provides the F-function coefficients shown in Table B.5. The corresponding equivalent area A_e, F-function and the ground signature obtained after the propagation from a flight level of 15 km in a standard atmosphere are shown respectively in Figures B.14, B.15 and B.16. The equivalent area distribution obtained using AIDA - from now on AIDA configuration - is compared with the one of the reference configuration. The new one shows less curvature changes aiming at reducing the F-function discontinuities of the first derivative that corresponds to shocks. The new configuration shows a flat-top ground signature with a maximum shock overpressure of 26 Pa, reduced by more than 10 Pa compared to the reference JAXA configuration. The secondary shock that occurs in the reference configuration is completely avoided in the AIDA shaped configuration. The evaluation of the deciBel metrics is shown in Table B.6. The PLdB level is reduced from 99 to 89 simply acting on the shape of the configuration. One can note that, if the evaluation of the geometry that corresponds

H	D	C_0	y_R	λ
0.17298	0.02479	0.03828	221.05817	103.27988

Table B.5: F- function coefficients (Imperial system unit).

dB	dBA	dBC	PLdB
112.04	75.26	95.27	89.41

Table B.6: Ground signature acoustics metrics. AIDA shaped configuration.

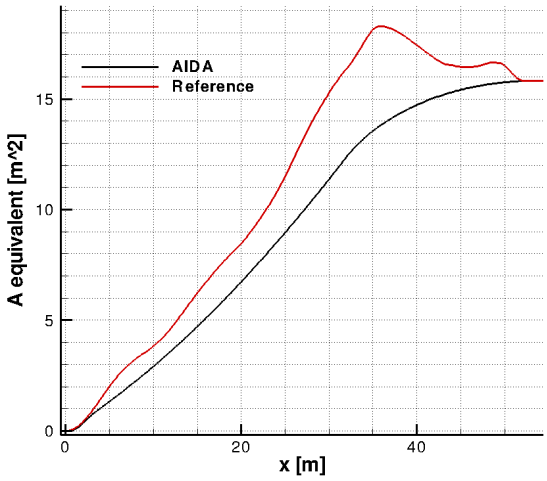

Figure B.14: Equivalent area. AIDA shaped configuration.

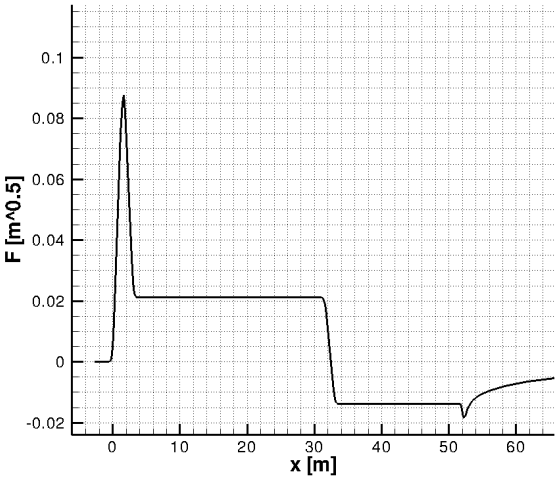

Figure B.15: Whitham F-function. AIDA shaped configuration.

to the shaped A_e distribution is based on the fuselage tailoring, the volume of the designed shape is reduced. Volume constraints are not considered in the shaped sonic boom formulation, but could be required in the development of a real aircraft design process. The formulation proposed in [15] and [16] can be modified in order to introduce a sort of volume constraints that enable the designer to relax the modifications of the configuration without compromising the shaping of the ground signature. The idea is to fix only a local value of the equivalent area distribution at a location defined by the designer. In the present case $A_e(\lambda) = 15\ m^2$ is considered. AIDA tends to satisfy this value but a complete satisfaction of the constraint is not guaranteed. This is mainly due to the fact that AIDA is based on a L-BFGS-B optimization algorithm to solve for the unknown coefficients. Variable boundaries are fixed and a solution that strictly respects the volume constraint could not be assured. Using the same input values shown in Table B.4 a modified version of AIDA that takes into account a volume soft constraint provides the coefficients shown in Table B.7 The evaluation of the loudness metrics is shown in Table B.8.
In Figures from B.17 to B.19 are shown comparisons between the reference and the shaped configurations. The two shaped configurations show the desired flat-top in the signal, but the introduction of the volume constraint induces significative differences. The amplitude of the front shock overpressure

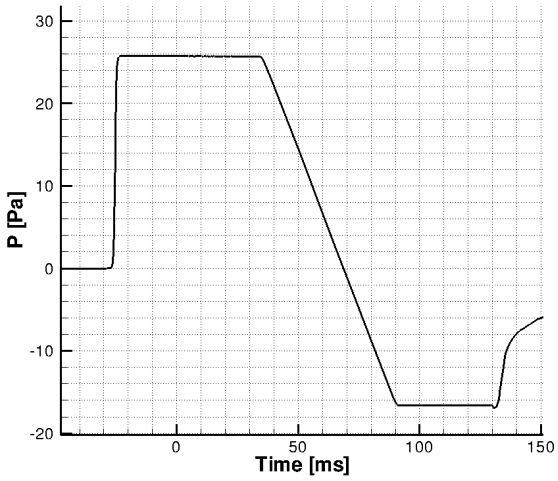

Figure B.16: Ground signature. AIDA shaped configuration.

H	D	C_0	y_R	λ
0.18010	0.024067	0.03902	222.0267	100.4025

Table B.7: F- function coefficients (Imperial system unit).

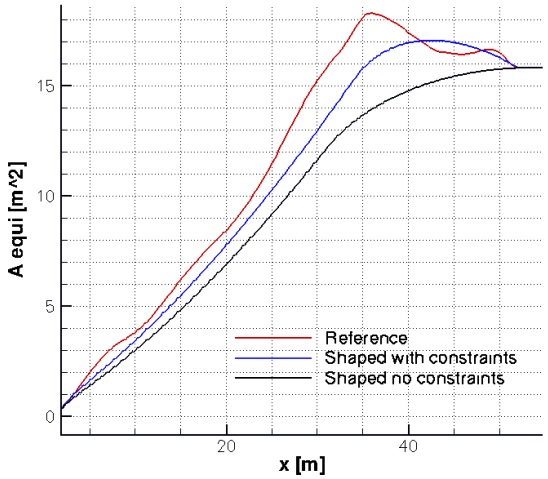

Figure B.17: Equivalent area. Shaped configuration with and w/o volume constraint.

is increased and the rear shock shows a limited flat-top region with an amplitude twice the shaped one without constraints. Both shaped configurations show shocks amplitude reduced with respect to the reference configuration and multiple shocks are avoided. Once the constraint is introduced into the design, to reduce the PLdB level of the configuration with constraint, the methodology proposed in section 4.5 and shown in Figure 4.28 is applied. The user defined parameters of AIDA are optimized in order to define a low-PLdB configuration. In particular the design variables and their respective lower and upper bounds are shown in Table B.9. The optimization is performed using GADO [89], a genetic algorithm implemented in the optimizer Dakota [90]. The other inputs required are shown in Table B.10.

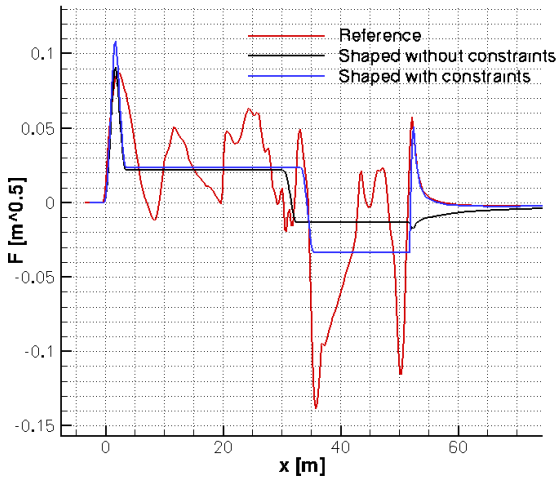

Figure B.18: Whitham F-function. Shaped configuration with and w/o volume constraint.

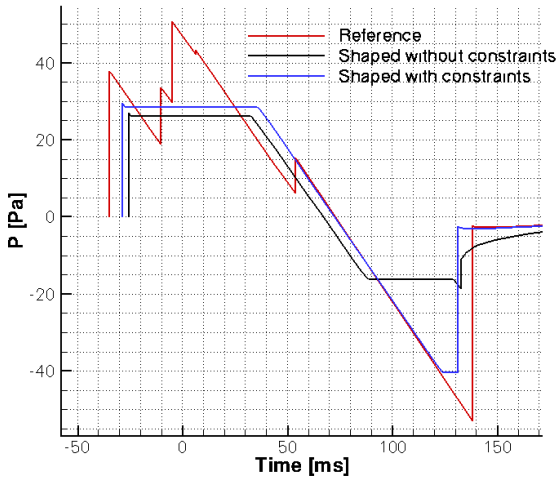

Figure B.19: Ground signature. Shaped configuration with and w/o soft constraint.

dB	dBA	dBC	PLdB
114.118	81.851	100.334	95.912

Table B.8: Ground signature acoustic metrics. Shaped configuration.

The optimized coefficients (Table B.11) results in a configuration that creates a 93.139 PLdB ground signature (see Table B.12). The low-boom configuration is shown in Figure B.20.
The F-function shows an increased amplitude of the first peak followed with a negative slope segment that results in a decompression in the ground signature instead of a flat-top. The rear shock shows a reduction of more than 5 Pa with respect to the flat-top shaped configuration. The equivalent area clearly shows that the volume constraint is well-satisfied by both configurations. All three shaped configurations are valuable candidates for the re-shaping of the JAXA wing-body configuration.

Variable		Lower bound	Upper bound
B_i	$\forall i \in [1, N+P]$	-3 x 10^{-4}	8 x 10^{-4}
β_0		1 x 10^{-5}	0.1
β_2		-0.1	0.1
t		0	5
η		0.2	0.8
y_f		5	15

Table B.9: Design variables and bounds for F-function optimization.

Variable	Value	Variable		Value
M	1.6	$\lambda_{1,1}$		$y_f + 30$
L	52.096 m	$\lambda_{2,1}$		$\lambda + t + 5$
W	33,300 kg	$\lambda_{1,i}$	$\forall i \in [2, N]$	$\lambda_{1,i-1} + 30$
N, P	3	$\lambda_{2,i}$	$\forall i \in [2, P]$	$\lambda_{2,i-1} + 5$
H	15,000 m			

Table B.10: Additional fixed input values.

- Variable	Value	Variable	Value
B_1	-0.0001	B_4	9.982 x 10^{-5}
B_2	-0.0001	B_5	-5.049 x 10^{-5}
B_3	-0.0001	B_6	0.0001
η	0.2353	y_f	5.0350
β_0	0.1	t	0
β_2	-0.1		

Table B.11: Optimized value of the coefficients.

B.4 Free-form deformation

Free-form deformation (FFD) is a deformation technique that originates from computer graphics [161]. FFD approach operates on the whole space regardless of the representation of the objects to be deformated. Instead of manipulating the object directly, FFD deforms a lattice that was built around the object. The lattice is a space of an arbitrary volume which wraps around the object. It is a versatile approach, able to treat complex shapes avoiding remeshing. Displacements of the lattice control points modify the shape embedded in the space defined by the control volume. Any explicit parameterization is required [162]. The objective is to adopt this technique for the fuselage tailoring of the JAXA configuration. The lattice volume is defined as in Figure B.21. The lifting surfaces are outside the deformed volume to avoid modifications of the lift area distribution. The lattice is defined by 22 longitudinal sections. Each section is defined by 3 points in the y-axis direction, and 2 points in the z-axis direction. To avoid wavy configurations and deformations outside the domain defined by the symmetry plane, points are constrained to move only along the vertical axis. Furthermore points that belong to an edge are constrained to move toghether by the same displacement. Some edges of the lattice (shown in red in Figure B.21) are fixed in order to prevent undesired deformations of the wing and the tail plane. To sum up 25 edges (shown in blue in Figure B.21) are allowed to be modified and represent the design variables of the tailoring phase.

Geometry modifications on the rear part of the fuselage are limited, so that the target shaped design for this first experience is modified to be closer to the initial configuration area distribution aft part. An additional volume constraint is added $A_e(x = 35m) = 18m^2$. The obtained design is shown in Figure B.22.

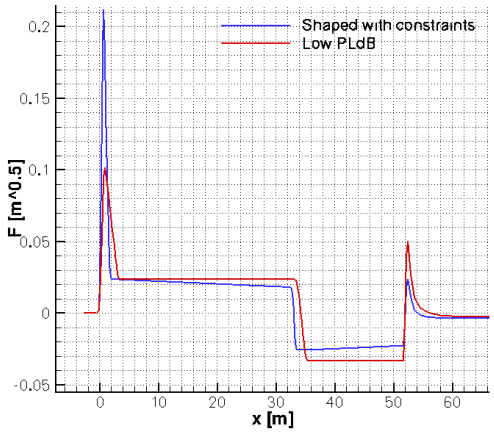

(a) F-function.

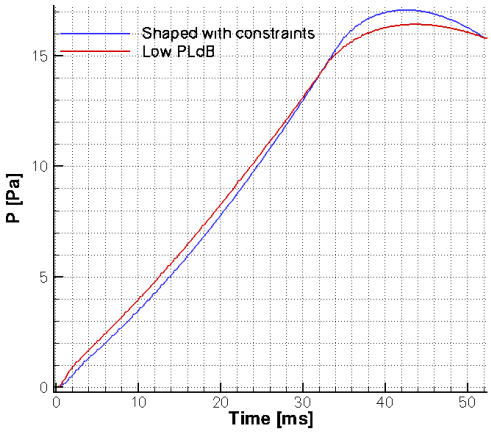

(b) Equivalent area.

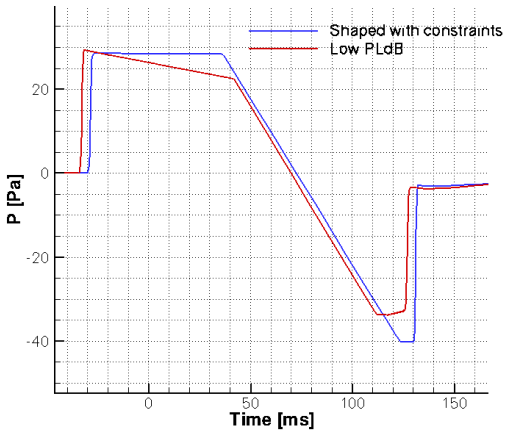

(c) Ground signature.

Figure B.20: Low-PLdB configuration.

dB	dBA	dBC	PLdB
113.169	78.984	98.469	93.139

Table B.12: Ground signature acoustic metrics. Low-PLdB configuration.

The fuselage tailoring is based on the minimization of the following functional:

$$J_{A_e} = \int_0^L |A_e(x) - A_e^{target}(x)|dx \tag{B.7}$$

The algorithm adopted is GADO implemented in the platform Dakota. Convergence is achieved after less than 3000 evaluations with a reduction of the cost function by more than 80% of the initial value (see Figure B.23). Figure B.24 shows the equivalent area distribution obtained after the fuselage tailoring via free-form deformation. The result shows a good approximation of the target in the region before the tail plane ($x < 35m$). This is essentially due to the fact that in this region the volume term of the tail plane and the lift contribution are preponderant with respect to the fuselage volume term. If one wants to reduce the difference among the tailored and the target configuration, modifications of the tail plane are strictly required. Despite this and the oscillations shown in the

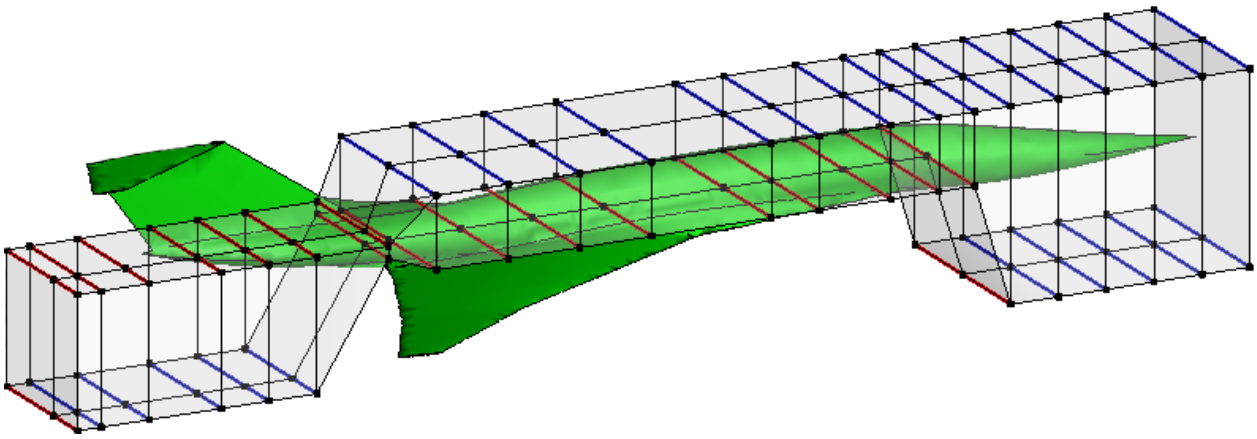

Figure B.21: Initial configuration and the corresponding free-form lattice. In red the fixed edges, in blue the free edges.

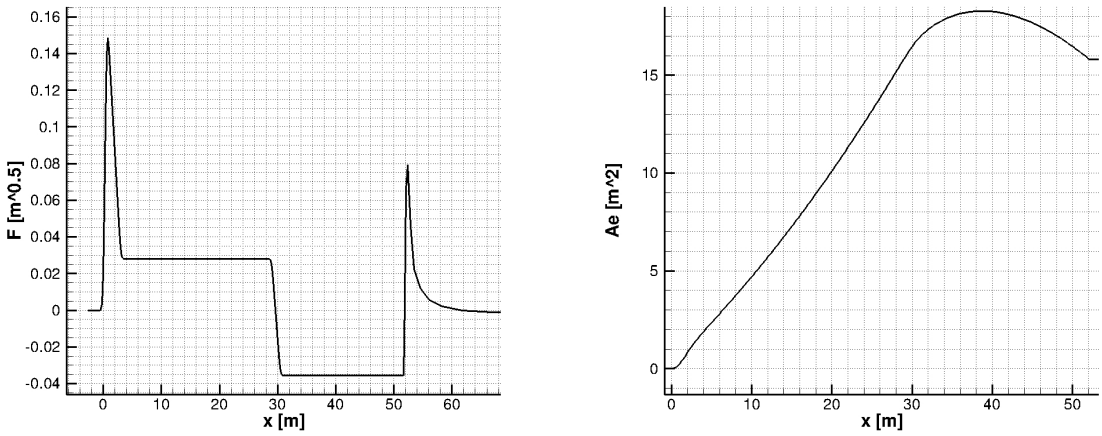

(a) F-function

(b) Equivalent area

Figure B.22: Shaped design for Free-Form deformation.

F-function (see Figure B.25) the resulting ground signature (Figure B.26)shows a flat-top described by a multi-shocks pattern. Figures B.27 and B.28 shows the initial and the tailored configurations. The tailored configuration has a nose deflected upward, while the fuselage cabin radius is increased in order to achieve the target equivalent area distribution. Further studies on the parameterization are required. In particular lifting surfaces must be deformed by the free-form lattice at least at the beginning of the tailoring process.

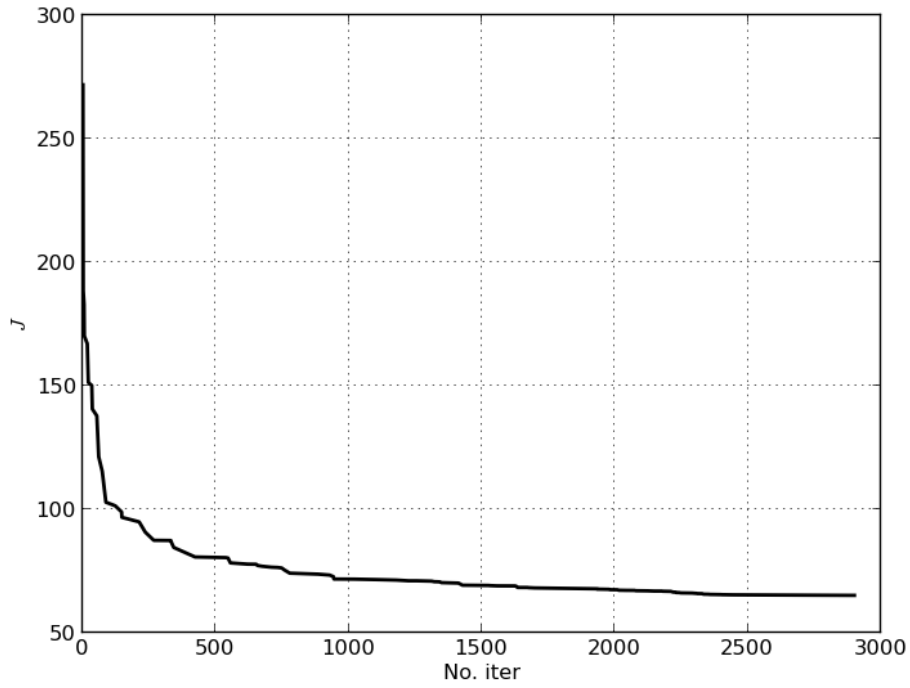

Figure B.23: Convergence of the objective function for geoemtry deformation.

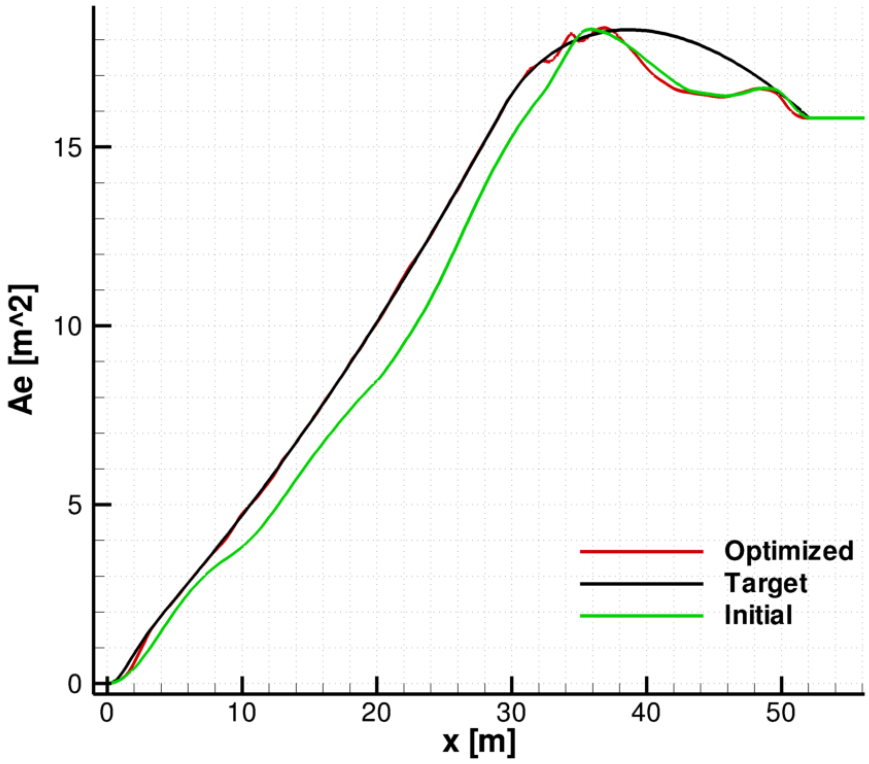

Figure B.24: Comparison of the obtained equivalent area distribution.

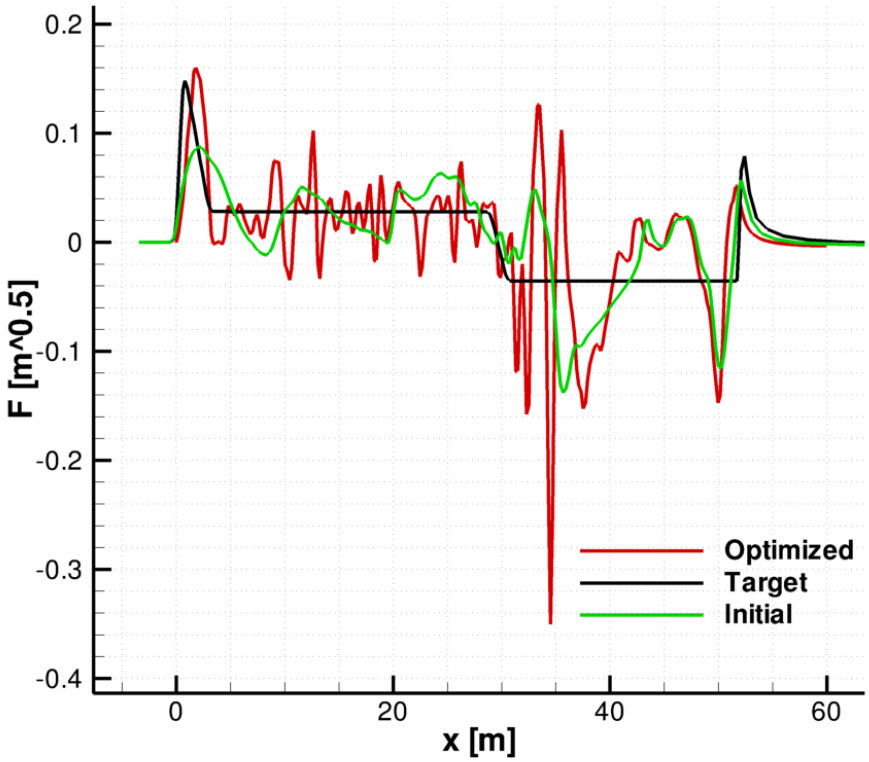

Figure B.25: Comparison of the F-function.

B.5 Conclusions and perspectives

The present study shows that our methodology for the prediction of sonic boom, which was previously applied only to structured mesh, now has been improved in order to perform CFD computations and sonic boom assessment using unstructured grids. This opens new possibilities in terms of analysis and design of configurations of increased geometrical complexity. CFD near-field prediction shows that adaptation is mandatory. Future work will aim to improve the quality of the CFD solutions considering mesh adaptation strategy. This will increase the quality of the solution and reduce the number of the grid elements required.

The use of the inverse method provides guidelines to design low-boom configurations. In particular in the present work, the re-design of the JAXA configuration has provided a flat-top ground signature with a level of PLdB reduced by 10 counts. A local volume constraint has been introduced in the AIDA module and a PLdB minimization has been performed on the constrained shaped configuration. Some additional efforts are required to define the geometry that corresponds to the equivalent area distribution, but interesting preliminary results are encouraging. To match the shaped area distribution, further investigations on the free-form deformation capabilities for fuselage tailoring are required.

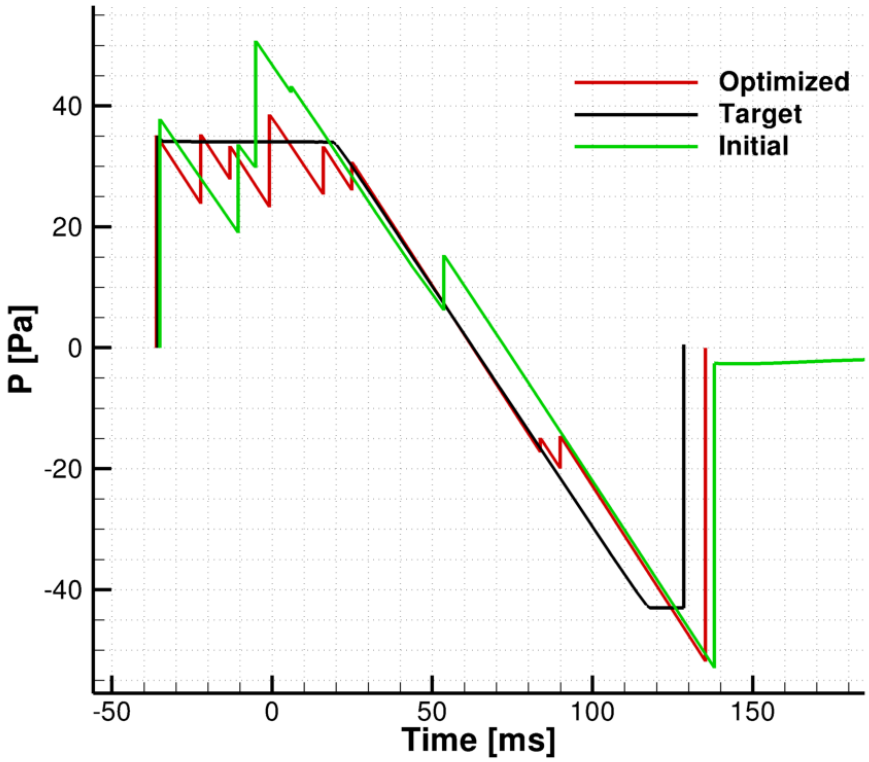

Figure B.26: Comparison of the obtained ground signature.

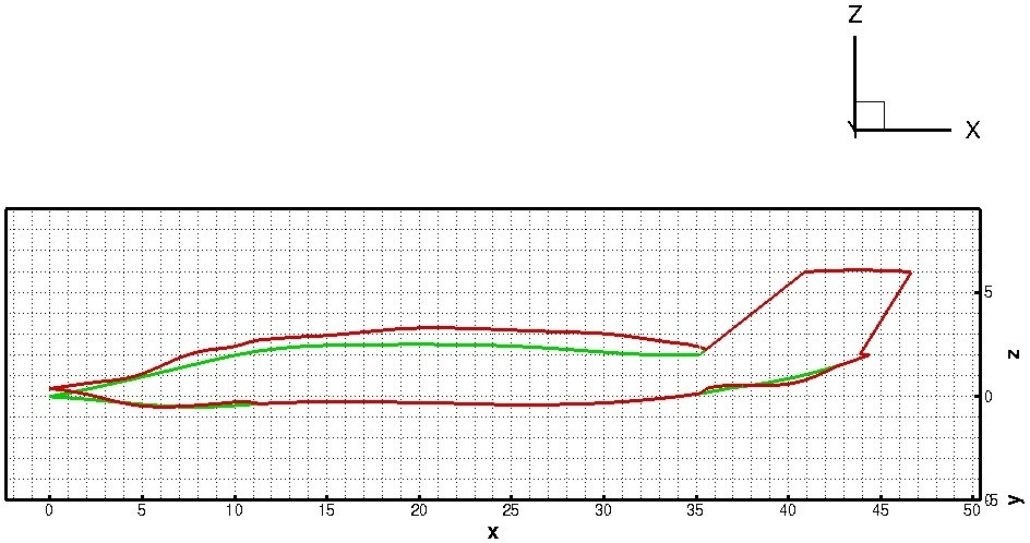

Figure B.27: Symmetry plane comparison of the initial and deformed geometry.

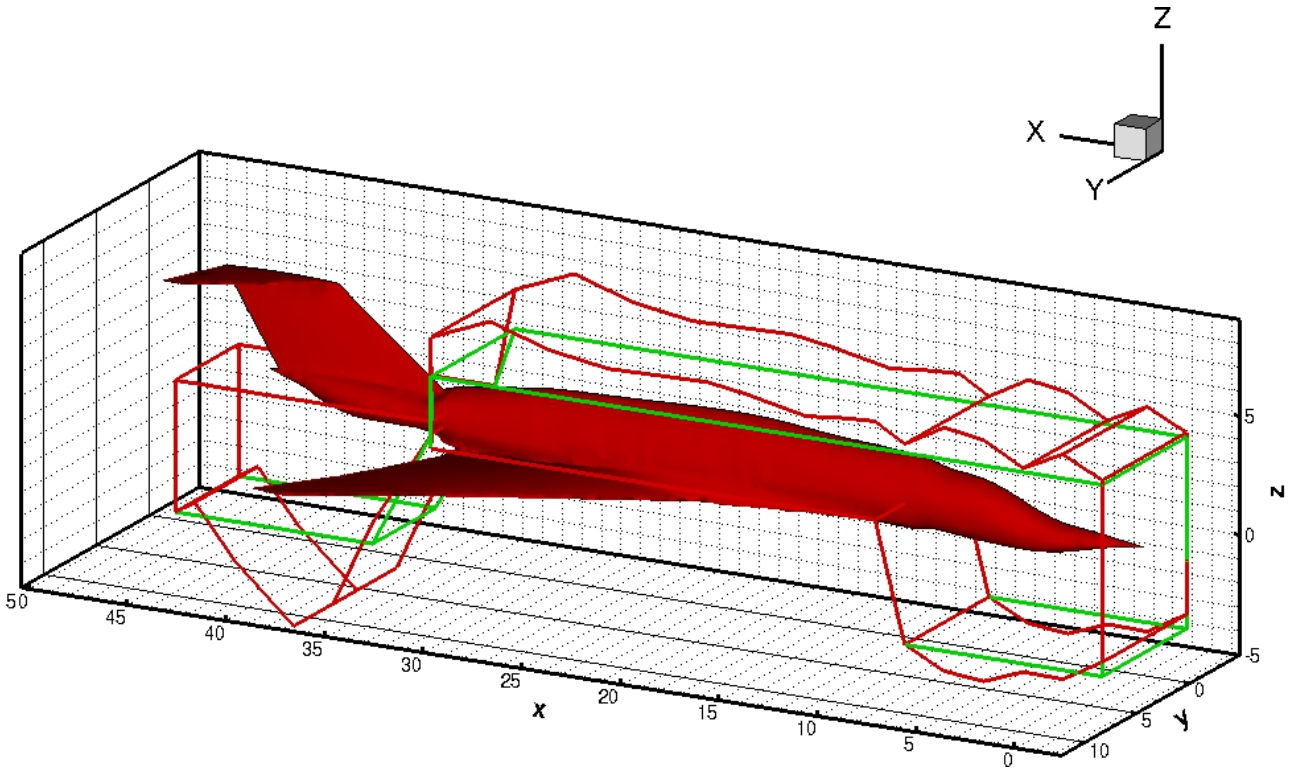

Figure B.28: Comparison of the initial and the shaped configuration.

Appendix C

NSGA-II

Since the principal reason why a problem has a multi-objective formulation is because it is not possible to have a single solution which simultaneously optimizes all objectives, an algorithm that gives a large number of alternative solutions lying on or near the Pareto-optimal front is of great practical value.
Kalyanmoy Deb

Contents

NSGA-II is a genetic algorithm that represents the state of the art in terms of multi-objective optimizers. This chapter introduces the main features of the algorithm as well as the implementation details. The algorithm is implemented in a Python version with a graphical user interface, constraint handling and a restart feature. This version has been tested on several benchmark test cases.

C.1 NSGA-II coded with DEAP: fundamentals

The Python library DEAP [163] has been adopted in order to implement the multi-objective algorithm NSGA-II with constraints handling originally developed by Deb [140]. NSGA-II in its original formulation is written in the language C. The adoption of the DEAP library permits easy modification of single aspects of the algorithm, an easy to use interface, a strong adaptation to the ONERA optimization framework based on the Python language. In addition DEAP permits to create from

scratch a genetic algorithm using a smart library of functions already implemented, or the possibility to define new functions (e.g different mutation operators) adopting an appropriate environment.

Two main issues are required for the solution of an engineering MDO problem: the possibility to handle problems with constraints and to consider restart of the optimization from the last population generated. Both aspects have been considered during the algorithm implementation and further details will be given later.

A Pareto based evolutionary algorithm does not combine the objectives, but it evaluates the value of the fitness function using a comparison of the objective function vectors. Typical problems that arise when stochastic algorithms are adopted to find a Pareto set are the slow convergence and the poor performance with high number of design variables. NSGA-II adopts a fast-non-dominated sorting that improves its efficiency. A classical non dominated sorting algorithm has to compare each solution to the entire population in order to evaluate if it is dominated. NSGA-II compares each individual to a partially filled population. The pseudo-code of the *non-dominated sorting* looks like:

$\mathcal{F}_1 = \emptyset$

for each $p \in P$:

    for each $q \in P$:

        $S_p = []$

        $n_p = 0$

            if $p \prec q$ then:

                $S_p = S_p \cup q$

            else if $q \prec p$ then:

                $n_p = n_p + 1$

    if $n_p = 0$ then:

        $p_{rank} = 1$

        $\mathcal{F}_1 = \mathcal{F}_1 \cup p$

$i = 1$

while $\mathcal{F}_i \neq \emptyset$:

    $\mathcal{Q} = \emptyset$

    for each $p \in \mathcal{F}_i$:

        for each $q \in S_p$:

            $n_q = n_q - 1$

            if $n_q = 0$ then:

                $q_{rank} = i + 1$

                $\mathcal{Q} = \mathcal{Q} \cup q$

$i = i + 1$

$\mathcal{F}_i = \mathcal{Q}$

Consider an individual p of the population P. n_p is the domination count, defined as the number of solutions which dominate the solution p, while S_p is a set of solutions that the solution p dominates. The sorting algorithm evaluates the parameters n_p and S_p for the entire population, comparing the different solutions. If for a solution $p \in P$ the domination count n_p is equal to 0 at the end of the comparison, it means that the solution belongs to the first non-dominated front $\mathcal{F}_1$. Once the first front has been defined, the following fronts can be identified. For each element $p \in \mathcal{F}_1$, we look at all the solution $q \in S_p$ and we reduce the domination count n_q by one. If $n_q = 0$, it means that q belongs to the next front $\mathcal{F}_2$. This procedure can be repeated for the other fronts (see Figure C.1).

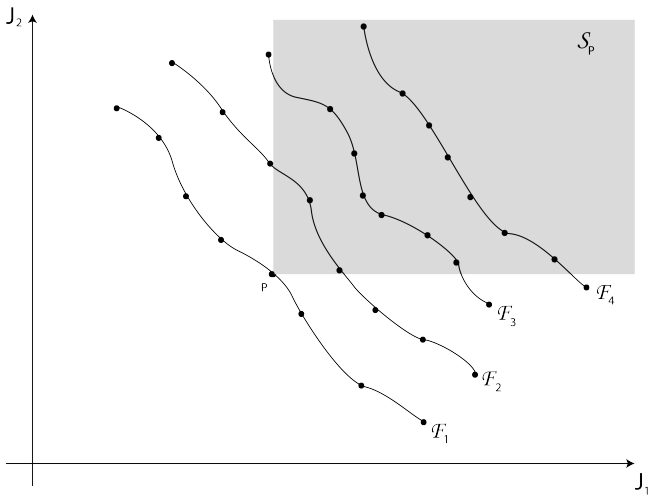

Figure C.1: Dominated front strategy for the fast-non-dominated-sorting algorithm.

The developed fast non-dominated sorting approach aims to reduce the computational complexity by a factor equal to the population size.

Additional requirements for a stochastic MDO algorithm are the preservation of diversity among solutions of the same non dominated front and the assignment of a fitness measure to population members based on dominated sorting. Genetic algorithms suffer from the genetic drift phenomenon. Without counter-measures population tends to form few-clusters in multi-objective GA. In order to obtain a good spread of the solutions without increasing the number of computations required, NSGA-II uses a crowded comparison approach that do not need any user defined parameters. If two points are

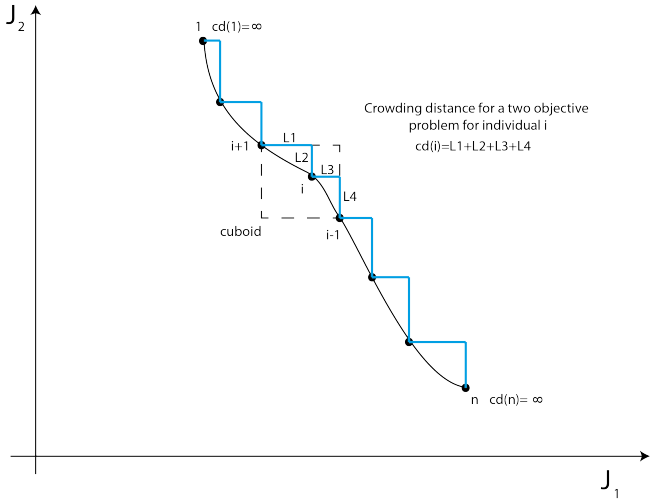

Figure C.2: Crowding distance definition.

considered and both belong to the same front, the crowded comparison operator prefers the point that is located in a region with a low number of points (higher value of the crowding distance). Considering a non dominated set, the crowding distance is defined as the average distance of two points on either side of the analyzed point along each of the objectives. To evaluate the crowding distance for each individuals that belong to a Pareto front, for each objective function k the solutions are first sorted in ascending order. For the individual i the crowding distance $cd_k(\mathbf{x}_i)$ is then evaluated as:

$$cd_k(\mathbf{x}_i) = \frac{J_k(\mathbf{x}_{i+1}) - J_k(\mathbf{x}_{i-1})}{J_k^{max} - J_k^{min}} \tag{C.1}$$

so that the total crowding distance of the individual i with respect to all the objectives is obtained as $cd(\mathbf{x}_i) = \sum_k cd_k(\mathbf{x}_i)$. The crowding distance for the points at the extremity of the Pareto front is

fixed and equal to ∞ in order to preserve these points in the next generation.

The algorithm starts producing a random population P_0 with a size μ. Each individual has two fitness vectors $\mathbf{J}$ and $\mathbf{g}$ that respectively corresponds to the vector of the cost functions and the vector of the constraint functions. At this point the generational process can starts. The first genetic operator applied to the population is the crowded tournament selection, which is based on dominance and crowding distance. The selection priority is given first to the respect of the constraints and then to dominance and to the crowding distance. Consider two solutions A and B. If both satisfy the constraints then dominance and the crowding distance discriminate the solution. If one of the two satisfy the constraint, then it dominates the other, otherwise if both do not satisfy the constraints and are not dominated the solution that shows the smaller value of the crowding distance is better. Using this method instead of a classical penalty function method or the complete removal of the unfeasible solutions aims to use information on the distance from the feasibility region, thus improving the convergence of the method. If both A and B satisfy the constraints and are not dominated by other solutions, selection is based on the crowding distance. If $cd(A) > cd(B)$ then A is retained.

Simulated binary tournament, selection, recombination and mutation are used to produce the child population Q with a size $\lambda = \mu$. The combined population $R = P \cup Q$ is formed with the size 2μ. In this way the population R ensure the elitism maintaining elitist solutions in the population without any external storage.

At this point the following iterations are performed starting from the generation t:

1. *fast-non-dominated sort*(R_t) : identify the non dominated fronts $\mathcal{F}$ of the population R_t;
2. until $P_{t+1} < \lambda$:
   - calculate the crowding distance$(\mathcal{F}_i)$;
   - include the i-th front to the population $P_{t+1} = P_{t+1} \cup \mathcal{F}_i$;
3. sort in ascending order P_{t+1};
4. $P_{t+1} = P_{t+1}\,[0 : \lambda]$ choose the first λ elements of the population;
5. make a new population (Q_{t+1}) using selection cross-over and mutation.

The procedure is repeated until a stopping criterion is satisfied. In this case the only stop criterion available is the maximum number of generations.

The restart feature is simply obtained stocking the last non dominated population. Each individual is defined by its design variables, its fitness and its constraints vector. In addition it is possible to stock also the history of the Pareto front during the different generations for post-processing.

The graphical user interface (GUI) is based on the Tkinter module [164], the standard Python interface to the Tk GUI toolkit. The user is asked first if he wants to use the restart option and if the problem considered is constrained or not. This option is very important due to the fact that the algorithm operators as well as the storage of the population fitness change. A selection GUI (Figure C.3) asks to select a function to be analyzed. Several benchmark test functions are implemented. In addition the user can specify other generic functions. The next step consists in the definition of the optimization parameters (Figure C.4): number of design variables and their upper and lower bounds, size of the population and number of generations. If the problem selected in the previous step is a benchmark function, the standard parameters of the problem are suggested by the dialog box. Using only three steps, we are able to solve the multi-objective problem specified.

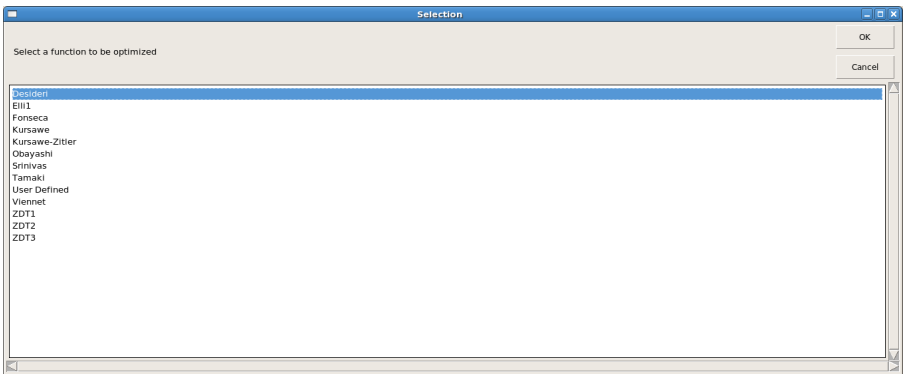

Figure C.3: GUI for function selection. Predefined test functions as well as user defined functions can be adopted.

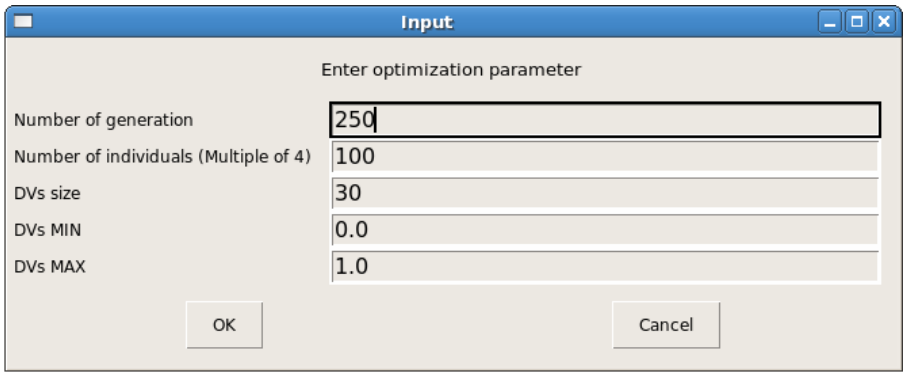

Figure C.4: GUI for optimization input parameters.

C.2 Benchmark tests

Some analytical test cases are here proposed in order to validate the implementation of NSGA-II using the Python library DEAP and in particular the constraints handling technique. The problems specifications are defined in Table C.1 while the definition and the results of each test case are presented in the following sections.

Problem	Generations	Individuals	DVs	Min	Max
ZDT1	250	100	30	0	1
ZDT2	250	100	30	0	1
Kursawe	100	100	3	-1000	1000
Obayashi	100	12	2	0	1
Srinivas	100	12	2	-20	20
Tamaki	100	3	3	0	1
Viennet	100	2	2	-2	2

Table C.1: Problem specifications.

ZDT1

The ZDT1 problem has been proposed in [165]. The bi-objective unconstrained minimization problem states as follows:

$$\begin{cases} f_1(x_1) = x_1 \\ f_2(f_1, g) = 1 - \sqrt{f_1/g} \end{cases} \tag{C.2}$$

where $g(x_2, ..x_m) = 1 + 9\sum_{i=2}^{m} x_i/(m-1)$, $m = 30$, and $x_i \in [0, 1]$.

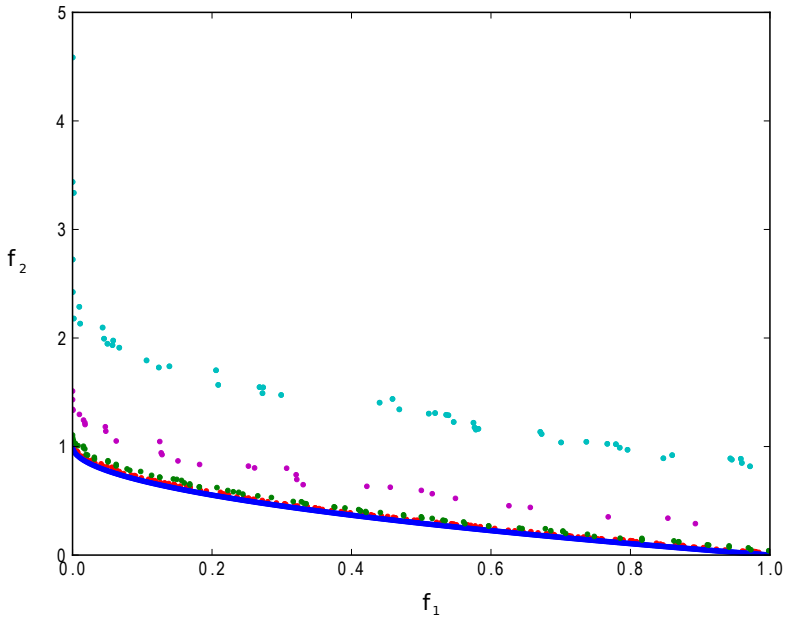

Figure C.5: ZDT1 Pareto front. Red=NSGA-II, Blue=Pareto front, Green = SPEA, Magenta = NSGA, Cyan = MO-CMA-ES.

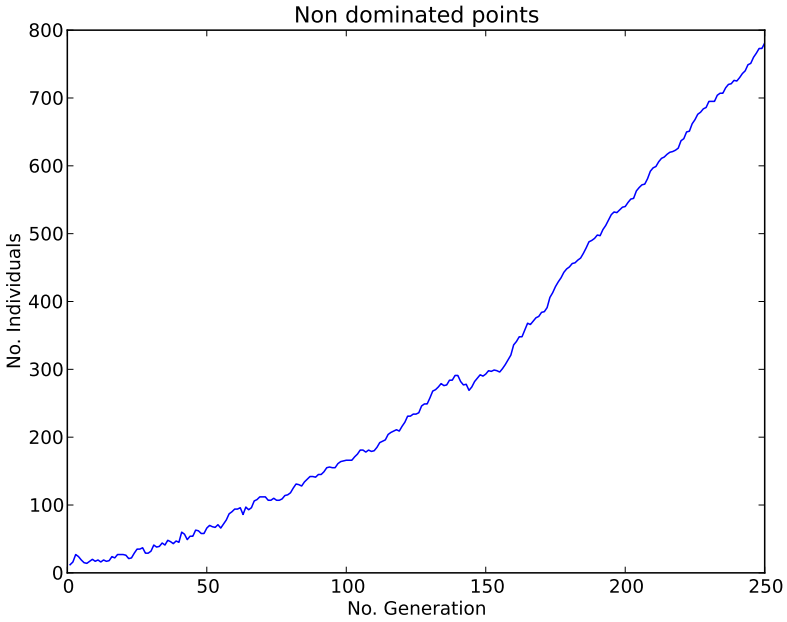

Figure C.6: ZDT1 Pareto front population. Number of non dominated solutions.

The hypervolume indicator I_H is a measure used in evolutionary multi-objective optimization to evaluate the performance of the search algorithm [166]. The hypervolume indicator I_H gives the volume of the objective subspace that is enclosed between a reference solution N called Nadir point and the non dominated set (see Figure C.7). The unary Hypervolume indicator is defined as:

$$\hat{I}_H = 1 - \frac{I_H}{\sum f_i(N)} \tag{C.3}$$

A non-dominated set $\mathcal{F}_1$ is better with respect to $\mathcal{F}_2$ if $\hat{I}_H(\mathcal{F}_1) < \hat{I}_H(\mathcal{F}_2)$.

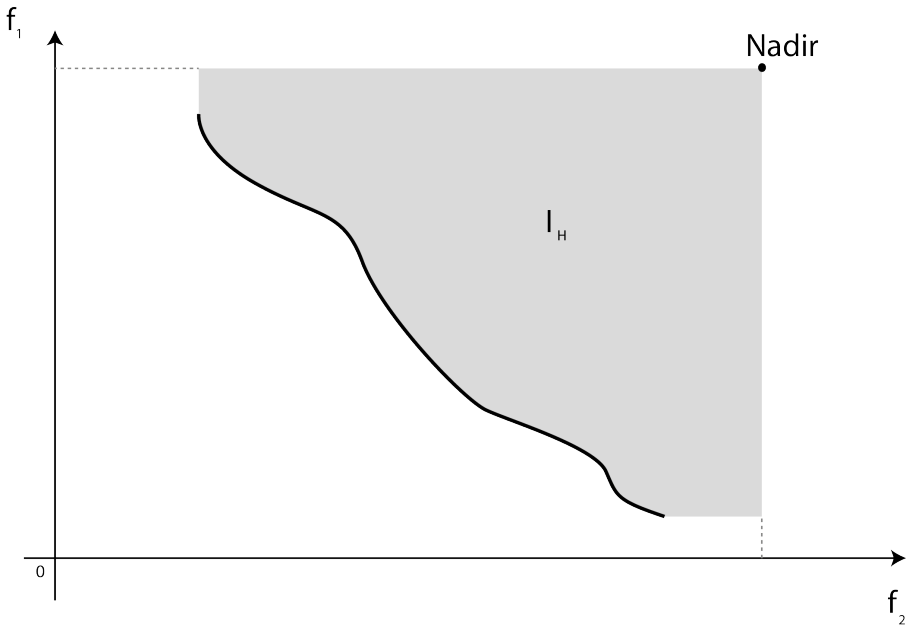

Figure C.7: Hypervolume indicator.

Another useful indicator is the unary epsilon indicator I_ϵ that gives the minimum factor ϵ such that if every point in the reference set B is multiplied by ϵ then the resulting approximation set is weakly dominated by A. B is generally taken equal to the Pareto front if it is known or to a reference set.

The two indicators are evaluated on the ZDT1 problem test case performed 50 times. Results (Figure C.8) shows the effectiveness of NSGA-II. After 250 generations the two metrics are reduced by more than two orders of magnitude.

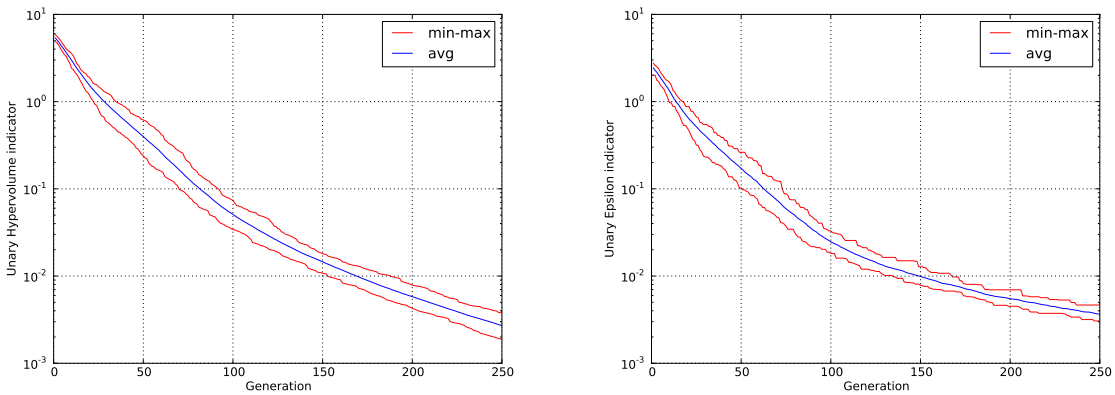

(a) Unary hypervolume indicator

(b) Unary Epsilon Indicator

Figure C.8: Performance metrics for NSGA-II adopting as a nadir point (2,10) after 50 runs.

ZDT2

The ZDT2 problem has been proposed in [165]. The bi-objective unconstrained minimization problem states as follows:

$$\begin{cases} f_1(x_1) = x_1 \\ f_2(f_1, g) = 1 - (f_1/g)^2 \end{cases} \tag{C.4}$$

This problem is interesting because it presents a non-convex Pareto front.

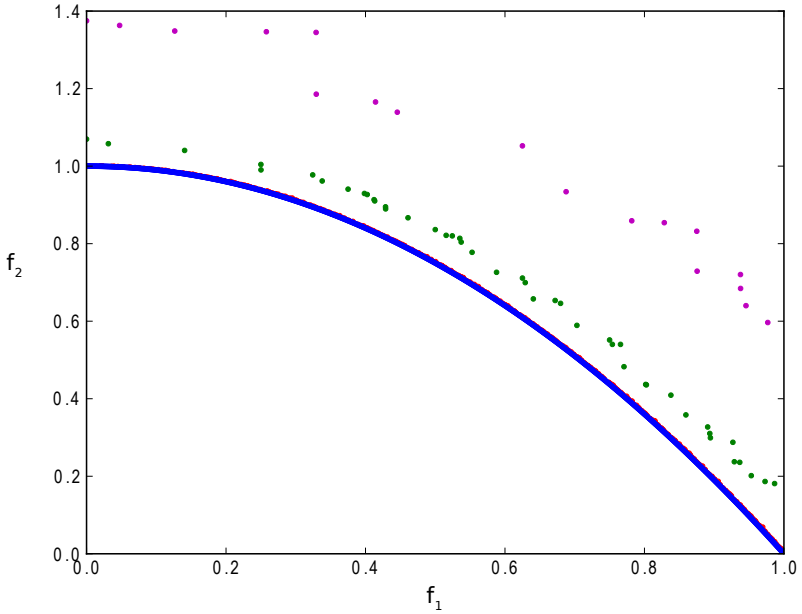

Figure C.9: ZDT2 Pareto front. Red=NSGA-II, Blue=Pareto front, Green = SPEA, Magenta = NSGA.

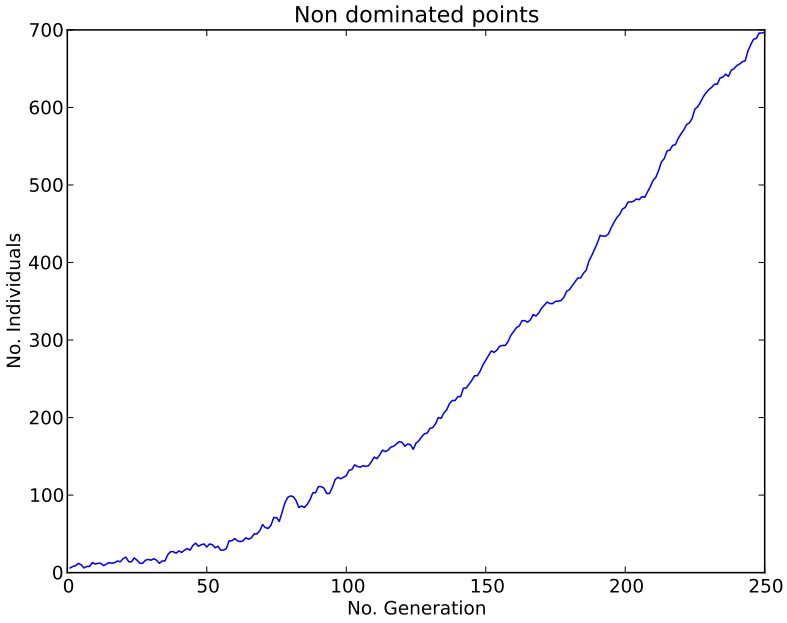

Figure C.10: ZDT2 Pareto front population. Number of non dominated solutions.

Kursawe

The Kursawe problem has been proposed in [167]. The bi-objective unconstrained minimization problem states as follows:

$$\begin{cases} f_1(x) = \sum_{i=1}^{n-1}(-10\exp^{-0.2\sqrt{x_i^2+x_{i+1}^2}}) \\ f_2(x) = \sum_{i=1}^{n}(|x_i|^{0.8} + 5\sin(x_i)^3) \end{cases} \tag{C.5}$$

The problem is a valuable test case because it presents a discontinuous Pareto front.

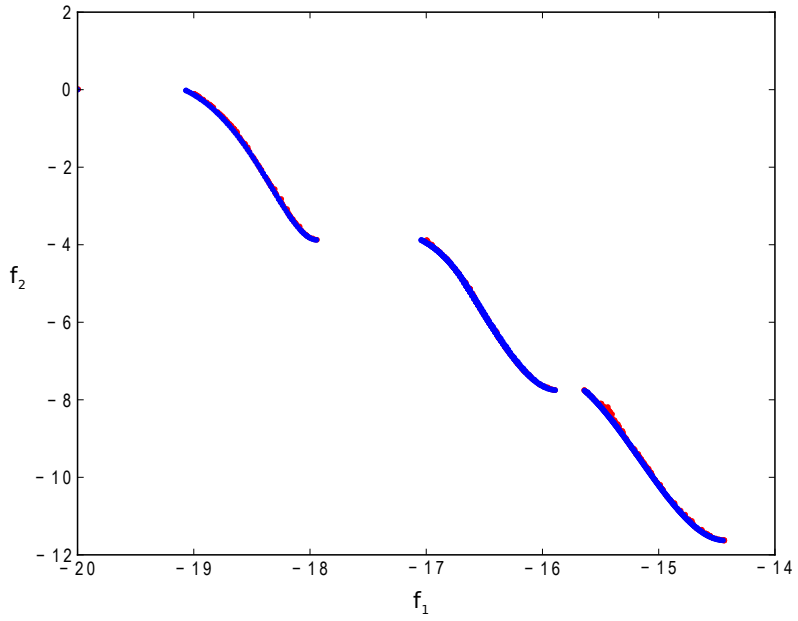

Figure C.11: Kursawe Pareto front. Red=NSGA-II, Blue=Pareto front.

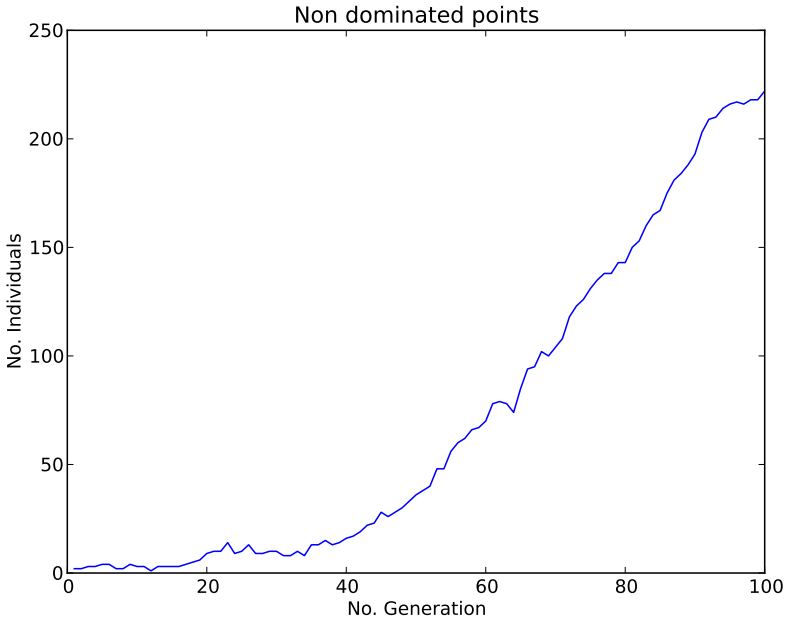

Figure C.12: Kursawe Pareto front population. Number of non dominated solutions.

Obayashi

The bi-objective constrained maximization problem states as follows:

$$\begin{cases} f_1(x_1) = x_1 \\ f_2(x_2) = x_2 \end{cases} \tag{C.6}$$

with $g(x_1, x_2) = x_1^2 + x_2^2 \leq 1$.
The problem is interesting because is a simple constrained problem.

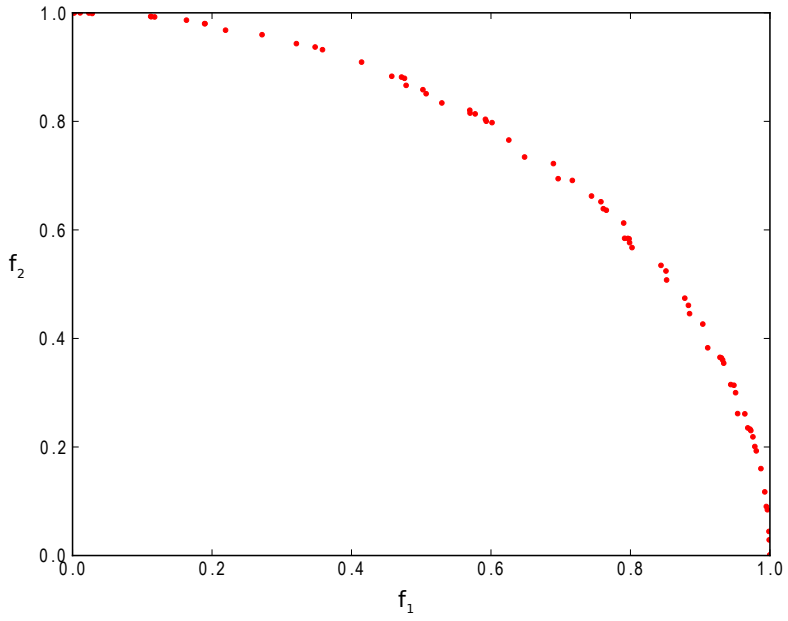

Figure C.13: Obayashi Pareto front.

Srinivas

The Srinivas problem has been proposed in [168]. The bi-objective constrained minimization problem states as follows:

$$\begin{cases} f_1(x_1, x_2) = (x_1 - 2)^2 + (x_2 - 2)^2 + 2 \\ f_2(x_1, x_2) = 9x_1 - (x_2 - 1)^2 \end{cases} \tag{C.7}$$

with $g_1(x_1, x_2) = x_1^2 + x_2^2 - 225 \leq 0$, $g_2(x_1, x_2) = x_1 - 3x_2 + 10 \leq 0$ and $x_i \in [-20, 20]$.
This problem is interesting because it presents two constraint functions.

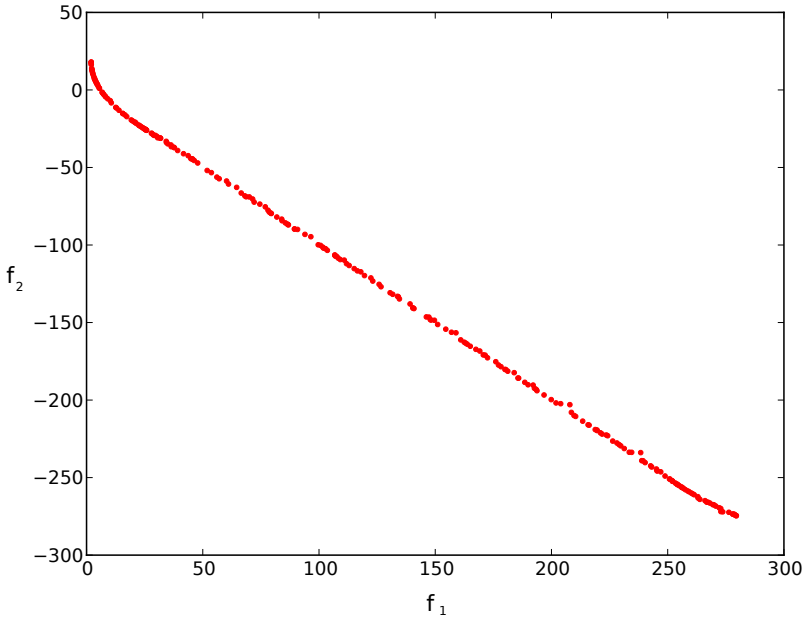

Figure C.14: Srinivas Pareto front.

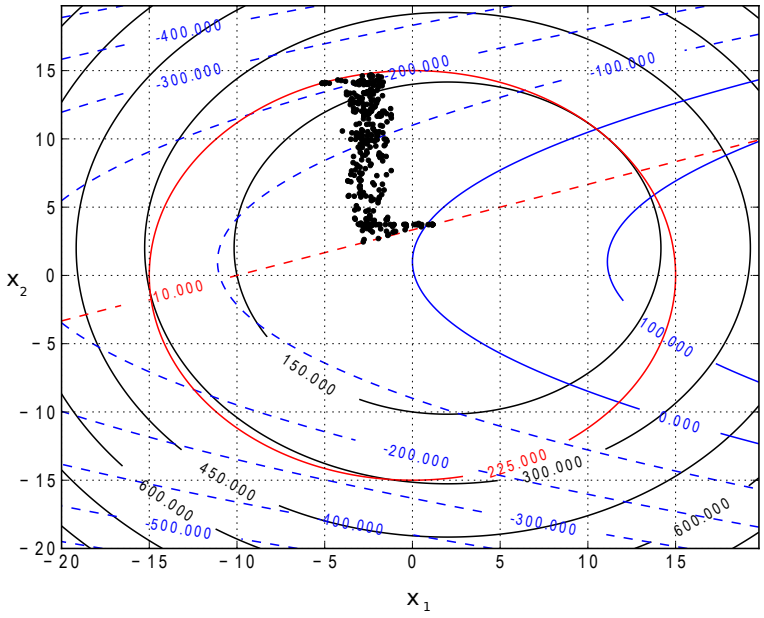

Figure C.15: Pareto set of the Srinivas problem with the functions contour (f_1 black, f_2 blue) and the constraints in red.

The result shows that the algorithm and in particular the implementation of the constraints in NSGA-II is accurate. In fact the algorithm is able to find solutions also in the proximity of the activation of the constraints.

Tamaki

Consider the following constrained maximization tri-objective problem:

$$\begin{cases} f_1(x_1) = x_1 \\ f_2(x_2) = x_2 \\ f_3(x_3) = x_3 \end{cases} \tag{C.8}$$

with $g(x_1, x_2, x_3) = x_1^2 + x_2^2 + x_3^2 \leq 1$.
The problem is interesting because it represents an optimization problem with more than 2 objectives.

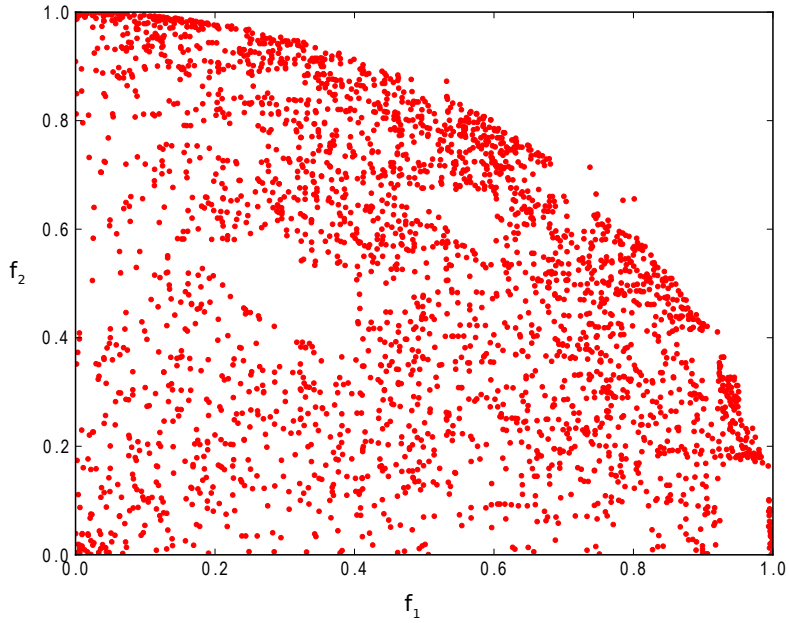

Figure C.16: Pareto set. f_1 and f_2.

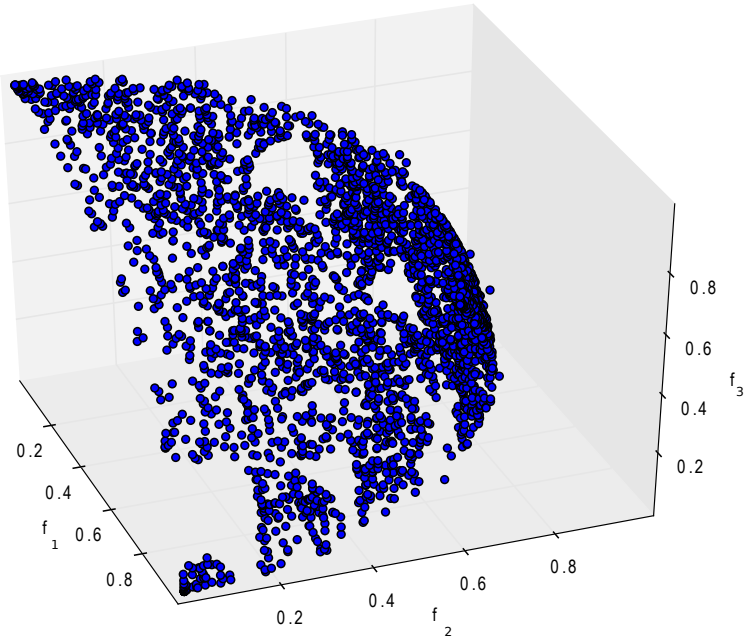

Figure C.17: Pareto set.f_1, f_2 and f_3.

Viennet

Consider the following unconstrained minimization problem:

$$\begin{cases} f_1(x_1) = x_1^2 + (x_2 - 1)^2 \\ f_2(x_2) = x_1^2 + (x_2 + 1)^2 + 1 \\ f_3(x_3) = (x_2 - 1)^2 + x_2^2 + 2 \end{cases} \tag{C.9}$$

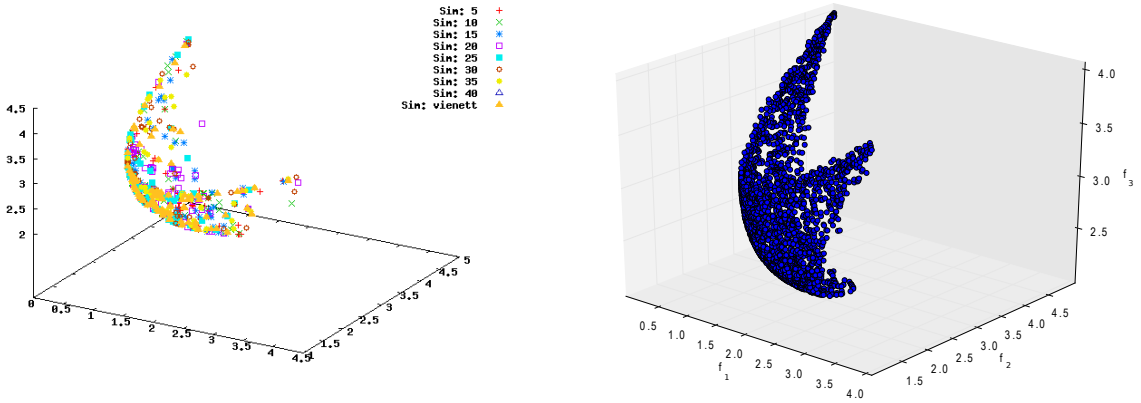

(a) SPEA-2 (b) NSGA-II

Figure C.18: Pareto set.f_1, f_2 and f_3.

The problem has been modified by the introduction of a constraints $g = f_2 < 2$. Figure C.19 shows the Pareto set for the constrained and the unconstrained problem.

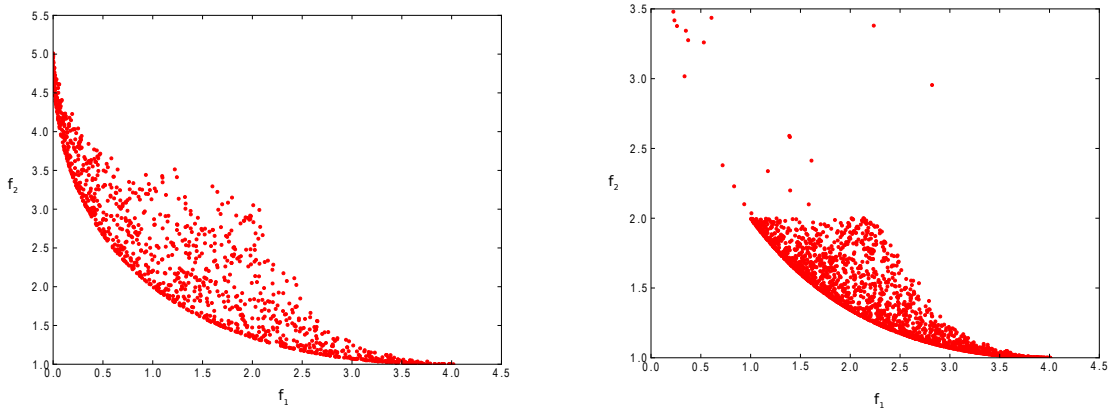

(a) Viennet no constraint

(b) Viennet constraint on $f_2 < 2$

Figure C.19: Pareto set.f_1, f_2

C.3 Conclusions

The NSGA-II algorithm has been introduced in this section. To enable the user modifications of the algorithm operators and at the same time to improve its compatibility with the optimization chain in use at Onera, the Python library DEAP has been exploited for the NSGA-II implementation. Several multi-objective problems have been considered to validate the algorithm and test its efficiency. The results, for both constrained and unconstrained problems, show that the algorithm is able to converge to the non-dominated set with a reduced number of function evaluations and with a good distribution of the solutions on the front. The algorithm implemented with the Python library DEAP is ready for its application to industrial multi-objective optimization problems.

Appendix **D**

Curiosity about Supersonic transportation

It is a miracle that curiosity survives formal education.
Albert Einstein

Contents

Human beings during history have shown a constant need for speed. The reasons have changed along the time, from the need of feed on, to climate modifications, work opportunities and economics. Today the world we live in, with the considerable growth of the globalization process in economics, culture, politics, shows a strict interdependence between different continents. This process has been encouraged by advances in communications and in the efficiency and increase of speed in transportation and it has the tendency to feeds on itself. For this reason the supersonic research has impacted many aspects of the actual society. In this section several aspects more or less known related to the development of the supersonic civil transportation are presented.

D.1 The Nasa logo

The National Aeronautics and Space Administration (NASA) logo has three main official designs, although the one with stylized red curved text (the "worm") has been retired from official use since 1992. The three logos include the NASA insignia (also known as the "meatball"), the NASA logotype (also known as the "worm"), and the NASA seal.

The NASA seal was approved by President Dwight D. Eisenhower in 1959, and slightly modified by John F. Kennedy in 1961 by the executive order 10942 here reported:
By virtue of the authority vested in me as President of the United States, and upon the recommendation of the Administrator of the National Aeronautics and Space Administration, I hereby amend Executive Order No. 10849 of November 27, 1959, by revising the description of the design of the seal of the

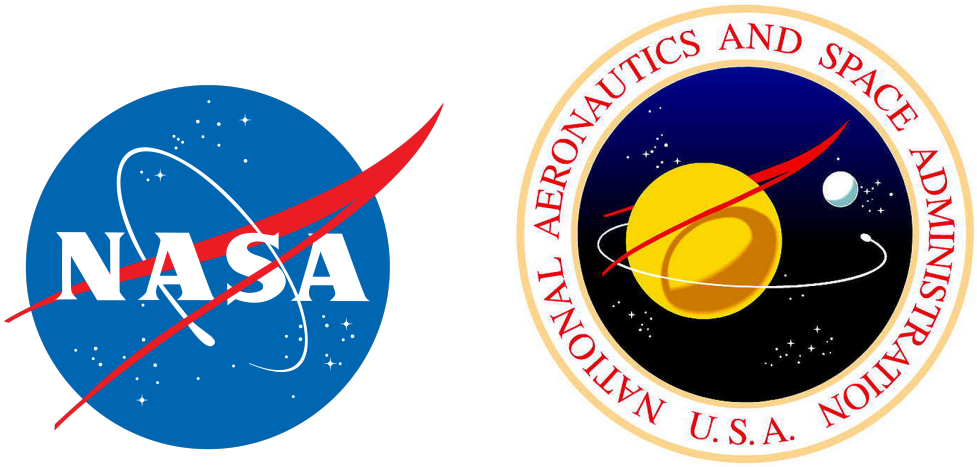

Figure D.1: Nasa insignia and seal.

National Aeronautics and Space Administration as set out in that order to read as follows: On a disc of the blue sky strewn with white stars, to dexter a large yellow sphere bearing a red flight symbol apex in upper sinister and wings enveloping and casting a brown shadow upon the sphere, all partially encircled with a horizontal white orbit, in sinister a small light-blue sphere; circumscribing the disc a white band edged gold inscribed National Aeronautics and Space Administration U.S.A. in red letters.

John F. Kennedy
The White House
May 19, 1961

As described in the executive order, the red chevron represents aeronautics. In the late 1950s, Clinton E. Brown and F. Edward McLean developed an arrow wing for supersonic applications based on analytical studies and subsequent wind-tunnel tests that verified the configuration's high aerodynamic efficiency at high speeds. Following the test program, the wind-tunnel model was put on display and observed by James J. Modarelli, a visitor from the NACA Lewis Laboratory. Modarelli headed the Lewis Research Reports Division when NACA Executive Secretary John Victory requested suggestions for an appropriate seal for the new NASA organization. Impressed by the sleek, futuristic aspects of the Langley model, Modarelli and his graphic artists included an interpretation of it in a logo insignia that was subsequently adopted for the NASA logo.

D.2 The Montreal protocol

The possibility of anthropogenic interference with the ozone layer was raised as early as 1964, when John Hampson of the Canadian Armaments and Research Development Establishment noted the potential for ozone damage as a result of water vapor emissions from rockets and high-flying aircrafts. Over the ensuing decade, proposals for the development of supersonic commercial aircraft that would fly in the lower stratosphere brought further attention to the issue, as did the debate over the environmental effects of nuclear weapons. In 1974, however, two articles were published that brought an entirely new dimension to the problem of ozone depletion. The first of these, published in the Canadian Journal of Chemistry by Richard Stolarski and Ralph Cicerone of the University of Michigan, described a process by which chlorine from rocket exhausts could catalyze the destruction of large amounts of ozone in the stratosphere over a period lasting many decades. One year after the US Department of Transportation presented the results of the Climatic Impact Assessment Program (CIAP), which studied the effects of a fleet of Supersonic Transports (SSTs) on the upper atmosphere giving new insights into the debate. The conclusion states as follows: "*If 500 Boeing SST's had been built as planned, equipped with the engines they were expected to use before this study was undertaken, and if each had flown on the average between 7 and 10 hours per day at an altitude of 20 km as planned,*

their effect would very probably have been to reduce the average global content of the ozone layer by between 10 and 20%, with most of the effect occurring in the northern hemisphere. The result of this ozone reduction would have been an increase in erythemal solar ultraviolet radiation by approximately 20 to 40 and consequently a serious threat to the biosphere in the worst case, or an extremely great increase (by about 20% per year) in effects such as skin cancer incidence among the white Caucasian population of the world" [169].

Independently and almost simultaneously, two University of California researchers, Mario Molina and Sherwood Roland, voiced similar concerns about chlorine-catalyzed ozone loss but suggested the existence of a much larger source of anthropogenic chlorine in the stratosphere that already acts to the reduction of the Ozone layer. In their article published on Nature they argued that many widely used industrial chlorofluorocarbons (CFCs) had the potential to migrate into the stratosphere, where they would eventually break down as a result of exposure to intense ultraviolet radiation and release significant quantities of chlorine. The combined implications of these articles were disturbing. Society appeared to face a choice between preserving the integrity of the ozone layer, which prevents biologically destructive levels of ultraviolet radiation from reaching the earth's surface, or preserving the economic benefits provided by CFCs, a valuable and otherwise benign group of chemicals that had become essential to a broad range of applications, including refrigeration and the manufacture of foams and electronic components. The potential risks to ecosystems and human health were large and unprecedented, while the costs of abandoning CFCs appeared considerable. In addition, although ozone destruction by chlorine catalysis was highly plausible, there was as yet no empirical evidence of ozone loss in the stratosphere. After the first warnings in the early 1970's only in 1987 the Montreal Protocol on substances that deplete the Ozone Layer formally recognized the significant threat of the ozone depleting substances (ODSs) to the ozone layer and provided a strategy to reduce and phase-out the global production and consumption of ODSs. Under the Montreal Protocol and national regulations, significant decreases have occurred in the production, use, emissions, and observed atmospheric concentrations of CFC. Without this protocol the depletion of the ozone layer would be much greater than observed today [170].

D.3 The first commercial flight of Concorde

Concorde : premier vol régulier Paris-New York

Trajet effectué en 3 heures 39 minutes

Un vol historique trop court

Quand « Normandie » reliait Le Havre à New York en quelque quatre jours ou plus, on avait le temps de prendre la mesure des choses. Mais un événement historique qui ne dure pas plus de trois heures et trente-neuf minutes laisse, à vrai dire, une impression de frustration. Voilà bien le seul problème que « Concorde » a posé aux heureux privilégiés qui ont accompli hier le vol Paris-New York « A.F. 001 », c'est-à-dire la liaison inaugurale en « Concorde » entre Roissy-Charles-de-Gaulle et l'aéroport Kennedy.

A BORD DE CONCORDE :
de notre envoyé spécial
Pierre BRANCHE

Décollant très exactement à 11 h 12, passant à 11 h 22 à 8.500 mètres à la verticale du Havre, volant à 17.000 mètres et 2.200 kilomètres à l'heure au-dessus de l'Atlantique, « Concorde » a atterri à 14 h 47 (8 h 47 heure locale). Et encore ce temps sera-t-il réduit dès la seconde liaison puisque, hier, il a fallu d'une certaine façon, faire « piétiner » le « Bravo Delta » aux couleurs françaises pour permettre à son jumeau des British Airways, parti de Londres, d'atterrir quasi simultanément sur ce ruban de béton dont si longtemps la ville de New York a refusé l'accès au supersonique franco-anglais.

Oui, un vol historique que le commandant Pierre Dudal n'oubliera pas de sitôt puisque parmi ses passagers se trouvaient, parmi d'autres, deux hommes qui savouraient intensément cette victoire si péniblement acquise : Maurice Bellonte qui, avec Dieudonné Costes, avait réalisé la première liaison Paris-New York le 1er et le 2 septembre 1930 en trente-sept heures de vol sans escale à bord de leur monomoteur le « Point d'Interrogation » et aussi André Turcat. Premier « essayiste » du « Concorde », il l'a piloté pour la dernière fois le 31 mars 1976. Emouvante image que celle du pionnier octogénaire savourant un demi-siècle de progrès en compagnie de l'ancien pilote en chef de l'Aérospatiale qui résumait d'une phrase tout ce que cette nouvelle liaison avec New York représente pour « Concorde » : « **The knot of the net** » (le nœud du réseau), disait-il aux Américains présents à bord.

Parmi ceux-là, un invité que Marcel Cavaillé, secrétaire d'Etat aux Transports, Pierre Giraudet, président-directeur général d'Air France et Gilbert Pérol, directeur général, recevaient avec une satisfaction non dissimulée : Walter Cronkite, le présentateur vedette de la chaîne américaine C.B.S., qui vient de réussir le fameux direct « Begin-Sadate ». Celui-là même qui, voici quelque trois ans, avait refusé l'invitation d'Air France de tester « Concorde » pour ne pas se rendre impopulaire auprès de ses compatriotes ; et qui hier, découvrait et reconnaissait que « Concorde » n'était pas un monstre bruyant mais un bel et bon appareil qui rapproche un peu plus l'Amérique de la France. Un constat que font désormais avec lui les Newyorkais et tous les Américains.

Marcel Cavaillé : "L'avion servira les intérêts de New York"

NEW YORK :
de notre envoyé spécial permanent
Charles LAMBROSCHINI

« Les Américains ont trop le sens du fair play pour ne pas très vite reconnaître que l'arrivée de Concorde, loin d'être un désastre, servira les intérêts de New York ».

En prononçant ces mots après l'atterrissage, Marcel Cavaillé, secrétaire d'Etat aux Transports, était déjà sûr de ne pas se tromper : pour accueillir le supersonique franco-britannique les hommes d'affaires, hier, étaient plus nombreux que les manifestants. Malgré leur promesse, ceux-ci, échaudés par l'échec de la démonstration de dimanche, se sont en effet montrés si discrets qu'ils en étaient invisibles.

Le premier « Concorde », celui d'Air France — l'avion britannique qui s'était posé en tête à Washington, l'an dernier, rendait la politesse — apparaît au-dessus de l'aéroport Kennedy, vers 8 h 45. Très reconnaissable malgré la distance, il arrive cabré, son nez baissé vers la terre.

Gracieux comme un planeur

Lourd comme un oiseau préhistorique et pourtant gracieux comme un planeur, il semble faire peur à l'essaim d'hélicoptères de la télévision et de la police qui s'écarte précipitamment. L'avion se pose sur la piste 31 à 8 h 47. Dans la tour de contrôle où la presse s'est rassemblée, tous les journalistes sans distinction applaudissent.

L'appareil de la British Airway suit à deux minutes. Les deux avions s'étaient d'abord retrouvés à 12.000 mètres d'altitude, au sud-ouest de la Grande-Bretagne, pour voyager de concert. Ou presque. Ils étaient quand même à 12 minutes l'un de l'autre, soit quelque 210 km. Ils se sont rapprochés dans la région de Boston.

Arrivé en bout de course, le pilote français attend son collègue britannique. L'un suivant l'autre, les avions roulent doucement vers les voitures officielles. Trois minutes encore, et ils se séparent, afin de gagner leur terminal respectif.

Une arrivée sans fanfare

C'est une arrivée sans fanfare. Contrairement à ce qui s'était passé à Washington, la direction de l'aéroport de New York a refusé que les deux « Concorde » terminent leur tour d'honneur en se retrouvant nez à nez. Le porte-parole de l'autorité portuaire a d'abord avancé des raisons de sécurité : « **Il y a trop d'appareils qui vont et viennent dans cette zone.** » Il a ensuite reconnu : « **Inutile de provoquer les adversaires de Concorde.** » Les Français et les Britanniques se sont inclinés ; pas de triomphalisme. Maintenant, il s'agit de gagner de l'argent !

Figure D.2: First commercial flight of Concorde.

The first US flight for the Concorde 002 has taken place in 1973 for the inauguration of the actual

Dallas/Fort-Worth airport. Three years later, the first commercial flights from London and Paris to New York have taken place the 21st January 1976. The following article taken from the French newspaper "Le Figaro" describes the chronicle of this historical day. The Air France and the British Airways Concorde have flown in tandem over the Atlantic ocean with a distance of only 12 minutes, landing at the same time at the JFK airport without too many honors due to the proximity of the Concorde direct rivals.

D.4 Celebrities and Concorde

Concorde has always been a luxury mode of travel used by only very richest travelers and business men. It's glamor has attracted many famous passengers during its service years. Music celebrities and actors were the routine in the Concorde flight passenger lists like Elton John, Mick Jagger, Joan Collins, Robert Redford, Luciano Pavarotti, Sean Connery, Elizabeth Taylor, Annie Lennox and Rod Stewart. The supersonic jet helped make rock history in 1985 at the 16-hour pop and rock marathon LiveAid. Musician Phil Collins played on stage in London and then took Concorde to New York followed by a helicopter to Philadelphia in time to play drums for Eric Clapton before the televised event was over.

Not only common people but also royals favor Concorde. The Queen Elizabeth II favors Concorde when she flies and the Queen Mother is even reported to have taken the controls of one of the aircraft during a flight test. During the last years of service, not contradicting its history, it has continued to be the center of the show business. In 1999 the US soul diva Diana Ross made the headlines when she was arrested on Concorde after she assaulted a female security officer trying to search the star before she boarded the plane. Ms Ross was later cautioned and released - she went on to travel home in style - on Concorde. Posh Spice Victoria Beckham flew Concorde for three wedding dress fittings in New York in 1999, just before the wedding with David Beckham. When boxer Mike Tyson arrived in the UK for his controversial fight with Lou Savarese in 2000 it was aboard a scheduled Concorde flight from New York. Customs and Immigration officers went on board the jet to check Mr Tyson's documents before allowing him to leave the airport. He was the last passenger off the flight.

Figure D.3: Queen Elizabeth II at a Concorde presentation.

D.5 Supersonic Seattle

In 1967 the Seattle basketball team has joined NBA. Seattle fans have to vote for a new name for their team. At the time the airplane manufacturer Boeing is operated out of Seattle and was working on a supersonic civil aircraft that would rival the Concorde. The Boeing SST plane never took off, but Seattle fans voted for the name Seattle Supersonics. This to represents the local aerospace industry and because it was the common thought that all planes would soon be supersonic.

Figure D.4: First logo of the Seattle SuperSonics.

List of Figures

List of Tables

Bibliography

[1] J. Chambers. Innovation in Flight Research at the NASA Langley Research Center on Revolutionary Advanced Concept for Aeronautics. *NACA SP-2005-4539*, 2005.

[2] K. Plotkin and J. Page. Extrapolation of Sonic Boom Signatures from CFD Solution. *AIAA-2002-0922*, 2002.

[3] G.B. Whitham. The Flow Pattern of a Supersonic Projectile. *Communications on pure and applied mathematics*, 5:301–348, 1952.

[4] J.J. Alonso and M.R. Colonno. Multidisciplinary Optimization with Applications to Sonic-Boom Minimization. *Annual Review of Fluid Mechanics*, 44:505–526, 2012.

[5] C. Thomas. Extrapolation of Sonic Boom Pressure Signatures by the Waveform Parameter Method. Technical Report D-6832, NASA, 1972.

[6] W.D. Hayes, R.C. Haefeli, and H.E. Kulsrud. Sonic boom propagation in a stratified atmosphere, with computer program. Technical Report CR-1299, NASA, 1969.

[7] K.J. Plotkin. State of the Art of Sonic Boom Modeling. *Journal of the Acoustical Society America*, 111:530–536, 2002.

[8] S. Rallabhandi. Advanced Sonic Boom Prediction using Augmented Burger's Equation. *AIAA-2011-1278*, 2011.

[9] I. Salah el Din, M.-C. Le Pape, A. Minelli, R. Grenon, and G Carrier. Impact of Multipole Matching Resolution on Supersonic Aircraft Sonic Boom Assesment. *4th EUCASS*, 2011.

[10] NASA LRC. High-Speed Research: Sonic Boom, vol. I. Technical Report CP-3172, NASA, 1992.

[11] NASA LRC. High-Speed Research: Sonic Boom, vol. II. Technical Report CP-3173, NASA, 1992.

[12] J. Morgenstern, N. Norstrud, M. Stelmack, and P. Jha. Advanced Concept Studies for Supersonic Commercial Transport Entering Service in 2030-35 (N+3) . *AIAA paper 2010-5114*, 2010.

[13] L.B. Jones. Lower Bounds for the Pressure Jump of the Bow Shock of a Supersonic Transport. *Aeronautical Quarterly*, 21:1–17, 1970.

[14] J. Petty. Lower Bounds for Sonic Boom Considering the Negative Overpressure Region. *Journal of Aircraft*, 7:375–377, 1970.

[15] R. Seebass and R. George. Sonic Boom Minimization. *The Journal of the Acoustical Society of America*, 51:686–694, 1971.

[16] C. Darden. Sonic-Boom Minimization With Nose-Bluntness Relaxation. *NASA TP-1348*, 1979.

[17] J.W. Pawlowski, D.H. Graham, C.H. Boccadoro, P.G. Coen, and D.J. Maglieri. Origins and Overview of the Shaped Sonic Boom Demonstration Program. *AIAA paper 2005-5*, 2005.

[18] M. Honda and K. Yoshida. D-SEND Project for Low Sonic Boom Design Technology. *In Proceedings of 28th International Congress of the Aeronautical Sciences*, 2012.

[19] J. Reuther and A. Jameson. Supersonic Wing and Wing-Body Shape Optimization Using an Adjoint Formulation. *AIAA paper 95-0123*, 1995.

[20] J. Reuther, J.J. Alonso, M.J. Rimlinger, and A. Jameson. Aerodynamic shape optimization of supersonic aircraft configurations via an adjoint formulation on distributed memory parallel computers. *Computers & fluids*, 28(4):675–700, 1999.

[21] D. Sasaki, M. Morikawa, Obayashi. S., and K. Nakahashi. Aerodynamic Shape Optimization of Supersonic Wings by Adaptive Range Multi-objective Genetic Algorithms. *In Proceedings of the First International Conference on Evolutionary Multi-Criterion Optimization*, pages 639–652.

[22] B. Mohammadi and O. Pironneau. Shape optimization in fluid mechanics. *Annu. Rev. Fluid Mech.*, 36:255–279, 2004.

[23] S. Choi, J.J. Alonso, I.M. Kroo, and M. Wintzer. Multifidelity Design Optimization of Low-Boom Supersonic Jets. *AIAA Journal*, 41:106–118, 2008.

[24] N. Seto. Multi-Disciplinary Design Optimization of Supersonic Transport Wing using Surrogate Model. *In Proceedings of 27th International Congress of the Aeronautical Sciences*, 2010.

[25] A. Minelli, I. Salah el Din, and G. Carrier. Inverse Design Method for Low-Boom Supersonic Configurations. *Submitted to AIAA Journal*.

[26] A. Minelli, I. Salah el Din, G. Carrier, A. Zerbinati, and J.-A. Desideri. Cooperation and Competition Strategies in Multi-objective Shape Optimization - Application to Low-boom/Low-drag Supersonic Business Jet. *AIAA paper*, 2013.

[27] D.J. Maglieri. Sonic Boom Flight Research: Some Effects of Airplane Operations and the Atmosphere on Sonic Boom Signatures. Technical note SP-147, NASA, 1967.

[28] E.J. Kane. Some Effects of the Atmosphere on Sonic Boom. Technical note SP-147, NASA, 1967.

[29] Y. Hiroshi and S. Obayashi. Sonic boom variability due to homogeneous atmospheric turbulence. *Journal of Aircraft*, 46(6):1886–1893, 2009.

[30] F. Coulouvrat. The Challenges of Defining an Acceptable Sonic Boom Overland. *AIAA Paper 2009-3384*, 2009.

[31] Aerion corporation. http://aerioncorp.com/uploads/press/20.pdf. *Press release*, 2009.

[32] R. Marchiano, F. Coulouvrat, and R. Grenon. Numerical simulation of shock wave focusing at fold caustics, with application to sonic boom. *The Journal of the Acoustical Society America*, 114.

[33] F. Coulouvrat. Focusing of weak acoustic shock waves at a caustic cusp. *Wave Motion*, 32(3):233–245, 2000.

[34] F. Walkden. The Shock Pattern of a Wing-Body Combination, far from the Flight Path. *Aeronautical quarterly*, IX:164–194, 1958.

[35] L.W. Hunton, R.M. Hicks, and J.P. Mendoza. Some Effects of the Mach Number and Geometry on Sonic Boom. Technical note TN D-4214, NASA.

[36] C.M. Darden. Limitations of linear theory for sonic boom calculations. *Journal of Aircraft*, 30:309–314, 1993.

[37] A.D. Taylor. The TRAPS Sonic Boom Program. Technical memorandum ERL-ARL-87, NOAA, 1980.

[38] D. Blokhintzev. The Propagation of Sound in an Inhomogeneous and Moving Medium. *The Journal of the Acoustical Society of America*, 18:322–328, 1946.

[39] A.R. George. Reduction of Sonic Boom by Azimuthal Redistribution of Overpressure. *AIAA paper 68-159*, 1968.

[40] I. Salah el Din. *Contribution aĺ'Optimisation de la Forme Aérodynamique d'un Avion de Transport Supersonique en Vue de la Réduction du Bang Sonique.* PhD thesis, Université de Poitiers, 2004.

[41] E.A. Haering, J.E. Murray, D.D. Purifoy, D.H. Graham, K.B. Meredith, C.E. Ashburn, and M. Stucky. Airborne Shaped Sonic Boom Demonstration Pressure Measurements with Computational Fluid Dynamics Comparisons. *AIAA paper 2005-9*, 2005.

[42] K.B. Meredith, J.A. Dahlin, D.H. Graham, M.B. Malone, E.A. Haering, J.A. Page, and K.J. Plotkin. Computational Fluid Dynamics Comparison and Flight Test Measurement of F-5E Off-Body Pressures. *AIAA paper 2005-6*, 2005.

[43] R.L. Campbell, M.B. Carter, K.A. Deere, and K.A. Waithe. Efficient Unstructured Grid Adaptation Methods for Sonic Boom Prediction. *AIAA paper 2008-7327*, 2008.

[44] M.B. Carter and K.A. Deere. A grid sourcing and adaptation study using unstructured grids for supersonic boom prediction. *AIAA Paper 6595*, 2008.

[45] W.T. Jones, E.J. Nielsen, and M.A. Park. Validation of 3D Adjoint Based Error Estimation and Mesh Adaptation for Sonic Boom Prediction. *AIAA-2006-1150*, 2006.

[46] A. Loseille and R. Lohner. Anisotropic Mesh Generation Application To High-Fidelity Simulation in CFD. *AIAA paper 2010-0169*, 2010.

[47] A. Loseille and R. Lohner. On 3D anisotropic local remeshing for surface, volume, and boundary layers. *Proc. in 18th International Meshing Roundtable, Springer-Verlag*, pages 611–630, 2009.

[48] Adrien Loseille and Frédéric Alauzet. Continuous mesh framework, Part I: well-posed continuous interpolation error. *SIAM Journal on Numerical Analysis*, 49(1):38–60, 2011.

[49] Adrien Loseille and Frédéric Alauzet. Continuous mesh framework, Part II: validations and applications. *SIAM Journal on Numerical Analysis*, 49(1):61–86, 2011.

[50] P.N. Borsky. Community Reactions to Sonic Booms in the Oklahoma City Area (Parts I and II). Technical report.

[51] C.W. Nixon and H.H. Ubbard. Results of the USAF-NASA-FAA Flight Program to Study Community Responses to Sonic Booms in the Greater St. Louis Area. Technical Report TN D-2705, NASA, 1965.

[52] M. Leatherwood and B.M. Sullivan. A Laboratory Study of Subjective Annoyance Response to Sonic Booms and Aircraft Flyovers. Technical memorandum 109113, NASA, 1994.

[53] T. Ohnuki, K. Hirako, and K. Sakata. National experimental supersonic transport project. *In Proceedings of 25th International Congress of the Aeronautical Science*, 2006.

[54] S. Stevens. Perceived Level of Noise by Mark VII and Decibels(E). *The Journal of the Acoustical Society of America*, 54:575–601, 1972.

[55] CHABA. *Community Response to High-Energy Impulsive Sounds: An Assessment of the Field Since 1981.* The National Academies Pres, Washington, DC, 1996.

[56] J. Kang and A.D. Pierce. The effect of molecular relaxation processes in air on the rise time of sonic booms. *International Congress on Recent Developments in Air- and Structure-Borne Sound and Vibration, Proceedings.*, 1:97–104, 1990.

[57] K.R. Elmer and M.C. Joshi. Variability of measured sonic boom signatures: volume 1 - technical report. Contractor Report CR-191483, NASA, 1994.

[58] T.H. Higgins. Psychophisical tests of potential design/certification criteria for advanced supersonic aircraft. Technical note AD-A009 296, NTIS, 1975.

[59] K.J. Plotkin, N. Sizov, and J.M. Morgenstern. Examination of Sonic Boom Minimization Experienced Indoors. *AIAA paper 2008-57*, 2008.

[60] B.L. Clarkson and W.H. Mayes. Sonic Boom Induced Building Structure Responses Including Damage. *Journal of the Acoustical Society America.*, 51:742–757, 1971.

[61] L.C. Sutherland and J. Czech. Evaluation of human response to structural vibrations induced by sonic booms. *Wyle Research Report.*

[62] N.V. Sizov, K.J. Plotkin, and C.M. Hobbs. Predicting transmission of shaped sonic booms into a residential house structure. *The Journal of the Acoustical Society of America*, 127:33–47, 2010.

[63] J.R. Wilson. Sst research. breaking new barriers. *Aerospace America*, pages 20–31, January 2013.

[64] K.W. Sidwell, P.K. Bornach, and J.E. Bussoletty. PANAIR - A Computer Program for Predictind Subsonic or Supersonic Linear Potential Flows About Arbitrary Configurations Unsing an Higher Order Panel Method. Volume II, User's Manual. Contract report CR 3252, NASA, 1980.

[65] W. R. Sears. *General Theory of High Speed Aerodynamics.* Princeton University Press, 1954.

[66] L. Cambier and J.-P. Veuillot. Status of the elsA CFD Software for Flow Simulation and Multidisciplinary Applications. *AIAA paper 2008-664*, 2008.

[67] T.T. Bui. CFD Analysis of Nozzle Jet Plume Effects on Sonic Boom Signature. Technical Report TM-2009-214650, NASA, 2009.

[68] P.L. Roe. Approximate Riemann Solvers, Parameter Vectors and Difference Schemes. *Journal of Computational Physics*, 43:357–372, 1981.

[69] A. Harten, J.M. Hyman, and P.D. Lax. On Finite-Difference Approximations and Entropy Conditions for Shocks. *Comm. Pure Appl. Math.*, 29:297–322, 1976.

[70] G.D. Van Albada, B. Van Leer, and W.W. Roberts. A Comparative Study of Computational Methods in Cosmic Gas Dynamics. *Astron. Astrophysics*, 108:76–84, 1982.

[71] D. Brown and L.C. Sutherland. Sonic boom (human response and atmospheric effects) outdoor-to-indoor response to minimized sonic booms. 1(In 1st Annual High-Speed Research Workshop):1345–1363, 1992.

[72] P. Chevalier, B. Courbet, D. Dutoya, P. Klotz, E. Ruiz, J. Troyes, and P. Villedieu. CEDRE: Development and Validation of a Multiphysic Computational Software. *In Proceedings of 1st EUCASS congress*, 2005.

[73] A. Loseille and F. Alauzet. Continuous mesh model and well-posed continuous interpolation error estimation. Technical report.

[74] F. Mclean. Some Nonasymptotic Effects on The Sonic Boom of Large Airplanes. *NASA TN D-2877*, 1965.

[75] W.D. Hayes. Brief Review of the Basic Theory. *Sonic Boom Research, NASA SP-147*, 1967.

[76] A. Haas and I. Kroo. A Multi-Shock Inverse Design Methid for Low-Boom Supersonic Aircraft. *AIAA paper 2010-843*, 2010.

[77] W.D. Hayes, J.H. Gardner, D.A. Coughey, and F.B. Weiskopf. Theoretical Problems Related to Sonic Boom. *NASA SP-255*, 1970.

[78] C. Howell, A. Sigalla, and E. Kane. Sonic Boom Considerations in Aircraft Design. *AGARD conference proceedings*, 46, 1969.

[79] S.K. Rallabhandi and D.N. Mavris. Sonic Boom Minimization Using Inverse Design and Probabilistic Acoustic Propagation. *Journal of Aircraft*, 43(6):1815–1828, 2006.

[80] R. Mack. A Supersonic Business-Jet Concept Designed for Low Sonic Boom. *NASA TM-2003-212435*, 2003.

[81] K.J. Plotkin, S.K. Rallabhandi, and W. Li. Generalized Formulation and Extension of Sonic Boom Minimization Theory for Front and Aft Shaping. *AIAA paper 2009-1052*, 2009.

[82] A. George and K.J. Plotkin. Sonic Boom Waveforms and Amplitudes in a Real Atmosphere. *AIAA Journal*, 7:1978–1981, 1969.

[83] Ciyou Zhu, Richard H Byrd, Peihuang Lu, and Jorge Nocedal. Algorithm 778: L-bfgs-b: Fortran subroutines for large-scale bound-constrained optimization. *ACM Transactions on Mathematical Software (TOMS)*, 23(4):550–560, 1997.

[84] R.L. Barger and M.S. Adams. Fuselage Design for a Specified Mach-Sliced Area Distribution. Technical Report TP-2975, NASA, 1990.

[85] R. J. Mack and K. E. Needleman. A Semiempirical Method for Obtaining Fuselage Normal Areas from Fuselage Mach Sliced Areas. Technical report TM-4228, NASA, 1991.

[86] W. Li, W. Shields, and D. Le. Interactive Inverse Design Optimization of Fuselage Shape for Low-Boom Supersonic Concepts. *AIAA paper 2008-136*, 2008.

[87] F. Palacios, J.J. Alonso, M. Colonno, J. Hicken, and T. Lukaczyk. Adjoint-based method for supersonic aircraft design using equivalent area distributions. *AIAA paper 2012-0269*.

[88] L. Cambier and M. Gazaix. An Efficient Object-Oriented Solution to CFD Complexity. *AIAA paper 02-0108*, 2002.

[89] K. Rasheed. GADO: A Genetic Algorithm for Continuous Design Optimization. Technical Report DCS-TR-352, The State University of New Jersey, 1998.

[90] DAKOTA, A Multilevel Parallel Object-Oriented Framework for Design Optimization, Parameter Estimation, Uncertainty, Quantification, and Sensitivity Analysis. Reference manual, Sandia National Laboratoires, 2007.

[91] J.R. Martins, P. Sturdza, and J.J. Alonso. The complex-step derivative approximation. *ACM Transactions on Mathematical Software (TOMS)*, 29(3):245–262, 2003.

[92] A. Jameson. Optimum aerodynamic design using control theory. *Computational Fluid Dynamics Review*, 3:495–528, 1995.

[93] N. Hansen and A. Ostermeier. Completely derandomized self-adaptation in evolution strategies. *Evolutionary Computation*, 9:159–195, 2001.

[94] J. Samareh. A Survey of Shape Parameterization Techniques. *NASA-CP-1999-209136*, 28:675–700, 1999.

[95] R.J. Renka. Interpolatory tension splines with automatic selection of tension factors. *SIAM Journal on Scientific and Statistical Computing*, 8(3):393–415, 1987.

[96] T.W. Simpson, J.D. Poplinski, P.N. Koch, and J.K. Allen. Metamodels for computer-based engineering design: survey and recommendations. *Engineering with computers*, 17:129–150, 2001.

[97] N.V. Queipo, R.T. Haftka, W. Shyy, T. Goel, R. Vaidyanathan, and P. Kevin Tucker. Surrogate-based analysis and optimization. *Progress in Aerospace Sciences*, 41:1–28, 2005.

[98] A. Saltelli, M. Ratto, T. Andres, F. Campolongo, J. Cariboni, D. Gatelli, M. Saisana, and S. Tarantola. *Global Sensitivity Analysis. The Primer*. John Wiley & Sons., 2008.

[99] J. Roskam. *Airplane Design. Part VI: Preliminary Calculation of Aerodynamic, Thrust and Power Characteristics*. DARCorporation, 2000.

[100] R. Whitcomb. A Study of the Zero-Lift Drag-Rise Characteristics of Wing-Body Combinations Near the Speed of Sound. *NACA Research Memorandum L52H03*, pages 519–539, 1952.

[101] Hoerner S. *Résistance a l'avancement dans les fluides*. Gauthier-Villars, Paris, 1965.

[102] D. Hamby. A Review of Techniques for Parameter Sensitivity Analysis of Environmental Models. *Environmental Monitoring and Assessment*, 32:135–154, 1994.

[103] I.M. Sobol. Global sensitivity indices for nonlinear mathematical models and their Monte Carlo estimates. *Mathematics and computers in simulation*, 55:271–280, 2004.

[104] W.J. Welch, R.J. Buck, J. Sacks, H.P. Wynn, T.J. Mitchell, and M.D. Morris. Screening, predicting, and computer experiments. *Technometrics*, 34(1):15–25, 1992.

[105] W.D. Middleton and J.L. Lundry. A system for aerodynamic design and analysis of supersonic aircraft. Technical Report CR - 3351, NASA, 1980.

[106] Wervaecke C. DTP OPTIMISATION 2 - Hybrid stochastic-gradient based method for aerodynamic shape optimization. (RT 2/16642 DAAP), 2012.

[107] J.R.R.A. Martins and A.B. Lambe. Multidisciplinary design optimization: A Survey of architectures. *In press AIAA Journal*, 2013.

[108] J. Sobieszczanski-Sobieski and R.T. Haftka. Multidisciplinary aerospace design optimization: survey of recent developments. *Structural and Multidisciplinary Optimization*, 14:1–23, 1997.

[109] R.T. Marler and J.S. Arora. Survey of Multi-Objective Optimization Methods for Engineering. *Structural and Multidisciplinary Optimization*, 26:369–395, 2004.

[110] K. Miettinen. *Nonlinear multiobjective optimization.* Springer, New York, 1999.

[111] J.A. Desideri. Multiple-Gradient Descent Algorithm (MGDA). Research Report 6953, INRIA, 2009.

[112] E. Zitzler and L. Thiele. Multiobjective evolutionary algorithms: a comparative case study and the strength Pareto approach. *IEEE Trans Evol Comput*, 3:257–271, 1999.

[113] E. Zitzler, K. Deb, and L. Thiele. Comparison of multiobjective evolutionary algorithms: empirical results. *Evol. Comput.*, 8:173–195, 2000.

[114] C. Coello, G.B. Lamont, and D.A. Van Veldhuizen. *Evolutionary algorithms for solving multi-objective problems*. Springer, 2007.

[115] A. Konak, D. Coit, and A. Smith. Multi-objective optimization using genetic algorithms: a tutorial. *Reliab. Eng. Syst. Saf.*, 91:992–1007, 2006.

[116] S.F. Adra, I. Griffin, and P.J. Fleming. A Comparative Study of Progressive Preference Articulation Techniques for Multiobjective Optimisation. *Evolutionary Multi-Criterion Optimization*, 4403:908–921, 2007.

[117] C.M. Darden. Sonic Boom Theory: Its Status in Prediction and Minimization. *Journal of Aircraft*, 14:569–576, 1977.

[118] M. Sato, T. Kumano, M. Yonezawa, H. Yamashita, S. Jeong, and S. Obayashi. Low-Boom and Low-Drag Optimization of the Twin Engine Version of Silent Supersonic Business Jet. *Journal of Fluid Science and Technology*, 3:576–585, 2008.

[119] K. Chiba, Y. Makino, and T.i Takatoya. Multidisciplinary design exploration of wing shape for silent supersonic technology demonstrator. *AIAA paper 4167*, 2007.

[120] H.-S. Chung and J.J. Alonso. Multiobjective optimization using approximation model-based genetic algorithms. *AIAA paper*, 4325, 2004.

[121] S.K. Rallabhandi and D.N. Mavris. Aircraft Geometry Design and Optimization for Sonic Boom Reduction. *Journal of Aircraft*, 44:35–47, 2007.

[122] N. Khasdeo, O.A. Kandil, and I.A. Ozcer. Optimization of Delta Wing Geometry parameters for Sonic Boom Mitigation. *AIAA paper 2007-4109*, 2007.

[123] A. Chattopadhyay and J. Rajadas. Enhanced Multiobjective Optimization Technique for Comprehensive Aerospace Design. Contract Report 99-206125, NASA, 1998.

[124] S. Nadarajah, A. Jameson, and J.J. Alonso. An adjoint method for the calculation of remote sensitivities in supersonic flow. *AIAA paper 02-261*, 2002.

[125] M. Chan. *Supersonic Aircraft Optimization for Minimizing Drag and Sonic Boom.* PhD thesis, Stanford University, 2003.

[126] M. Vázquez, A. Dervieux, and B. Koobus. Aerodynamical and sonic boom optimization of a supersonic aircraft. Technical Report RR-4520, INRIA, July 2002.

[127] S.S. Rao. *Engineering optimization: theory and practice.* Wiley, 2009.

[128] L. Zadeh. Optimality and non-scalar-valued performance criteria. *IEEE Trans Automat Contr.*, 8:59–60, 1963.

[129] I. Das and J. Dennis. A closer look at drawbacks of minimizing weighted sums of objectives for pareto set generation in multicriteria optimization problems. *Structural Optimization*, 14:63–69, 1997.

[130] A. Minelli, G. Carrier, J.A. Desideri, R. Duvigneau, and I. Salah El Din. Aeroacoustic optimization of a supersonic business jet. Research Report RR-7477, INRIA, December 2010.

[131] P. Hajela and C.-Y. Lin. Genetic search strategies in multicriterion optimal design. *Structural optimization*, 4(2):99–107, 1992.

[132] E. Zitzler, M. Laumanns, and L. Thiele. SPEA2 : Improving the strength Pareto evolutionary algorithm. Technical report 103, Swiss Federal Institute of Technology (ETH) Zurich, 2001.

[133] G.G. Yen and H. Lu. Dynamic multiobjective evolutionary algorithm: adaptive cell-based rank and density estimation. *IEEE Trans Evol Comput*, 7:253–274, 2003.

[134] D. Corne, N.R. Jerram, J. Knowles, and J. Oates. PESA-II: region-based selection in evolutionary multiobjective optimization. *Proceedings of the genetic and evolutionary computation conference (GECCO- 2001)*, 2001.

[135] Knowles J and Corne D. The pareto archived evolution strategy: a new baseline algorithm for pareto multiobjective optimisation. *Proceedings of the 1999 congress on evolutionary computation- CEC99*, 1999.

[136] H. Lu and G.G. Yen. Rank-density-based multiobjective genetic algorithm and benchmark test function study. *IEEE Trans Evol Comput*, 7:325–343, 2003.

[137] J. Horn, N. Nafpliotis, and D.E. Goldberg. A niched Pareto genetic algorithm for multiobjective optimization. *In Proceedings of the first IEEE conference on evolutionary computation.*, 1994.

[138] C.M. Fonseca and P.J. Fleming. Multiobjective genetic algorithms. *IEEE colloquium on Genetic Algorithms for Control Systems Engineering*, 1993.

[139] JD. Schaffer. Multiple objective optimization with vector evaluated genetic algorithms. *Proceedings of the international conference on genetic algorithm and their applications*, 1985.

[140] K. Deb, A. Pratap, S. Agarwal, and T. Meyarivan. A fast and elitist multiobjective genetic algorithm: NSGA-II. *Evolutionary Computation, IEEE Transactions on*, 6(2):182–197, 2002.

[141] M.A. Potter and K.A. de Jong. Cooperative coevolution: An architecture for evolving coadapted subcomponents. *Evolutionary Computation*, 8:1–29, 2000.

[142] P. Gill, W. Murray, and M. Wright. *Practical optimization.* Academic Press Inc. Harcourt Brace Jovanovich Publishers, 1981.

[143] K. Deb, L. Thiele, M. Laumanns, and E. Zitzler. Scalable Test Problems for Evolutionary Multi-Objective Optimization. Technical Report 112, Institut für Technische Informatik und Kommunikationsnetze, 2001.

[144] A. Zerbinati, J.A. Désidéri, and R. Duvigneau. Comparison between MGDA and PAES for multi objective optimization. Research Report 7667, INRIA, 2011.

[145] J.-A. Desideri A. Zerbinati and R. Duvigneau. Application of Metamodel-Assisted Multiple-Gradient Descent Algorithm (MGDA) to Air-Cooling Duct Shape Optimization. In *Proceedings of ECCOMAS 2012*, 2012.

[146] G.N. Vanderplaats. CONMIN - A FORTRAN program for constrained function minimization: user's manual. Technical manual TM X-62,282, NASA, 1973.

[147] J. Sobieszczanski-Sobieski. Optimization by decomposition: A step from hierarchic to non-hierarchic systems. Contractor Report CP 3031, NASA, 1988.

[148] T.L. Vincent. Game theory as a Design Tool. *Jo. of Mech., Trans., and Autom. in Design.*, 105:165–170, 1983.

[149] J. Periaux, H.Q. Chen, B. Mantel, M. Sefrioui, and H.T. Sui. Combining game theory and genetic algorithms with application to DDM-nozzle optimization problems. *Finite Elements in Analysis and Design*, 37:417–429, 2001.

[150] J.F. Nash. Non-cooperative games. *Ann. Math.*, 54:286–295, 1951.

[151] M. Simaan and J.B. Cruz. On the Stackelberg Strategy in Nonzero-Sum Games. *Journal of Optimization Theory and Applications.*, 11:533–555, 1973.

[152] Z. Tang, J.A. Désidéri, and J. Périaux. Multicriterion aerodynamic shape design optimization and inverse problems using control theory and nash games. *Journal of Optimization Theory and Applications*, 135(3):599–622, 2007.

[153] J.A. Désidéri. Cooperation and competition in multidisciplinary optimization - Application to the aero-structural aircraft wing shape optimization. *Computational Optimization and Application*, 52:3–28, 2012.

[154] J.A. Désidéri. Split of Territories. Research Report 6108, INRIA, 2007.

[155] M.J.D. Powell. A direct search optimization method that models the objective and constraint functions by linear interpolation. *Advances in Optimization and Numerical Analysis*, 275:51–67, 1994.

[156] `http://docs.scipy.org/doc/scipy/reference/index.html`.

[157] T. Kohonen. Self-Organized Formation of Topologically Correct Feature Maps. *Biological Cybernetics*, 43:59–69, 1982.

[158] National Aeronautics, Space Administration, and United States Air Force. US Standard Atmosphere 1976. *TM-X-74335*, 1976.

[159] ICEM 13.0 user manual. 2010. User manual, ANSYS INC. Canonsburg, PA, 2010.

[160] J.-L. Godard, S. Ben Khelil, V. Brunet, G. Carrier, S. Esquieu, R. Grenon, J.-L. Hantrais-Gervois, and F. Möens. Activities performed in 2008 by DAAP/ACI Unit under Internal Resources (RGF). Technical report RTS 7/13514 DAAP, ONERA, 2008.

[161] T.W. Sederberg and S.R. Parry. Free-form deformation of solid geometric models. *SIGGRAPH Comput. Graph.*, 20(4):151–160, August 1986.

[162] T. Lehnhäuser and M. Schäfer. A numerical approach for shape optimization of fluid flow domains. *Computer methods in applied mechanics and engineering*, 194(50):5221–5241, 2005.

[163] `http://deap.gel.ulaval.ca/doc/default/examples/index.html`.

[164] `http://docs.python.org/2/library/tkinter.html`.

[165] K. Deb, A. Sinha, and S. Kukkonen. Multi-objective test problems, linkages, and evolutionary methodologies. In *Proceedings of the 8th annual conference on Genetic and evolutionary computation*, pages 1141–1148. ACM, 2006.

[166] S. Obayashi. Evolutionary Multi-Criterion Optimization. In *4th International Conference, EMO.* Springer, 2007.

[167] F. Kursawe. A variant of evolution strategies for vector optimization. *Parallel Problem Solving from Nature*, pages 193–197, 1991.

[168] N. Srinivas and K. Deb. Multiobjective Optimization Using Nondominated Sorting in Genetic Algorithms. *Evolutionary Computation*, 2:221–248, 1994.

[169] T.M. Donahue and A.J. Grobecker. Climatic Impact Assessment Program. *Eos, Transactions American Geophysical Union*, 56(4):210, 1975.

[170] G.J.M. Velders, S.O. Andersen, J.S. Daniel, D.W. Fahey, and M. McFarland. The importance of the Montreal Protocol in protecting climate. *Proceedings of the National Academy of Sciences*, 104(12):4814–4819, 2007.